

Arbeit zur Erlangung des akademischen Grades
eines Doktors der Naturwissenschaften (Dr. rer. nat.)

Enabling Next-generation Particle Cascade Simulations

Implementing the Propagation Software PROPOSAL as an
Interaction Model for CORSIKA 8

Jean-Marco Alameddine
geboren in Iserlohn

2024

Astroteilchenphysik
Fakultät Physik
Technische Universität Dortmund

Erstgutachter: Prof. Dr. Dr. Wolfgang Rhode
Zweitgutachter: Prof. Dr. Kevin Kröniger
Abgabedatum: 19. Januar 2024

Abstract

The observation of cosmic messenger particles provides unique insights into astrophysical processes. As high-energy nuclei or photons reach the Earth's atmosphere, a particle cascade called extensive air shower is initiated. By detecting secondary shower particles, the energy, direction, and identity of the initial messenger particle can be reconstructed. This task heavily relies on an accurate simulation of particle cascades. A major challenge in this context is the muon puzzle – a significant, as yet unresolved muon deficit in air shower simulations compared to experimental observations.

To overcome limitations of existing shower simulation codes, the next-generation simulation framework CORSIKA 8 is currently under development. This work describes the implementation of the Monte Carlo simulation code PROPOSAL as the first electromagnetic and muonic interaction model in CORSIKA 8. PROPOSAL describes muon interactions with maximal precision, minimizing possible systematic uncertainties in the description of the muonic shower component in CORSIKA 8. The code structure of PROPOSAL is modularized, and a description of electromagnetic processes is implemented. An interface between CORSIKA 8 and PROPOSAL is written, which is validated by comparisons with previous CORSIKA versions. Notably, these validations reveal that CORSIKA 8 shows a 5% increase of muons in hadronic showers. As this number is insufficient to solve the muon puzzle, inaccuracies in muon propagation are ruled out as a possible cause. Furthermore, this work allows for the first physics-complete shower simulations with CORSIKA 8, which is a crucial step toward its first release. For the scientific community, CORSIKA 8 is going to be a powerful tool for the simulation and investigation of particle cascades, especially to further understand and solve the muon puzzle.

Kurzfassung

Die Beobachtung kosmischer Botenteilchen ermöglicht einzigartige Einblicke in astrophysikalische Prozesse. Hochenergetische Atomkerne und Photonen initiieren beim Erreichen der Erdatmosphäre eine Teilchenkaskade, welche Luftschauer genannt wird. Durch die Detektion ausgelöster Sekundärteilchen können Energie, Richtung und Teilchenart des Ursprungsteilchens rekonstruiert werden. Diese Aufgabe erfordert präzise Simulationen der Teilchenkaskaden. Eine bedeutende Herausforderung in diesem Zusammenhang ist das Myonrätsel – ein signifikantes, jedoch bislang ungeklärtes Defizit der Anzahl an Myonen in Luftschauersimulationen im Vergleich zu experimentellen Beobachtungen.

Aufgrund der Einschränkungen bestehender Software zur Simulation von Teilchenkaskaden befindet sich das Simulationsframework CORSIKA 8 aktuell in der Entwicklung. In dieser Arbeit wird die Implementierung des Monte-Carlo-Simulationsprogramms PROPOSAL als erstes elektromagnetisches und myonisches Interaktionsmodell für CORSIKA 8 beschrieben. PROPOSAL ermöglicht eine höchst präzise Beschreibung von Myoninteraktionen, wodurch die systematische Unsicherheit in der Beschreibung der myonischen Schauerkomponente in CORSIKA 8 minimiert werden kann. Die Codestruktur von PROPOSAL wurde modularisiert, sowie eine Beschreibung elektromagnetischer Wechselwirkungen implementiert. Zudem wurde ein Interface zwischen PROPOSAL und CORSIKA 8 geschrieben und durch Vergleiche mit früheren CORSIKA-Versionen validiert. CORSIKA 8 weist in diesen Vergleichen eine um 5 % erhöhte Anzahl an Myonen in Simulationen von hadronischen Schauern auf. Dieser Anstieg ist nicht ausreichend, um die Diskrepanz im Myonpuzzle zu erklären, sodass Ungenauigkeiten in der Myonpropagation als mögliche Erklärung ausgeschlossen werden können. Des Weiteren ermöglicht diese Arbeit die ersten physikalisch vollständigen Simulationen von Teilchenkaskaden mit CORSIKA 8, was einen entscheidenden Schritt im Hinblick auf die Veröffentlichung von CORSIKA 8 darstellt. CORSIKA 8 stellt ein mächtiges Werkzeug für die Simulation und Untersuchung von Teilchenkaskaden zur Verfügung, welches insbesondere zum Verständnis sowie zur Lösung des Myonrätsels beitragen wird.

Contents

1	Introduction	1
2	Astroparticle Physics	3
3	Extensive Air Showers	8
3.1	Description of Electromagnetic Particle Cascades	9
3.2	Description of Hadronic Particle Cascades	12
3.3	Detection of Extensive Air Showers	15
3.4	The Muon Puzzle in Extensive Air Showers	19
4	The Lepton and Photon Propagator PROPOSAL	24
4.1	Simulation Principles	25
4.2	Recent Updates	32
4.3	Applications in Neutrino Astronomy and Particle Physics	36
5	The Shower Simulation Framework CORSIKA	42
5.1	Extensive Air Shower Simulations with CORSIKA 7	43
5.2	CORSIKA 8: The Next Generation of Particle Cascade Simulations	46
5.3	Usage of PROPOSAL as an Interaction Model for CORSIKA 8	52
6	Physics in Electromagnetic Showers	57
6.1	Electron and Positron Interactions	57
6.2	Photon Interactions	76
6.3	The Landau-Pomeranchuk-Migdal Effect	93
7	Air Shower Simulations with CORSIKA 8	103
7.1	Comparison of the Utilized Cross Sections	104
7.2	Comparison of Electromagnetic Showers	106
7.3	Comparison of Hadronic Showers	121
7.4	Radio Emission of Electromagnetic Showers	126
7.5	Simulation of Cross-Media Showers	131
8	Discussion and Outlook	134

A Supplementary Material	136
A.1 Derivation of the Energy Integral	136
A.2 Hadronic Interaction Models in CORSIKA 7 and CORSIKA 8	138
A.3 Visualization of the Step Function of CORSIKA 8	138
A.4 Default Interaction Parametrizations in CORSIKA 8	140
A.5 Atomic Form Factors	141
A.6 Radiation Logarithm Constants	144
A.7 Kinematics of Two-body Interactions with Atomic Electrons	144
A.8 Description of Resonances for the Photohadronic Cross Section	145
A.9 Parametrization of the Structure Function F_2	146
A.10 Comparison of the Utilized Electron Cross Section	148
A.11 Parametrization of the U.S. Standard Atmosphere	148
A.12 Simulation of the LPM Effect for Proton Showers	150
A.13 Full Radio Simulations of Electromagnetic Showers	151
B Reproducibility Information	156
C Additional Software Used for this Work	157
Glossary	158
Author's Publications Related to this Work	159
Bibliography	160
Acknowledgements	178

1 Introduction

The general goal of astroparticle physics is the expansion of knowledge about astrophysical processes, particle physics, or cosmology by the observation of cosmic messenger particles. When atomic nuclei or high-energy photons reach the Earth, they interact with nuclei in the atmosphere, initiating a particle cascade called an extensive air shower. As the particle flux decreases sharply with increasing energy, two observational approaches for the detection of cosmic messengers are possible: For energies where the corresponding particle flux is sufficient, which is below ≈ 100 TeV for cosmic nuclei [96] and below ≈ 100 GeV for photons [80], direct observations via space-based telescopes are feasible. For higher energies, the scarcity of events requires an indirect, ground-based observation, where the secondary particles created in the extensive air showers are detected. However, reconstructing the properties of the initial messenger particle based on measurements of secondary particles is a challenging task, as the initial information is convoluted over several generations of stochastic particle interactions. Furthermore, the detector signal of air shower experiments can not be calibrated, as artificial sources with known properties do not exist. Therefore, computer simulations, which accurately model the complex dynamics of particle cascades, are needed. It is crucial to minimize systematic uncertainties of air shower simulations, as these limit the prospects of high-energy astroparticle physics. A key challenge in this context is the muon puzzle, which describes a significant excess in experimentally detected muons compared to the expectation from air shower simulations.

For over 30 years, the Monte Carlo program CORSIKA [113] has been the standard for the simulation of extensive air showers, used by the majority of experiments in astroparticle physics. However, several limitations, both from a technical and physical point of view, restrict the possibilities of the existing code: For example, the code structure is monolithic, which severely complicates the extension and maintenance of the software, and particle cascades can only be simulated in air with limited options to parametrize the atmospheric density. To overcome these limitations, a complete rewrite of the existing code, named CORSIKA 8, was started in 2018. CORSIKA 8 has the goal of providing a modular, flexible, and well-understood framework for the simulation of particle cascades in arbitrary environments [88]. Within CORSIKA 8, the electromagnetic and muonic shower component is simulated by the lepton and photon propagation software PROPOSAL

[29, 143]. PROPOSAL is a well-established framework, as it has been verified for the simulation of muon and tau interactions, especially in the context of simulations for underground observatories. Using PROPOSAL within CORSIKA 8 guarantees the highest precision for the propagation of muons in particle showers, which is especially important to minimize the impact of corresponding systematic uncertainties on the muon puzzle. Additionally, PROPOSAL has been extended to allow for the simulation of electrons, positrons, and high-energy photon processes.

This work describes the preparation of PROPOSAL for its usage in the context of particle cascade simulations, both from a physical and technical point of view; the implementation of an interface to CORSIKA 8; and finally, the analysis and validation of simulated particle cascades. This allows for the production of the first physics-complete simulations of particle cascades with CORSIKA 8. This thesis is structured as follows: In [Chapter 2](#), the foundations and research goals of astroparticle physics are briefly outlined. [Chapter 3](#) provides an introduction to the theory of extensive air showers, the underlying observation methods, and the muon puzzle. In [Chapter 4](#), the software PROPOSAL is presented. This includes an introduction of the basic methodical principles, as well as the description of improvements and preparations necessary to use PROPOSAL as a framework in the context of particle cascade simulations. [Chapter 5](#) introduces the framework CORSIKA, beginning with a description of CORSIKA 7 and its restrictions, followed by the introduction of the concept and methodology of CORSIKA 8, and finally, the description of the implemented interface between CORSIKA 8 and PROPOSAL. In [Chapter 6](#), the theoretical foundations of interaction processes relevant to electrons, positrons, and high-energy photons, their methodical treatment, and the consequent implementation in PROPOSAL are explained. Notable challenges in this context are the implementation of electronuclear processes, multiple scattering of charged particles, and the description of the [Landau-Pomeranchuk-Migdal \(LPM\)](#) suppression. Lastly, in [Chapter 7](#), the implemented methods and processes are validated by comparing CORSIKA 8 shower simulations with simulations from earlier CORSIKA versions. This includes the analysis of the underlying cross sections, longitudinal and lateral shower characteristics, and the radio emission of air showers, where the latter is highly correlated to a correct description of the electromagnetic shower development. Furthermore, the impact on the muon number in air showers is evaluated.

2 Astroparticle Physics

Astroparticle physics describes the systematic study of elementary particles that originate from space, providing insights into astrophysics, particle physics, and cosmology. The discovery of cosmic rays by Victor Hess in 1912, who measured an increasing ionization rate with height in a series of balloon experiments, is often seen as the origin of this field of research [89]. Over the last century, astroparticle physics has evolved drastically, shaping a field diverse in its research questions and experimental methods. Figure 2.1 shows an illustration of three different cosmic messenger particles that are commonly used for observations in modern astroparticle physics: Cosmic rays, gamma rays, and neutrinos. The properties of these messengers and their context in the current state of research in astroparticle physics are described in the following.

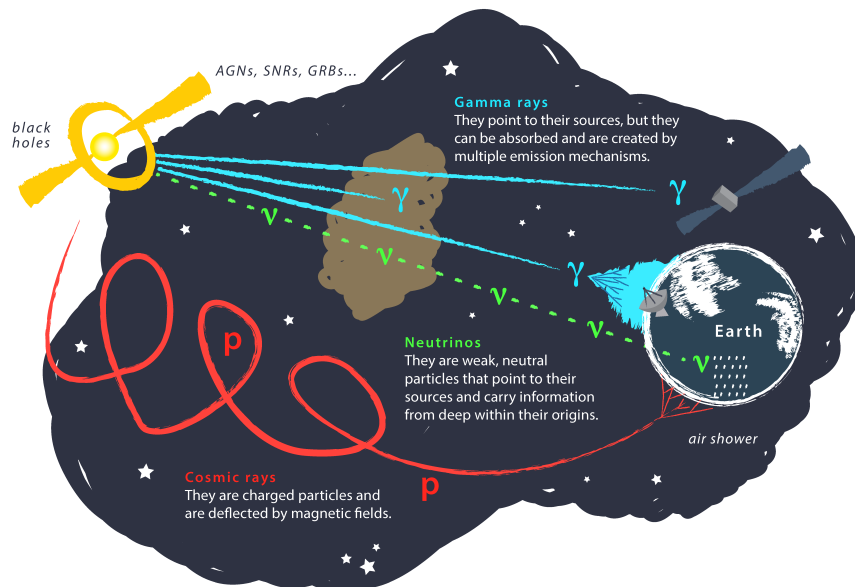


Figure 2.1: Visualization of messenger particles in astroparticle physics and their basic characteristics. Figure from [127].

Cosmic Rays

Every second, approximately 1000 atomic nuclei per square meter, originating almost exclusively from outside the solar system, reach the Earth's atmosphere [96]. These charged particles, composed of $\approx 90\%$ protons, $\approx 9\%$ helium, and of heavier nuclei, are called cosmic rays. Their energy distribution starts below 1 GeV and extends to energies of more than 10^{11} GeV, as recently confirmed by the cosmic ray experiment Telescope Array which detected a cosmic ray with an estimated energy of 2.44×10^{11} GeV [8]. Despite spanning more than twelve orders of magnitude, the cosmic ray energy spectrum can be described by a power law of the form $E \propto E^{-\gamma}$ with relatively few features, as shown in Figure 2.2. Because cosmic rays are charged,

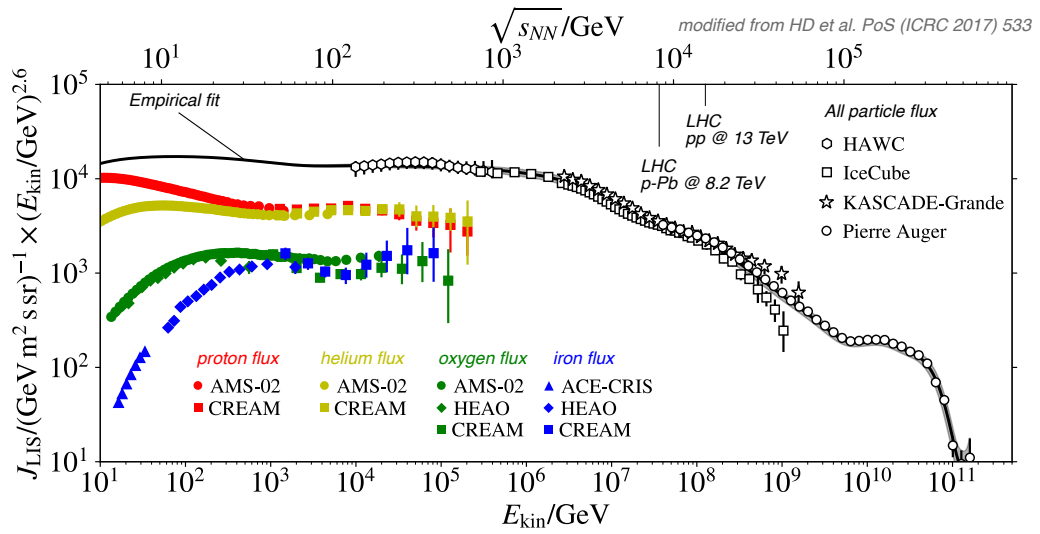


Figure 2.2: Measurements of the cosmic ray energy spectrum for both the all-particle flux, shown in black, and the flux for different types of nuclei, shown in color. Note that the flux is scaled by a factor of $E^{2.6}$ to highlight the substructures of the spectrum. The upper x-axis shows the corresponding center-of-mass energies of nucleon-nucleon collisions together with the maximum collision energies at the Large Hadron Collider, illustrating that the energies of cosmic rays can far exceed the highest energies reached by man-made accelerators. Figure from [34].

they are deflected in the interstellar medium, meaning that the correlation between their arrival direction and origin is lost. This makes it impossible to pinpoint their sources, except for cosmic rays of the highest energies. By studying the energy distribution as well as the energy-dependent composition of cosmic rays, which is also illustrated in Figure 2.2, information about the possible source classes of cosmic rays, the underlying acceleration mechanisms, and their propagation in the interstellar medium can be obtained.

As cosmic rays approach the Earth, they interact with nuclei in the atmosphere, initiating a particle cascade called extensive air shower, explained in detail in [Chapter 3](#). Therefore, their direct detection from the Earth's surface is not possible. One approach to observe cosmic rays is to measure them at very high altitudes before they cascade, using space-based experiments such as AMS-02 (**A**lpha **M**agnetic **S**pectrometer) [25] or balloon experiments like CREAM (**C**osmic **R**ay **E**nergetics **A**nd **M**ass) [227]. However, since the cosmic ray flux falls rapidly with increasing energy, in combination with the limited detection area of these types of experiments, this approach is only feasible up to energies of ≈ 100 TeV. Therefore, the only possible approach at higher energies is the indirect detection of cosmic rays via the air showers they initiate, using ground-based observatories. The underlying experimental methods and challenges in reconstructing the properties of cosmic ray particles from air shower observations are described in [Section 3.3](#). Note that due to the abundance of cosmic ray particles in comparison to other messengers, which are described in the following, cosmic rays and their induced secondary particles often pose a background for other experiments, e.g., in gamma-ray astronomy or underground neutrino observatories.

Gamma Rays

Gamma-ray astronomy describes the observation of photons with energies above ≈ 0.5 MeV [80], up to energies of more than a PeV, where the current upper energy limit has been established by LHAASO (**L**arge **H**igh **A**ltitude **A**ir **S**hower **O**bservatory), reporting the observation of a gamma ray with an energy of 1.4 PeV [72]. In contrast to cosmic rays, gamma rays are uncharged and propagate in a nearly straight line from their origin toward Earth, which makes it possible to pinpoint their sources. This property makes their observation crucial for the understanding of cosmic ray accelerators and their underlying mechanisms. Additional scientific questions related to gamma-ray observations are indirect searches for dark matter, answering questions in cosmology, and performing tests of fundamental physics [17]. Gamma-ray sources can be found both within our galaxy, notably in supernova remnants, and outside our galaxy, notably in active galactic nuclei and gamma-ray bursts. However, gamma rays can be absorbed, e.g., when their energy is high enough to interact with the extragalactic background light, a process limiting the possibilities of extragalactic gamma-ray astronomy. There are two possible production channels for gamma rays: Leptonic gamma-ray emission is generated by synchrotron radiation of electrons or positrons in magnetic fields, or by the acceleration of low-energy photons through interaction with high-energy

electrons and positrons, a process known as Inverse Compton Scattering.¹ Hadronic gamma-ray emission is generated from interactions of high-energy protons or heavier nuclei with matter, producing neutral mesons such as the π^0 , which decay into photons.

As is the case for cosmic rays, the Earth's atmosphere is also opaque to gamma rays, since they initiate electromagnetic particle cascades in interactions with atmospheric nuclei, as described in [Section 3.1](#). Below energies of 100 GeV, gamma rays can be efficiently detected using satellite experiments [80], for example, with the Fermi Gamma-ray Space Telescope [212]. For higher energies, an indirect detection approach via the secondary particles of the induced particle cascade, using ground-based observatories, is necessary. The different ground-based detection methods of gamma rays are presented in [Section 3.3](#).

Neutrinos

Neutrinos are uncharged particles with very low masses, only interacting gravitationally and via the weak force, resulting in very small interaction rates. This makes neutrinos unique in their capability to escape very dense production regions and carry information from within their sources, without deflections or absorptions. Within cosmic accelerators, protons interact with the surrounding media or radiation fields in hadronic interactions such as

$$p + p \rightarrow \pi^\pm + X, \quad (2.1)$$

where X denotes the remaining final hadronic state, or in photohadronic interactions such as

$$p + \gamma \rightarrow \Delta^+ \rightarrow \pi^+ + n \quad (2.2)$$

via a Delta resonance Δ^+ . In both cases, neutrinos are produced in the subsequent decay of pions, e.g., $\pi^+ \rightarrow \mu^+ + \nu_\mu$, as well as in the subsequent decay of muons, e.g., $\mu^+ \rightarrow e^+ + \nu_e + \bar{\nu}_\mu$ [133]. The small interaction rates of neutrinos, which makes their observation highly valuable, are also the reason why their detection on Earth is challenging. The underlying detection mechanisms therefore rely on the usage of large instrumented volumes. The IceCube Neutrino Observatory, for example, instrumented 1 km³ of ice at the geographic South Pole with 5160 digital optical modules [5]. The concept of neutrino detection, as well as different detector designs for the observation of astrophysical neutrinos, are described in [Section 4.3.1](#) and [Section 4.3.2](#).

¹Inverse Compton Scattering is identical to Compton Scattering, as described in [Section 6.2.2](#), but the involved photon gains energy during the interaction process.

A major milestone in modern neutrino astronomy has been the detection of a high-energy extraterrestrial neutrino flux, reported by the IceCube Collaboration in 2013 [3]. The first identified sources of this astrophysical flux are the blazar TXS 0506+056, from which a high-energy neutrino has been detected coincident with a gamma-ray flare in 2017 [4], and the active galaxy NGC 1068, from which an excess of 79 neutrinos has been reported in 2022 [9]. Furthermore, neutrino emission from the Galactic plane has been observed for the first time as recently as 2023 by the IceCube Neutrino Observatory [11].

Other Messengers

For completeness, two additional messengers in astroparticle physics are mentioned here: Firstly, the observation of photons below energies of ≈ 0.5 MeV is possible as well. This ranges from X-ray astronomy, over optical astronomy, down to radio astronomy at the smallest photon energies. Secondly, the newest addition to the list of cosmic messengers are gravitational waves, opening the field of gravitational-wave astronomy. They allow for observations not possible using other messenger particles, such as observations of black hole mergers or processes in the early universe [51]. In 2016, LIGO (**L**aser **I**nterferometer **G**ravitational-Wave **O**bservatory) and the Virgo interferometer announced the first direct detection of gravitational waves by observing the signal from a binary black hole merger [12].

3 Extensive Air Showers

As cosmic rays enter the Earth’s atmosphere, they interact with atmospheric nuclei and initiate a particle cascade called an extensive air shower. Their contents can be divided into three components: An electromagnetic component, a hadronic component, and a muonic component, as illustrated in Figure 3.1. The electromagnetic

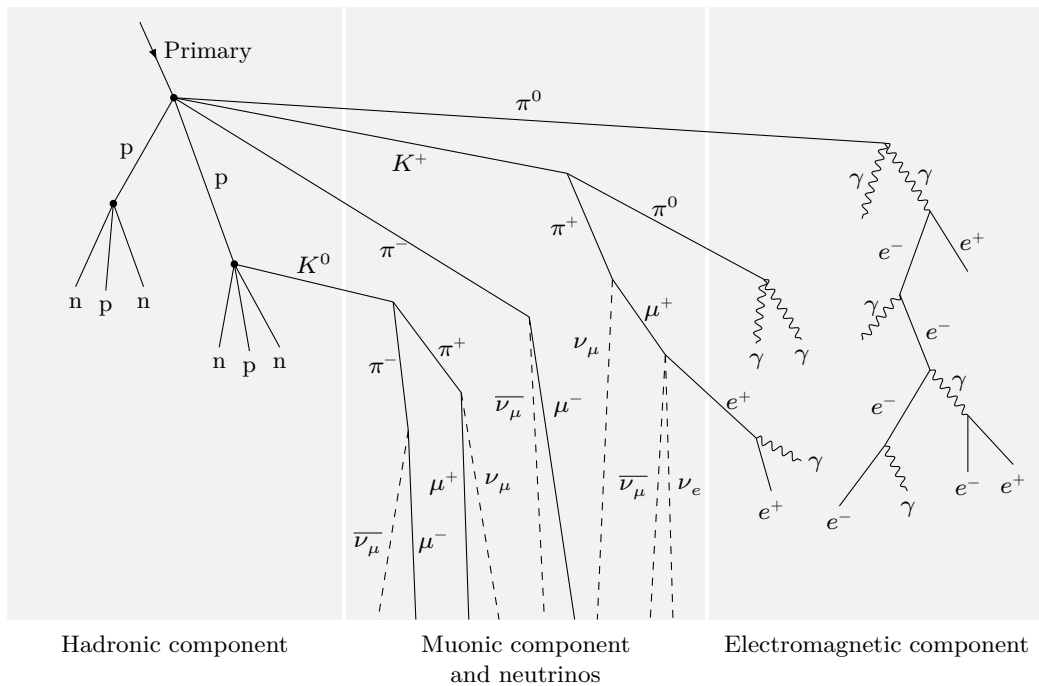


Figure 3.1: Illustration of the development of an exemplary extensive air shower, divided into the three shower components. Adapted from [149].

component consists of electrons, positrons, and photons. For high energies, it is governed by electron-positron pair production and bremsstrahlung processes. Models describing the development of electromagnetic particle cascades are introduced in Section 3.1, while the entirety of possible interactions in the electromagnetic shower component is described in detail in Chapter 6. The hadronic shower component is governed by the decay and interactions of hadrons, whose description contributes the largest source of uncertainty in the description of air showers. Models describing

the development of hadronic particle cascades are introduced in Section 3.2. Muons, which mainly result from decays of hadronic particles, form the muonic shower component. In Section 3.3, different approaches and the underlying physical effects for the detection of extensive air showers are described. Lastly, in Section 3.4, the so-called muon puzzle in extensive air showers – a significant, but yet unexplained deviation in the number of high-energy muons between simulations and experimental observations – and its connection to this work is introduced.

3.1 Description of Electromagnetic Particle Cascades

Electrons, positrons, and photons of sufficient energy produce electromagnetic particle cascades. These cascades can either be initiated as a standalone particle shower, e.g., through a gamma ray interacting with the Earth’s atmosphere, or as a subshower in a hadronic shower, e.g., from a π^0 decaying into two photons. A simple model describing the basic processes in an electromagnetic cascade is the *Heitler* model [115, 159], illustrated in Figure 3.2. Despite its simplicity, it is

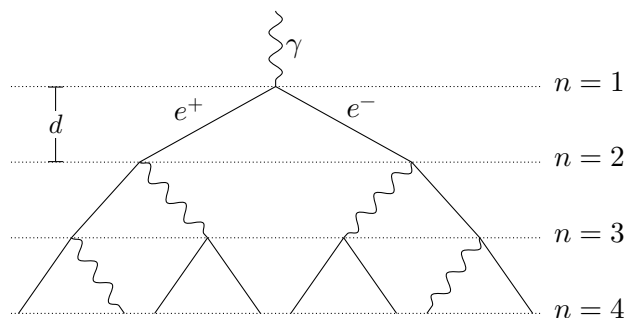


Figure 3.2: Illustration of the Heitler model for electromagnetic particle cascades, adapted from [159].

capable of quantitatively predicting the key characteristics of the underlying shower development. In this model, a primary particle with energy E_0 , in this case, a photon, interacts after a characteristic splitting length $d = X_0 \ln(2)$, producing an electron-positron pair through pair production (see Section 6.2.1). Here, X_0 denotes the radiation length in the medium. After traveling another length d , both the produced electron and positron emit a bremsstrahlung photon (see Section 6.1.1). In the Heitler model, it is assumed that in each interaction, the initial energy is split symmetrically between the two outgoing particles. According to these

approximations, after n cascade interactions, the total number of particles N is given by

$$N = 2^n = e^{X/X_0}, \quad (3.1)$$

where X describes the length of the shower development. The energy E per cascade particle is given by

$$E = E_0/N = \frac{E_0}{e^{X/X_0}}. \quad (3.2)$$

These splitting processes continue until the particles have reached a critical energy $E = E_c^{\text{em}}$, defined as the energy below which ionization losses outweigh radiative losses, with $E_c^{\text{em}} \approx 85$ MeV in air [159]. Therefore, the maximum number of particles is given by $N_{\text{max}} = E_0/E_c^{\text{em}}$, which, inserted into (3.1), yields

$$X_{\text{max}} = X_0 \cdot \ln(E_0/E_c^{\text{em}}) \quad (3.3)$$

as the distance after which the shower maximum is reached. Notably, the Heitler model predicts that the maximum number of shower particles is proportional to the primary particle energy, $N_{\text{max}} \propto E_0$, and that the depth of the shower maximum is proportional to the logarithm of the primary particle energy, $X_{\text{max}} \propto \ln(E_0)$, which are both relations that are confirmed by more sophisticated calculations and simulations [159].

To obtain a more detailed description of particle cascades, their development can be described via a system of so-called cascade equations. For electromagnetic particle cascades, these equations are given by [96]

$$\frac{d\gamma}{dt} = -\frac{\gamma(E, t)}{\lambda_{\text{pair}}} + \int_E^\infty \pi(E', t) \frac{dn_{e \rightarrow \gamma}}{dE dt} dE', \quad (3.4)$$

$$\begin{aligned} \frac{d\pi}{dt} = & -\frac{\pi(E, t)}{\lambda_{\text{brems}}} + \int_E^\infty \pi(E', t) \frac{dn_{e \rightarrow e}}{dE dt} dE' \\ & + 2 \int_E^\infty \gamma(E', t) \frac{dn_{\gamma \rightarrow e}}{dE dt} dE', \end{aligned} \quad (3.5)$$

where γ describes the number of photons for a given depth t , π the number of electrons and positrons, λ the characteristic interaction lengths of the corresponding processes, and $n_{i \rightarrow j}$ the average number of particles of type j produced by interactions of particles with type i . Under the assumption that ionization losses and Compton scattering, see Section 6.2.2, can be neglected, i.e., $E > E_c^{\text{em}}$, solutions of the electromagnetic cascade equations under the name *Approximation A* can be obtained [96]. One result from this solution, given the initial condition of a single primary of energy E_0 initiating the particle cascade, is that the number of electrons and

positrons N_{e^\pm} above an energy E at the shower maximum, and respectively the number of photons N_γ , can be approximated by

$$N_{e^\pm}(E) \approx \frac{0.14}{\sqrt{\ln(E_0/E) - 0.33}} \frac{E_0}{E}, \quad (3.6)$$

$$N_\gamma(E) \approx \frac{0.14}{\sqrt{\ln(E_0/E) - 0.25}} \frac{E_0}{E}. \quad (3.7)$$

Furthermore, the shower maximum X_{\max} is given by

$$X_{\max} \approx X_0 \cdot \left(\ln \left(\frac{E_0}{E} \right) - n \right), \quad (3.8)$$

with $n = -0.5$ for charged particles in photon-induced showers, $n = 0$ for charged particles in electron- or positron-induced showers, $n = 0$ for photons in photon-induced showers, and $n = 0.5$ for photons in electron- or positron-induced showers. Notably, this means that photon-induced particle cascades reach their shower maximum later than particle cascades initiated by electrons or positrons. A deviation and more details on this solution are given in [96].

In order to describe the total particle number in electromagnetic cascades down to energies $E < E_c^{\text{em}}$, the assumptions made for Approximation A are not fulfilled anymore. In this case, the *Greisen Formula* can be used [223], which yields the number of particles in a photon-induced shower as

$$N(X) = \frac{0.31}{\sqrt{\ln(E_0/E_c^{\text{em}})}} \exp \left[\frac{X}{X_0} \left(1 - \frac{3}{2} \ln(s) \right) \right], \quad (3.9)$$

with the age parameter

$$s = \frac{3X}{X + 2X_{\max}}, \quad (3.10)$$

and X_{\max} defined as in (3.3).

As an alternative to analytical solutions, the cascade equations (3.4) and (3.5) can be solved numerically, which is, for example, done by the tool EmCa [162]. A different approach to describe electromagnetic particle cascades is their simulation using Monte Carlo methods. In this case, each particle and its interactions are sampled individually, providing a very precise description of the particle cascade at the expense of a high computational effort. In contrast to the approach based on cascade equations, the Monte Carlo method is also capable of describing the entire phase space as well as individual shower events, and not only average particle fluxes, as described in more detail in Section 4.1. The implementation and validation of a Monte Carlo method to simulate electromagnetic cascades for the particle cascade simulation framework CORSIKA 8 will be described in the following chapters.

3.2 Description of Hadronic Particle Cascades

Protons and heavier nuclei of sufficient energy produce a hadronic particle cascade. In an approach similar to the description of electromagnetic cascades with the Heitler model, explained in Section 3.1, an approximate description of hadronic particle cascades is possible using the *Heitler-Matthews* model [159], as illustrated in Figure 3.3. In this model, a primary hadron traverses one characteristic length

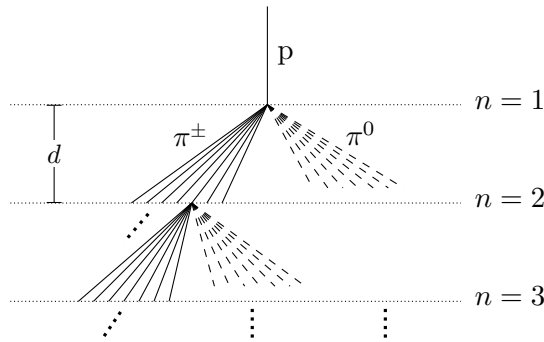


Figure 3.3: Illustration of the Heitler-Matthews model for hadronic particle cascades, adapted from [217].

$d = \lambda_i \ln(2)$, with the hadronic interaction length λ_i , before producing N_{ch} charged pions and $0.5N_{\text{ch}}$ neutral pions in an interaction. While each of the neutral pions immediately decays into two photons, initiating electromagnetic subshowers, the charged pions initiate the next generation n of the hadronic cascade, interacting after traversing another length d . This process continues until the charged pions have reached a critical energy E_c^π , defined as the energy below which their decay length is smaller than their interaction length. As soon as this energy is reached, the model assumes that each charged pion immediately decays into a muon. These muons, as well as the corresponding neutrinos, are capable of covering large distances in air, and are therefore described as the messengers of the hadronic particle cascade. After n generations, the number of charged pions is given by $N_\pi = N_{\text{ch}}^n$. Given an initial proton with energy E_0 , and assuming that for each interaction, the energy is split equally between all secondary particles, the total energy remaining in charged pions after n generations is given by $E_{\text{had}} = (2/3)^n E_0$. Therefore, the energy per pion is given by

$$E_\pi = \frac{E_0}{(3/2N_{\text{ch}})^n}. \quad (3.11)$$

Solving (3.11) with $E_\pi = E_c^\pi$ for n yields the maximal number of hadronic generations

$$n_c = \frac{\ln(E_0/E_c^\pi)}{\ln(3/2N_{\text{ch}})}. \quad (3.12)$$

While neither the multiplicity N_{ch} , which increases slowly with energy, nor the hadronic interaction length λ_i , which decreases with energy, are constant, a valid approximation for particle cascades in air is $N_{\text{ch}} \approx 10$, $\lambda_i \approx 120 \text{ g/cm}^2$, and $E_c^\pi \approx 20 \text{ GeV}$ [159]. Given the maximum number of electrons N_e and the maximum number of muons N_μ in a shower, the energy of the primary particle can be estimated with

$$E_0 = gE_c^{\text{em}}N_e + E_c^\pi N_\mu \approx 0.85 \text{ GeV}(N_e + 24N_\mu), \quad (3.13)$$

where E_c^{em} is the critical energy for the electromagnetic shower component as defined in Section 3.1, and $g = N/N_e \approx 10$ a correction factor to approximate the total number N of particles in an electromagnetic cascade from N_e [159]. Note that according to this linear relation, the primary energy of a hadronic cascade can be inferred from the number of particles, although the exact numerical values depend on the experimental conditions. The number of muons as a function of the primary energy E_0 can be obtained by inserting (3.12) in $N_\mu = N_\pi = N_{\text{ch}}^{n_c}$, yielding

$$N_\mu = \left(\frac{E_0}{E_c^\pi} \right)^\beta, \quad (3.14)$$

with

$$\beta = \frac{\log(N_{\text{ch}})}{\log(3/2N_{\text{ch}})} \approx 0.85. \quad (3.15)$$

Note that in more realistic scenarios, the value of β is slightly higher, e.g., $\beta \approx 0.92$ [159], since the approximation that the entire energy in hadronic interactions goes into pions is invalid. Instead, a fraction of energy can be carried away by particles such as protons and antiprotons [96]. The depth of the shower maximum X_{max} of a hadron-induced particle cascade can be estimated by the depth of the electromagnetic cascades initiated for $n = 1$, since these subshowers account for the majority of particles in the entire cascade. In the first interaction, an energy of $1/3E_0$ is divided equally between $0.5N_{\text{ch}}$ neutral pions, where each pion decays into two photons. This means that the energy per photon is given by $E_0/(3N_{\text{ch}})$, which yields a shower maximum of

$$X_{\text{max}} = \lambda_i \ln(2) + X_{\text{max}}^{\text{em}} = \lambda_i \ln(2) + X_0 \ln \left(\frac{E_0}{3N_{\text{ch}}E_c^{\text{em}}} \right), \quad (3.16)$$

where $X_{\text{max}}^{\text{em}}$ from Section 3.1 is used. Note that for a more realistic estimation of X_{max} , the energy dependence of both λ_i and N_{ch} , as well as the particle contributions of additional generations $n > 1$, must be taken into account [159].

To estimate the characteristics of a particle cascade induced by heavier nuclei using the equations derived above, the *superposition model* can be applied. This model approximates that a nucleus of mass A and energy E_0 can be treated as A individual nucleons with energy E_0/A , where each nucleon independently initiates a particle cascade. Using this approximation with (3.14) yields

$$N_{\mu}^A = A \left(\frac{E_0/A}{E_c^{\pi}} \right)^{\beta} = A^{1-\beta} \left(\frac{E_0}{E_c^{\pi}} \right)^{\beta} > N_{\mu}^p, \quad (3.17)$$

meaning that particle cascades with the same primary energy E_0 , but initiated by heavier nuclei, produce more muons than showers initiated by protons. For the shower maximum according to (3.16), this yields

$$X_{\max}^A = \lambda_i \ln(2) + X_0 \ln \left(\frac{E_0}{3N_{\text{ch}} E_c^{\text{em}}} \right) - X_0 \ln(A) < X_{\max}^p, \quad (3.18)$$

meaning that the shower maximum for particle cascades initiated by heavier nuclei is reached earlier compared to showers initiated by protons.

To obtain more detailed insights into the development of hadronic particle cascades, their description via cascade equations, similar to (3.4) and (3.5) for the electromagnetic cascade, is possible. Analytical approximations of particle fluxes from air showers based on cascade equations are derived in [96]. A numerical tool to solve cascade equations is MCEq [91, 92]. MCEq has originally been developed to provide a longitudinal description of the particle flux, but has recently been extended to also provide angular distributions by solving two-dimensional cascade equations [148]. As described in Section 3.1, the most detailed and versatile, but also computationally expensive approach to describe hadronic particle cascades is their simulation with Monte Carlo methods. In this case, each hadronic interaction is sampled individually, relying on their modeling by hadronic event generators such as SIBYLL [185] or EPOS [179]. These event generators are codes, providing interaction cross sections and methods to sample secondary particle spectra for hadronic particle interactions. In the context of air shower simulations, they need to describe a phase space inaccessible with particle accelerators and therefore rely on phenomenological descriptions. As a consequence of the large uncertainties, different event generators provide different descriptions of hadronic interactions, causing the largest source of systematic uncertainties in air shower simulations. This issue is elaborated in more detail in Section 3.4 in the context of the muon puzzle.

3.3 Detection of Extensive Air Showers

Extensive air showers can be detected using various techniques, based on different physical effects. In this section, three important methods and the corresponding detector designs are presented: Cherenkov, fluorescence, and radio emission. Note that each method has its own advantages and disadvantages, which is why many observatories use a hybrid approach that combines different methods. One notable example of this approach is the Pierre Auger Observatory [76] and its upgrade AugerPrime [41], combining all three aforementioned methods in addition to the usage of scintillation detectors.

3.3.1 Cherenkov Emission

Charged particles traveling through a dielectric medium are capable of exciting surrounding molecules. As these molecules return to their ground state, they emit photons, whose wavefronts constructively interfere if the velocity v of the initial particle is larger than the speed of light in the medium, given by c/n , where n denotes the refractive index of the medium. This emission is called Cherenkov radiation. The angle θ_c under which the Cherenkov light is emitted, named Cherenkov angle, is given by

$$\cos(\theta_c) = \frac{1}{\beta n}, \quad (3.19)$$

with $\beta = v/c$. Given the condition $v > c/n \Leftrightarrow \beta > 1/n$, the energy threshold E_{\min} above which a charged particle with mass m induces Cherenkov light is

$$E_{\min} > \frac{m}{\sqrt{1 - 1/n^2}}. \quad (3.20)$$

For $n = 1.000289$, corresponding to the refractive index of air at a temperature of 0°C and pressure of 1 atm [225], this leads to an energy threshold of $E_{\min} \approx 21.26$ MeV for electrons and positrons, with an increasing threshold for heavier particles and higher altitudes due to the density dependence of n .

There are two general Cherenkov-based approaches for the detection of extensive air showers, as shown in Figure 3.4. In the first approach, the Cherenkov light induced by charged cascade particles in the atmosphere is measured, for example, via *Imaging Air Cherenkov Telescopes (IACTs)*, effectively using the atmosphere as a detector volume. IACTs, primarily designed for the detection of showers initiated by very-high-energy gamma rays between energies of 30 GeV and 100 TeV [96], point at a chosen location in the sky, collect the Cherenkov light, and reflect it into a camera using large, segmented reflectors. The properties of the showers are



(a) LST-1, a prototype IACT for the Cherenkov Telescope Array. Image from [208].



(b) The HAWC observatory. The individual water tanks are visible. Image from [170].

Figure 3.4: Exemplary images of observatories using Cherenkov-based detection approaches.

reconstructed with high accuracy using the time-resolved camera images, where the simultaneous observations of an air shower using two or more IACTs and combining their information can significantly improve this process. However, the field of view of IACTs is limited, the atmospheric conditions need to be closely monitored, and the operation requires dark nights with good weather conditions, which limits the duty cycle to $\approx 15\%$. Examples of currently operating IACTs are MAGIC (Major Atmospheric Gamma Imaging Cherenkov) [35] and VERITAS (Very Energetic Radiation Imaging Telescope Array System) [119]. The next generation of IACTs is going to be introduced with the Cherenkov Telescope Array [17], where the first construction stage foresees an array of 13 telescopes with different sizes in the Northern Hemisphere, and an array of 51 telescopes in the Southern Hemisphere [157]. They will cover an energy range from 20 GeV up to 300 TeV.

The second Cherenkov-based detection approach uses an array of particle detectors placed in a regular pattern on the ground. Each detector is a closed tank, usually containing water and several photosensors, detecting Cherenkov light induced by charged cascade particles crossing the tank. The delay in arrival times between different detectors is used to reconstruct the shower direction, while the primary energy can be inferred from the total signal strength. While the angular resolution is worse, and the energy threshold higher compared to IACTs, sensitivities up to the highest energies can be reached, a large field of view can be covered, and the duty cycle is close to 100% as the detection approach can be applied regardless of the time of day and weather conditions. The spacing between individual detector stations depends on the target energy range of the observatory: It ranges from several meters for the 300 stations at HAWC (High-Altitude Water Cherenkov Gamma-Ray Observatory), focusing on the detection of gamma-rays between 0.1 TeV and 100 TeV [33], up to 1.5 km for the 1660 stations of the Pierre Auger Observatory,

focusing on the detection of cosmic rays above energies of 100 PeV [76]. Another relevant factor is the height of the observatory, as it determines the distance from the observation level to the approximate height of the shower maximum: While the Pierre Auger Observatory is located at a mean altitude of 1.4 km, HAWC is located 4.1 km above sea level.

3.3.2 Fluorescence Emission

Charged particles in an extensive air shower can excite nitrogen molecules in the atmosphere. The consequent de-excitation, corresponding to transitions of electronic states, leads to an isotropic emission of light with wavelengths between 300 nm and 400 nm, an effect called fluorescence light emission [96]. For air showers of sufficient energy, this emission can be detected by fluorescence telescopes, even for large distances to the shower of up to 35 km [96]. Since the number of fluorescence photons is related to the ionization energy deposit in the atmosphere, fluorescence telescopes perform a calorimetric shower measurement, allowing for a reconstruction of the primary energy and of the longitudinal energy profile. Even more crucially than for IACTs, their operation requires dark nights and precise monitoring of atmospheric conditions, limiting the possible duty cycle to $\approx 15\%$. While a standalone usage of one or more fluorescence telescopes for air shower detection is possible, and has been done successfully in the past [201], their application today is limited to hybrid measurements in combination with surface detectors. For example, the Pierre Auger Observatory uses 24 fluorescence telescopes which overlook the surface array [76].

3.3.3 Radio Emission

A detectable radio emission from electromagnetic showers has already been predicted in 1961 by Askaryan [47]. Although the first detection of radio pulses induced by an air shower was successful in 1965 [128], the usage of this method to investigate air showers has not been established, and only improvements in digital signal processing over the last 15 years initiated further progress in this field [124].

There are two dominant sources of radio emission from particle cascades. The geomagnetic emission is caused by the opposite deflection of electrons and positrons in the geomagnetic field. Due to the firstly increasing and later decreasing development of the particle cascade, and the corresponding change in the number of electrons and positrons, this process induces a time-varying current and therefore a radio signal [96]. As illustrated in the left panel of Figure 3.5, the polarization of this radio emission is oriented perpendicular to both the magnetic field and the shower axis. The second important source of radio emission is due to the charge excess

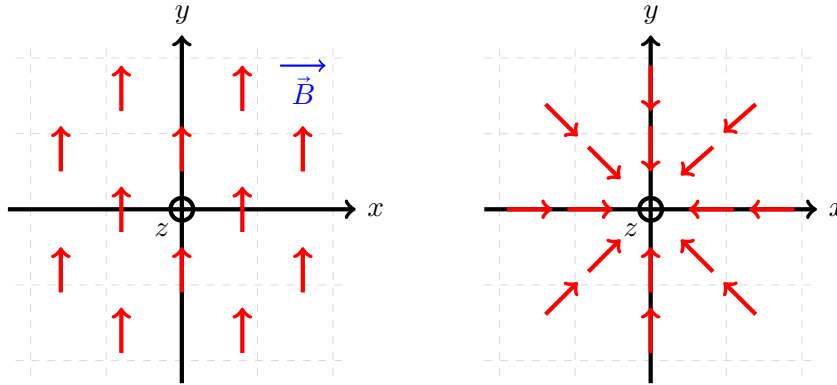


Figure 3.5: Polarization of the radio emission in air showers for the geomagnetic emission (left) and the charge excess emission (right), indicated with red arrows. The geomagnetic field is homogeneous and oriented in x-direction, and the shower propagates in the negative z-direction. Note that in literature, an alternative coordinate system spanned by \vec{v} , $\vec{v} \times \vec{B}$, and $\vec{v} \times \vec{v} \times \vec{B}$ is often used, where \vec{v} denotes the shower axis. The relation between both coordinate systems is defined by $\vec{x} = -\vec{v} \times \vec{v} \times \vec{B}$, $\vec{y} = -\vec{v} \times \vec{B}$, and $\vec{z} = -\vec{v}$ [70].

contribution, also known as the Askaryan effect [47]. Due to ionization, electron-positron annihilation, and Compton scattering, electromagnetic particle cascades exhibit an excess of electrons over positrons in their shower front, with a difference of around 20 % for air showers, as shown in Figure 7.25. Since the charge excess is time-dependent as it varies during shower development, radio emission is induced, with a polarization pointing radially inwards [96], as illustrated in the right panel of Figure 3.5. Note that for air showers, the charge excess emission only accounts for 10 % to 15 % of the radio emission [96], while the dominant contribution comes from the geomagnetic emission. For particle cascades in dense media, however, the geomagnetic emission is negligible, and only the Askaryan emission is relevant.

In general, a coherent radio signal is produced if the involved wavelength is large compared to the size of the emission region. For air showers, where the emission region is defined by the longitudinal extent of the shower front, which is on the order of meters, this leads to an upper frequency limit for coherent radio emission of ≈ 100 MHz [198]. As the emission processes are induced directly behind the shower front, which itself moves close to the speed of light in a medium with a refractive index $n > 1$, additional coherent radio emission is expected on a cone with an opening angle of [220]

$$\cos(\theta) = \frac{1}{n}. \quad (3.21)$$

This feature, which is clearly visible in the simulated fluence maps in [Figure 7.28](#), is called Cherenkov ring. In this region, the radio emission can include frequencies extending to several GHz [\[198\]](#).

By using an array of relatively simple antennas, radio pulses can be detected to infer the properties of extensive air showers, where most radio arrays are operating between frequencies of 30 MHz and 80 MHz [\[198\]](#). The primary energy can be reconstructed accurately from the signal strength, the shower maximum can be inferred from the slope of the lateral profile, and an angular reconstruction with a resolution of down to 0.1° is possible [\[124\]](#). Since the zenith angle of the shower determines the footprint of the radio emission, the angular range in which a radio detector is sensitive highly depends on the detector spacing. The duty cycle of radio detectors is close to 100 %, only limited by nearby thunderstorms, whose strong electric fields can induce an additional, complex radio signal from air showers. Significant radio background originates from continuous emission from the galaxy and pulsed emission from anthropogenic sources, where the latter currently prevents the usage of self-triggering radio detectors [\[124\]](#). Examples of radio arrays are AERA (**A**uger **E**ngineering **R**adio **A**rray), consisting of 153 radio detector stations on the site of the Pierre Auger Observatory [\[76\]](#), and the currently deployed AugerPrime, where radio antennas will be installed on each surface detector station of the Pierre Auger Observatory [\[120\]](#).

3.4 The Muon Puzzle in Extensive Air Showers

All methods to derive the properties of a primary particle initiating an extensive air shower require correct modeling of the underlying particle cascade. One important property of the cosmic ray spectrum is its energy-dependent mass composition, often characterized by the mean-logarithmic mass $\langle \ln A \rangle$, where A is the nuclear mass of the cosmic ray particle. Since the characteristics of $\langle \ln A \rangle$ can provide insights into the possible sources of cosmic rays [\[130\]](#), its measurement is of great importance to constrain specific source models. As visible in [\(3.17\)](#) and [\(3.18\)](#), both the number of muons in an air shower, N_μ , and the depth of the shower maximum, X_{\max} , are sensitive to A , and can therefore be used for its reconstruction. However, comparing measurements of the muon number in cosmic ray experiments with the expected muon number from simulations reveals a significant excess in experimentally detected muons [\[2\]](#). This observation is called the *Muon Puzzle* [\[34\]](#). As this discrepancy has been reported by several independent experiments, a meta-analysis, gathering all available results and combining them to increase their statistical significance,

has been conducted in [202]. To obtain a quantity comparable between different experiments, the muon scale parameter z is used. It is defined as

$$z = \frac{\ln \langle N_\mu \rangle - \ln \langle N_\mu \rangle_p}{\ln \langle N_\mu \rangle_{\text{Fe}} - \ln \langle N_\mu \rangle_p}, \quad (3.22)$$

where $\ln \langle N_\mu \rangle$ denotes the average number of muons obtained experimentally, $\ln \langle N_\mu \rangle_p$ the expected average muon number from simulations of proton showers, and $\ln \langle N_\mu \rangle_{\text{Fe}}$ the corresponding number for iron showers. Note that in the absence of a discrepancy between experiment and simulations, a value of $z = 0$ indicates a cosmic ray composition where $\langle \ln A \rangle$ corresponds to the mass of a proton, whereas $z = 1$ corresponds to the mass of an iron nucleus. Furthermore, z depends on the underlying simulations, specifically the used hadronic event generator, the influence of which is described later in this section. Figure 3.6 shows the variation of z with cosmic ray energy E for observations by different experiments, split into results obtained for different event generators. Notably, for high energies, several

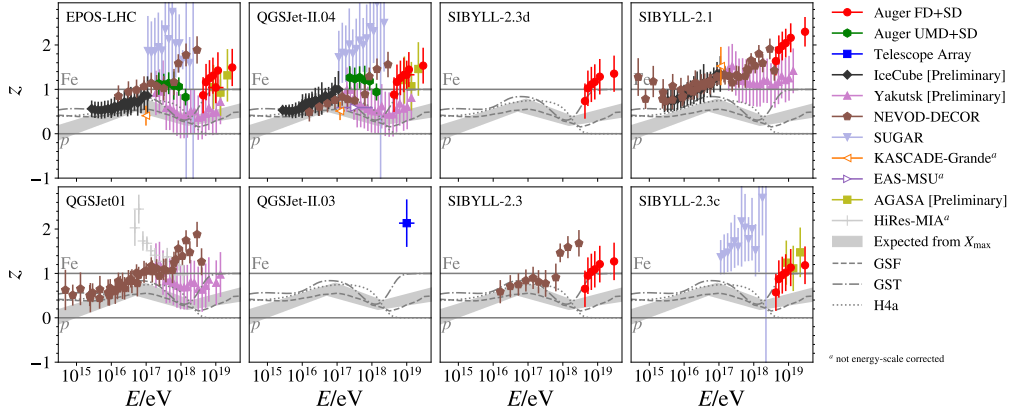


Figure 3.6: Results for the muon scale parameter z , as defined in (3.22), for several combinations of experimental results and simulations using different hadronic event generators. The gray band and lines indicate independent calculations of z based on X_{max} measurements. To ensure compatibility between experiments, an energy cross-calibration has been performed, as described in [202]. Figure from [202].

data points predict unphysical values with $z > 1$, corresponding to an average mass composition heavier than iron. In addition, the expected variation of z based on independent measurements of X_{max} is shown in a gray band, a quantity called z_{mass} . The quantitative disagreement $\Delta z = z - z_{\text{mass}}$ between both calculations is visualized in Figure 3.7. Assuming a correct calculation of z_{mass} , Δz can be interpreted as a measure for the relative muon excess. A significant excess $\Delta z > 0$

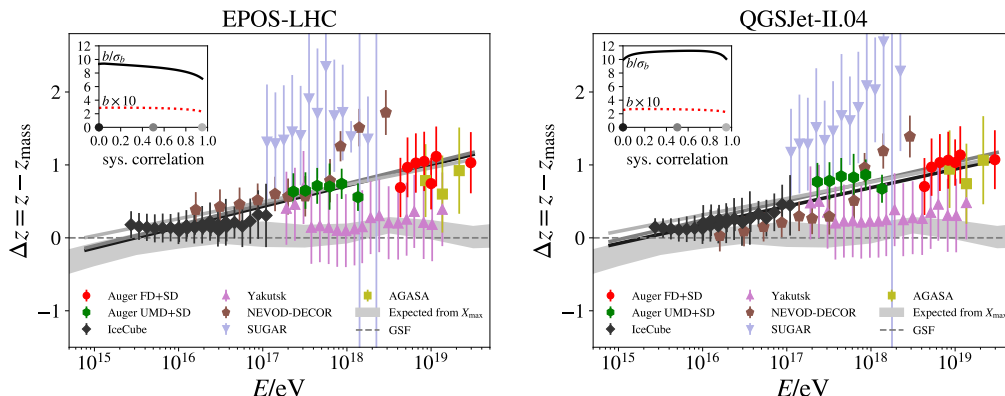


Figure 3.7: Development of Δz , revealing the discrepancy between the measurement of z via the muon number and the expected development of z according to independent X_{max} measurements. Figure from [202].

is reported by almost all experiments, increasing approximately linearly with energy. A linear fit of Δz reveals a non-zero slope with a significance of 8σ [202], confirming the energy-dependent behavior of the muon excess. Notably, the excess starts at energies of ≈ 40 PeV, corresponding to a center-of-mass energy of ≈ 8 TeV which is accessible by the Large Hadron Collider [34].

It is important to note that different hadronic event generators, which are used to describe cross sections and secondary particle spectra of hadronic interactions, can yield significantly varying predictions, especially for the muon content in air showers, as visible in Figure 3.6 and Figure 3.7. These uncertainties are related to the fact that hadronic event generators heavily rely on input from man-made accelerator experiments, where the properties of the beam are precisely known. However, the phase space relevant for interactions in air showers, i.e., very-high-energy and highly forward-boosted interactions, are currently experimentally inaccessible [93]. Additionally, forward-boosted interactions involve small momentum transfers – a regime that can not be described with perturbative quantum chromodynamics [34]. It is therefore necessary to apply effective theories and phenomenology to model hadronic interactions relevant for shower simulations. However, even the most up-to-date event generators are unable to solve the muon excess within the scope of their free parameters without violating accelerator measurements. Therefore, changes in the physics descriptions of extensive air showers are necessary. While these changes need to address the muon deficit, they must not change the prediction of other air shower characteristics, notably the fluctuation of N_μ , the mean of X_{max} , and the fluctuation of X_{max} , where current simulations and experimental observations are consistent [1, 2]. The analysis in [217] suggests that, in the context

of hadronic interactions, only a modification of $R = E_{\text{em}}/E_{\text{hadrons}}$, i.e., the ratio of energy per hadronic interaction going into the electromagnetic component compared to the energy remaining in the hadronic component, fulfills these requirements. Notably, comparably small modifications of R accumulate over several hadronic generations, influencing the shower development sufficiently to possibly explain the large deviation in N_{μ} . Recent measurements at the Large Hadron Collider by the ALICE collaboration reveal a universal enhancement in strangeness production in proton-proton collisions at mid-rapidity, i.e., in interactions with comparably large angles to the beam axis [19]. Since an increase in strangeness would lead to a decrease of the energy available to pions, and therefore the electromagnetic component, this effect might provide a possible solution for the muon puzzle [54]. However, this requires that the strangeness enhancement also occurs for high-rapidity interactions, i.e., the forward region which is relevant for hadronic interactions in air showers, which needs to be experimentally verified.

To confirm that changes in the description of hadronic interactions provide a solution to the muon puzzle, additional analyses and measurements at collider experiments are necessary. This includes studies of hadronic interactions in the forward region, as well as studies of proton-oxygen collisions [78], since the extrapolation from proton-proton, proton-lead or lead-lead collisions, which have already been performed at the Large Hadron Collider, to collision systems typically occurring in air showers includes considerable theoretical uncertainties [34].

Next to the description of hadronic interactions, additional uncertainties in the context of air shower simulations might contribute to the muon puzzle. Therefore, their impact is considered in the context of this work. Firstly, it is desirable to minimize uncertainties in the particle cascade simulation itself. A vast majority of analyses are based on air shower simulations performed by the program CORSIKA 7, or earlier versions of CORSIKA [113, 114]. While the usage of a common framework ensures comparability between different analyses, intrinsic inaccuracies may lead to a bias affecting all derived results. Therefore, the implementation of CORSIKA 8 – which is a complete rewrite independent of the old CORSIKA 7 code – as a modern, well-understood particle cascade code is crucial to rule out this possibility. This process is described in detail in Chapter 5. Another potential uncertainty comes from the muon propagation within air shower simulations, where inaccuracies can lead to a wrong description of both the muon number and of muon energy spectra. In order to minimize this uncertainty, the software PROPOSAL is implemented as an interaction model for CORSIKA 8. PROPOSAL, as described in detail in Chapter 4, is a well-established framework for the propagation of muons, as it is used in a wide range of applications, especially in the context of underground observatories where a precise muon propagation over large distances is crucial. The corresponding detailed treatment of muons within CORSIKA 8 represents a

significant update compared to their treatment in previous shower simulation codes. The process of including PROPOSAL inside CORSIKA 8 is a main part of this work and is described in [Section 5.3](#). An in-depth comparison of shower simulation results between CORSIKA 8 and CORSIKA 7 is presented in [Chapter 7](#). Note that additionally, CORSIKA 8 in combination with PROPOSAL provides unique features that allow for an in-depth investigation and modification of particle cascades beyond the boundaries of existing simulation codes. These features, which are described in [Section 5.2](#), are especially relevant to perform more advanced studies in the context of the muon puzzle.

4 The Lepton and Photon Propagator PROPOSAL

PROPOSAL (**PR**opagator with **O**ptimal **P**recision and **O**ptimized **S**peed for **A**ll **L**eptons) is a Monte Carlo simulation library, providing three-dimensional simulations of individual charged leptons and photons. It is an open-source software written in the programming language C++, but also accessible in Python via code bindings.¹

The history of PROPOSAL started in 2004 with the development of the Java tool MMC (**M**uon **M**onte **C**arlo) [77], which was written to simulate muon interactions in the context of muon and neutrino underground observatories, such as AMANDA (**A**ntarctic **M**uon **A**nd **N**eutrino **D**etector **A**rray) [43] and its successor project, the IceCube Neutrino Observatory [18]. The main task was the precise propagation of muons from the Earth’s surface to the detector and the description of the energy losses inside. Tau leptons and electrons could, in principle, also be propagated with MMC, although the latter was not the focus of the code. While other muon propagation tools already existed at the time (such as PROPMU [154], MUDEDX [155], or MUSIC [46]), MMC was developed to resolve discrepancies between these tools by minimizing algorithmic inaccuracies. Furthermore, MMC provided the possibility to use different parametrizations of muon energy loss cross sections, including up-to-date cross sections that were not available in other codes. This made it possible to analyze the systematic uncertainties of muon propagation due to the uncertainties of the cross sections, which exist, for example, for radiative corrections to the pair production cross section and the description of nuclear shadowing [195].

After the development of MMC was completed, the choice of Java as a programming language turned out to be a disadvantage. One issue was the version dependency of Java, which required the installation of identical Java versions on different machines to guarantee reproducible simulation results. Especially for the usage on large computer clusters, this demanded an unreasonable administrative effort. Furthermore, existing simulation chains were mostly based on C++ and Python, for example in the case of IceCube – an issue that complicated the implementation of MMC. Therefore, in 2013, MMC was rewritten in C++ and renamed to PROPOSAL

¹The source code and development of PROPOSAL is publicly visible on GitHub: <https://github.com/tudo-astroparticlephysics/PROPOSAL>.

[143, 144]. While the physical and algorithmic foundations remained the same, meaning that MMC and PROPOSAL produced identical results, improvements in the code structure, taking advantage of the possibilities provided by C++, were implemented. This made maintaining, extending, and testing PROPOSAL simpler, especially due to the usage of a more modular code design [144].

In the following, the code structure of PROPOSAL has been further improved by introducing a modern C++ coding style, making use of polymorphism [83, 84]. Additionally, an interface to Python, a programming language commonly used in the astroparticle physics community, was included. In terms of physics, updates to the description of decay processes and the implementation of new parametrizations for energy losses and multiple scattering were the most notable additions.

Over time, more and more users, primarily in the context of neutrino astronomy, started to use PROPOSAL, especially due to its high flexibility. One additional, new use case for PROPOSAL which emerged was its usage for the description of extensive air showers. The most common software for the simulation of extensive air showers is CORSIKA 7 [114], a monolithic Fortran code based on the first CORSIKA version released in 1989 [113]. The successor of this software, called CORSIKA 8, is currently under development. It represents a complete rewrite of CORSIKA in the programming language C++ [88, 183]. In this context, the developers of CORSIKA looked for an external framework to describe the interaction of muons, as well as a framework to describe the electromagnetic shower component, which was previously done with EGS4 [171]. The necessary preparations to enable PROPOSAL to perform both these tasks triggered the most recent phase of restructuring and extensions, which is a key part of this thesis.

The following chapter is structured as follows: In the first section, the general concept of particle propagation with PROPOSAL is introduced and its functionalities are presented. Next, the most recent updates of PROPOSAL are described, with a focus on the extensions in the context of CORSIKA 8. Lastly, an overview of different applications of PROPOSAL in neutrino astronomy and particle physics is given.

4.1 Simulation Principles

Propagation in the context of PROPOSAL describes the development of an individual particle state, defined by its position, direction, and energy, over time. During this process, particles can undergo collisions, where an initial particle of energy E_i loses a fraction of its energy v , leaving it with an energy $E_f = E_i \cdot (1 - v)$ after the interaction. In each of these interactions, the direction of the initial particle can change. Additionally, the accumulation of individual, elastic collisions with the

surrounding medium can lead to a macroscopic particle deflection, a process called multiple scattering (see [Section 6.1.6](#)). Lastly, particles with a limited lifetime, for leptons the muon ($\tau \approx 2.197 \times 10^{-6}$ s) and tau lepton ($\tau \approx 290 \times 10^{-15}$ s) [225], can decay during propagation.

Especially in the case of muons, which can travel distances of several kilometers even through dense media, hundreds, thousands, or even more interactions might occur during propagation. A precise simulation of each of these interactions is necessary, since otherwise, an accumulation of even small errors from each calculation can lead to a large uncertainty for the overall propagation. Furthermore, this aspect highlights the necessity of stochastic methods like Monte Carlo to describe particle propagation: The phase space of possible outcome particle states is very large due to the high stochasticity of the involved processes. While other approaches, such as the modeling via cascade equations (see [Section 3.1](#)), exist, and have the advantage of a much smaller computational effort, they are only capable of providing a discretized average of the particle density and cannot describe individual event signatures, which is, for example, relevant to establish event reconstruction algorithms.

The probability for the interaction of a particle with a medium via a specific process is described by a total cross section $\sigma(E)$, or a differential cross section such as $d\sigma/dv$, from which the total cross section can be calculated. From the total cross section, the mean free path λ , i.e., the average distance between two interactions, can be inferred via

$$\lambda \propto \frac{1}{n\sigma}, \quad (4.1)$$

where n describes the number density of the target medium. In principle, it would

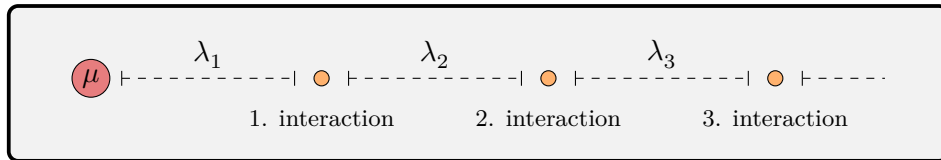


Figure 4.1: Naive propagation algorithm by repeatedly sampling an interaction length from (4.1). The orange circles illustrate the individual interactions where energy is lost.

already be sufficient to propagate a particle by repeatedly sampling a path length λ_i from (4.1), displacing the particle in each step by λ_i , and sampling an energy loss v from the differential cross section for each interaction, as illustrated in [Figure 4.1](#). While this naive approach can be used for particles such as photons, problems arise for the propagation of charged particles: The differential bremsstrahlung cross

section behaves as $d\sigma/dv \propto v^{-1}$ and therefore diverges for $v \rightarrow 0$ due to the vanishing mass of the photon, which can be seen in Figure 4.2. This would mean that the mean free path approaches zero, making the propagation impossible, or at least highly inefficient.² Even for a non-diverging bremsstrahlung cross section, treating all interactions individually, no matter how small, would require a very large number of propagation steps, making the propagation process too runtime-expensive to be feasible.

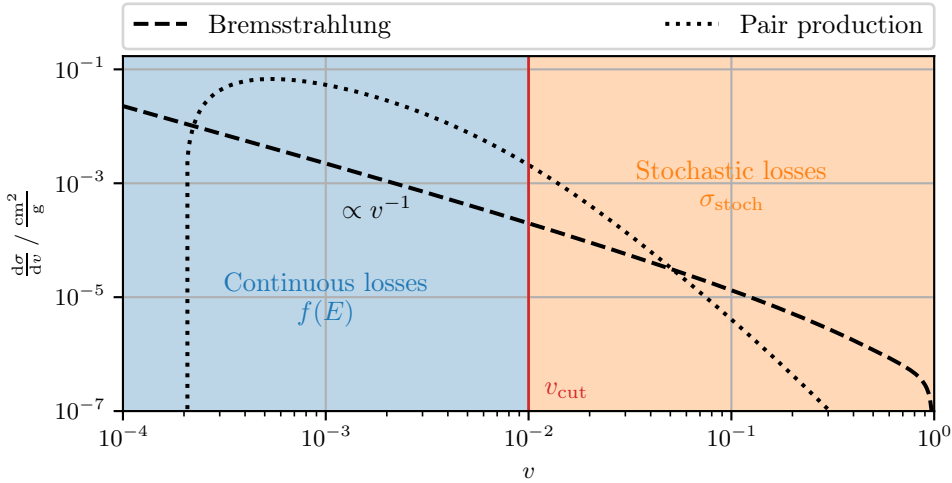


Figure 4.2: Differential cross sections for muons in *standard rock* at $E = 10^4$ MeV, for bremsstrahlung and pair production. While the pair production cross section has an intrinsic cut-off v_{\min} , the bremsstrahlung cross section continues to rise and diverges for $v \rightarrow 0$. The colored areas illustrate the division of the differential cross section into a continuous and a stochastic part, according to (4.3) and (4.4).

The approach to solve this problem is to divide the energy losses into continuous and stochastic losses by the introduction of a threshold v_{cut} , as illustrated in Figure 4.2. In PROPOSAL, this threshold is given either by an absolute energy loss E_{cut} , by a relative energy loss v'_{cut} , or a combination of both, defined by

$$v_{\text{cut}} = \min [E_{\text{cut}} / E, v'_{\text{cut}}]. \quad (4.2)$$

²For propagation in dense media, the *Ter-Mikaelian (TM)* effect changes the behavior of the differential bremsstrahlung cross section to $d\sigma/dv \propto v$ for small v , resolving the divergence. However, the total cross section still approaches very large values, and a numerical calculation would be unstable. Details about the *TM* effect are given in Section 6.3.

Energy losses below this threshold are treated as an averaged, continuous energy loss per grammage,³ defined as

$$f(E) := -\frac{dE}{dX} = E \frac{N_A}{A} \int_{v_{\min}}^{v_{\text{cut}}} v \frac{d\sigma}{dv} dv, \quad (4.3)$$

with the Avogadro constant N_A , the atomic mass of the medium A , and the lower kinematic limit of the interaction process v_{\min} . Energy losses above this threshold are treated individually as stochastic energy losses, with a stochastic cross section

$$\sigma_s := \int_{v_{\text{cut}}}^{v_{\max}} \frac{d\sigma}{dv} dv, \quad (4.4)$$

where v_{\max} denotes the upper kinematic limit of the interaction process. For an individual stochastic loss, the type of interaction is sampled from the contributions of the individual processes $\sigma_{s,i}$ to the total stochastic cross section. Afterward, the size v of the stochastic loss is sampled from the differential cross section of the selected interaction type i by solving

$$\frac{1}{\sigma_{s,i}} \int_{v_{\text{cut}}}^v \frac{d\sigma_i}{dv} dv = \xi_{\text{rnd}} \quad (4.5)$$

for v , where $\xi_{\text{rnd}} \in [0, 1)$ is a random number.

Due to the introduction of continuous energy losses, the particle energy during a propagation step is not constant, meaning that the mean free path length and cross section, which are energy-dependent, vary. This aspect needs to be taken into account when sampling the length of a step, especially in the case of large propagation steps. One approach to achieve this is by sampling E_f , the energy at which the next stochastic interaction will occur, by solving the integral equation

$$\int_{E_i}^{E_f} \frac{\sigma_s(E)}{-f(E)} dE = -\log(\xi_{\text{rnd}}) \quad (4.6)$$

for E_f , where E_i is the initial particle energy and $\xi_{\text{rnd}} \in (0, 1]$ a random number [77]. The derivation of (4.6) is given in [Appendix A.1](#). An alternative approach to treat the decreasing energy when sampling a propagation step length, which is for example used in the CORSIKA framework, is described in [Section 5.2.2](#).

The connection between the initial energy and distance of a particle, E_i and x_i , with a final energy and distance, E_f and x_f , is given by

$$X := \int_{x_i}^{x_f} \rho(x) dx = - \int_{E_i}^{E_f} \frac{dE}{f(E)}, \quad (4.7)$$

³Grammage is defined as the density integrated over a distance x , i.e., $X = \int \rho(x) dx$, where $\rho(x)$ describes the density distribution along the trajectory of the particle.

where $\rho(x)$ describes the medium density along the trajectory of the particle. This relation is, for example, used to calculate the length of a propagation step when E_f has been sampled from (4.6). Similarly, the relation between the initial energy and time of a particle, E_i and t_i , with a final energy and time, E_f and t_f , is given by

$$t_f = t_i + \int_{x_f}^{x_i} \frac{dx}{v(x)} = t_i - \int_{E_i}^{E_f} \frac{dE}{f(E)v(E)\rho(x(E))} \approx t_i - \int_{E_i}^{E_f} \frac{dE}{f(E)v(E)\rho(x_i)}. \quad (4.8)$$

A summary of the steps during propagation is visualized in Figure 4.3.

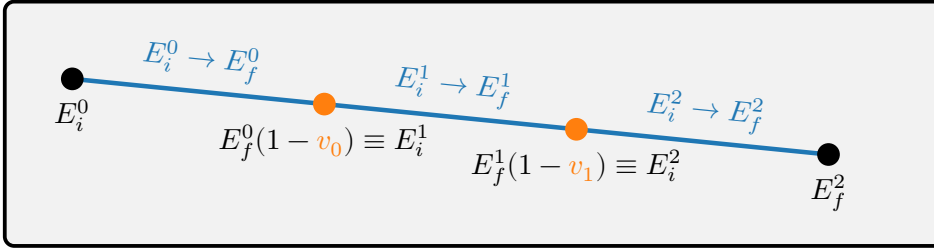


Figure 4.3: Visualization of the PROPOSAL propagation algorithm, adapted from [28]. Starting with an initial energy E_i^0 , the energy E_f^0 where the next stochastic interaction occurs is sampled according to (4.6). The continuous energy loss therefore corresponds to $E_i^0 - E_f^0$. Afterward, the stochastic loss v_0 is sampled from (4.5), leading to a new energy E_i^1 . With this energy, the next propagation step is started.

It is important to note that the threshold v_{cut} , as defined in (4.2), is an artificial simulation parameter and not intrinsically given by nature. Therefore, a careful choice of v_{cut} is necessary. Small values of v_{cut} produce small propagation steps, leading to a very precise, but also computationally expensive simulation. On the other hand, large values of v_{cut} lead to larger propagation steps, which are faster to compute, but less precise. When v_{cut} is set too high, stochasticity might not be sufficiently described by the simulation, which can lead to simulation artifacts. One example can be seen in Figure 4.4, where the final energy spectrum of 1 TeV muons, propagated for a fixed distance, is shown. For an energy threshold of $v_{\text{cut}} = 10^{-4}$, a continuous spectrum, as expected, is visible. However, for an energy threshold of $v_{\text{cut}} = 0.05$, the energy spectrum is not continuous, and a nonphysical accumulation of muons with an identical final energy is visible. This spike corresponds to all muons where only one propagation step, i.e., only one continuous energy loss without any stochastic losses, is simulated. While the smaller energy threshold $v_{\text{cut}} = 10^{-4}$ avoids this artifact, at least for the bin size chosen for the histogram in Figure 4.4, the simulation requires a much longer computation time, as is shown in Figure 4.5.

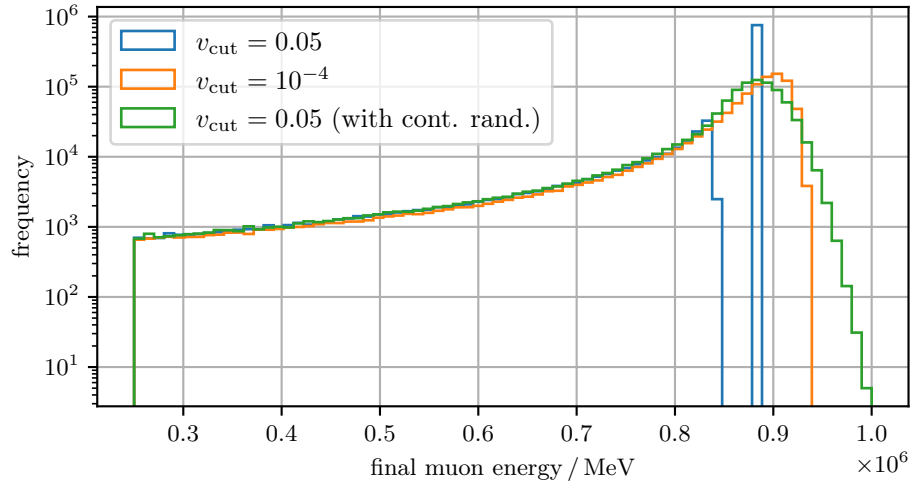


Figure 4.4: Final energy spectrum of 10^5 muons with an initial energy of 1 TeV, propagated through 100 m of *standard rock*, using different thresholds v_{cut} . The green line introduces the approach of continuous randomization according to (4.9).

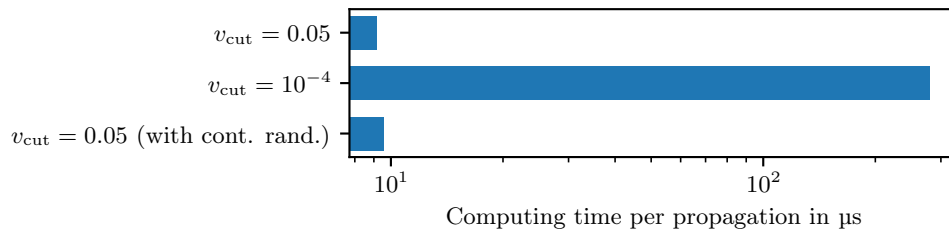


Figure 4.5: Computing time for simulating the energy spectra in Figure 4.4.

A different approach to avoid this problem, without the increased runtime, is to apply random fluctuations on the continuous energy losses. In PROPOSAL, this approach is called continuous randomization: The final energy after a continuous loss is sampled from a Gaussian function, where the mean of the distribution is given by the initially calculated final energy, and the variance of the distribution is calculated according to [77]

$$\langle \Delta(\Delta E)^2 \rangle = \int_{E_i}^{E_f} \frac{E^2}{-f(E)} \left\langle \frac{d^2 E}{dX^2} \right\rangle dE, \quad (4.9)$$

with

$$\left\langle \frac{d^2 E}{dX^2} \right\rangle \propto \int_{v_{\min}}^{v_{\text{cut}}} v^2 \frac{d\sigma}{dv} dv. \quad (4.10)$$

As shown in Figure 4.4, this approach produces a continuous energy spectrum close to the one produced with $v_{\text{cut}} = 10^{-4}$ but no continuous randomization, albeit using $v_{\text{cut}} = 0.05$. The additional runtime due to the calculation of continuous randomization is negligible, as shown in Figure 4.5.

Adjusting the threshold setting via E_{cut} , v'_{cut} , and the option to enable continuous randomization, allows to steer the performance and precision of the propagation process. Within PROPOSAL, these settings can not only be set for an entire simulation but also individually for different geometries in the propagation environment. This allows for a detailed performance optimization of the simulation, as illustrated with an example in Figure 4.6.

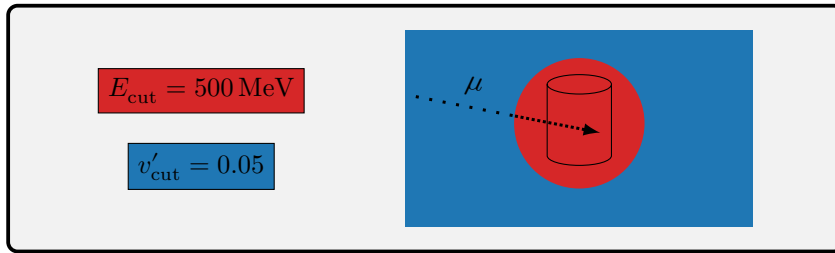


Figure 4.6: Exemplary steering of the threshold settings for a simulation environment. In this example, surrounding muons are entering a detector, visualized by a cylinder. Outside of the detector, a more approximate treatment of the muon propagation, in this case with a setting of $v'_{\text{cut}} = 0.05$, is used. In the vicinity of and inside the detector, a more precise treatment is necessary. In this case, the threshold can be set to an E_{cut} value corresponding to the energy above which the detector becomes sensitive to individual energy losses. Here, this is assumed to be at $E_{\text{cut}} = 500$ MeV.

Note that a crucial step in increasing the performance of PROPOSAL is to store the evaluations of the integrals outlined in this section in interpolation tables. The basic concepts and limitations of this approach are described in [Section 6.3.1](#), with more details provided in [\[143, 29\]](#).

4.2 Recent Updates

In this section, two recent updates of PROPOSAL relevant for its application in the context of particle cascade simulations are presented: The modularization of the code structure of the propagation algorithm, and the functionality to sample individual secondary particles from energy losses. The implementation of physics processes of electromagnetic particles in PROPOSAL is described separately in [Chapter 6](#).

A complete description of the most recent updates in PROPOSAL is given in [\[29\]](#).

4.2.1 Modularization of the Code Structure

In the context of software development, modularization describes the organization of a given code structure in individual modules, where each module is responsible for a clearly defined task. This also allows for the standalone usage of each module, which is the main motivation for the modularization efforts inside PROPOSAL. This has especially been necessary in the context of CORSIKA 8, see [Section 5.2](#), but is equally useful for other use cases.

Until now, the main and most important interface provided by PROPOSAL has been the `Propagator` class, which is responsible for the entire propagation process. To initialize a `Propagator`, the propagation environment needs to be defined at first. This environment is assembled by one or more sectors, where each sector is defined by its medium, density distribution, geometry, and propagation settings. These propagation settings include, among other settings, the propagation threshold (see [\(4.2\)](#)) as well as the names of the parametrizations used to describe the physics, e.g., the descriptions of energy losses and multiple scattering. As an input, the `Propagate` method provided by the `Propagator` class receives the initial state of the particle to be propagated, which is defined by its particle type, position, direction, and energy. Furthermore, the user can specify termination conditions for the propagation, e.g., a minimal energy or a maximum propagation distance. With this information, calling the `Propagate` method executes the entire propagation process. As an output, the method returns information about the final particle state, as well as information about the intermediate energy losses of the particle. The interface to this output

has recently been improved, providing more options to easily access the available information. These improvements also include the possibility of obtaining the particle state for arbitrary positions and energies, even after the initial propagation process has been completed. The underlying approach, as well as a description of the output of the `Propagator` class with its recent improvements, are described in [29].

This structure, where the propagation is centralized inside a single class, is sufficient for use cases where only the output of the propagation is relevant. For example, for muon and tau lepton simulations for the IceCube Neutrino Observatory, only the information about the individual energy losses is relevant for the subsequent simulation steps, as described in detail in Section 4.3.1. However, this structure does not allow the user to access the individual calculations, listed in Section 4.1, that are performed during the propagation process.

This is changed with a modularization of the `Propagator` class, where the calculation tasks during propagation have been distributed over six modules: `Interaction`, `Displacement`, `Decay`, `Time`, `Scattering`, and `ContRand`. Each of these modules is now responsible for performing a limited part of the propagation process. The structure of the modules is visualized in Figure 4.7, and a description of the methods they provide is given in Table 4.1. With this new structure, the `Propagator` class

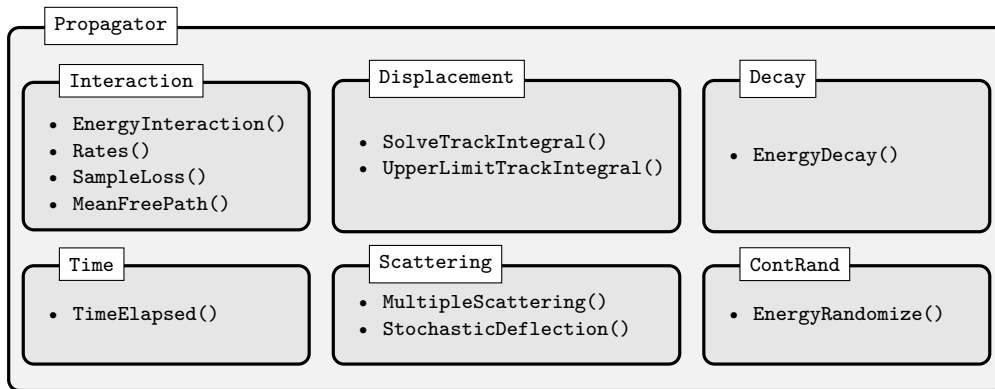


Figure 4.7: Modularization of the `Propagator` class. The boxes visualize the individual classes, together with the methods that they provide. A description of the methods is given in Table 4.1.

delegates the necessary propagation tasks to the modules. The relevant improvement for the user is that these individual modules can now be used as standalone classes. This allows PROPOSAL not only to be used as a self-contained particle propagator but also as a modular library for particle propagation tasks.

Table 4.1: Definitions of the methods provided by the modules responsible for executing the propagation tasks.

Method	Method description
Interaction:	
EnergyInteraction()	Calculate the energy where the next stochastic loss occurs by solving (4.6) for E_f .
Rates()	Calculate stochastic cross sections σ_s , see (4.4), for each interaction type.
SampleLoss()	Given the stochastic cross sections, sample the type and size v of a stochastic energy loss.
MeanFreePath()	Calculate the mean free path length λ , i.e., the inverse of the sum of the total stochastic cross section σ_s .
Displacement:	
SolveTrackIntegral()	For a given initial energy E_i and a given final energy E_f , calculate the covered grammage X according to (4.7).
UpperLimitTrackIntegral()	For a given initial energy E_i and covered grammage X , calculate the final energy E_f after a continuous step according to (4.7).
Decay:	
EnergyDecay()	Calculate the energy at which the particle decays, similar to the calculation of the energy of the next stochastic loss in (4.6).
Time:	
TimeElapsed()	Given an initial energy E_i , a final energy E_f , and the local medium density ρ , calculate the time elapsed during a continuous step according to (4.8).
Scattering:	
MultipleScattering()	Calculate displacement and directional change during a continuous step due to multiple scattering, see Section 6.1.6.
StochasticDeflection()	For a given stochastic interaction, sample the deflection of the particle in this interaction.
ContRand:	
EnergyRandomize()	Calculate randomization of the final energy E_f of a continuous propagation step according to (4.9).

This alternative, modular interface is particularly important for CORSIKA 8, where PROPOSAL serves as an interaction model for the description of the electromagnetic and muonic component of extensive air showers and other particle cascades. In this context, CORSIKA 8 manages the simulation of the particle cascade, while PROPOSAL is only used for the physics description, similar to the usage of hadronic interaction models such as SIBYLL [185] or EPOS [179]. For this purpose, the interface of CORSIKA 8 needs access to the individual modules. A description of the usage of PROPOSAL in CORSIKA 8 is given in Section 5.3

4.2.2 Calculation of Individual Secondary Particles

Initially, PROPOSAL only provided information about the energy deposition and the underlying interaction type of stochastic energy losses during propagation. This has been sufficient in many cases, for example in muon and tau lepton simulations for IceCube, see Section 4.3.1, where the observed Cherenkov light yield can be inferred solely from this information.

In the case of CORSIKA 8, however, the description of particle cascades requires information about the individual secondary particles produced in stochastic interactions. Therefore, methods to convert a stochastic energy loss into individual secondary particles are implemented in PROPOSAL. The underlying concept is illustrated in Figure 4.8. A `CalculateSecondaries()` method receives a `StochasticLoss` object,

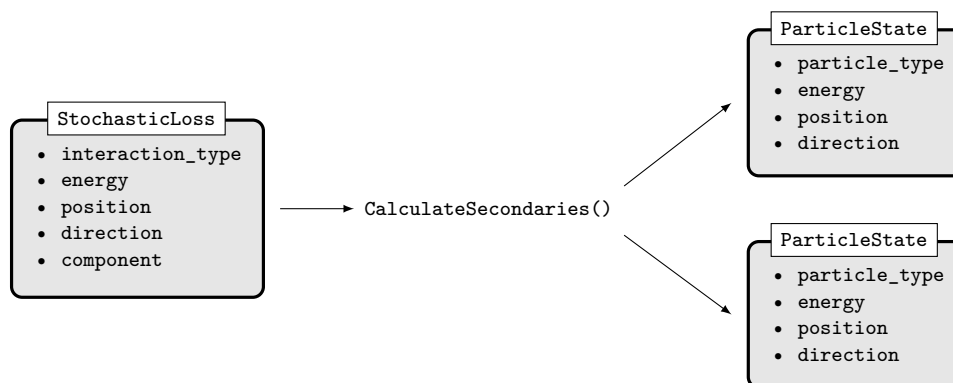


Figure 4.8: Illustrated concept of the `CalculateSecondaries()` methods, which convert information about stochastic energy losses into information about individual secondary particles. The item `component` describes the medium or nucleus with which the initial particle has interacted. Note that the amount of created `ParticleState` objects can vary. In this illustration, two secondary particles are created. Figure from [29].

characterizing the energy loss, and returns a list of sampled `ParticleState` objects, defining the secondary particles. For each interaction type, one or more realizations of the `CalculateSecondaries()` method are provided. The general tasks to be performed in these methods are the calculation of the energy distribution between the secondary particles, in case two or more particles are produced, as well as calculating the directions of the outgoing particles. In many cases, these properties can be sampled from analytical descriptions of the differential cross sections. For some interaction types, approximations can be made to decrease the computational effort of the sampling process, which is especially relevant for regularly occurring interaction types, such as electron-positron pair production and bremsstrahlung in electromagnetic showers. For photonuclear interactions, however, the sampling of the secondary particles is more complex, as different hadronic processes play a role, and different output states are possible. This requires a dedicated treatment, involving the usage of external hadronic event generators. The details about the implemented secondary calculation methods for electron, positron, and high-energy photon interactions are described in [Chapter 6](#).

Note that the calculation of secondary particles is independent of the propagation process. The individual secondary particles can be sampled optionally, which means that the performance of the initial propagation is not affected.

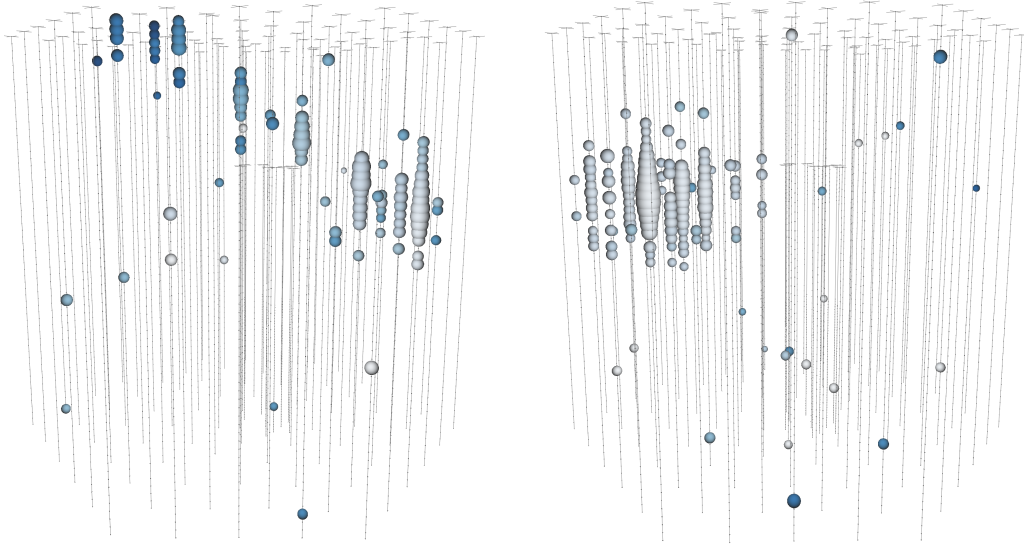
4.3 Applications in Neutrino Astronomy and Particle Physics

Due to the flexibility of its functionalities, PROPOSAL simulations are used in a lot of different experiments, especially in neutrino astronomy, but also in other areas such as particle physics. This section is not intended to give a complete overview of all applications, but rather an insight into different areas where PROPOSAL is utilized.

4.3.1 Very-Large Volume Neutrino Telescopes: IceCube, KM3NeT, Baikal-GVD, P-ONE, and TRIDENT

The common concept of neutrino observatories is to use a large, instrumented volume in a transparent medium to observe neutrino interactions. In the case of the IceCube Neutrino Observatory, this is done at the geographical South Pole, where 5160 [Digital Optical Modules \(DOMs\)](#), each containing a downward-facing photomultiplier tube, have been deployed between a depth of 1450 m and 2450 m in the ice [5]. They are evenly distributed along 86 strings, placed on a triangular grid, with a spacing of approximately 125 m between them, leading to an instrumented volume of around

1 km³. While neutrinos themselves do not leave a detectable signature behind, they can interact, albeit rarely, with the ice inside or in front of the detector via the weak interaction. In these interactions, charged secondary particles are created, which can be detected via the Cherenkov light they produce. Depending on the flavor of the involved neutrino and whether it undergoes a charged-current interaction (i.e., under exchange of a W^\pm boson) or a neutral-current interaction (i.e., under exchange of a Z boson), signatures can be classified as track-like or cascade-like: Track-like events are produced by charged-current ν_μ interactions, where an outgoing muon, which can travel several kilometers through ice, deposits energy along its track. Charged-current ν_e and ν_τ interactions, as well as all neutral-current interactions, produce a cascade-like event, creating a hadronic cascade at the point of interaction.⁴ Exemplary signatures of a track-like event and a cascade-like event are shown in Figure 4.9. The main backgrounds when searching for astrophysical neutrinos are



(a) Track-like event signature of an up-going event from a charged-current ν_μ interaction. (b) Cascade-like event signature of a charged-current ν_e interaction inside the detector.

Figure 4.9: Visualization of typical IceCube event signatures. Each sphere represents a DOM, the sizes of the spheres correspond to the amount of detected light, and the color of the spheres corresponds to the arrival time. Darker colors represent a later arrival time. Figure adapted from [7].

⁴Note that due to the average tau decay length of $l_\tau \approx E_\tau \cdot 50 \text{ m/PeV}$, charged-current ν_τ interactions will also be seen as a track-like event for sufficiently high energies [161].

atmospheric muons and neutrinos created in cosmic-ray-induced air showers. While atmospheric neutrinos can reach the detector from both the Northern and the Southern hemispheres, atmospheric muons can only be seen as down-going track-like events (i.e., originating from the Southern Hemisphere) in the detector because of the shielding of the Earth [6]. Due to the rarity of neutrino interactions and the relative abundance of cosmic rays, atmospheric muons dominate the astrophysical neutrino signal by several orders of magnitude. To be able to separate different signal and background signatures and reconstruct the physical properties of events, accurate simulations are necessary to train the underlying algorithms.

The simulation chain of IceCube can generally be divided into three parts: Generation, propagation, and detector simulation. Generation describes the injection of initial particles which might produce signatures in the detector. For the generation of atmospheric muons, the air shower simulation tool CORSIKA 7 [113, 114], creating complete air shower simulations, is used. Alternatively, the code MuonGun, which is an implementation of MUPAGE [75] for IceCube and injects muons on a cylinder-shaped surface based on parametric formulas, is available. For the generation of neutrinos and their interactions, the tools LeptonInjector [10], as well as implementations of ANIS [98] and GENIE [42], are available. Afterward, the created muons and taus are propagated from their injection point toward and through the detector by PROPOSAL. Particles outside the detector are simulated with a relative energy threshold of $v_{\text{cut}} = 0.05$, with continuous randomization enabled, to ensure an effective propagation until they enter the detector. Inside the detector, a more accurate simulation with an absolute energy threshold of $E_{\text{cut}} = 500 \text{ MeV}$ is used since a precise description of the individual muon and tau energy losses inside the detector is important. For the conversion of stochastic and continuous energy losses given by PROPOSAL into Cherenkov photons, a module called Cascade Monte Carlo is used, which provides parametrizations based on GEANT4 [99] simulations. The path of Cherenkov photons toward the DOMs is simulated using `clsim`⁵, a photon-tracking algorithm based on ray-tracing techniques, relying on models which describe the properties of the Antarctic ice [221]. In the last step, the detector simulation is performed using tailored tools to describe detector noise (thermal noise or energy deposit from radioactive decay), the response from the photomultiplier tubes, DOM electronics, and triggers.

Apart from IceCube, two other large-scale neutrino telescopes, using the same detection principle, are currently under construction: KM3NeT is a neutrino observatory in the Mediterranean Sea [21], consisting of two detector sites: One in a configuration optimized for the detection of neutrinos in an energy range from 1 TeV to 100 PeV, and one optimized for neutrino detection down to energies of 100 MeV due to denser

⁵Code documented in <https://github.com/claudiok/clsim>.

spacing of the detector modules. Both sites are currently under construction, but first scientific results are already available [55]. For the simulations in KM3NeT, the code gSeaGen [26] has been developed, which includes its own muon propagator, called PropaMuon. As alternatives, gSeaGen also provides interfaces to MUSIC [46] and PROPOSAL. Performed comparisons between the three propagation algorithms show a good agreement [26, 203]. At Lake Baikal, another neutrino telescope, called Baikal-GVD (Baikal **G**igaton **V**olume **D**etector), is currently being deployed [158]. The layout of Baikal-GVD is organized in clusters of strings, where ten clusters are currently operational. Muon simulations for Baikal-GVD are produced with the tool MUM [200], although PROPOSAL can also be used within the simulation chain [177]. Lastly, two neutrino detectors are currently in the planning phase: P-ONE (**P**acific **O**cean **N**eutrino **E**xperiment) is planned to be located in the Pacific Ocean in the Cascade Basin region [22], and TRIDENT (**T**he **tR**opical **D**Eep-sea **N**eutrino **T**elescope) is planned to be located in the Northeastern region of the South China Sea [226]. First simulations for both experiments have already been produced, each using PROPOSAL for muon and tau lepton simulations [215, 226].

4.3.2 Alternative Approaches to Neutrino Astronomy: NuRadioMC and TAMBO

The above-mentioned existing and planned neutrino telescopes are sensitive to neutrinos of energies up to the PeV range. To efficiently observe neutrinos with even higher energies, the rarity of the events requires larger instrumented volumes, which is infeasible with the Cherenkov approach due to the high costs. As an alternative, the radio technique can be used: The idea of this approach is that particle cascades, induced by neutrino interactions, produce a radio signal with frequencies between MHz and GHz due to the Askaryan effect, as described in Section 3.3.3 and illustrated in Figure 4.10, which can be detected with radio antennas [103]. Since the attenuation length for radio emission is much higher compared to visible light, for example up to 1 km in ice [48], the distance between individual detection units can be much larger, making it possible to instrument larger volumes in a cost-effective way. This approach has been pioneered by experiments such as ARA (**A**skaryan **R**adio **A**rray) [36] or ARIANNA (**A**ntarctic **R**oss **I**ce-**S**helf **A**Ntenna **N**eutrino **A**rray) [44], with larger projects currently planned or under deployment, such as RNO-G (**R**adio **N**eutrino **O**bservatory **G**reenland), where 35 detector stations with a spacing of 1.25 km will be deployed [24, 23]. To provide simulations for neutrino observatories, including the simulation of the first neutrino and its interaction, the generation of the radio pulse and its propagation through the surrounding medium, and lastly, the simulation of the detector response, the framework NuRadioMC is available [103]. NuRadioMC has been designed as a

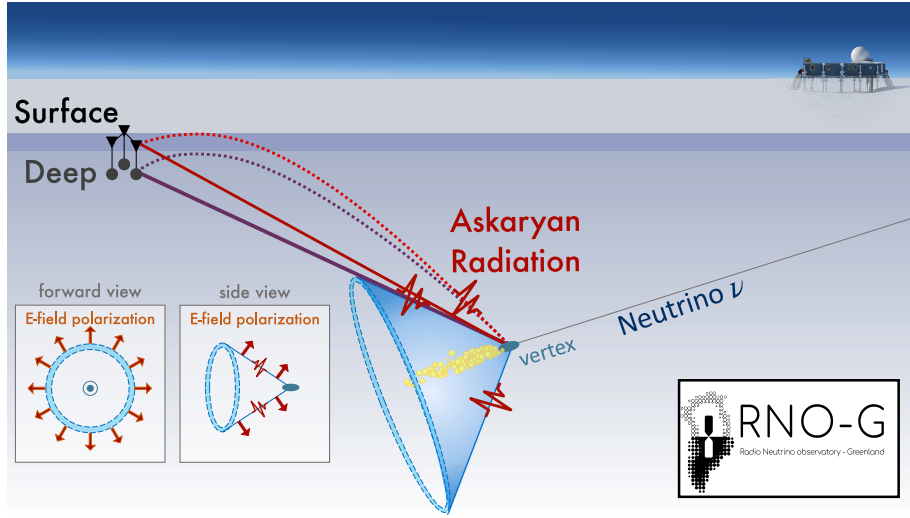


Figure 4.10: Illustration of the in-ice radio neutrino detection technique. The radio signal is mainly emitted on a Cherenkov angle, indicated in blue, and detected by radio antennas, indicated in black. For a varying refractive index, the radio signal can follow bent trajectories. Figure from [23].

flexible software framework, not limited to a specific experiment, so it can be used to analyze the performance of different detector designs. While the main radio signal is generated from the cascade produced in the primary neutrino interaction, additional radio signals can be produced by energy losses from muons and taus stemming from the neutrino interaction. Therefore, NuRadioMC uses PROPOSAL to propagate muons and taus from charged-current neutrino interactions, as well as muons from tau decays, and simulates the radio signal from the corresponding energy losses. This effect needs to be taken into account because it can increase the effective volume of the detector, as well as mimic the typical “double bang” signature from charged-current ν_τ interactions. Furthermore, NuRadioMC with PROPOSAL has been used to investigate the radio background induced by atmospheric muons, which has been found to be non-negligible [97].

Another proposal for a next-generation neutrino observatory, designed to detect tau neutrinos, is TAMBO (Tau Air Shower Mountain-Based Observatory) [189, 213]. The concept of TAMBO, as illustrated in Figure 4.11, is to place an array of detector modules, for example, water Cherenkov detectors, on the side of a mountain in a valley of the Peruvian Andes. If a tau neutrino traverses the mountain, it can undergo a charged-current interaction, producing a tau lepton. If this tau lepton decays after leaving the mountain, it will create a particle shower in the air, which can be measured with the detector array. The proposed detector design will be

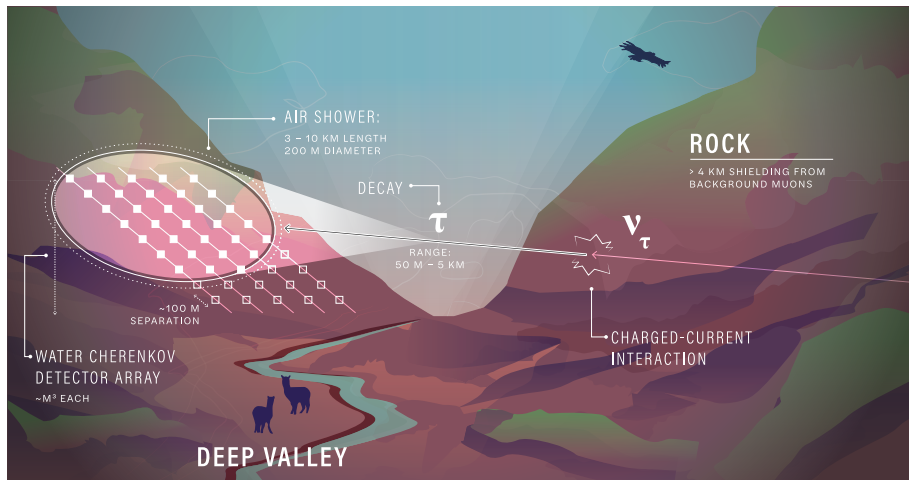


Figure 4.11: Detection concept of TAMBO. Figure adapted from [213].

sensitive in an energy range between 1 PeV and 100 PeV, i.e., between the upper energy limit of the very-large neutrino telescopes described in Section 4.3.1 and the lower energy limit of radio neutrino observatories [189]. The current simulations for TAMBO use PROPOSAL to propagate the tau leptons until they decay, and CORSIKA 8 to simulate the cascades created by the decay products [152].

4.3.3 Particle Physics: $\text{NO}\nu\text{A}$

The $\text{NO}\nu\text{A}$ (NuMI **O**ff-Axis ν_e **A**ppearance) experiment is a particle physics experiment, designed to observe neutrino oscillations, especially $\nu_\mu \rightarrow \nu_e$ [16]. It consists of two detector sites: One near detector, about 1 km away from the neutrino source, which is the Fermilab NuMI neutrino beam [20], and a far detector, around 810 km away. Both detectors are identically designed scintillation detectors, with a total mass of 290 t for the near detector and 14 kt for the far detector. Details about the technical design of the $\text{NO}\nu\text{A}$ experiment are given in [49]. The general analysis idea is to compare the number of neutrinos observed in both detectors to infer the sensitive oscillation parameters. However, charged-current interactions of ν_μ in the rock in front of the detector can create muons, which itself can produce signatures in the detector and therefore need to be taken into account. To propagate these muons, the framework GEANT4 [99] is currently used. To optimize this runtime-intensive part of the simulation chain, the usage of PROPOSAL is being investigated. First results show a reasonable agreement with GEANT4 simulations for most muon energy regimes, with a significant improvement in computation time by at least two orders of magnitude [176].

5 The Shower Simulation Framework CORSIKA

The first ideas of simulating particle cascades with the Monte Carlo technique date back to attempts conducted as early as 1952: To simulate an electromagnetic particle cascade in lead, Robert R. Wilson used a mechanical “wheel of chance” – a cylinder, powered by a high-speed motor and stopped at random – to sample the interactions of individual particles [224]. With the increased availability of computational resources in the following decades, Monte Carlo codes have become a substantial tool to understand and interpret extensive air showers, especially for the data analysis of experiments in astroparticle physics. At first, a variety of different codes were developed, mostly specific for an individual experiment, where each code used its own algorithms, physics descriptions, and approximations. However, this meant that for disagreeing results between experiments, it was hard to determine whether the disagreement stemmed from experimental or simulational differences. Using a common framework for air shower simulations, even if it does not provide a perfect description of nature, would mitigate this problem by providing a common baseline, thus making comparisons more consistent [89].

For the KASCADE (**K**arlsruhe **S**hower **C**ore and **A**rray **D**ETECTOR) experiment, a former air shower experiment located in Karlsruhe [45], the extensive air shower simulation program CORSIKA (**C**OSMIC **R**AY **S**IMULATIONS for **K**ASCADE) has been developed, with the first version released in 1989 [113]. By now, CORSIKA has become the standard tool used for air shower simulations, used by the majority of experiments in astroparticle physics, but also in related contexts. This is emphasized by the fact that the CORSIKA physics description [113] has been cited over 1100 times.¹

This chapter starts with a description of CORSIKA 7, the most recent version of CORSIKA still based on the original code developed in 1989. After highlighting the limitations of CORSIKA 7, and outlining the requirements for a new, modern framework to simulate particle cascades, the principles of CORSIKA 8 are introduced. Afterward, the usage of PROPOSAL as an electromagnetic and muonic interaction model within the CORSIKA 8 framework is explained.

¹According to the library INSPIRE-HEP, as of January 15, 2024 (<https://inspirehep.net/literature/469835>).

5.1 Extensive Air Shower Simulations with CORSIKA 7

The first version of CORSIKA, version 1.0, was released in October 1989 [114]. Developed in Fortran, the original code base has since been continuously revised, optimized, and expanded with numerous extensions. In this work, the term CORSIKA 7 refers to the most recent release, which is currently version 7.7500. A complete description of CORSIKA 7 is given by its user guide [114] and its physics description [113]. This section gives an overview of the treatment of the three physics components of an extensive air shower in CORSIKA 7: The hadronic, the electromagnetic, and the muonic shower component.

Treatment of Hadronic Interactions

The description of hadronic interactions is the main systematic uncertainty for the simulation of extensive air showers. The reason is that the phase space important for air showers, which includes forward-boosted interactions at high energies, is both inaccessible to current experiments and hard to describe theoretically. These problems are described in more detail in the context of the muon puzzle in Section 3.4. As a consequence, different interaction models to describe hadronic interactions exist, which all provide varying predictions. To take these systematic uncertainties into account, CORSIKA 7 provides a selection of different hadronic interaction models. A differentiation between low-energy and high-energy hadronic interaction models is made, where the transition energy (i.e., the energy deciding whether a particle is treated by the low-energy or high-energy interaction model) is by default set to 80 GeV [114]. A list of hadronic interaction models available in CORSIKA 7 is provided in Table A.1 and Table A.2. An overview of the physics applied in these models as well as their connection to the development of extensive air showers is given in [86].

Treatment of Electromagnetic Interactions

For the description of electrons, positrons, and photons, two different approaches are available. A full Monte Carlo description, where each electromagnetic particle is individually tracked, is provided by the code EGS4 (**E**lectron **G**amma **S**hower) [171]. The details of EGS4, as well as the adaptations of the code made for its usage in CORSIKA 7, are described in Section 5.1.1. Alternatively, an analytical approach can be chosen by describing the electromagnetic shower component using the analytic NKG formula [74, 150]. In this case, for each electromagnetic subshower initiated by an electron, positron, or photon, the longitudinal shower development,

as well as the lateral particle density on the observation plane, is estimated. The overall electromagnetic content of the extensive air shower is then calculated by summing up the contributions from all subshowers. While this approach has the advantage of a significantly smaller simulation time compared to the full Monte Carlo Simulation using EGS4, it provides a less accurate description of, as well as less information about, the electromagnetic shower component.

Treatment of Muons

The propagation of muons is treated internally by CORSIKA 7. Continuous ionization losses are described by the Bethe-Bloch formula and multiple scattering is parametrized either by Molière theory or a Gaussian approximation to it (see [Section 6.1.6](#)). As inelastic muon interactions, CORSIKA 7 only considers bremsstrahlung and electron-positron pair production, neglecting hadronic interactions as well as rare interaction processes such as muon pair production [113]. The energy loss parametrizations are based on their description in the framework GEANT3 [66]. From these cross sections, the step length is sampled from an exponential distribution.

5.1.1 Description of Electromagnetic Interactions by EGS4

EGS4 is a simulation package released in 1985, consisting of subroutines written in Mortran3, to describe the transport of electrons, positrons and photons in arbitrary geometries [171].² Given an initial electromagnetic particle, the code provides a full Monte Carlo simulation of the initiated electromagnetic shower. For the transport of electrons and positrons, EGS4 samples discrete interactions, where the processes bremsstrahlung, annihilation, as well as Bhabha and Møller scattering, are possible [171]. For the steps between these interactions, multiple scattering according to Molière theory and continuous energy losses, consisting of ionization and soft (i.e., sub-threshold) bremsstrahlung losses, are applied. The decrease of the total cross section during a transport step, caused by the continuous energy loss, is taken into account using a rejection sampling method. This approach is also used in CORSIKA 8 and is explained in [Section 5.2.2](#). The transport of photons is described with discrete interactions only, taking into account electron-positron pair production, Compton scattering, and the photoelectric effect. The interaction cross sections, including a comparison with the cross sections used in CORSIKA 8, are visualized in [Section 7.1](#).

²Mortran (More Fortran) is an extension of the programming language Fortran.

To meet additional requirements, CORSIKA 7 uses a modified version of EGS4, which is deeply integrated into the CORSIKA 7 source code. The list of modifications is given as follows: Firstly, to describe the muon content induced by electromagnetic subshowers, muon pair production [108] and photonuclear reactions [109] of photons have been added as additional processes. To correctly take into account the varying atmospheric density, the particle tracking and the density correction for ionization losses, which has previously only been calculated for a fixed density, have been adapted [113]. As the approximations made for the tracking in magnetic fields are only valid for small deflection angles, step sizes in EGS4 have been limited to restrict the deflection in a single transportation step to 11.5° . By default, the physics descriptions in EGS4 are valid for energies between 1 keV and several TeV [171]. To be able to describe extensive air showers of the highest energies, an approach to treat the Landau-Pomeranchuk-Migdal (LPM) effect (see Section 6.3 for a detailed description) has been implemented [112]. An additional challenge in simulating high-energy showers is the computational effort, as runtimes increase approximately linearly with the primary particle energy. Therefore, runtime-related optimizations for EGS4 have been performed: Firstly, the default limitation of the step size due to multiple scattering has been increased by a factor of ten, allowing for larger transportation steps at the expense of a less detailed description of the lateral particle distribution. Secondly, particles that are unlikely to reach a specified observation level are discarded early. This is achieved by estimating the probability of a particle reaching an observation level before each transportation step, and discarding it if specific conditions are met [113].

The development of EGS has been continued independently by the codes EGS5 [118] and EGSnrc [134].

5.1.2 Limitations of CORSIKA 7

The most recent version of CORSIKA 7 is still based on the original code, which was written over 30 years ago with its application in the context of the KASCADE experiment [45] in mind. Although its development continued, contributions from different developers were often uncoordinated, and code quality control was limited. It comes as no surprise that today, the resulting code base of CORSIKA 7 is highly complex and monolithic. Another important aspect is the used programming language: Fortran, especially the primarily used FORTRAN 77 standard, comes with a limited set of features, especially regarding the requirements of modern programming. Additionally, the number of scientists knowing or learning Fortran is decreasing with the presence of new and modern programming languages. These aspects make the development of new features, and even the simple maintenance of the code,

hard to accomplish, especially for a new generation of developers. In addition to these technical obstacles, several aspects concerning the physics description limit the possibilities of the code [88]: For example, only shower simulations in air are possible, with limited options to describe the atmospheric density via a 5-layer model [114]. Simulations in other, or even across different media, are impossible. Physics modules inside CORSIKA 7, like the Cherenkov calculation module, are unable to directly impact the shower simulation. However, this can be important for specific applications, for example, to impose restrictions such as a maximum path length. Another aspect is the production history of particles reaching the observation plane, where only information about the parent and grandparent particle, but no earlier generations, can be retrieved [111].

5.2 CORSIKA 8: The Next Generation of Particle Cascade Simulations

As outlined in the previous section, CORSIKA 7 is not sufficient to fulfill the requirements of a modern particle shower simulation framework, both from a technical and physical point of view. Therefore, the development of CORSIKA 8 has been initiated in 2018 [88]. While the name highlights its role as a successor to CORSIKA 7, the code base of CORSIKA 8 has been rewritten from scratch and is independent of previous CORSIKA versions. While CORSIKA 7 served as a code to simulate extensive air showers in air, CORSIKA 8 is developed as a framework for the general simulation of particle cascades, extending its range of possible use cases.

Core principles for the development of CORSIKA 8 are, among other aspects, flexibility, efficiency, and reliability. To provide a suitable foundation, CORSIKA 8 is written in the programming language C++. This choice is motivated by the flexibility of C++, its support of modern programming techniques, and its widespread usage, also outside the scientific community, which guarantees long-time support. The flexibility of CORSIKA 8 is highlighted by its modularity: Each building block of the code structure, which is explained in Section 5.2.1, is written in a modular way and can be adapted or entirely exchanged. This also prepares CORSIKA 8 for its usage in applications that are not yet foreseen, both from a physical and technical standpoint. To allow for optimized efficiency, the code is designed to intrinsically support techniques such as hardware acceleration, for example on graphics processing units, or multi-core computations. By organizing CORSIKA 8 as an open-source project, the development of the code is made transparent, encouraging improvements

and extensions by the community.³ Reliability is closely related to a high coding standard, which is guaranteed by enforcing code reviews, automatic unit testing, careful documentation, and transparent issue tracking.

More details, especially regarding the technical aspects of the code design of CORSIKA 8, are described in [88]. The most recent summary of the status of the project is given in [125].

5.2.1 Code Design

The main building blocks of CORSIKA 8 are the **Cascade**, **Tracking**, **Environment**, **Process List**, and **Output** code. Together with their relations among each other, they are illustrated in Figure 5.1.

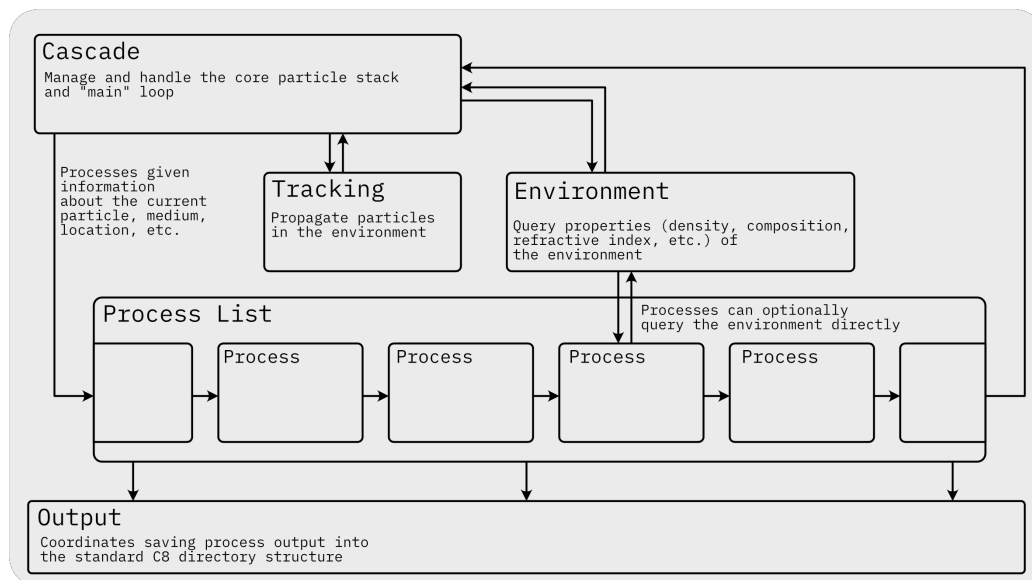


Figure 5.1: Overview of the design of CORSIKA 8. Figure from [125].

The **Cascade** code is the core algorithm, responsible for managing the particle cascade simulation. Its functionality is explained in detail in Section 5.2.2. The code also includes the particle stack, which is responsible for the intermediate storage of particle information during the cascade simulation. Optionally, the stack can

³The code is available on GitLab, hosted by the Institute for Astroparticle Physics at the Karlsruhe Institute of Technology: <https://gitlab.iap.kit.edu/AirShowerPhysics/corsika>.

store the full history of each particle, which allows for in-depth studies of particle interactions [39, 182].

The **Environment** code defines the properties of the medium in which the particle cascade is simulated. For this purpose, the environment is built from simple geometric objects. Currently, only cuboids and spheres are available, although new geometries are straightforward to implement. All geometries are organized in a tree-like structure, describing their relations among each other (e.g., overlapping or containing) [183]. For each geometry, media properties such as the density distribution and the elementary composition are assigned. These properties can be modularly extended by additional information such as temperature or refractive index in case they are of importance for specific physics processes. This design concept allows for the flexible construction of arbitrary environments.

The **Tracking** code models the transport of the particles through the environment, taking into account additional effects like magnetic field deflections. The default tracking algorithm currently used in CORSIKA 8 to describe the trajectory of charged particles in a magnetic field is based on an implementation of the leapfrog algorithm [197].

The **Process List** code provides a list of processes that will affect or observe the simulation. The list itself can be flexibly assembled for different use cases. Each process is a separate module, making the addition of new processes possible. Processes are divided into *Discrete Processes*, which are point-like interactions, and *Continuous Processes*, which model effects on the particle trajectory between two *Discrete Processes*. Moreover, *Discrete Processes* can be divided further into *Interaction Processes*, which are described by an interaction length, *Decay Processes*, which are described by a decay time, *Boundary Crossing Processes*, which are called when a particle traverses from one medium into another, and *Secondary Processes*, which are called on every secondary particle that has been created in an interaction or decay. For example, a list of hadronic interaction models that can serve as *Interaction Processes* in CORSIKA 8 is given in Table A.1 and Table A.2.

Lastly, the **Output** code handles the storage of data, which are gathered by the processes, and their transfer out of CORSIKA 8, for example, by writing them to a disk or passing them to other frameworks.

5.2.2 Cascade Algorithm

The particle cascade simulation is realized by the Cascade code, which combines the functionalities of the previously described building blocks. The core functionality is shown in Algorithm 1.

Algorithm 1 Functionality of the CORSIKA 8 Cascade algorithm.

```

Initialize stack
while Stack is not empty do
    Extract particle from stack
    Execute Step function for particle
end while
    
```

At the beginning of the simulation, the stack is populated, usually by adding the particle initializing the particle cascade. Afterward, a while loop is entered. Inside the loop, one particle is extracted from the stack.⁴ For the extracted particle, a propagation step is performed via the **Step** method, during which the particle can be returned to the stack, usually with changed properties, or newly created particles can be added to the stack. The loop is left if the stack is empty, after which the shower simulation is terminated.

The **Step** method, which is called from [Algorithm 1](#), models a complete propagation step. At the beginning of the method, the total interaction length λ_{tot} of the particle is calculated via

$$\lambda_{\text{tot}} = \frac{\bar{A}}{N_{\text{A}} \sigma_{\text{tot}}} = \frac{\bar{A}}{N_{\text{A}} \sum_i \sigma_i}, \quad (5.1)$$

where σ_i are the cross sections from the individual *Interaction Processes*, \bar{A} the average atomic mass of the medium, and N_{A} the Avogadro constant. Based on λ_{tot} , a proposed interaction length X_{interact} is sampled from the exponential probability distribution

$$p(X) = \lambda_{\text{tot}}^{-1} \exp(-X/\lambda_{\text{tot}}). \quad (5.2)$$

Similarly, the lifetime τ_{tot} of the particle is calculated via

$$\tau_{\text{tot}} = \left(\sum_i \frac{1}{\tau_i} \right)^{-1}, \quad (5.3)$$

where τ_i are the contributions to the lifetime from the individual *Decay Processes*. Based on τ_{tot} , a proposed decay time t_{decay} is sampled from the exponential distribution

$$p(t) = \tau_{\text{tot}}^{-1} \exp(-t/\tau_{\text{tot}}), \quad (5.4)$$

and the sampled decay time is converted to a distance via $x_{\text{decay}} = \beta c t_{\text{decay}}$. Next, the Tracking code is used to calculate the possible trajectory of the particle, taking into account external effects such as magnetic field deflections. This trajectory can

⁴Per default, the stack in CORSIKA 8 processes particles via the ‘‘Last In, First Out’’ principle.

either be limited by a transition into a different medium or by enforcing a maximum allowed deflection in the magnetic field, yielding an upper geometric step length x_{geom} . Using the calculated trajectory and the density distribution provided by the Environment code, the previously sampled interaction length X_{interact} is converted from grammage to a geometric distance x_{interact} . Furthermore, each *Continuous Process* can specify an upper limit for the propagation step, mainly motivated by the fact that approximations made in calculations of the processes might be invalidated for large propagation steps. Therefore, each *Continuous Process* is queried for its upper limit, and the minimum of all limits is determined, which provides the continuous step length limitation x_{cont} . Afterward, the length of the actual propagation step is calculated via

$$x = \min(x_{\text{interact}}, x_{\text{decay}}, x_{\text{geom}}, x_{\text{cont}}), \quad (5.5)$$

and the particle is moved along its trajectory for the distance x . Next, all *Continuous Processes*, in order of their appearance in the Process List, are applied on the trajectory. Each of these processes can, but is not required to, affect the properties of the particle, for example, by decreasing its energy which corresponds to a continuous energy loss. The last action of the propagation step depends on the type of process that limits the step length. For $x = x_{\text{cont}}$, no additional processes are executed, and the propagation step is finished by returning the propagated particle to the stack. In the case of $x = x_{\text{geom}}$, an additional distinction is made: In case the propagation step ended because a medium transition has been reached, all *Boundary Crossing Processes* are called, which can, for example, model transition radiation. Otherwise, no processes are executed, and the propagation step is finished. For $x = x_{\text{interact}}$, an interaction from the list of *Interaction Processes* is performed. To decide which *Interaction Process* is selected, the individual process cross sections $\sigma_{i,f}$ are recalculated, using the updated particle properties after the continuous step. In case the cross sections did not change, i.e., $\sigma_i = \sigma_{i,f} \forall i$, the probability p_i for a process i to be selected is simply

$$p_i = \sigma_{i,f} / \sigma_{\text{tot},f}, \quad \text{with} \quad \sigma_{\text{tot},f} = \sum_i \sigma_{i,f}.$$

However, in case the total cross section has decreased during the propagation step, e.g., due to continuous energy losses, an interaction is only selected with probability $\sigma_{\text{tot},f} / \sigma_{\text{tot}}$. Otherwise, no interaction process is performed and the propagation step is terminated. This treatment is necessary because the sampling of X_{interact} , according to (5.2), only considers the process cross sections at the beginning of the propagation step, neglecting a possible change of the cross sections during the propagation step itself. Figure 5.2 shows a Toy Monte Carlo study that verifies this approach by comparing it to the PROPOSAL algorithm, described in Section 4.1,

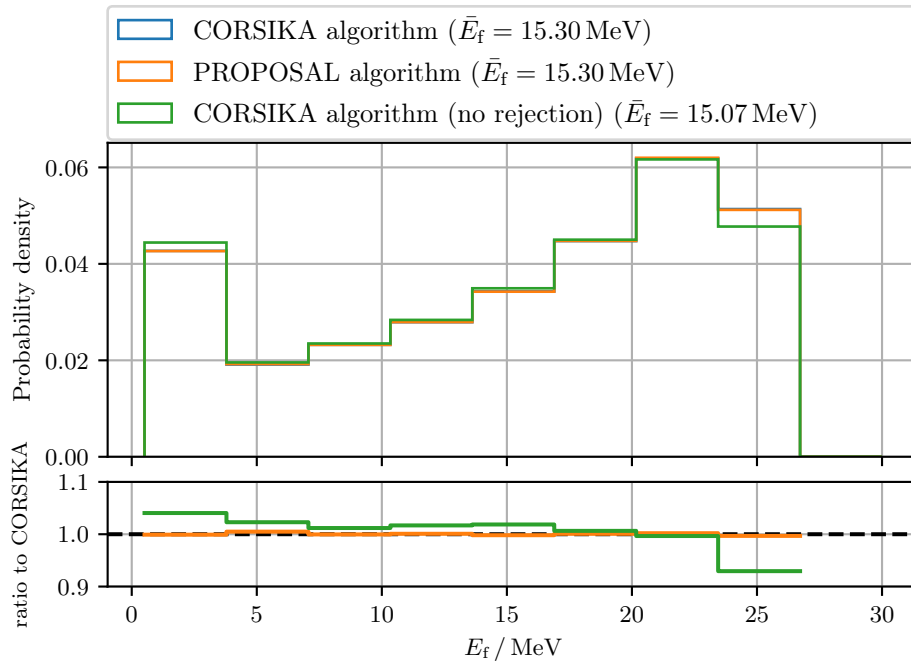


Figure 5.2: Results of a Toy Monte Carlo study, comparing the propagation algorithm of PROPOSAL (see Section 4.1) with the algorithm used in CORSIKA 8. For this study, electrons with an energy of 50 MeV are propagated over a distance of 100 m through air at standard density. The plot shows the final energy spectrum. The results from the CORSIKA 8 and PROPOSAL algorithms agree. However, when the CORSIKA 8 algorithm is used without the rejection sampling, a bias toward lower energies is visible.

which intrinsically treats the decrease of the cross section correctly when sampling stochastic interactions. A mathematical description and proof of this approach is given in [205]. Lastly, for $x = x_{\text{decay}}$, a *Decay process* is performed, where the selection is performed analogously to the treatment of *Interaction Processes*. For each secondary particle that is produced within an *Interaction Process* or a *Decay process*, all *Secondary Processes* from the Process List are called. One notable *Secondary Process* that is essential for the development of the particle cascade is the *ParticleCut* process: It defines a variable E_{track} , which specifies down to which kinetic energy particles of the cascade are tracked. If the kinetic energy of a produced secondary particle is below E_{track} , the particle is discarded. Note that the value of E_{track} can be set individually for the different particle types.

A flow chart, summarizing and visualizing the entire propagation step algorithm, is shown in [Figure A.1](#).

5.3 Usage of PROPOSAL as an Interaction Model for CORSIKA 8

PROPOSAL is used to describe the propagation of electrons, positrons, photons, muons, and taus for CORSIKA 8. For this purpose, an interface between CORSIKA 8 and PROPOSAL is implemented, as described in this section. The main interface consists of three classes inside CORSIKA 8: `ProposalProcessBase`, which provides general functionalities for the interface; `InteractionModel`, serving as a module to describe discrete energy loss processes and the consequent secondary particle production; and `ContinuousProcess`, serving as a module to describe continuous energy losses and multiple scattering between two discrete interactions. The general structure of the interface is illustrated in [Figure 5.3](#). At the moment, the PROPOSAL interface provides the only physics-complete description of the electromagnetic and muonic shower component available in CORSIKA 8.

This section describes the technical and algorithmic details of the interface. The physical descriptions of the implemented electromagnetic processes are described in [Chapter 6](#).

5.3.1 ProposalProcessBase: General Interface Functionalities

The `ProposalProcessBase` class is not a standalone module but serves as a basis for the `ContinuousProcess` and `InteractionModel` classes by providing vital functionalities. Firstly, this includes the conversion of particle type and medium

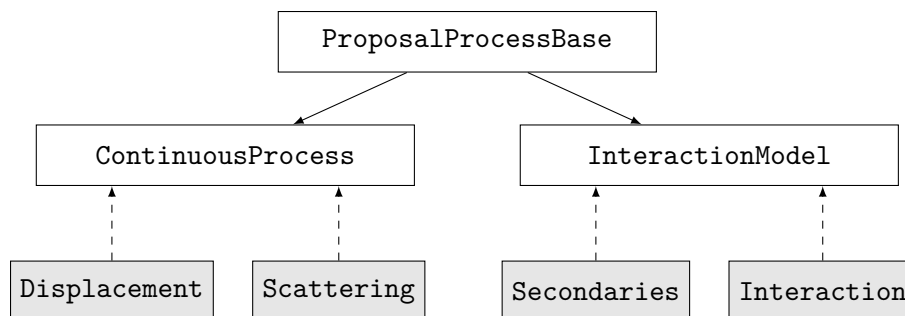


Figure 5.3: General structure of the PROPOSAL interface for CORSIKA 8. The white boxes represent classes of CORSIKA 8, while the gray boxes represent modules provided by PROPOSAL (see Section 4.2.1). The solid arrows indicate inheritance, which means here that the classes `ContinuousProcess` and `InteractionModel` can access methods provided by `ProposalProcessBase`. The dashed lines indicate the usage of PROPOSAL modules by CORSIKA 8.

definitions between CORSIKA 8 and PROPOSAL. Secondly, the particle-dependent parametrizations of the PROPOSAL cross sections are defined and stored, where the default parametrizations used inside CORSIKA 8 are listed in Appendix A.4. However, the modular structure of both PROPOSAL and CORSIKA 8 allows for exchanging, enabling, or disabling individual parametrizations, depending on the specific use case. Lastly, the stream of random numbers as well as the interpolation table files are managed. Note that the generation of random numbers is performed by CORSIKA 8, which are passed to the corresponding PROPOSAL methods.

5.3.2 ContinuousProcess: Description of Continuous Processes

The `ContinuousProcess` class provides a *Continuous Process* module (as defined in Section 5.2.1), describing continuous energy losses and multiple scattering effects of a charged particle along its trajectory. For photons, this module is not used, since every interaction is individually described as a discrete process. For the underlying calculations, the `ContinuousProcess` class uses the PROPOSAL modules `Displacement` and `Scattering` and the methods they provide (see Table 4.1 for the definitions of all PROPOSAL modules and the corresponding methods).

Continuous energy losses describe all sub-threshold energy losses, i.e., all energy losses that are not described by discrete, stochastic interactions in the Monte Carlo simulation (see Section 4.1 for a detailed explanation of this concept). In particular, this means that continuous energy losses do not produce secondary particles. For CORSIKA 8, the absolute threshold between continuous and stochastic energy

losses, i.e., E_{cut} by the definition in (4.2), is set to E_{track} , which is the lower kinetic energy until which particles in the cascade are tracked (see Section 5.2.2 for a description of E_{track}). This ensures that every energy loss in which a secondary particle with an energy above E_{track} might be produced is treated as a stochastic interaction. In addition to the absolute energy loss threshold E_{cut} , a relative threshold of $v'_{\text{cut}} = 0.01$ is applied to ensure that significant energy losses are treated as stochastic interactions as well, improving the stochasticity and therefore the precision of the particle propagation.

As described in Section 5.2.2, each *Continuous Process* can specify an upper limit x_{cont} for the possible length of a propagation step. For this module, this limit is defined by the distance after which, due to continuous energy losses, the particle has lost 10% of its initial energy or has reached the tracking threshold energy E_{track} . The former condition is made to avoid large changes of the particle energy during a propagation step, which is, for example, necessary for the Tracking algorithm and its current treatment of magnetic field deflections as well as a correct description of multiple scattering. The value x_{cont} is calculated by solving the integral in (4.7), given the particle energy E_i at the beginning of the continuous step and $E_f = \min(E_{\text{track}} + m, 0.9E_i)$ with particle mass m . This calculation is performed by calling the `SolveTrackIntegral()` method from the `Displacement` module. Afterward, the obtained X_{cont} is converted from grammage to a geometrical distance x_{cont} , using the information about the trajectory given by the Tracking code as well as the density distribution defined by the Environment code.

For a given propagation step with grammage X , the continuous energy loss along the trajectory is calculated using the `UpperLimitTrackIntegral()` method from the `Displacement` module. Internally, this method solves the integral equation (4.7) for E_f , given the traversed grammage X along and the particle energy E_i at the beginning of the trajectory. This yields E_f as the particle energy at the end of the continuous process.

Multiple scattering is taken into account by updating the direction of the particle at the end of its trajectory. The change of the particle direction is described by the scattering angle

$$\theta = \sqrt{\theta_x^2 + \theta_y^2}, \quad (5.6)$$

where θ_x and θ_y are sampled independently from one of the multiple scattering distributions described in Section 6.1.6. The underlying calculation is provided by the `Scattering` module. In addition to the change of the direction by the zenith angle θ , the corresponding azimuthal change is sampled uniformly in $[0, 2\pi)$. Note that the lateral displacement due to multiple scattering, i.e., the change of the particle position at the end of its trajectory, is currently neglected as it severely

complicates the description of the particle trajectory by the Tracking code. A discussion of the application of multiple scattering in transport algorithms, including the associated challenges, is given in [Section 6.1.6](#).

5.3.3 InteractionModel: Description of Interaction Processes

The `InteractionModel` class provides an *Interaction Process* module (as defined in [Section 5.2.1](#)), which is responsible for modeling stochastic particle interactions. For the underlying calculations, the methods provided by the PROPOSAL modules `Interaction` and `Secondaries` are used (see [Table 4.1](#) for the definitions of all PROPOSAL modules and the corresponding methods).

At first, the Cascade algorithm requires the definition of an interaction length, which describes the probability for an *Interaction Process*. This information is provided by the `MeanFreePath()` method from the `Interaction` module. Given the particle energy, this method calculates the inverse of the total stochastic cross section as defined in (4.4). Note that the particle-specific, energy-dependent total interaction length is stored in a separate interpolation table, independent of the interpolation tables used for the individual interaction processes described in [Section 6.3.1](#). As a consequence, the total interaction length can be obtained with a single interpolation table evaluation, instead of summing the cross section contributions from each interaction type and medium component, where the calculation of each contribution would require a separate interpolation table evaluation.

If the PROPOSAL module is selected by the Cascade algorithm as the *Interaction Process* to be performed, an interaction is sampled and the corresponding secondary particles are calculated. For this purpose, the total stochastic cross section is split into the individual cross section contributions. Each contribution corresponds to a combination of interaction type and interaction target, where interaction target refers to the specific medium component. This calculation is performed by the `Rates()` method. Based on the individual cross sections, one combination of interaction type and target is selected, and the relative size v of the corresponding stochastic energy loss is sampled using the `SampleLoss()` method. The obtained information about the stochastic energy loss is passed to the `Secondaries` module, where the produced secondary particles are sampled by calling the `CalculateSecondaries()` method of the corresponding interaction type. This procedure is described in [Section 4.2.2](#). All created secondary particles, including the updated initial particle if applicable, are returned to the stack. However, there are two notable exceptions where additional steps need to be performed:

Firstly, bremsstrahlung and electron-positron pair production interactions can be suppressed by the LPM effect, as described in Section 6.3. In case one of these interaction types is selected, a rejection sampling, as described in detail in Section 6.3.1, is performed to check whether the interaction is discarded or not. The corresponding discard probability is proportional to the LPM suppression factor c . This rejection sampling is implemented by the method `CheckForLPM()`, which is called for every eligible interaction type. Note that c depends on the local medium density and the properties of the individual secondary particles. Therefore, this method requires that the secondary particles are sampled prior to the calculation of c . If the interaction is discarded, the original particle is returned to the stack without performing any stochastic interaction.

Secondly, for photonuclear interactions, PROPOSAL does not provide a method for the calculation of the secondary particles. Instead, CORSIKA 8 passes the information about the photonuclear interaction to a hadronic event generator, either SOPHIA [169] or SIBYLL 2.3D [185], which performs the sampling of the secondary particles. This procedure is described in detail in Section 6.2.5.

6 Physics in Electromagnetic Showers

Originally, PROPOSAL was developed as a Monte Carlo software for the simulation of muon and tau lepton propagation, as described in [Chapter 4](#). As a consequence, PROPOSAL already provides implementations of interaction processes relevant for high-energy muons and taus, with parametrizations optimized for these particles, as documented in [\[77, 144, 199\]](#). To enable the description of electromagnetic particle cascades in the context of shower simulations for CORSIKA 8, parametrizations and additional interaction processes relevant for electrons, positrons and high-energy photons are added to PROPOSAL. This chapter describes the underlying physics parametrizations, the corresponding methodologies, and their implementation in PROPOSAL, where [Section 6.1](#) deals with the processes for electrons and positrons, [Section 6.2](#) with the processes for high-energy photons, and finally [Section 6.3](#) with the suppression of interactions due to the [Landau-Pomeranchuk-Migdal \(LPM\)](#) and [Ter-Mikaelian \(TM\)](#) effect.

Throughout this chapter, E denotes the energy of an interacting particle, v the relative energy loss of the particle during the interaction, and Z the charge of the nucleus the particle is interacting with.

6.1 Electron and Positron Interactions

In this section, the interaction processes relevant for electrons and positrons, as well as their implementation inside PROPOSAL, are described. [Figure 6.1](#) shows the contributions of all processes to the average energy loss of positrons.

6.1.1 Bremsstrahlung

Bremsstrahlung describes the process where an incoming electron or positron is scattered by a virtual photon from the atomic nucleus, creating an additional free photon, resulting in

$$e^{\pm} + Z \rightarrow e^{\pm} + Z + \gamma.$$

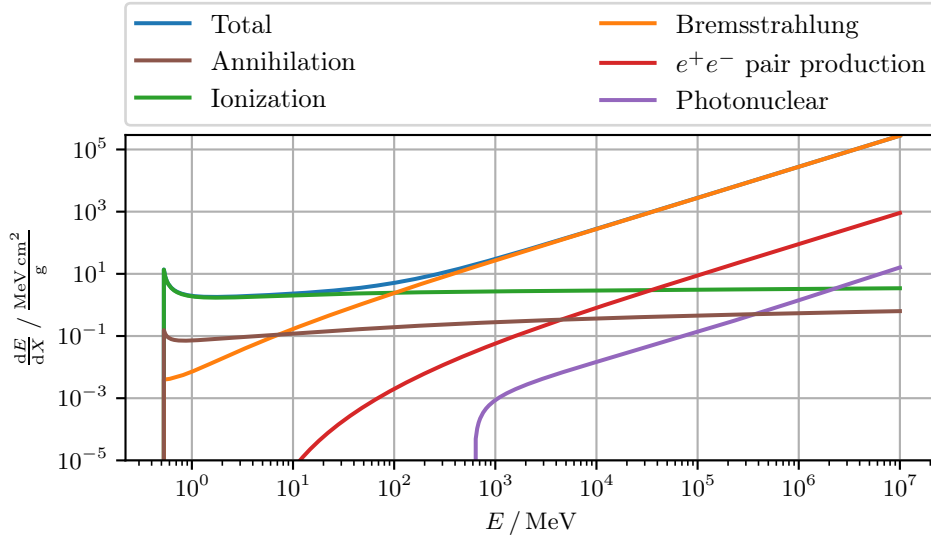


Figure 6.1: Average energy loss of positrons in air at standard density, according to the parametrizations of the interaction processes described in this section. The average energy loss of electrons differs by the absence of the annihilation process, as well as minor differences in the ionization energy loss as shown in Figure 6.3.

For high-energy electrons and positrons, bremsstrahlung is the dominant interaction type, as visible in Figure 6.1 and Figure 7.1, which means that an accurate description of its cross section is crucial. The implemented parametrization of bremsstrahlung to be used for electrons and positrons in PROPOSAL is based on the cross section given by Koch and Motz [142], which is also used by the EGS code system and described in detail in [118], where an in-depth discussion of the formulae below is given. It is divided into a low-energy and a high-energy part. The high-energy cross section, which is used for incoming electrons and positrons with an energy $E \geq 50$ MeV, is given by

$$\frac{d\sigma}{dv} = \frac{Z(Z + \xi(Z)) r_e^2 \alpha}{v} \left[(2 - 2v + v^2) \left(\Phi_1(x) - \frac{4}{3} \ln(Z) - 4f_c(Z) \right) - \frac{2}{3} (1 - v) \left(\Phi_2(x) - \frac{4}{3} \ln(Z) - 4f_c(Z) \right) \right], \quad (6.1)$$

where

$$x = 136Z^{-1/3} \frac{2\delta}{m_e}, \quad \delta = \frac{m_e^2 v}{2E(1 - v)}. \quad (6.2)$$

This corresponds to an ultra-relativistic cross section with Coulomb corrections. The Coulomb corrections, i.e., higher-order corrections in the nuclear coupling constant αZ , are described by the analytical expression $f_c(Z)$, which is given by

$$f_c(Z) = a^2 \left(\frac{1}{1+a^2} + 0.20206 - 0.0369a^2 + 0.0083a^4 - 0.002a^6 \right), \quad (6.3)$$

with $a = \alpha Z$ [79]. Screening effects are described by the expressions

$$\Phi_1(x) = \begin{cases} 20.867 - 3.242x + 0.625x^2 & \text{if } x \leq 1, \\ 21.12 - 4.184 \ln(x + 0.952) & \text{if } x > 1, \end{cases} \quad (6.4)$$

$$\Phi_2(x) = \begin{cases} 20.029 - 1.930x - 0.086x^2 & \text{if } x \leq 1, \\ 21.12 - 4.184 \ln(x + 0.952) & \text{if } x > 1, \end{cases} \quad (6.5)$$

which are approximations of the Thomas-Fermi form factors [68]. The contribution from interactions of the incoming particle with atomic electrons is taken into account using the function

$$\xi(Z) = \frac{L'_{\text{rad}}(Z)}{L_{\text{rad}}(Z) - f_c(Z)}, \quad (6.6)$$

with the radiation logarithms [214]

$$L'_{\text{rad}} = \begin{cases} \ln(1194Z^{-2/3}) & \text{if } Z > 4, \\ 5.924 & \text{if } Z = 4, \\ 5.805 & \text{if } Z = 3, \\ 5.621 & \text{if } Z = 2, \\ 6.144 & \text{if } Z = 1, \end{cases} \quad L_{\text{rad}} = \begin{cases} \ln(184.15Z^{-1/3}) & \text{if } Z > 4, \\ 4.710 & \text{if } Z = 4, \\ 4.740 & \text{if } Z = 3, \\ 4.790 & \text{if } Z = 2, \\ 5.310 & \text{if } Z = 1. \end{cases}$$

For very high energies, the LPM effect leads to a significant suppression of small bremsstrahlung losses. Details about the LPM effect and its influence on the bremsstrahlung cross section are given in Section 6.3.

The low-energy cross section, which is used for energies $E < 50$ MeV, is given by

$$\frac{d\sigma}{dv} = \frac{A'(E, Z)Z(Z + \xi(Z))r_e^2\alpha}{v} \left[(2 - 2v + v^2) \left(\Phi_1(x) - \frac{4}{3} \ln(Z) \right) - \frac{2}{3}(1 - v) \left(\Phi_2(x) - \frac{4}{3} \ln(Z) \right) \right]. \quad (6.7)$$

Note that the Coulomb correction $f_c(Z)$ is absent, while an empirical correction factor $A'(E, Z)$ is introduced. These corrections rescale the total cross section in such a way that the energy loss is in agreement with the calculations given in [57].

The values for A' have been generated in [82], and are given as a two-dimensional table in E and $\ln(Z)$. Within PROPOSAL, an interpolation routine is used to calculate A' for arbitrary E and Z .

The limits of the bremsstrahlung cross sections are determined by the process kinematics and are given by

$$v_{\min} = 0, \quad v_{\max} = 1 - \frac{m_e}{E}. \quad (6.8)$$

An energy loss v from the differential cross section is sampled by numerically solving the integral equation (4.5).

To sample the angular distribution of the emitted bremsstrahlung photon, two methods are implemented. The first method is an approximation introduced in early versions of EGS [171], where the angle θ between the ingoing electron or positron and the created photon is set to

$$\theta = \frac{m_e}{E}, \quad (6.9)$$

independent of v and the underlying medium. Using such a simple approximation is motivated by the fact that for higher energies, the created photon is strongly peaked in the forward direction, while for lower energies, the lateral particle distribution is dominated by multiple scattering effects (see Section 6.1.6). In the following, this approach is called **EGS4Approximation**. As an alternative, a more sophisticated sampling algorithm, adapted from [82] and described in detail in [60], is implemented. This method is a rejection sampling, based on the double differential (in v and θ) bremsstrahlung cross section by Koch and Motz [142]. Firstly, a candidate scattering angle $\hat{\theta}$ is sampled via

$$\hat{\theta} = \frac{m_e}{E} \sqrt{\frac{\xi_1}{1 - \xi_1 + (\frac{m_e}{\pi E})^2}}, \quad (6.10)$$

where ξ_1 is a random number $\xi_1 \in [0, 1)$. Afterward, the normalization of the rejection function is calculated from

$$N_r = 1 / \max \left[g(0), g(1), g \left(\frac{\pi^2 E^2}{m_e^2} \right) \right], \quad (6.11)$$

where the function $g(x)$ is defined as

$$g(x) = 3(1 + r^2) - 2r - (4 + \ln(m(x))) \left((1 + r^2) - \frac{4xr}{(1+x)^2} \right), \quad (6.12)$$

with

$$m(x) = \left(\frac{m_e(1-r)}{2rE} \right)^2 + \left(\frac{Z^{1/3}}{111(1+x)} \right)^2, \quad r = 1 - v. \quad (6.13)$$

The value for $\hat{\theta}$ is accepted as the scattering angle if

$$\xi_2 \leq N_r \cdot g \left(\frac{E^2 \cdot \hat{\theta}^2}{m_e^2} \right) \quad (6.14)$$

is satisfied, where $\xi_2 \in [0, 1)$ is another random number. Otherwise, the process is repeated from (6.10), using a new pair of random numbers (ξ_1, ξ_2) . This method, which, in comparison to the `EGS4Approximation`, yields an entire angular distribution at the expense of a higher computational cost, is called `KochMotzSampling`. A comparison of both approaches is shown in Figure 6.2. Note that for both methods,

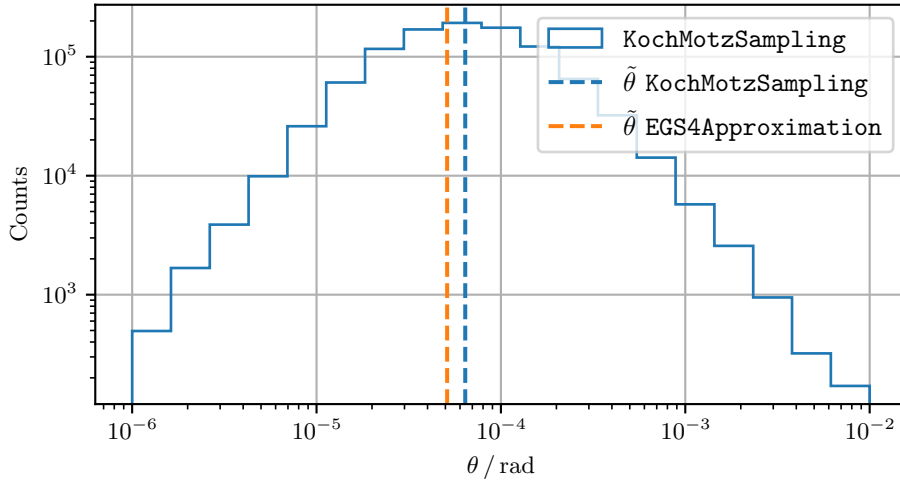


Figure 6.2: Comparison of the two sampling methods for the scattering angle θ of bremsstrahlung photons. Firstly, energy losses v according to (6.1) are sampled, given an initial electron energy of 10^4 MeV. Afterward, the deflection angles are calculated according to the two methods. A nitrogen atom is assumed as the interaction target. The dashed lines indicate the median $\tilde{\theta}$ of the distributions. Figure adapted from [29].

the azimuth angle of the photon is sampled uniformly in $[0, 2\pi)$, while the charged particle receives the opposite azimuth. Furthermore, the angle of the outgoing lepton is calculated assuming momentum conservation, neglecting the momentum transfer to the nucleus. The comparison illustrates that both approaches show a sufficient

agreement in their description of the median scattering angle. A comparison of both methods for the direct application in air shower simulations is performed in [Section 7.2.3](#), revealing a negligible impact on the lateral development of the particle showers.

6.1.2 Ionization

When propagating through media, charged particles can lose energy by collisions with atomic electrons. For sufficient energy transfers, this can cause the atomic electrons to be ejected, a process called ionization. For electrons and positrons at lower energies, these collisions are the dominating energy loss process. In air, for example, ionization losses dominate over bremsstrahlung losses for particle energies below ≈ 100 MeV, as visible in [Figure 6.1](#). If the energy transfer of the ingoing electron or positron to the atomic electron is much higher compared to electron binding energies, the atomic electron can be considered as free. In this case, the interaction processes are known as Møller scattering ($e^- + e^- \rightarrow e^- + e^-$) and Bhabha scattering ($e^+ + e^- \rightarrow e^+ + e^-$). For electromagnetic cascades, ionization processes contribute to an excess of negative charges over positive charges. This is relevant for radio emission from electromagnetic particle cascades due to the Askaryan effect [47], as described in [Section 3.3.3](#).

The differential cross section for Møller scattering (i.e., for electrons) is given as [118, 188]

$$\begin{aligned} \frac{d\sigma}{dv} = \frac{2\pi r_e^2 Z\gamma}{\beta^2(\gamma-1)^2} & \left[\frac{(\gamma-1)^2}{\gamma^2} + \frac{1}{\epsilon} \left(\frac{1}{\epsilon} - \frac{2\gamma-1}{\gamma^2} \right) \right. \\ & \left. + \frac{1}{1-\epsilon} \left(\frac{1}{1-\epsilon} - \frac{2\gamma-1}{\gamma^2} \right) \right] \end{aligned} \quad (6.15)$$

with

$$\epsilon = \frac{vE}{E - m_e}, \quad \gamma = \frac{E}{m_e}, \quad \beta = \sqrt{1 - \frac{1}{\gamma^2}}, \quad v_{\max} = \frac{1}{2} \left(1 - \frac{m_e}{E} \right). \quad (6.16)$$

For Bhabha scattering (i.e., for positrons), the differential cross section is given as [118, 188]

$$\frac{d\sigma}{dv} = \frac{2\pi r_e^2 Z\gamma}{(\gamma-1)^2} \left[\frac{1}{\beta^2\epsilon^2} - \frac{B_1}{\epsilon} + B_2 - B_3\epsilon + B_4\epsilon^2 \right] \quad (6.17)$$

with

$$B_1 = 2 - y^2, \quad B_2 = (1 - 2y)(3 + y^2), \quad (6.18)$$

$$B_3 = (1 - 2y)^2 + (1 - 2y)^3, \quad B_4 = (1 - 2y)^3, \quad (6.19)$$

and

$$y = \frac{1}{\gamma + 1}, \quad v_{\max} = 1 - \frac{m_e}{E}. \quad (6.20)$$

If the energy cut v_{cut} is chosen to be large enough so that the energy transfers of stochastic energy losses are larger than the electron binding energies, the differential cross sections in (6.15) and (6.17) can be used for the description of stochastic ionization losses, and therefore to sample individual energy losses v according to (4.5). However, for the calculation of continuous energy losses, which considers all energy losses with $v < v_{\text{cut}}$, small energy transfers in the order of the electron binding energies need to be considered as well. This is done in the work by Berger and Seltzer [56], whose work is also referred to by the EGS code system [118]. The derived formula describes the continuous ionization energy loss and is given by

$$-\left(\frac{dE}{dX}\right) = \frac{2\pi r_e^2 m_e}{\beta^2} \left[\ln\left(\frac{2m_e(\tau + 2)}{I}\right) + F^\pm(\tau, \Delta) - \delta \right], \quad (6.21)$$

with

$$\tau = \gamma - 1, \quad \Delta = \min\left(\frac{v_{\max} E}{m_e}, \frac{v_{\text{cut}} E}{m_e}\right), \quad (6.22)$$

where I is the medium-dependent mean ionization energy. The density correction is described by δ , where the correction by Sternheimer is used [206], defined as

$$\delta = \begin{cases} \delta_0 10^{2(X-X_0)} & \text{if } X < X_0, \\ 2 \ln(10)X + c + a(X_1 - X)^m & \text{if } X_0 \leq X < X_1, \\ 2 \ln(10)X + c & \text{if } X_1 \leq X, \end{cases} \quad (6.23)$$

with $X = \log_{10}(\beta\gamma)$ as well as the medium-dependent constants X_0 , X_1 , a , c , and m [105]. The expression $F^\pm(\tau, \Delta)$ is different for electrons and positrons and is defined by

$$F^+(\tau, \Delta) = \ln(\tau\Delta) - \frac{\beta^2}{\tau} \left[\tau + 2\Delta - \frac{3\Delta^2 y}{2} - \left(\Delta - \frac{\Delta^2}{3}\right) y^2 - \left(\frac{\Delta^2}{2} - \frac{\tau\Delta^3}{3} + \frac{\Delta^4}{4}\right) y^3 \right], \quad (6.24)$$

$$F^-(\tau, \Delta) = -1 - \beta^2 + \ln((\tau - \Delta)\Delta) + \frac{\tau}{\tau - \Delta} + \frac{1}{\gamma^2} \left[\frac{\Delta^2}{2} + (2\tau + 1) \ln\left(1 - \frac{\Delta}{\tau}\right) \right]. \quad (6.25)$$

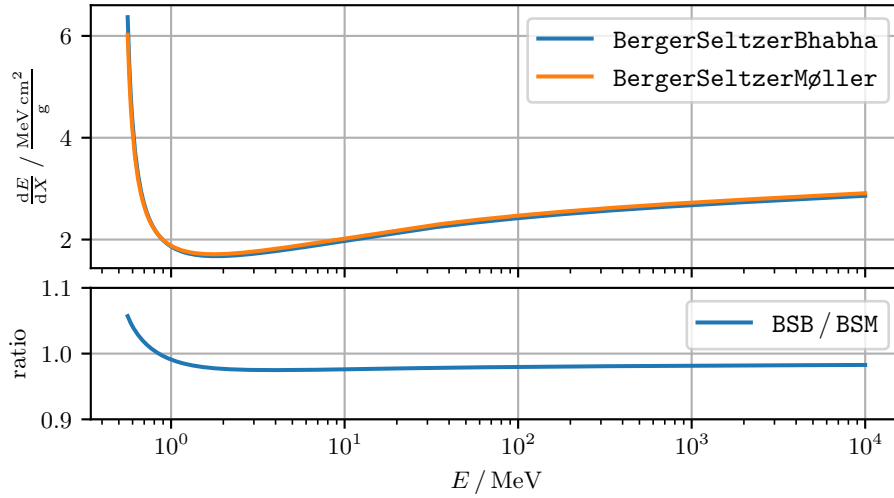


Figure 6.3: Continuous ionization energy losses for electrons and positrons in air according to formula (6.21). For the plot, $v = v_{\max}$ is used, which means that all ionization losses are treated continuously and are included in the displayed energy loss. Figure adapted from [29].

Figure 6.3 shows the continuous ionization energy losses according to (6.21) for electrons and positrons.

Using the assumption that the atomic electron is at rest, the deflection of the ingoing electron or positron as well as the production angle of the ionized atomic electron can be calculated using the kinematics of two-body interactions. This is done by using (A.35) with

$$\begin{aligned} E_1 &= E, & E'_1 &= (1 - v)E, \\ E'_2 &= m_e + vE, & m_1 &= m'_1 = m'_2 = m_e, \end{aligned}$$

which yields

$$\cos \theta_1 = \frac{(E + m_e)(1 - v)E - Em_e - m_e^2}{\sqrt{E^2 - m_e^2}\sqrt{E^2(1 - v)^2 - m_e^2}}, \quad (6.26)$$

$$\cos \theta_2 = \frac{(E + m_e)(m_e + vE) - Em_e - m_e^2}{\sqrt{E^2 - m_e^2}\sqrt{E^2v^2 + 2m_eEv}}, \quad (6.27)$$

where θ_1 describes the deflection of the ingoing electron or positron, and θ_2 the angle between the ingoing electron or positron and the outgoing atomic electron. The azimuth angle for one particle is sampled uniformly, while the other particle receives the opposite azimuth.

6.1.3 Annihilation

When a positron propagates through a medium, it can annihilate with an atomic electron, producing two photons in the process, i.e.,

$$e^+ + e_{\text{atomic}}^- \rightarrow \gamma + \gamma.$$

Notably, annihilation processes remove positive charges out of electromagnetic cascades, contributing to an overall negative charge excess. This is relevant for the radio emission from electromagnetic particle cascades due to the Askaryan effect [47], described in Section 3.3.3. Assuming that the atomic electron is free and at rest, this process is described by the Heitler formula [115], where the notation from the GEANT4 Physics Reference Manual [99] is used, given by

$$\frac{d\sigma}{d\epsilon} = \frac{\pi r_e^2}{\gamma - 1} \frac{1}{\epsilon} \left[1 + \frac{2\gamma}{(\gamma + 1)^2} - \epsilon - \frac{1}{(\gamma + 1)^2} \frac{1}{\epsilon} \right], \quad (6.28)$$

with

$$\gamma = \frac{E}{m_e}, \quad \epsilon = \frac{E_{\gamma_1}}{E + m_e}, \quad 1 - \epsilon = \frac{E_{\gamma_2}}{E + m_e},$$

where $E_{\gamma_{1/2}}$ are the energies of the created photons. The annihilation process can be described as a two-body interaction with an atomic electron at rest. This means that the production angles are determined by using (A.35) with

$$\begin{aligned} E_1 &= E, & E'_1 &= \epsilon(E + m_e), & E'_2 &= (1 - \epsilon)(E + m_e), \\ m_1 &= m_e, & m'_1 &= m'_2 = 0, \end{aligned}$$

which yields

$$\cos \theta_1 = \frac{(\gamma + 1)\epsilon - 1}{\epsilon \sqrt{\gamma^2 - 1}}, \quad \cos \theta_2 = \frac{(\gamma + 1)(1 - \epsilon) - 1}{(1 - \epsilon) \sqrt{\gamma^2 - 1}}. \quad (6.29)$$

Here, $\theta_{1/2}$ describes the angles between the ingoing positron and the outgoing leptons. From this, the kinematic limits of ϵ are obtained by setting $\cos \theta_1 = \pm 1$ in (6.29), which leads to

$$\epsilon_{\min} = \frac{1}{2} \left(1 - \sqrt{\frac{\gamma - 1}{\gamma + 1}} \right), \quad \epsilon_{\max} = \frac{1}{2} \left(1 + \sqrt{\frac{\gamma - 1}{\gamma + 1}} \right). \quad (6.30)$$

Integrating the differential cross section in (6.28) over the entire kinematic range of ϵ is analytically possible, and yields the total cross section

$$\sigma = \frac{\pi r_e^2}{\gamma + 1} \left[\frac{\gamma^2 + 4\gamma + 1}{\gamma^2 - 1} \ln \left(\gamma + \sqrt{\gamma^2 - 1} \right) - \frac{\gamma + 3}{\sqrt{\gamma^2 - 1}} \right]. \quad (6.31)$$

Since the average energy loss due to annihilation scales with $\ln(E)$, while the average energy loss due to bremsstrahlung scales approximately linearly with E , the contribution from annihilation only becomes relevant at low energies. In air, the contribution of annihilation to the average energy loss of positrons is around 5% to 10% for energies below 10^2 MeV, as visible in [Figure 6.1](#).

To sample ϵ for a given annihilation process, the equation

$$\frac{1}{\sigma} \int_{\epsilon_{\min}}^{\epsilon} \frac{d\sigma}{d\epsilon'} d\epsilon' = \xi, \quad (6.32)$$

with a random number $\xi \in [0, 1)$ is solved. The integration itself can be performed analytically, so (6.32) becomes

$$F(\epsilon) - F(\epsilon_{\min}) - \xi [F(\epsilon_{\max}) - F(\epsilon_{\min})] = 0, \quad (6.33)$$

with

$$F(\epsilon) = \ln(\xi) \left(1 + \frac{2\gamma}{(\gamma + 1)^2} \right) + \frac{1}{\epsilon(\gamma + 1)^2} - \epsilon, \quad (6.34)$$

which is solved numerically using the bisection method. [Figure 6.4](#) shows the distribution of ϵ , sampled for different energies of the initial positron.

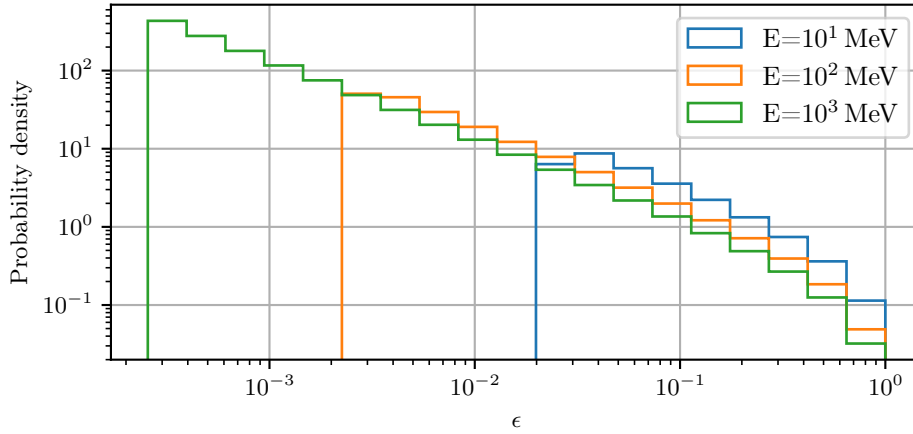


Figure 6.4: Sampling of ϵ in annihilation interactions, according to (6.33). Nitrogen is assumed as the interaction target. The distribution is shown for three different energies of the initial positron.

6.1.4 Electron-Positron Pair Production

Electron-positron pair production describes the formation of an electron-positron pair by an ingoing electron or positron in the field of an atomic nucleus, i.e.,

$$e^\pm + Z \rightarrow e^\pm + e^+ + e^- + Z.$$

The cross section for this process is based on the parametrization of the same process for ingoing muons ($\mu^\pm + Z \rightarrow \mu^\pm + \mu^+ + \mu^- + Z$) [137], where nuclear form factor effects are removed since they are negligible for electrons and positrons as ingoing particles. With the definition

$$\rho = \frac{E_+ - E_-}{E_+ + E_-}, \quad (6.35)$$

where E_- and E_+ are the energies of the produced electron and positron, the differential cross section is given by [29]

$$\frac{d\sigma}{dv d\rho} = \frac{2}{3\pi} (Z\alpha r_e)^2 \frac{1-v}{v} \Phi \ln X, \quad (6.36)$$

with

$$\begin{aligned} \Phi = & [(2 + \rho^2)(1 + \beta) + \xi(3 + \rho^2)] \ln \left(1 + \frac{1}{\xi} \right) \\ & + \left[(1 + \rho^2) \left(1 + \frac{3}{2}\beta \right) - \frac{1 + 2\beta}{\xi} (1 - \rho^2) \right] \ln(1 + \xi) \\ & - 1 - 3\rho^2 + \beta(1 - 2\rho^2), \end{aligned} \quad (6.37)$$

$$X = 1 + U(E, v, \rho) - U(E, v, \rho_{\max}), \quad (6.38)$$

$$U(E, v, \rho) = \frac{BZ^{-1/3}}{1 + \frac{2\sqrt{e}m_e BZ^{-1/3}(1+\xi)(1+Y)}{Ev(1-\rho^2)}}, \quad (6.39)$$

with the radiation logarithm constant B as defined in Table A.7, and

$$\beta = \frac{v^2}{2(1-v)}, \quad \xi = \frac{v^2(1-\rho^2)}{4(1-v)}, \quad \rho_{\max} = 1 - \frac{2m_e}{Ev}, \quad Y = 12\sqrt{m_e/E}.$$

Compared to the dominant electron and positron processes, which are ionization and annihilation for lower energies and bremsstrahlung for higher energies, the cross section for pair production is strongly suppressed, as visible in Figure 7.1. In air, for example, the contribution to the total electron or positron energy loss is smaller than 0.5%, as shown in Figure 6.1.

To sample ρ for a given energy loss v , the integral equation

$$\left(\frac{d\sigma}{dv}\right)^{-1} \int_0^\rho \frac{d^2\sigma}{dv d\rho'} d\rho' = \xi \quad (6.40)$$

with a random number $\xi \in [0, 1)$ is solved. Since this process is strongly peaked in the forward direction, it is assumed that both produced particles inherit the direction of the initial electron or positron.

6.1.5 Photonuclear Interactions

Photonuclear interactions describe the inelastic interaction of an ingoing electron or positron with an atomic nucleus. They can provide a significant contribution to the total energy loss of charged leptons with higher masses, for example, around 10 % for the energy loss of muons with an even higher contribution for tau leptons [199]. However, for electrons and positrons, the contribution from photonuclear interactions is negligible, e.g., below 0.01 % to the average energy loss in air, as visible in Figure 6.1. Since photonuclear interactions are the only direct source of hadrons produced by electrons and positrons, and because the cross sections for photonuclear interactions of muons and taus that are already implemented in PROPOSAL can directly be applied to electrons and positrons as well, these interactions are still taken into account.

The photonuclear process is dominated by interactions with small momentum transfers, which is a kinematic region where the theory of perturbative quantum chromodynamics is not applicable. Therefore, a phenomenological approach must be used to describe the cross section. The following parametrization is based on Regge theory. Following [50], the differential cross section is given by

$$\frac{d^2\sigma}{dv dQ^2} = \frac{4\pi\alpha^2}{Q^4} \frac{F_2}{v} \left[1 - v - \frac{Mxv}{2E} + \left(1 - \frac{2m_e^2}{Q^2} \right) \frac{v^2(1 + 4M^2x^2/Q^2)}{2(1 + R)} \right] \quad (6.41)$$

where Q^2 is the negative square of the four-momentum transfer from the electron or positron to the nucleus, and x the Bjorken scaling variable

$$x = \frac{Q^2}{2MEv}, \quad (6.42)$$

with the average nucleon weight M . The structure functions F_1 and F_2 describe the internal structure of the target nucleon and are expressed by $F_2(x, Q^2)$ and $R(x, Q^2) = F_1/F_2$, where the approximation $R(x, Q^2) = 0$ is used [77]. The parametrization of $F_2(x, Q^2)$, which is determined based on a fit to data from

experiments at the HERA collider as well as data from fixed target experiments [14, 15], is described in [Appendix A.9](#).

The kinematic limits of v and Q^2 are given by

$$v_{\min} = \frac{m_\pi}{E} + \frac{m_\pi^2}{2ME}, \quad v_{\max} = 1 - \frac{M}{2E} \left(1 + \frac{m_e^2}{M^2} \right), \quad (6.43)$$

$$Q_{\min}^2 = \frac{m_e^2 v^2}{1-v} - \frac{m_e^4}{2(1-v)E^2}, \quad Q_{\max}^2 = 2M(vE - m_\pi) - m_\pi^2, \quad (6.44)$$

where m_π is the pion mass. By numerical integration of (6.41), these limits are used to obtain the differential cross section $d\sigma/dv$, used to sample energy losses v according to (4.5), and the total cross section σ_{tot} .

Treatment of Photonuclear Secondaries within CORSIKA 8

The differential cross section (6.41) provides information about the frequency of photonuclear interactions, given by σ_{tot} , as well as information about the distribution of v and Q^2 . However, for particle cascade simulations, not only the relative energy loss of the initial particle but also the individual final particle states of the hadronic interaction are important. These final states can be simulated by an hadronic event generator, which receives information about the energy loss by PROPOSAL, and calculates a list of secondary particles that are created in the interaction. Within CORSIKA 8, this is realized with the implementation of an interface to the hadronic event generators SOPHIA [169] and SIBYLL [185]. This procedure is described in more detail in [Section 6.2.5](#). Note that in [Section 6.2.5](#), the method is described for the photonuclear interaction of a real photon. However, the same method can be used to describe photonuclear interactions of leptons, assuming the interaction of a virtual photon with energy $v \cdot E$.

6.1.6 Multiple Scattering

When charged particles traverse a medium, they perform elastic interactions with atomic nuclei, where the energy loss is negligible but the direction of the ingoing particle is changed. The accumulative sum of these scatterings during a propagation step can cause a significant deflection of the particle, an effect called multiple scattering. While deflections are taken into account explicitly in stochastic energy losses, the effect of multiple scattering in continuous energy losses needs to be taken into account as well. For extensive air showers, multiple scattering effects have the highest impact on the lateral shower development, as illustrated in the analysis in

Section 7.2.3, which is why an accurate description of multiple scattering is crucial. Within PROPOSAL, multiple scattering parametrizations by Molière [164, 165] and the Highland approximation [116] are available. They are implemented within the classes `Moliere` and `Highland`, as well as the derived classes `MoliereInterpol` and `HighlandIntegral`, as explained in the following section. Note that while these parametrizations have originally been implemented for muon scattering, their implementation can directly be applied to electrons and positrons as well.

Molière parametrization The Molière parametrization, provided by the `Moliere` class, is based on the mechanism and calculations described in [164, 165]. The formulae have been adapted for the usage in PROPOSAL and are described in more detail in [100]. Let Θ be the scattering angle, i.e., the angle an ingoing charged particle is deflected during a propagation step. Introducing a reduced angle

$$\theta = \frac{\Theta}{\chi_c \sqrt{B}}, \quad (6.45)$$

the distribution of θ is given by

$$f(\theta)d\theta = \frac{d\theta}{\sqrt{\pi}} \left(\exp(-\theta^2) + \frac{1}{B} f^{(1)}(\theta) + \frac{1}{B^2} f^{(2)}(\theta) \right), \quad (6.46)$$

where higher-order terms $f^{(i)}(\theta)$ with $i > 2$ are neglected. The parameter B is defined via the relation

$$B - \ln(B) = 1 - 2C + \ln\left(\frac{\chi_c^2}{\chi_a^2}\right), \quad (6.47)$$

with Euler's constant C and the definitions

$$\chi_a^2 = \chi_0^2 \left(1.13 + 3.76 \frac{\alpha^2 Z^2}{\beta^2} \right), \quad (6.48)$$

$$\chi_0^2 = \frac{\alpha^2 m_e^2}{p^2} \left(\frac{128Z}{9\pi^2} \right)^{2/3}, \quad (6.49)$$

$$\chi_c^2 = 4\pi\hbar^2\alpha^2 \frac{X}{\beta^2 p^2} \frac{\sum_i (w_i Z_i (Z_i + 1))}{\sum_j (w_j A_j)}, \quad (6.50)$$

with the traversed grammage X within a continuous step, $\beta = v/c$, and the weights

$$w_i = \frac{k_i A_i}{\sum_j k_j A_j}. \quad (6.51)$$

The index i runs over all components included in the medium, with k_i being the number of atoms of component i . With this, B is determined by solving (6.47) for each component using the Newton-Raphson method. For $B < 4.5$, the underlying theory is not valid, and no deflections are assumed. The functions $f^{(1)}(\theta)$ and $f^{(2)}(\theta)$ are described as series expansions

$$f^{(1)}(\theta) = \sum_{n=0}^{\infty} a_n^{(1)} \theta^{2n}, \quad f^{(2)}(\theta) = \sum_{n=0}^{\infty} a_n^{(2)} \theta^{2n}, \quad (6.52)$$

where the rules to calculate $a_n^{(1)}$ and $a_n^{(2)}$ are described in [164, 100]. The results for $a_n^{(1)}$, $a_n^{(2)}$ are directly stored within `PROPOSAL` and used to evaluate $f^{(1)}(\theta)$ and $f^{(2)}(\theta)$ with Horner's method. Note that for improved numerical stability, for larger θ ($\theta^2 > 12$ for $f^{(1)}(\theta)$, and $\theta > 4.25$ for $f^{(2)}(\theta)$), a different evaluation for the functions $f^{(1)}(\theta)$, $f^{(2)}(\theta)$ is used, which is described in [100]. The distribution $f(\theta)$ in a given medium with several components is now defined as

$$f_{\text{compound}}(\theta) d\theta = \frac{\sum_i (w_i Z_i^2 f(\theta_i) d\theta_i)}{\sum_j (w_j Z_j^2)}, \quad (6.53)$$

where again, the index i runs over all components of the medium, and $f(\theta_i)$ is evaluated for each Z [69]. To sample θ from (6.53), and therefore Θ , the equation

$$\int_0^\theta f(\theta) d\theta = \xi, \quad (6.54)$$

with a random number $\xi \in [-0.5, 0.5]$ is solved, again using the Newton-Raphson method.

Since the evaluation of the functions $f^{(1)}(\theta)$ and $f^{(2)}(\theta)$ using Horner's method is numerically expensive and the most time-consuming process for the scattering angle calculation, the class `MoliereInterpol` stores the results of the evaluations in interpolation tables for $\theta \in [0, 20)$ [29]. This improves the runtime for calculating a deflection angle, compared to the standard `Moliere` implementation, by a factor of more than two, as shown exemplarily in Figure 6.6, while providing the same results, as illustrated in Figure 6.5.

Highland parametrization As an alternative and simplification to the parametrization by Molière, a Gaussian approximation of the angular distribution can be used. While this approximation is unable to properly take into account the tails of the angular distribution, its description can be sufficient in several use cases. The parametrization has been calculated by Highland [116], based on ideas in [191], and

has been revised in [156] where a maximum likelihood fit to a scattering distribution according to the theory of Molière has been performed. The distribution of the scattering angle θ is given by the Gaussian distribution

$$f(\theta) d\theta = \frac{1}{\sqrt{2\pi}\theta_0} \exp\left(-\frac{\theta^2}{2\theta_0^2}\right) d\theta, \quad (6.55)$$

with

$$\theta_0 = \frac{13.6 \text{ MeV}}{\beta p} \sqrt{\frac{X}{X_0}} \left(1 + 0.088 \log_{10} \left(\frac{X}{X_0}\right)\right), \quad (6.56)$$

with the medium-dependent radiation length X_0 and the traversed grammage X . To sample a scattering angle θ from (6.55), the integral equation (6.54) is solved, where the solution is known analytically by

$$\theta = \sqrt{2}\theta_0 \operatorname{erf}^{-1}(2\xi - 1), \quad (6.57)$$

with a random number $\xi \in [0, -1)$ and the inverse error function $\operatorname{erf}^{-1}(x)$.

In the parametrization in (6.56), it is assumed that β and p remain constant over the entire propagation step, and are evaluated at the beginning of the step. However, this assumption becomes invalid for large propagation steps. To take into account that β and p are, in fact, decreasing, (6.56) can be adapted as

$$\begin{aligned} \theta_0 &= 13.6 \text{ MeV} \sqrt{\int_{E_i}^{E_f} \frac{dX}{\beta^2 p^2 X_0}} \left(1 + 0.088 \log_{10} \left(\frac{X}{X_0}\right)\right), \\ &= 13.6 \text{ MeV} \sqrt{\int_{E_i}^{E_f} dE \frac{E^2}{f(E) p^4 X_0}} \left(1 + 0.088 \log_{10} \left(\frac{X}{X_0}\right)\right), \end{aligned} \quad (6.58)$$

where $f(E) = dE/dX$ describes the average energy loss per grammage as defined in (4.3). Within PROPOSAL, the sampling method according to (6.56) is implemented in the class called `Highland`, while the method according to (6.58) is implemented in the class called `HighlandIntegral`. Note that only the `HighlandIntegral` parametrization is capable of correctly describing multiple scattering for large propagation steps with significant energy losses, which is, for example, relevant for muon propagation [199].

Figure 6.5 shows a comparison of the different methods to sample the scattering angle θ . Notably, only the theory by Molière describes the non-Gaussian tail of the distribution which extends to large scattering angles, while `Highland` and `HighlandIntegral` provide an acceptable approximation for small scattering angles.

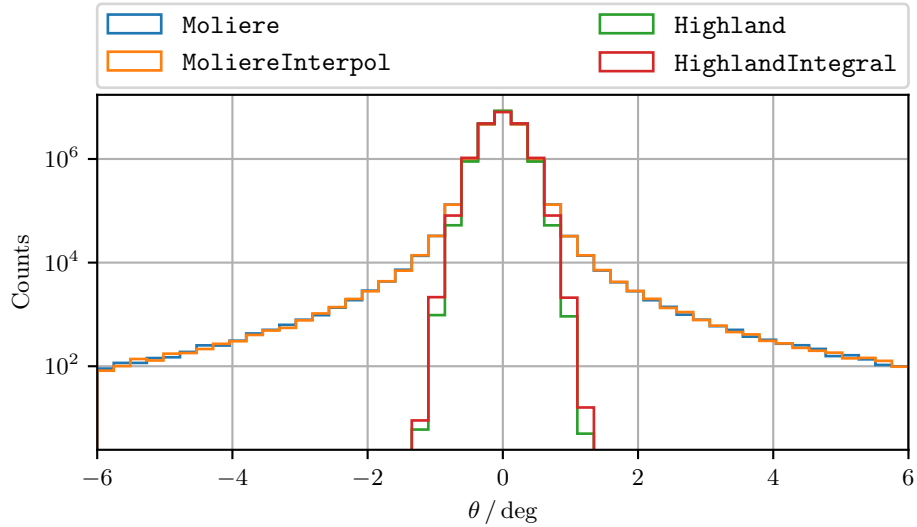


Figure 6.5: Scattering angles θ sampled according to Moliere (6.46), MoliereInterpol, Highland (6.56), and HighlandIntegral (6.58). The angles are sampled for electrons in air at standard density, with a fixed initial energy of $E_i = 1$ GeV and a fixed final energy of $E_f = 0.9$ GeV, which corresponds to a grammage of $X \approx 3.52$ g/cm², or a distance in air of $x \approx 39.22$ m. Note that the distribution for Moliere extends to even larger angles, which are truncated in the histogram for better visibility.

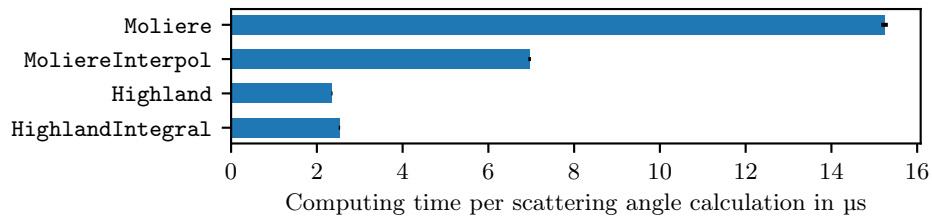


Figure 6.6: Comparison of the average runtime to compute the scattering angles from Figure 6.5 according to the different provided methods. The bars indicate the mean, while the lines indicate the standard deviation of the computation time per scattering angle calculation. Figure adapted from [29].

The disadvantage of the calculation according to *Moliere* is that the computational effort is significantly higher compared to the evaluation using *Highland*, as shown in [Figure 6.6](#). Note that the implementation of *MoliereInterpol* improves the runtime, but is still slower by a factor of about 3 compared to *Highland* and *HighlandIntegral*. A validation of the multiple scattering algorithms implemented in PROPOSAL has been done in [\[84, 106\]](#) by comparing PROPOSAL simulations of muon scattering to data, as well as to simulations produced with other Monte Carlo frameworks. A comparison between the different multiple scattering parametrizations when applied for air shower simulations is presented in [Section 7.2.3](#).

Application of Multiple Scattering in Transport Algorithms

The full picture of multiple scattering within a transport algorithm is visualized in [Figure 6.7](#). When a particle with initial direction \vec{d}_i is propagated over a distance Δx , it undergoes multiple scattering. This causes both a displacement of the particle during the propagation step, denoted by Δy , as well as a change of the initial direction to \vec{d}_f , denoted by θ . These quantities are correlated to each other, as described via [\[225\]](#)

$$\Delta y = \Delta x \frac{\theta_1}{\sqrt{12}} + \Delta x \frac{\theta_2}{2}, \quad (6.59)$$

$$\theta = \theta_1, \quad (6.60)$$

where θ_1 and θ_2 are scattering angles, sampled independently according to one of the distributions presented in the previous chapter. For the application of multiple

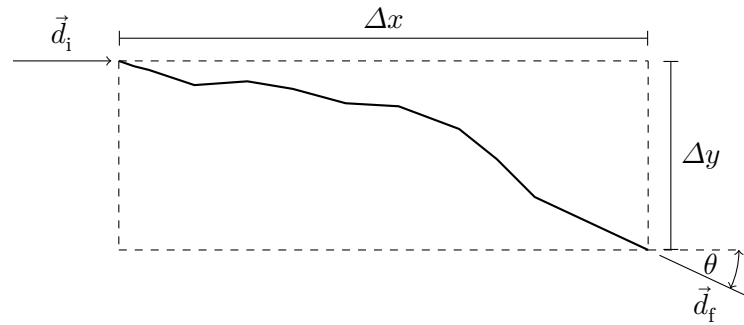


Figure 6.7: Application of multiple scattering in a transportation step, illustrated as a projection to a plane. A particle with initial direction \vec{d}_i is transported a distance of Δx . Due to multiple scattering, the particle is displaced during the transportation step by Δy . The initial direction is changed to \vec{d}_f , caused by a change of \vec{d}_i by the angle θ .

scattering in three dimensions Δy and θ are sampled independently for the two directions perpendicular to the initial direction.

In practice, the application of multiple scattering for a transport algorithm poses additional challenges. Firstly, applying lateral displacements during a transportation step can lead to unintentional transitions between volumes with different media, as illustrated in Figure 6.8. If the properties of the medium significantly change during the transition, this introduces a bias. Especially for large transportation steps, or for transportation in parallel to a border, these effects need to be taken into account. Secondly, the combination of multiple scattering with magnetic deflections is highly non-trivial, since both processes are correlated as they both introduce position-dependent deflections of the transported particle.

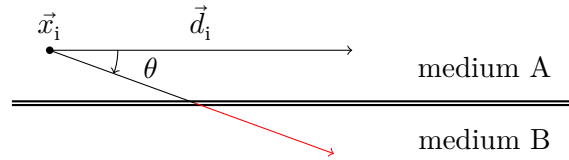


Figure 6.8: Illustration of the border transition problem. A particle at position \vec{x}_i within medium A is transferred along an initial direction \vec{d}_i . Due to multiple scattering, the initial direction is changed by an angle θ , which can cause the particle to enter a medium B. If this is not correctly taken into account, the particle will traverse a distance through medium B, indicated in red, while the algorithm assumes that the particle is still in medium A. Figure and caption from [29].

A recent update for the propagation algorithm in PROPOSAL improves the treatment of multiple scattering at border transitions. In this approach, if a particle crosses a medium transition during a propagation step, an iterative approach is used to find a valid combination of the propagation length and the scattering angle. The implementation of this approach is described in detail in [29].

Within EGS4, and therefore within CORSIKA 7, the lateral displacement Δy is entirely ignored, which avoids the necessity for a dedicated treatment at border transitions [171]. However, this limits the possible size of transportation steps, since for larger steps, ignoring the lateral displacement introduces a significant bias [118]. Since the step size is the driving factor for the performance of a transportation algorithm, this causes a performance bottleneck.

The PRESTA algorithm [61] provides an extension of the multiple scattering treatment within EGS4 where lateral displacements are taken into account. While this generally improves the performance by allowing for larger transportation steps, in

the vicinity of border transitions, the PRESTA algorithm still requires very small step lengths to deal with the problem of unintentional transitions [118].

Within the EGS5 code system, the random hinge transport mechanism is used, which is an approach ensuring both the correct treatment of lateral displacements as well as maintaining the possibility to perform large transportation steps [118, 52]. The general idea of the model is to divide a transportation step into two parts, where the point splitting both parts, called the hinge point, is chosen at random. During the transportation step, the particle is transported along its initial direction toward the hinge point, where its direction is updated. Afterward, the particle is transported toward the end of the transportation step. In [118], the method is described in detail, including additional modifications to correctly take continuous energy losses during a large propagation step into account by adding energy loss hinge points. The advantage of this algorithm, next to its intrinsic treatment of lateral displacements, is that boundary crossings do not need to be treated explicitly [118].

For CORSIKA 8, the effect of lateral displacements Δy is currently not taken into account, which corresponds to the treatment also used in CORSIKA 7. This means that the sizes of transportation steps need to be limited to ensure the validity of lateral particle distributions. When improving the transport mechanism within CORSIKA 8, the problems of border transitions, magnetic fields, and inhomogeneous media distributions need to be considered. The random hinge model might provide a basis for an improved mechanism. Further novel ideas for a transport mechanism based on numerically solving ordinary differential equations are described in [182], although their feasibility for full air shower simulations remains to be shown.

6.2 Photon Interactions

In this section, the interaction processes relevant for photons, as well as their implementation inside PROPOSAL, are described. Figure 7.2 and Figure 6.13 show their contributions to the total photon cross section.

6.2.1 Electron-Positron Pair Production

Electron-positron pair production describes the conversion of an ingoing photon into an electron-positron pair near an atomic nucleus, i.e., the process

$$\gamma + Z \rightarrow e^- + e^+ + Z.$$

By comparing this process equation with the bremsstrahlung interaction, as described in Section 6.1.1, it becomes clear that both processes are closely related. In terms of Feynman diagrams, they are directly connected by the substitution rule. Pair production is the dominant process for photons above the MeV energy range, as visible in Figure 7.2, making its description essential for the modeling of electromagnetic particle cascades.

Similar to the parametrization of the bremsstrahlung cross section, the description of pair production is based on the cross section used in the EGS code system, described in detail in [118]. It is divided into a low-energy and a high-energy part, where the high-energy part is used for photon energies $E \geq 50$ MeV and is given by

$$\begin{aligned} \frac{d\sigma}{dx} = & Z(Z + \xi(Z)) r_e^2 \alpha \left[(2x^2 - 2x + 1) \left(\Phi_1(\delta) - \frac{4}{3} \ln(Z) - 4f_c(Z) \right) \right. \\ & \left. + \frac{2}{3}(1-x) \left(\Phi_2(\delta) - \frac{4}{3} \ln(Z) - 4f_c(Z) \right) \right], \end{aligned} \quad (6.61)$$

with

$$\delta = \frac{136m_e Z^{-1/3}}{Ex(1-x)}, \quad x = \frac{E_{e^-}}{E}, \quad (6.62)$$

where E_{e^-} is the energy of the created electron. The terms $f_c(Z)$, describing the Coulomb correction, $\Phi_{1/2}(x)$, describing screening effects, and $\xi(Z)$, describing the contribution of interactions with atomic electrons, are identical to the definitions used for bremsstrahlung interactions as given in (6.3), (6.4), (6.5), and (6.6), respectively. For photon energies $E < 50$ MeV, the bremsstrahlung cross section becomes

$$\begin{aligned} \frac{d\sigma}{dx} = & A'_p(E, Z) Z(Z + \xi(Z)) r_e^2 \alpha \left[(2x^2 - 2x + 1) \left(\Phi_1(\delta) - \frac{4}{3} \ln(Z) \right) \right. \\ & \left. + \frac{2}{3}x(1-x) \left(\Phi_2(\delta) - \frac{4}{3} \ln(Z) \right) \right], \end{aligned} \quad (6.63)$$

where a correction factor $A'_p(E, Z)$, accounting for low-energy effects, is introduced. The factor $A'_p(E, Z)$ ensures that the total cross section agrees with the calculations from [207], where a table for the total pair production cross section for elements between $Z = 1$ and $Z = 100$, and for energies between 1 keV and 1 MeV, is provided. PROPOSAL interpolates this two-dimensional table to obtain A'_p for arbitrary E and Z .

In the work by Tsai [214], an alternative parametrization of the pair production cross section is described, which mainly differs in its description of the form factors and its treatment of atomic electron effects. This cross section is given by

$$\begin{aligned} \frac{d\sigma}{dx} = \frac{\alpha r_e^2 x E}{p} & \left\{ \left(\frac{4}{3}x^2 - \frac{4}{3}x + 1 \right) \right. \\ & \times \left[Z^2 \left(\varphi_1 - \frac{4}{3} \ln(Z) - 4f_{c,\text{Tsai}}(z) \right) + Z \left(\psi_1 - \frac{8}{3} \ln(Z) \right) \right] \\ & \left. - \frac{2}{3}x(1-x) \left[Z^2 (\varphi_1 - \varphi_2) + Z(\psi_1 - \psi_2) \right] \right\}, \end{aligned} \quad (6.64)$$

with the absolute electron momentum p and the Coulomb correction

$$f_{c,\text{Tsai}} = 1.202z - 1.0369z^2 + 1.008 \frac{z^3}{1+z}, \quad z = \left(\frac{Z}{137} \right)^2. \quad (6.65)$$

The analytic expressions for the atomic form factors φ_1 , φ_2 , ψ_1 , and ψ_2 are listed in [Appendix A.5](#).

A comparison of the two parametrizations of the pair production cross section is presented in [Figure 6.9](#). For energies above 50 MeV, the parametrizations show a good agreement, both reaching the expected high-energy limit of $\sigma \approx \frac{7}{9}X_0^{-1}$ with the radiation length X_0 [225]. At 50 MeV, a discontinuity, caused by the introduction

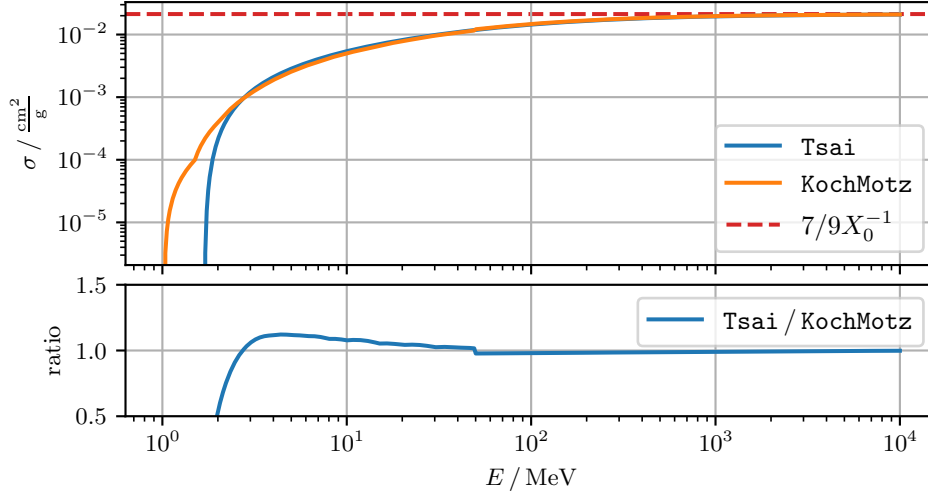


Figure 6.9: Comparison of the electron-positron pair production cross section in air. The parametrization given by (6.61) and (6.63) is called KochMotz, the parametrization given by (6.64) is called Tsai. Figure adapted from [29].

of the correction factor A'_p in (6.63), emerges. For lower energies, differences in the cross sections become visible. This is expected, since approximations made by Tsai are only valid for extremely relativistic particles [214], while in (6.63), low-energy effects are explicitly accounted for by the correction factor. Per default, PROPOSAL uses the parametrizations given in (6.61) and (6.63).

For very high energies, the pair production cross section is affected by the LPM effect, leading to a significant suppression of symmetric pair production events, and correspondingly of the total cross section. A detailed discussion of the LPM effect, including its treatment and effects, is given in Section 6.3.

The limits of the pair production cross section are determined by kinematics and are given by

$$x_{\min} = \frac{m_e}{E}, \quad x_{\max} = 1 - \frac{m_e}{E}. \quad (6.66)$$

To sample the energy distribution between the electron and the positron, the variable x is sampled from the differential cross section by solving

$$\frac{1}{\sigma} \int_{x_{\min}}^x \frac{d\sigma}{dx'} dx' = \xi \quad (6.67)$$

for x , where ξ is a random number $\xi \in [0, 1)$. Figure 6.10 shows the result of this method, comparing the usage of the two differential cross sections. Both parametrizations produce similar distributions for x , which vary in their shape depending on E .

To sample the angular distribution of the produced electron-positron pair, an expression for the double differential cross section from [214] is used, given by

$$\begin{aligned} \frac{d^2\sigma}{d\theta dp} \propto \sin(\theta) & \left[\left(\frac{2x(1-x)}{(1+l)^2} - \frac{12lx(1-x)}{(1+l)^4} \right) (Z^2 + Z) \right. \\ & \left. + \left(\frac{2x^2 - 2x + 1}{(1+l)^2} + \frac{4lx(1-x)}{(1+l)^4} \right) (X - 2Z^2 f_{c,\text{Tsai}}(z)) \right] \end{aligned} \quad (6.68)$$

with

$$l = \frac{E_-^2 \theta^2}{m_e^2},$$

where θ describes the angle between the ingoing photon and the outgoing electron or positron, and X is a description of the atomic form factors, defined in Appendix A.5. For given E and x , the integral equation

$$\left(\frac{d\sigma}{dp} \right)^{-1} \int_0^\theta \frac{d^2\sigma}{d\theta dp} d\theta = \xi \quad (6.69)$$

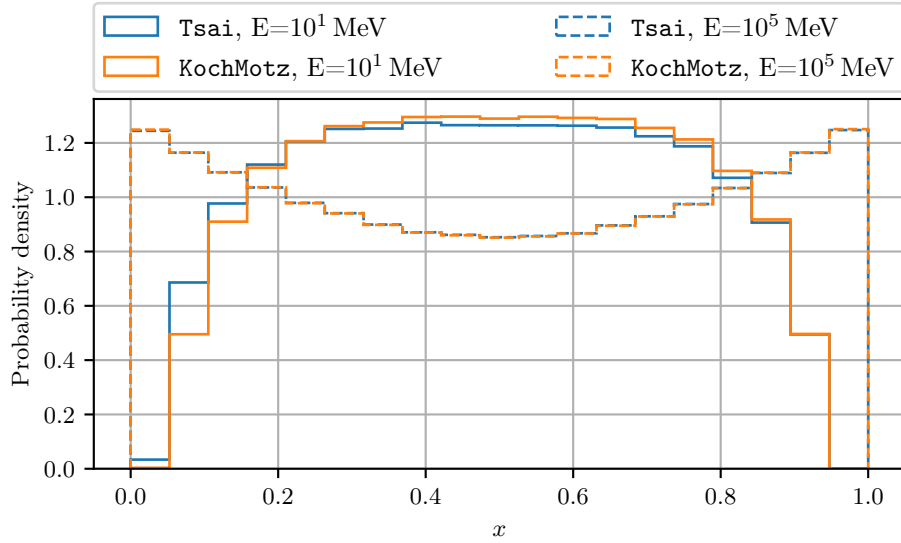


Figure 6.10: Sampling of the energy distribution x between the electron and the positron, for two different photon energies E in air. A nitrogen atom is assumed as the interaction target. The differential cross section given by (6.61) and (6.63) is called KochMotz, the differential cross section given by (6.64) is called Tsai.

is solved for θ , where $\xi \in [0, 1)$ is a random number. Note that the overall normalization of (6.68) is irrelevant, as long as it is independent of θ . As an alternative, [118] proposes a simplified method that has been used in early versions of EGS, where the production angle θ is set to

$$\theta = \frac{m_e}{E}. \quad (6.70)$$

Similar to the motivation of the sampling method in (6.9) for the scattering angle of bremsstrahlung photons, using such a simple approximation is justified by the fact that for high energies, the production is strongly peaked in the forward direction while for low energies, multiple scattering effects of the produced leptons dominate the lateral spread of the particles. As a second alternative, a simple angular distribution based on the leading order term of the Sauter-Gluckstern-Hull differential cross section [168] is used, which is given by

$$\frac{d\sigma}{d\theta_{\pm}} \propto \frac{\sin(\theta_{\pm})}{2p_{\pm} (E_{\pm} - p_{\pm} \cos(\theta_{\pm}))^2}. \quad (6.71)$$

The deflection angle is sampled from this distribution using [118]

$$\cos(\theta_{\pm}) = \frac{E_{\pm}(2\xi - 1) + p_{\pm}}{p_{\pm}(2\xi - 1) + E_{\pm}}, \quad (6.72)$$

with a random number $\xi \in [0, 1)$. **Figure 6.11** shows a comparison of the three sampling methods for θ . Notably, the median of θ according to the approximation in (6.70) is a factor of two smaller compared to the distributions from (6.69) and (6.72). Since the method in (6.69) is slower by almost two orders of magnitude compared to the other approaches, but its results are reproduced in good approximation by (6.72), the latter is used as a default parametrization inside PROPOSAL.

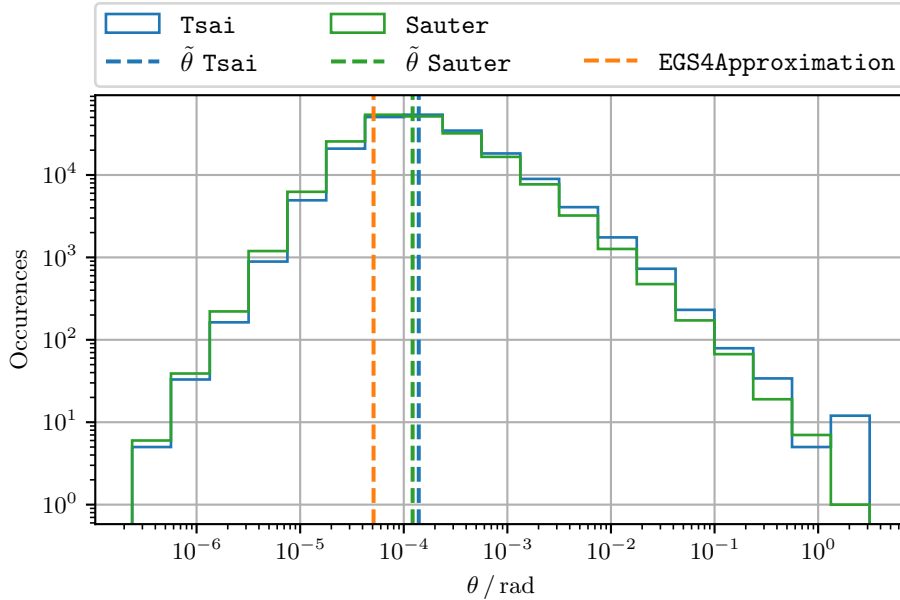


Figure 6.11: Comparison of the sampling methods for the pair production angle θ , given an initial photon energy of 10^4 MeV. A nitrogen atom is assumed as the interaction target. **EGS4Approximation** shows the approximation of (6.70), **Tsai** the calculation according to (6.69), and **Sauter** the sampling method using (6.72). For **Tsai** and **Sauter**, x is sampled according to (6.64). From this x , the production angle θ is sampled using the respective methods. The dashed lines indicate the median $\tilde{\theta}$ of the distributions. Figure adapted from [29].

6.2.2 Compton Scattering

When a photon propagates through a medium, it can scatter with an atomic electron, thus transferring part of its energy. This process is called Compton scattering. For photons in air, Compton scattering is the dominant interaction process between energies of $E \approx 30$ keV and $E \approx 20$ MeV, as visible in [Figure 6.13](#). In comparison to Compton scattering, Rayleigh scattering describes the elastic scattering of photons with particles small compared to the wavelength of the photon. While Compton scattering is taken into account in PROPOSAL, as described in this section, the process of Rayleigh scattering is currently not implemented.

Under the assumption that the atomic electrons are free and at rest, which is satisfied in good approximation for photons at high energies, the differential cross section is given by the Klein-Nishina formula [[118](#), [139](#)]

$$\frac{d\sigma}{dv} = \frac{Z\pi r_e^2 m_e}{E} \left(\frac{C_1}{(1-v)^2} + \frac{C_2}{(1-v)} + C_3 + 1 - v \right), \quad (6.73)$$

with

$$C_1 = \frac{m_e^2}{E^2}, \quad C_2 = 1 - 2C_1 \left(1 + \frac{E}{m_e} \right), \quad C_3 = C_1 \left(1 + 2\frac{E}{m_e} \right). \quad (6.74)$$

For lower photon energies, the influence of the atomic binding energy decreases the cross section in the forward direction, especially for media with high Z [[118](#)]. Furthermore, the non-zero motion of the atomic electrons influences the final energy spectrum, an effect called Doppler broadening. However, both effects become relevant for photon energies close to electron binding energies or smaller, which are at most in the order of keV. At these energies, photoelectric absorption, see [Section 6.2.3](#), becomes the dominant interaction type. Therefore, both effects are currently neglected by PROPOSAL, as is also the case in EGS4 [[171](#)].

Since Compton scattering can be described as a two-body interaction with an atomic electron at rest, [\(A.35\)](#) is used to determine the involved deflection angles. With

$$\begin{aligned} E_1 &= E, & E'_1 &= E(1-v), & E'_2 &= m_e + vE, \\ m_1 &= m'_1 = 0, & m'_2 &= m_e, \end{aligned}$$

this results in

$$\cos \theta_1 = 1 - \frac{vm_e}{E(1-v)}, \quad \cos \theta_2 = \frac{v(E + m_e)}{\sqrt{2vEm + E^2v^2}},$$

where θ_1 describes the deflection angle of the photon and θ_2 the angle between the ingoing photon and the recoiled atomic electron. The azimuth angle is sampled

uniformly for the photon, with the electron receiving the opposite azimuth. The kinematic limits in v are obtained by setting $\cos\theta_1 = \pm 1$, resulting in

$$v_{\min} = 0, \quad v_{\max} = \frac{1}{1 + 0.5m_e/E}. \quad (6.75)$$

Figure 6.12 shows the differential cross section (6.73) in dependence of θ_1 . It is clearly visible that for higher photon energies $E \gg m_e$, the differential cross sections peaks in the forward direction.

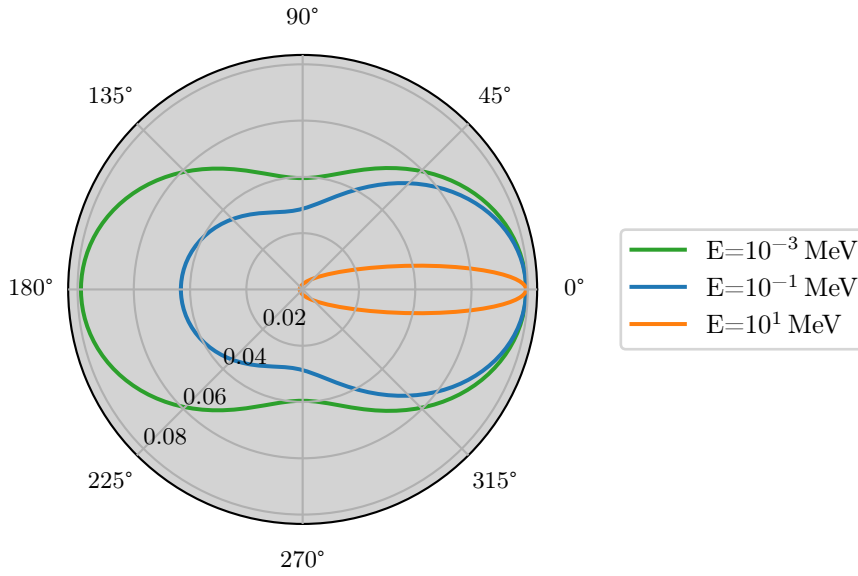


Figure 6.12: Compton cross section according to the Klein-Nishina formula for different photon energies, expressed as a differential cross section $\frac{d\sigma}{d\Omega} = \frac{d\sigma}{d\cos(\theta_1)d\phi}$ with azimuth ϕ . The polar axis indicates θ_1 , the radial axis the differential cross section in b/sr.

6.2.3 Photoelectric Absorption

The photoeffect is the absorption of a photon by an atom, where the photon energy is transferred to a bound electron, which is thereby ejected. This interaction becomes the dominant absorption process of photons at low energies, e.g., in air for photon energies below ≈ 30 keV, as visible in Figure 6.13.

While the exact description of the photoeffect depends on the atomic structure of the target medium, the implementation in PROPOSAL simply intends to give

an approximative description in the energy regime where the photoeffect becomes a significant correction to the Compton cross section. Parametrizations of the photoeffect cross section for the absorption by the K-shell electron, which provides the largest contribution to the photoeffect, are given in [115, 196]. In the relativistic case, i.e., for photons with energies large compared to the electron mass, and also large compared to the ionization energy I of the K-shell electron, the Born approximation can be applied, and the total cross section of the absorption by a K-shell electron is given by

$$\begin{aligned} \sigma_K &= 4\pi r_e^2 Z^5 \alpha^4 \left(\frac{m_e}{E}\right)^5 (\gamma^2 - 1)^{3/2} F_{\text{nonrel}} \\ &\times \left[\frac{4}{3} + \frac{\gamma(\gamma - 2)}{\gamma + 1} \left(1 - \frac{\ln(\gamma + \sqrt{\gamma^2 - 1})}{\gamma\sqrt{\gamma^2 - 1}} \right) \right], \end{aligned} \quad (6.76)$$

with

$$\gamma = 1 + \frac{E - I}{m_e}, \quad I = \frac{Z^2 \alpha^2 m_e}{2}. \quad (6.77)$$

The factor F_{nonrel} describes a correction term which improves the accuracy of the cross section in the non-relativistic energy regime. It is defined in [196], and given by

$$F_{\text{nonrel}} = \left[1 + \left(\frac{\alpha Z}{\beta} \right)^2 \right] \frac{\pi \alpha Z / \beta}{\sinh(\pi \alpha Z / \beta)} \exp \left[\frac{\alpha Z}{\beta} \left(\pi - 4 \arctan \left(\frac{\beta}{\alpha Z} \right) \right) \right]. \quad (6.78)$$

To obtain the total photoeffect cross section σ_{tot} , taking into account outer shell electrons as well, the empirical formula from [121] is used, which is given by

$$\frac{\sigma_{\text{total}}}{\sigma_K} = 1 + 0.01481 \ln^2 Z - 0.000788 \ln^3 Z. \quad (6.79)$$

If a photon is absorbed due to the photoeffect, the ejected electron receives the energy $E - I$, and it is assumed to inherit the direction of the initial photon.

Note that the given parametrizations are not accurate for low photon energies, especially in the vicinity of the absorption edges. Furthermore, the underlying Born approximation can not be applied for heavier elements. A more detailed treatment would be required to take these effects into account. However, to describe the development of an extensive air shower, energies $E \ll 2m_e$ and nuclei with $Z > 8$ are irrelevant. Figure 6.13 shows the photoeffect, Compton, and pair production cross sections of photons in air compared to the tabulated values from the NIST Standard Reference Database [122]. An agreement with the NIST data within 10% is visible, with a much better agreement at photon energies above 100 keV.

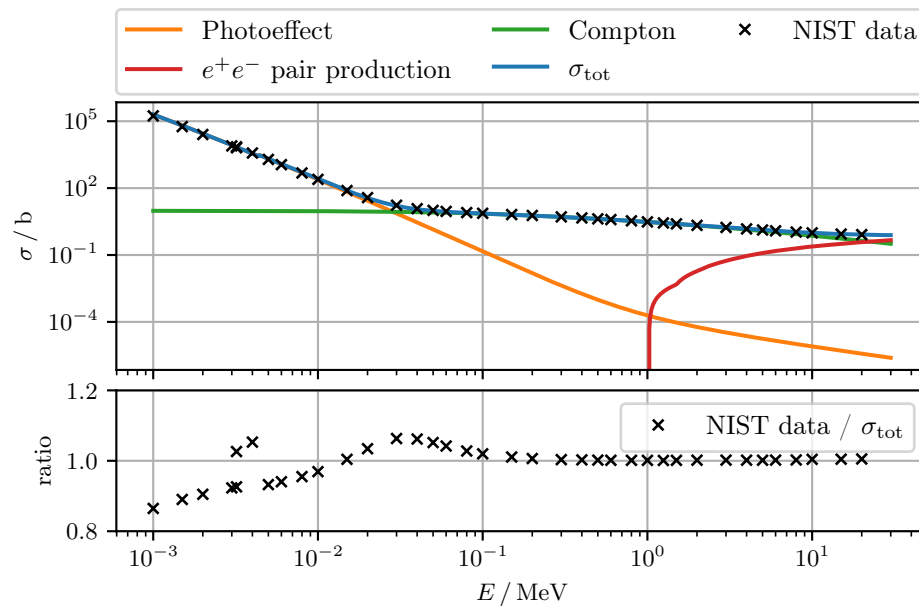


Figure 6.13: Cross sections of photons in air according to the default parametrizations used in PROPOSAL, as listed in Table A.3, compared to the tables from the NIST Standard Reference Database [122]. The K absorption line of argon is at $E \approx 3.2 \times 10^{-3}$ MeV, which leads to a discontinuity in the NIST data which is not well described by the photoeffect cross section in (6.76). Figure adapted from [30].

6.2.4 Muon Pair Production

In Section 6.2.1, the conversion of a photon into an electron-positron pair in the field of an atomic nucleus has been discussed. However, in pair production processes, the creation of a muon pair is also possible, i.e.,

$$\gamma + Z \rightarrow \mu^- + \mu^+ + Z.$$

This process is called muon pair production. Compared to electron-positron pair production, the muon pair production cross section is suppressed by a factor of $\approx (m_e/m_\mu)^2$, and is therefore negligible for the total photon cross section, as visible in Figure 7.2. However, muon pair production is, together with the decay of secondary particles from photohadronic interactions, see Section 6.1.5 and Section 6.2.5, the only source of muons in electromagnetic showers and therefore a process with a unique signature. Due to their ability to travel large distances, these muons can extract energy out of the core of an electromagnetic particle cascade.

The differential cross section is derived from the bremsstrahlung cross section of muons, given in [135], using crossing symmetry, which yields [29, 30]

$$\frac{d\sigma}{dx} = 4Z^2\alpha \left(r_e \frac{m_e}{m_\mu} \right)^2 \Phi(\delta) \left[1 - \frac{4}{3}(x - x^2) \right], \quad (6.80)$$

with

$$\Phi(\delta) = \underbrace{\ln \left(\frac{BZ^{-1/3}m_\mu/m_e}{1 + BZ^{-1/3}\sqrt{e}\delta/m_e} \right)}_{\Phi_0} - \underbrace{\ln \left(\frac{D_n}{1 + \delta(D_n\sqrt{e} - 2)/m_\mu} \right)}_{\Delta_n}, \quad (6.81)$$

where

$$x = \frac{E_{\mu^-}}{E}, \quad \delta = \frac{m_\mu^2}{2Ex(1-x)}, \quad D_n = 1.54A^{0.27}. \quad (6.82)$$

This result is identical to the differential cross section presented in [67]. For the radiation logarithm constant B , which depends on the value of Z , the values from [138] are used, which are listed in Table A.7. For the inelastic radiation logarithm B' , the definition

$$B' = \begin{cases} 446 & \text{for } Z = 1, \\ 1429 & \text{for } Z \neq 1, \end{cases} \quad (6.83)$$

is used. To take the contribution of pair production on atomic electrons into account, the substitution

$$\Phi(\delta) \rightarrow \Phi(\delta) + \frac{1}{Z} \left[\ln \left(\frac{m_\mu/\delta}{\delta m_\mu/m_e^2 + \sqrt{e}} \right) - \ln \left(1 + \frac{1}{\delta \sqrt{e} B' Z^{-2/3}/m_e} \right) \right] \quad (6.84)$$

is applied. For $Z > 1$, the effect of nucleus excitation is taken into account by substituting

$$\Delta_n \rightarrow \left(1 - \frac{1}{Z} \right) \Delta_n. \quad (6.85)$$

The kinematic limits of the cross section are given by [29]

$$\frac{1}{2} \left(1 - \sqrt{1 - 2\sqrt{e}m_\mu/E} \right) \leq x \leq \frac{1}{2} \left(1 + \sqrt{1 - 2\sqrt{e}m_\mu/E} \right). \quad (6.86)$$

For the produced muon pair, the approximation

$$\theta = \frac{m_\mu}{E}, \quad (6.87)$$

in analogy to (6.70) for electron-positron pair production, is used to describe the production angle θ . The azimuth angle is sampled uniformly for one muon, with the other muon receiving the opposite azimuth. A more accurate treatment to sample the polar and azimuth angles of the produced muon pairs is used in CORSIKA 7, as described in [108].

6.2.5 Photohadronic Interactions

For sufficiently high energies, photons perform photohadronic interactions in which they are absorbed by a nucleus, producing secondary particles in the process. The contribution of the photohadronic cross section to the total photon cross section is negligible, with a share of less than 1%, as visible in Figure 7.2. However, for energies where the LPM suppression of the pair production cross section becomes efficient, see Section 6.3, photohadronic interactions, which are not affected by the LPM effect, yield a significant contribution. Since photohadronic interactions are the only process where hadrons are produced within an electromagnetic shower, they are the only way to transfer energy back to the hadronic shower component. Furthermore, through the subsequent hadronic decays, for example of pions and kaons, photohadronic interactions are a significant source of muons in electromagnetic showers, as investigated in Section 7.2.4.

The total cross section for the absorption of a photon by a single nucleon $\sigma_{\gamma,N}$ can be described by different parametrizations, with several options available in PROPOSAL. The large amount of parametrizations, and the different predictions they provide, is mainly caused by the limited coverage of experimental measurements in the relevant phase space, especially for high energies and in the forward direction, resulting in significant uncertainties. The parametrization by *Bezrukov and Bugaev* is given by [59]

$$\sigma_{\gamma,N} = \left(114.3 + 1.647 \ln^2 \left(0.0213 \frac{\nu}{\text{GeV}} \right) \right) \mu\text{b}, \quad (6.88)$$

where ν is the photon energy in units of GeV. The parametrization by *Caldwell* is given by [71]

$$\sigma_{\gamma,N} = \left(49.2 + 11.1 \ln \left(\frac{\nu}{\text{GeV}} \right) + 151.8 / \sqrt{\frac{\nu}{\text{GeV}}} \right) \mu\text{b}. \quad (6.89)$$

The parametrization by *Kokoulin* uses different functions depending on the energy regime and is given by [145]

$$\sigma_{\gamma,N} = \begin{cases} \left(96.1 + 82 / \sqrt{\nu/\text{GeV}} \right) \mu\text{b}, & \text{for } \nu \leq 17 \text{ GeV}, \\ \left(114.3 + 1.647 \ln^2 (0.0213 \nu/\text{GeV}) \right) \mu\text{b}, & \text{for } 17 \text{ GeV} < \nu \leq 200 \text{ GeV}, \\ \left(49.2 + 11.1 \ln (\nu/\text{GeV}) + 151.8 / \sqrt{\nu/\text{GeV}} \right) \mu\text{b}, & \text{for } \nu > 200 \text{ GeV}, \end{cases} \quad (6.90)$$

where for energies $\nu > 200 \text{ GeV}$, the cross section coincides with (6.89). A parametrization using a fit to data taken by the *ZEUS* experiment at the HERA detector [65] is given by

$$\sigma_{\gamma,N} = (63.5s^{0.097} + 145s^{-0.5}) \mu\text{b}, \quad (6.91)$$

with $s = 2m_N\nu/\text{GeV}$, where m_N describes the average nucleon mass in units of GeV. In the parametrization by *Rhode* [184], for $E \leq 200 \text{ GeV}$, the data given by [65] is directly used by interpolating the measurements, which means that the parametrization explicitly considers resonances in the lower energy range. For energies $E > 200 \text{ GeV}$, the parametrization in (6.89) is used. Lastly, the photohadronic cross section based on the parametrization used in *CORSIKA 7* is implemented, given by [109]

$$\sigma_{\gamma,N} = \begin{cases} (73.3s^{0.073} + 191.7s^{-0.602}) \sqrt{1 - s_0/s} \mu\text{b}, & \text{for } \sqrt{s} \leq 19.39 \text{ GeV}, \\ (59.3s^{0.093} + 120.2s^{-0.358}) \mu\text{b}, & \text{for } \sqrt{s} > 19.39 \text{ GeV}, \end{cases} \quad (6.92)$$

with the squared center of mass energy $s = m_n^2 + 2m_n\nu$ and the pion production threshold $\sqrt{s_0} = 1.0761$ GeV. On top of this continuous cross section, the contributions from the $\Delta(1232)$, $N(1520)$, and $N(1680)$ resonances are added analytically. This method is described in [Appendix A.8](#).

To infer the cross section for the absorption of a photon by an atomic nucleus $\sigma_{\gamma,A}$ from the cross section for an individual nucleon $\sigma_{\gamma,N}$, the effect of nucleon shadowing needs to be taken into account. Shadowing causes the sum of the cross sections of the individual nucleons to be smaller than the cross section of the entire nucleus, i.e., $\sigma_{\gamma,A} \leq A \cdot \sigma_{\gamma,N}$. One explanation for this effect comes with the vector meson dominance model, proposed by [192], which assumes that the photon can fluctuate into vector mesons and their excited states, such as ρ , ω , which then interact with the nucleus. Since the mean free path of these vector mesons can be smaller than the radius of the nucleus, they primarily interact with nucleons facing toward the incoming photon, since the nucleons at the back are shielded. Based on the vector meson dominance model, the parametrization by [59] describes the shadowing effect using the screening function $G(x)$, which yields

$$\sigma_{\gamma,A} = A\sigma_{\gamma,N}(0.75G(x) + 0.25), \quad (6.93)$$

with

$$G(x) = \begin{cases} \frac{3}{x^2} \left(\frac{x^2}{2} - 1 + e^{-x}(1+x) \right) & \text{for } Z \neq 1, \\ 1, & \text{for } Z = 1, \end{cases} \quad (6.94)$$

where $x = 0.00282A^{1/3}\sigma_{\gamma,N}(E)$.

[Figure 6.14](#) shows a comparison of the different parametrizations for the photohadronic cross section. Toward the highest energies, the extrapolation shows a different behavior for almost all parametrizations. Only the parametrizations *Rhode* and *CORSIKA 7* take resonances into account. If the identical shadowing parametrization according to (6.94) is used, their description of the resonances is in good agreement. Within *CORSIKA 7*, however, the simplified shadowing parametrization $\sigma_{\gamma,A} = A^{0.91}\sigma_{\gamma,N}$ is used. This leads to a significant difference in the parametrization, both around the resonances and for the high-energy extrapolation.

Per default, *PROPOSAL* uses the *Rhode* parametrization. For the usage of *PROPOSAL* in *CORSIKA 8*, instead, the *CORSIKA 7* parametrization in combination with the shadowing parametrization according to (6.94) is used.

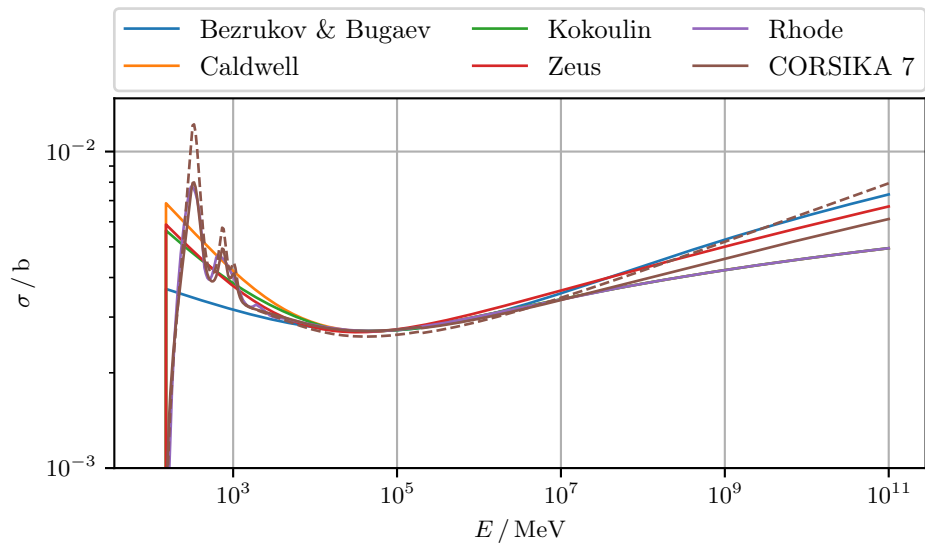


Figure 6.14: Comparison of the different parametrization of the photohadronic cross section for photons in air. For the CORSIKA 7 parametrization, the solid line indicates the cross section using the shadowing parametrization according to (6.94), while the dashed line shows the cross section with the shadowing parametrization internally used within CORSIKA 7 according to [109]. Figure adapted from [30].

Treatment of Photohadronic Secondaries within CORSIKA 8

The total cross section $\sigma_{\gamma,A}$ defines the mean interaction length for a photohadronic interaction. However, in the context of air shower simulations, information about the individual secondary particles produced within the photohadronic interaction is needed. To perform this task, dedicated tools called hadronic event generators are available. Therefore, an interface between PROPOSAL, providing the total photohadronic cross section and sampling the occurrence of a photohadronic interaction, and the hadronic event generators, sampling the secondary particles, is implemented. The general concept of this interface is based on the approach that PROPOSAL produces a pseudo-particle with the interaction type `ParticleType::Hadron`, including information about the interacting photon and its interaction target, which is used by the hadronic event generator as the basis for the secondary particle calculation.

For photon energies $E < E_{\text{thres}}$, where $E_{\text{thres}} = 10^{1.9} \text{ GeV} \approx 79.4 \text{ GeV}$ is set as a default, the hadronic event generator SOPHIA [169] is used. SOPHIA is designed to describe relativistic photon-nucleon interactions, applicable in astrophysical environments, collider experiments, as well as for air shower simulations. If CORSIKA 8 samples, based on the photohadronic cross section provided by PROPOSAL, that a photohadronic interaction occurs for a photon with energy E , CORSIKA 8 calls the `EVENTGEN` routine from SOPHIA. The target nucleon is assumed to be at rest, while its type, either proton or neutron, is sampled according to the A/Z ratio of the target component. SOPHIA distinguishes between four different processes: Resonance excitation, direct meson production, diffractive interactions, and non-diffractive multiparticle production. Based on the information about E and the target nucleus, one of these processes is selected, and the corresponding secondary particles are calculated. Finally, these particle states are put back on the particle stack of CORSIKA 8. In [169], a detailed description of the processes considered by SOPHIA as well as comparisons to accelerator data are provided.

For photohadronic interactions with $E \geq E_{\text{thres}}$, the hadronic interaction event generator SIBYLL 2.3D is used [185]. SIBYLL is an event generator explicitly designed to model hadronic interactions in air shower simulations up to the highest particle energies. A general overview of the concepts used in SIBYLL is given in [87]. Its usage for photohadronic interactions within CORSIKA 8 is similar to the methodology in the low-energy regime. However, while SOPHIA calculates the final particle states based on an interaction between the photon and a nucleon, SIBYLL bases its calculation on the interaction between a ρ_0 and an entire nucleus. This approximation is based on a real photon fluctuating into a virtual vector meson, here a ρ_0 as the lightest vector meson, which then interacts with the nucleus.

Note that the current implementation of the interface is connected to SOPHIA and SIBYLL 2.3D. However, the underlying code structure allows for the connection to any other hadronic interaction model implemented in CORSIKA 8.

Treatment of Photohadronic Secondaries within CORSIKA 7

The treatment of secondary particle production from photohadronic interactions in CORSIKA 7 depends on the energy E of the interacting photon: For $E < 0.4$ GeV, one pion is produced, for $0.4 \text{ GeV} \leq E < 1.4$ GeV, either one or two pions are produced, and for $1.4 \text{ GeV} \leq E < 2$ GeV, two pions are produced [113]. At energies above 2 GeV, either one of the vector mesons ρ^0 or ω is produced (with a ratio of 9 to 1) [109], or the secondary particles are generated via the hadronic event generator HDPM [73, 113]. At energies above 80 GeV, the selected high-energy hadronic event generator is called, where the interacting photon is replaced either by a pion or an η meson, depending on the hadronic interaction model.

Additional Photohadronic Effects

Currently not taken into account by the parametrizations provided by PROPOSAL is the photodisintegration regime at energies below the pion production threshold, which includes the giant dipole resonance of the nuclei [166]. One code taking these effects into account is the multi-particle transport code FLUKA [64, 94], and a comparison of the implementation in FLUKA with the implementation in PROPOSAL is shown in Figure 6.15.

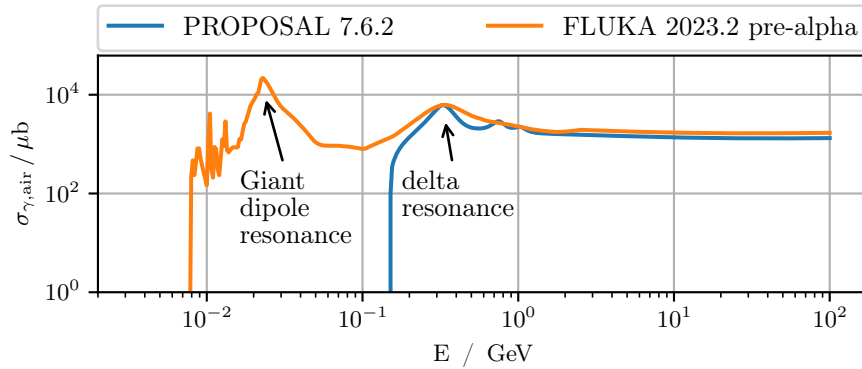


Figure 6.15: Comparison of the photohadronic cross section of photons in air, implemented in PROPOSAL according to the parametrization (6.92), with the implementation of the particle transport code FLUKA [64, 94].

6.3 The Landau-Pomeranchuk-Migdal Effect

For the previously presented cross sections, the approximation of an interaction with a single, isolated atom has been made. In realistic environments, interactions occur in media where many atoms are present. Their involvement can lead to suppression effects, which will be discussed in this chapter.

When conventionally describing a bremsstrahlung loss of an ingoing lepton, the assumption is made that the interaction happens at a single point. However, this assumption can not be valid when considering the uncertainty principle $\hbar \propto l\delta$, where δ describes the momentum transfer and l the formation length, which can be interpreted as the spread of the electromagnetic interaction. In bremsstrahlung interactions, the momentum transfer in the longitudinal direction is given by [140]

$$\delta_{\parallel} = \frac{m^2 v}{2E(1-v)}. \quad (6.95)$$

This means that the formation length becomes large for high lepton energies E , small lepton masses m , and small bremsstrahlung losses v . For sufficiently small δ_{\parallel} , the formation length can reach interatomic distances. In this case, the influence of other atoms affects the coherence of the wavefunctions of the ingoing lepton and the photon, which leads to a suppression of the interaction. When the radiating lepton undergoes multiple scattering, where the scattering angle is larger than the average emission angle of the bremsstrahlung photon, coherence is reduced and the cross section is suppressed. This effect is known as the **Landau-Pomeranchuk-Migdal (LPM)** effect [151, 163]. When the photon is affected by Compton scattering on surrounding electrons, the phase of the involved photon is shifted, leading to destructive interference and therefore suppression of the interaction. This effect is known as dielectric suppression, or as the **Ter-Mikaelian (TM)** effect [210]. Both effects are taken into account by PROPOSAL. Further suppression effects, which are currently not considered by PROPOSAL, are due to pair creation, which becomes relevant when the mean free path for pair production of the involved photon is in the same order of magnitude as the formation length, as well as due to magnetic deflection, when the radiating lepton is significantly influenced by external magnetic fields during the bremsstrahlung interaction [140].

Following [140], the parametrization of the **LPM** effect for the bremsstrahlung cross section of leptons is described in PROPOSAL using a correction factor, given by

$$\frac{d\sigma_{\text{LPM}}}{dv} = \frac{d\sigma}{dv} \cdot \frac{\xi(s)/3 (v^2 G(s) + 2(1 + (1-v)^2) \phi(s))}{4/3(1-v) + v^2}, \quad (6.96)$$

where $\frac{d\sigma}{dv}$ is the bremsstrahlung cross section without LPM correction. The functions $\phi(s)$, $G(s)$, and $\psi(s)$ are described in [163, 204], and are defined as

$$\phi(s) = \begin{cases} 1 - \exp\left\{-6s(1 + (3 - \pi)s) + \frac{s^3}{0.623 + 0.796s + 0.658s^2}\right\} & \text{if } s < 1.54954, \\ 1 - 0.012s^{-4} & \text{if } s \geq 1.54954, \end{cases} \quad (6.97)$$

$$G(s) = \begin{cases} 3\psi(s) - 2\phi(s) & \text{if } s < 0.710390, \\ 36s^2 / (36s^2 + 1) & \text{if } 0.710390 \leq s < 0.904912, \\ 1 - 0.022s^{-4} & \text{if } s \geq 0.904912, \end{cases} \quad (6.98)$$

$$\psi(s) = 1 - \exp\left\{-4s - \frac{8s^2}{1 + 3.936s + 4.97s^2 - 0.05s^3 + 7.5s^4}\right\}, \quad (6.99)$$

$$\xi(s) \approx \xi(s') = \begin{cases} 2 & \text{if } s' < s_1, \\ 1 + h - \frac{0.08(1-h)(1-(1-h)^2)}{\ln(s_1)} & \text{if } s_1 \leq s' < 1, \\ 1 & \text{if } s' \geq 1, \end{cases} \quad (6.100)$$

with the definitions

$$s = \frac{s'}{\sqrt{\xi(s')}}, \quad s' = \frac{1}{8} \sqrt{\frac{vE_{\text{LPM}}}{E(1-v)}}, \quad s_1 = \frac{\sqrt{2}Z^{2/3}m_e^2(1 + m^2/m_\mu^2 D_n^2)}{m^2 B^2}, \quad (6.101)$$

$$h = \frac{\ln(s')}{\ln(s_1)}, \quad E_{\text{LPM}} = \frac{2\alpha^2 m^2 X_0}{\pi m_e r_e}, \quad D_n = 1.54A^{0.27}, \quad (6.102)$$

where X_0 is the radiation length of the medium and B the radiation logarithm constant, given for different Z in Table A.7. To account for the TM effect, the parametrization from [180] is used, which introduces the replacements

$$\xi(s) \rightarrow \xi(\Gamma s), \quad \phi(s) \rightarrow \frac{\phi(\Gamma s)}{\Gamma}, \quad G(s) \rightarrow \frac{\psi(\Gamma s)}{\Gamma^2}, \quad (6.103)$$

with

$$\Gamma = 1 + 4\pi \frac{r_e^3 m_e^2}{v^2 m^2 \alpha^2} \rho N_A \frac{\sum_i k_i Z_i}{\sum_i k_i A_i}, \quad (6.104)$$

where the index i runs over all components included in the medium, with k_i being the number of atoms of component i . Figure 6.16 shows the differential

bremsstrahlung cross section of electrons according to (6.1), including the LPM and TM suppression. Firstly, it becomes clear that the suppression is most relevant for small v . Furthermore, the differential cross section without suppression follows v^{-1} , while in the regime where the LPM suppression is effective, the behavior of the function changes to $1/\sqrt{v}$. For even smaller v , the TM effect becomes relevant in the range where the LPM effect is already active, and causes the differential cross section to follow a v dependence.

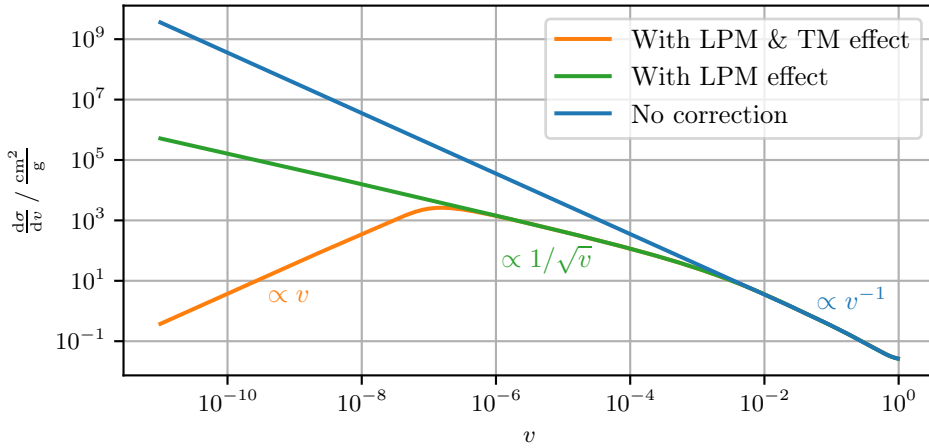


Figure 6.16: Differential bremsstrahlung cross section for electrons with $E = 1$ PeV in air at standard density. Nitrogen is assumed as the interaction target. The effect of the LPM and TM suppression on the differential cross section is shown.

Due to the close connection of the bremsstrahlung and pair production process ($\gamma + Z \rightarrow e^- + e^+ + Z$), it comes as no surprise that there is also an environmental suppression for electron-positron pair production. The motivation for this effect also relies on the uncertainty principle $\hbar \propto l\delta$, similar to the bremsstrahlung suppression. For an electron-positron pair production interaction, the longitudinal momentum transfer δ_{\parallel} is given by [140]

$$\delta_{\parallel} = \frac{m_e^2}{2xE(1-x)}, \quad (6.105)$$

with $x = E_{e^-}/E$, where E_{e^-} denotes the energy of the produced electron. Therefore, the formation length l is maximal for symmetric pair production events with $x = 0.5$, while it is minimal for $x \rightarrow 0$ or $x \rightarrow 1$. When the produced electron and positron undergo significant multiple scattering during the formation length, the coherence of the wavefunction is reduced, leading to a suppression of the cross section. Again, this

effect is called the **LPM** effect, although the suppression becomes relevant at larger energies compared to the **LPM** effect in bremsstrahlung. Since the involved photon always has a high energy compared to the energy of the photon in bremsstrahlung interactions, there is no suppression due to the **TM** effect for pair production [140].

Based on [140], the parametrization of the **LPM** effect for electron-positron pair production within PROPOSAL is given by the correction factor

$$\frac{d\sigma_{\text{LPM}}}{dx} = \frac{d\sigma}{dx} \cdot \frac{\xi(s)/3 (G(s) + 2(x^2 + (1-x)^2) \phi(s))}{1 - 4/3x(1-x)}, \quad (6.106)$$

where the functions and variables are identical to the definitions in the parametrization of the **LPM** effect for bremsstrahlung, apart from the replacements

$$s' = \frac{1}{8} \sqrt{\frac{E_{\text{LPM}}}{Ex(1-x)}}, \quad s_1 = \frac{\sqrt{2}Z^{2/3}}{B^2}. \quad (6.107)$$

Figure 6.17 shows the differential cross section for electron-positron pair production including the **LPM** suppression. While the **LPM** effect in air is still negligible for photon energies up to $E = 10^2$ PeV, a significant suppression of symmetric pair production events is visible as the photon energy becomes higher.

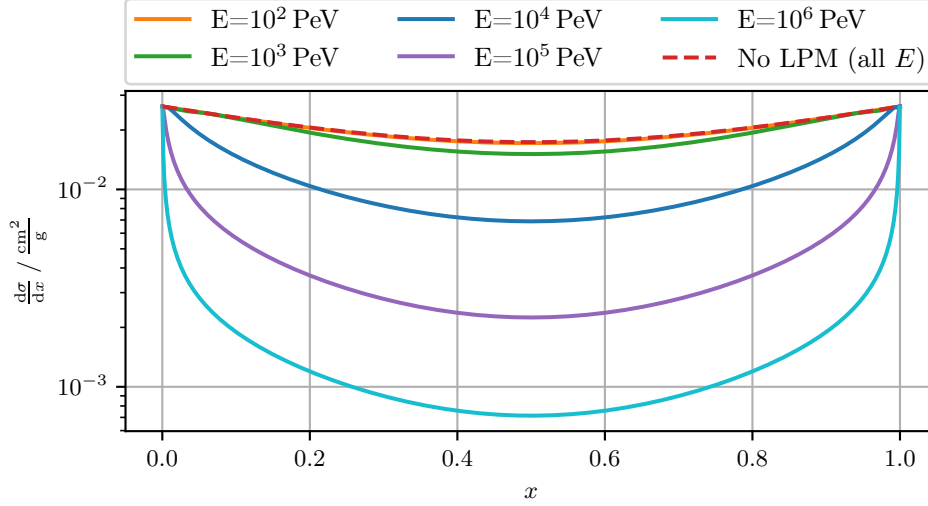


Figure 6.17: Differential electron-positron pair production cross section with **LPM** suppression for electrons in air at **standard density**. Nitrogen is assumed as the interaction target. Note that without **LPM** suppression, the differential cross section is identical for all energies shown in this plot. Figure adapted from [30].

Figure 6.18 shows the total energy loss for bremsstrahlung and electron-positron pair production under the influence of the LPM and TM effect. Note that the intermolecular distance depends on the medium density, which is reflected in the parametrizations via X_0 in the definitions of E_{LPM} . As a result, the LPM suppression becomes more effective for larger medium densities. For the Earth's atmosphere, this means that the LPM suppression becomes less effective as the atmospheric height h increases, as visible in Figure 6.18.

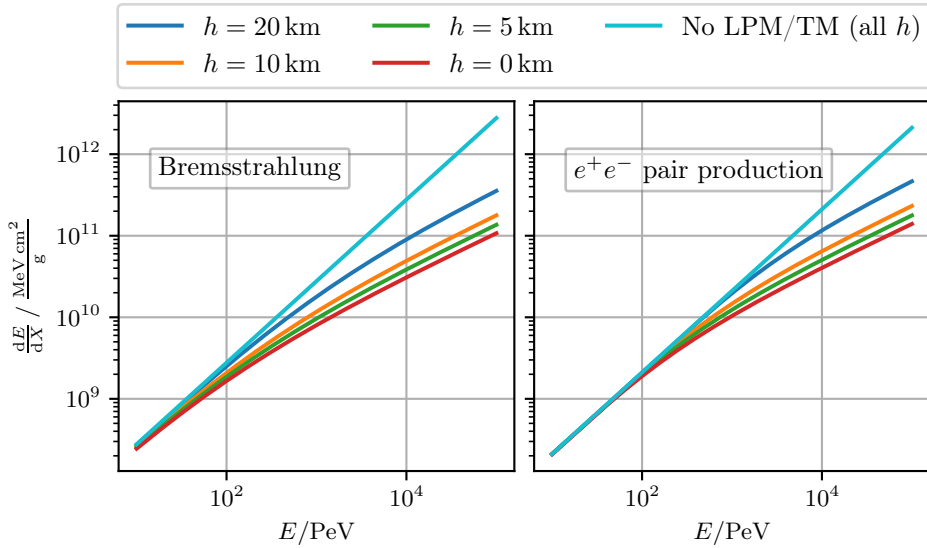


Figure 6.18: Average energy loss of electrons in air due to bremsstrahlung and photons in air due to electron-positron pair production, taking into account the LPM and TM suppression. The energy loss is shown for densities according to different atmospheric heights h . Values for the density of air are taken from [216].

6.3.1 Treatment of the LPM and TM Effect within CORSIKA 8

In principle, the physics parametrizations given in Section 6.1.1 and Section 6.2.1, together with the parametrizations of the LPM effect given in (6.96) and (6.106), allow for a complete description of bremsstrahlung and electron-positron pair production processes in media.¹ However, the simulation of these processes in inhomogeneous media poses a methodical challenge related to the usage of interpolation tables, as described in the following.

¹For the remainder of this section, the term ‘‘LPM effect’’ also includes the TM effect.

The evaluation of interaction processes by PROPOSAL, for example, the calculation of the total cross section according to (4.4) or the sampling of an energy loss according to (4.5), involves the calculation of integral equations. As the underlying differential cross sections are often highly complex, the only possible approach is to solve these equations numerically. Since this process is runtime-intensive, the performance of PROPOSAL is greatly improved by performing these numerical calculations only once and storing the results for selected parameters in interpolation tables.² For a given interaction process, PROPOSAL stores the information about the integral equation (4.5) inside a two-dimensional interpolation table T , defined as

$$T(E, v) = \int_{v_{\text{cut}}}^v \frac{d\sigma(E)}{dv'} dv', \quad (6.108)$$

where the results for different combinations of E and v are saved. This interpolation table is used to calculate the total cross section, as $\sigma_s = T(E, v = v_{\text{max}})$, and for the sampling of energy losses v , without having to recalculate integrals and integral equations for every evaluation. However, these interpolation tables only store the results of calculations for a given medium with density ρ . For air shower simulations such as CORSIKA 8, but also for other applications, the considered media are often inhomogeneous. In general, differential cross sections include a linear dependency on ρ ,

$$\frac{d\sigma(E, \rho)}{dv} = \rho \frac{d\sigma(E)}{dv}. \quad (6.109)$$

This case is unproblematic since ρ can be factored out as a linear term, making T independent of the medium density:

$$\int_{v_{\text{cut}}}^v \frac{d\sigma(E, \rho)}{dv'} dv' = \rho \int_{v_{\text{cut}}}^v \frac{d\sigma(E)}{dv'} dv' = \rho \cdot T(E, v). \quad (6.110)$$

However, in the case of the LPM effect, the dependency on ρ is non-linear, which means that this approach can not be applied.

To consider the LPM effect for stochastic interactions in inhomogeneous media, the technique of rejection sampling is used. Firstly, the interactions and secondary particles, i.e., the interaction energy E and the variables v or x , are sampled according to the differential and total cross sections without taking the LPM effect into account. If a bremsstrahlung or pair production interaction is sampled, the LPM correction factor $c(E, v, \rho)$, according to (6.96), or $c(E, x, \rho)$, according to

²Most numerical methods used in PROPOSAL regarding integration rely on algorithms described in [181]. Recent improvements of the interpolation routine in PROPOSAL are described in [29].

(6.106), is calculated, where ρ is evaluated at the point of interaction. Note that the evaluation of c does not involve the runtime-intensive calculation of integrals. Using a uniformly sampled random number $\xi \in [0, 1)$, the instruction

accept interaction, if $\xi \leq c(E, x/v, \rho)$,
discard interaction, if $\xi > c(E, x/v, \rho)$,

is used, where discarding the interaction means that the initial particle is put back on the particle stack without performing the interaction [112]. This way, the correct suppression due to the LPM effect for stochastic interactions is taken into account. The main disadvantage of this method is its inefficiency for small correction factors c , since in this case, many interactions according to the uncorrected cross sections are sampled and discarded. However, most of the computational effort in calculating the electromagnetic shower component is spent on the energy regime where the LPM effect is ineffective ($c \approx 1$), which means that the additional effort due to the rejection sampling is negligible.

For the calculation of continuous energy losses, a dedicated methodical treatment for the LPM suppression is necessary as well. Recalling the definitions given in Section 4.1, and their application in the context of CORSIKA 8 described in Section 5.3, the continuous energy loss per grammage $f(E) = -\frac{dE}{dX}$ is calculated according to (4.3). To obtain the continuous energy loss of a particle with energy E_i , traversing a propagation step defined by its grammage X , the integral equation (4.7) is solved for E_f . However, when taking the LPM effect into account, a linear factorization of ρ in the differential cross section is not possible, and the continuous energy loss per grammage becomes

$$f(E, \rho) \propto E \int_{v_{\min}}^{v_{\text{cut}}} v \frac{d\sigma(E, \rho)}{dv} dv, \quad (6.111)$$

where $f(E, \rho)$ is density dependent. For the calculation of E_f , this means that (4.7) becomes

$$X = - \int_{E_i}^{E_f} \frac{dE}{f(E, \rho(\vec{x}))}. \quad (6.112)$$

Note that $\rho(\vec{x})$ depends on the particle position, which changes during a propagation step in inhomogeneous media, making this integral non-trivial to evaluate. By applying approximations, however, different methods to solve (6.112) are possible. Firstly, the fact that $\rho(\vec{x})$ changes over a propagation step can be simplified by evaluating ρ at a single point of the step, for example, at the beginning, i.e., $\rho(\vec{x}_i)$. This approximation is justified for sufficiently small propagation steps over which the fluctuations of ρ are small. Based on this simplification, the following approaches, based on different additional approximations, are possible.

Two-dimensional interpolation of the continuous energy loss In this case, the results of the integral equation (6.112) are stored in a two-dimensional interpolation table $f(E, \rho) = T_{\text{cont}}(E, \rho)$. While this is feasible, it is necessary to find appropriate limits ρ_{min} and ρ_{max} for the interpolation table. However, these limits depend on the specific simulation environment, making the creation of different interpolation tables for different applications necessary.

Approximative correction factor for the continuous energy loss Alternatively, (6.112) can be formulated as

$$X = - \int_{E_i}^{E_f} \frac{dE}{c(E, v, \rho) f'(E)} \approx - \frac{1}{c} \int_{E_i}^{E_f} \frac{dE}{f'(E)}, \quad (6.113)$$

where $f'(E)$ describes the continuous energy losses without the LPM effect, while the correction factor $c(E, v, \rho)$ describes the LPM suppression according to (6.96). A reasonable approximation for c is to evaluate it at the beginning of the propagation step, and at the chosen relative energy cut v_{cut} , i.e., $c = c(E_i, v_{\text{cut}}, \rho(\vec{x}_i))$. Note that a single evaluation of c does not require the runtime-intensive calculation of integrals. Since the LPM suppression always becomes more extreme for smaller v , but is in this case only evaluated at $v = v_{\text{cut}}$, this effective approach has the disadvantage of underestimating the suppression.

Neglect LPM effect for continuous losses The simplest approximation is to neglect the effect of the LPM suppression on continuous losses altogether. While the LPM effect is most important for small v , and therefore especially relevant for continuous losses, the influence of continuous losses on the shower development is negligible for energies where the LPM effect is active, compared to the influence of stochastic energy losses.

Figure 6.19 compares the average energy loss per grammage due to stochastic interactions, i.e.,

$$- \left(\frac{dE}{dX} \right)_{\text{stochastic}} \propto E \int_{v_{\text{cut}}}^{v_{\text{max}}} v \frac{d\sigma(E)}{dv} dv,$$

with the continuous energy loss being evaluated using the presented approximations for the LPM effect. With the energy cut chosen in this example, $E_{\text{cut}} = 10 \text{ MeV}$, continuous losses are negligible compared to the energy loss due to stochastic interactions at energies where the LPM effect is relevant. The usage of the correction factor provides a much better approximation of the suppression behavior for continuous losses, although the suppression is, as expected, slightly underestimated.

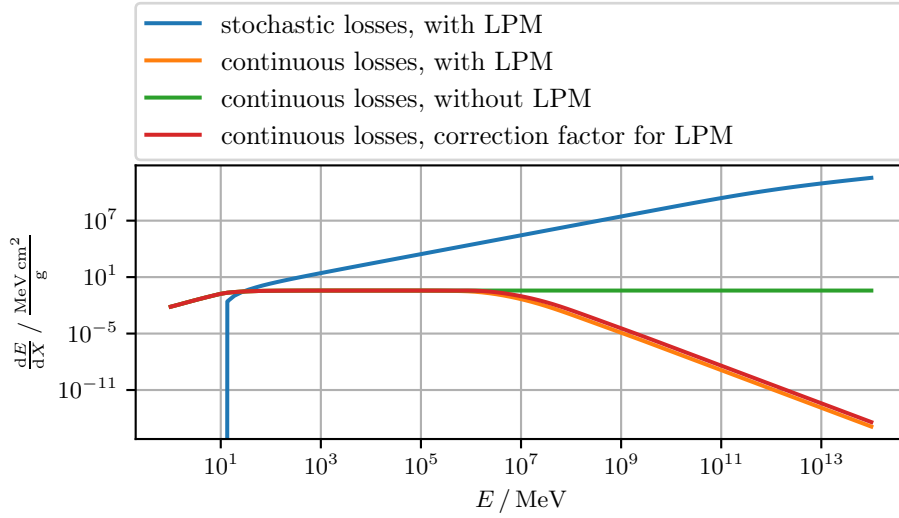


Figure 6.19: Bremsstrahlung energy losses per grammage for electrons in air at standard density. An energy cut of $E_{\text{cut}} = 10$ MeV is used. The line “stochastic losses” describes the energy loss per grammage due to stochastic losses. For the “correction factor” calculation, the LPM suppression factor has been evaluated at $v = v_{\text{cut}} = E_{\text{cut}}/E$, and multiplied to the continuous loss without LPM correction.

At the moment, CORSIKA 8 neglects the LPM suppression on continuous energy losses, making it crucial to ensure that this approximation is valid for the intended application. For analyses where continuous energy losses are explicitly important, simulations in dense media, or when using high energy cut settings, this might not be the case. A validation of the current implementation of the LPM effect in CORSIKA 8 is presented in Section 7.2.2. The ideas outlined in this section can be used as a basis to improve this implementation in the future.

6.3.2 The Influence of the LPM and TM Effect on Extensive Air Showers

Since air is a thin medium, the LPM effect only has a significant influence on extensive air showers of the highest energies. Furthermore, the energy of particles in air showers is maximal at highest altitudes, where the density is even smaller, as shown in Figure 6.18. As a result, the LPM effect only has a significant impact on the development of extensive air showers above energies of 10^{18} eV for electromagnetic showers, and for energies around 10^{20} eV for hadronic showers [141]. Note that the effect on hadronic showers induced by heavier nuclei is smaller compared to proton-induced showers due to the smaller energy per nucleon.

For a detailed, quantitative description regarding the influence of the LPM effect on air showers, full Monte Carlo simulations are necessary due to the complex dependencies. Qualitatively, showers where the LPM effect is significant develop slower, due to the suppressed interactions, and with increased fluctuations [140]. This effect is visible in the shower simulations presented in Figure 7.10. Furthermore, the production of symmetric electron-positron pairs is suppressed, as visible in Figure 6.17. This can lead to the creation of a low-energetic subshower at high altitudes, produced by the lepton receiving the smaller fraction of the energy, as well as the production of a lepton receiving a significant fraction of the photon energy. This lepton can, due to the LPM suppression of bremsstrahlung, travel a larger distance through the atmosphere, depositing its energy in a subshower relatively far down the atmosphere. [112, 147].

7 Air Shower Simulations with CORSIKA 8

In this chapter, simulations of particle cascades using the current status of CORSIKA 8 are presented, with a focus on the electromagnetic and muonic shower component.¹ As a validation, the results are, whenever possible, compared to simulations performed with CORSIKA 7, which is the standard for the simulation of extensive air showers used by the vast majority of the scientific community (see [Section 5.1](#)).² Note that simulations produced with CORSIKA 7 and its predecessors have been, and still are, used in the data analysis of countless experiments, and in this context, comparisons with experimental data have been conducted. Still, CORSIKA 7 does not provide a perfect description of reality, but should rather be seen as a baseline for the sake of comparison. Differences between CORSIKA 7 and CORSIKA 8 are expected, either due to different physics descriptions, algorithms, or made approximations. Comparisons of CORSIKA 7 with other shower simulation frameworks have been conducted, for example, in [\[141, 187\]](#), while a comparison of CORSIKA 8 with the tools AIRES and ZHS has been presented in [\[27\]](#).

This chapter is structured as follows: Firstly, the cross sections of electromagnetic processes used in CORSIKA 7 and CORSIKA 8, which provide the basis for the simulation of the electromagnetic shower component, are compared. Afterward, features of photon-induced air showers are analyzed, including the longitudinal and lateral shower development, the influence of the [Landau-Pomeranchuk-Migdal \(LPM\)](#) effect, and the formation of a hadronic and muonic sub-component. After analyzing key features of proton-induced air showers, the radio emission of high-energy electromagnetic showers is examined. This radio emission is highly sensitive to the development of the electromagnetic shower component, making its analysis suitable to test the correct simulation of the complex cascade dynamics. Lastly, the simulation of cross-media showers is presented, highlighting a feature that is exclusive to CORSIKA 8.

The first three sections of this chapter update and expand the results of the analyses presented by the author of this work in [\[27\]](#) and [\[194\]](#).

¹Details about the version of CORSIKA 8 used to create the results of this work are given in [Appendix B](#).

²For the results presented in this work, version 7.7500 is used.

7.1 Comparison of the Utilized Cross Sections

Before a reasonable comparison of air shower simulations between CORSIKA 7 and CORSIKA 8 is possible, a comparison of the underlying electromagnetic cross sections is necessary. The implementation of electromagnetic processes in PROPOSAL is described in Chapter 6, while the processes in EGS4 and the corresponding adaptations for CORSIKA 7 are described in Section 5.1.1. Note that the cross sections presented in this section exclude the LPM effect.

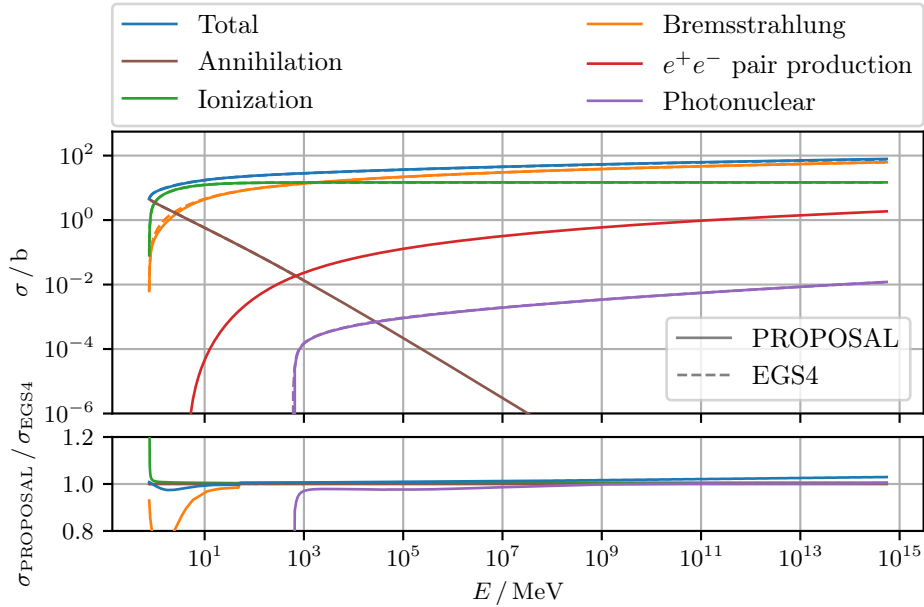


Figure 7.1: Comparison of the utilized positron cross sections from PROPOSAL, which are used in CORSIKA 8, with the adapted cross sections from EGS4, which are used in CORSIKA 7 [178]. The cross sections are presented for air at standard density. The photonuclear cross section from EGS4 is corrected according to [178].

Figure 7.1 shows the cross sections of positron interactions, where the energy cut is set to $E_{\text{cut}} = 250 \text{ keV}$. Notably, the agreement of the total cross section is better than 3%, although a better agreement is reached for most energies. The largest deviation at low energies stems from the bremsstrahlung cross section below 50 MeV, possibly caused by undocumented differences in the CORSIKA 7 implementation for the low-energy regime. For high energies, the total cross section for PROPOSAL is higher due to the additional contribution from electron-positron pair production, a process not implemented in EGS4. The comparison of the electron cross sections is presented in Figure A.3, and shows, as expected, similar results.

In Figure 7.2, the cross sections of photon interactions are shown. Note that the total photon cross section agrees on a sub-percent for all energies. At low energies, deviations are visible in the cross section of the photoeffect, which is expected since the implementation in PROPOSAL only provides an approximate treatment compared to the description in EGS4, as described in Section 6.2.3. Still, at energies where the photoeffect provides a significant contribution, the agreement is better than $\approx 8\%$. For the cross section of photohadronic interactions, differences in the implementation of the resonances, see Section 6.2.5, cause deviations of up to $\approx 15\%$ at energies around 1 GeV. Lastly, the muon pair production cross section of PROPOSAL is increased by $\approx 20\%$ compared to the implementation in CORSIKA 7. This difference can be attributed to the contribution from atomic electrons, taken into account by the substitution in (6.84), but not considered by CORSIKA 7. However, since muon pair production is subdominant, also compared to photoproduction as the second process that can indirectly induce muons from photon interactions, this difference can be neglected for the shower development.

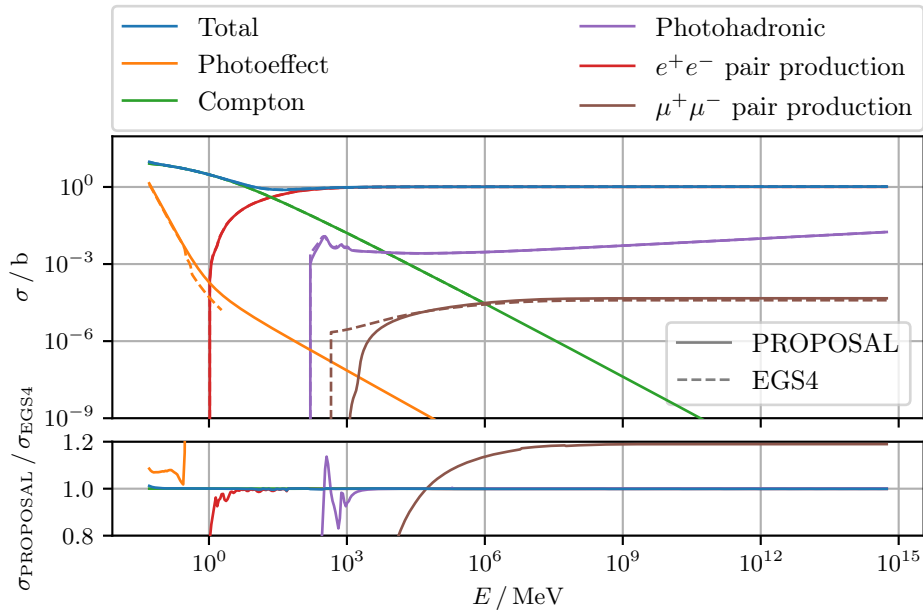


Figure 7.2: Comparison of the utilized photon cross sections from PROPOSAL, which are used in CORSIKA 8, with the adapted cross sections from EGS4, which are used in CORSIKA 7 [178]. The cross sections are presented for air at standard density.

7.2 Comparison of Electromagnetic Showers

To allow for a meaningful comparison between CORSIKA 7 and CORSIKA 8, an identical setup of the simulation environment is used, whenever possible. For all shower simulations, if not stated otherwise, this setup is defined as follows: The density of the atmosphere is described in both CORSIKA 7 and CORSIKA 8 by a five-layer parametrization of the U.S. Standard Atmosphere [216], as described in detail in [Appendix A.11](#). It consists of nitrogen, oxygen, and argon, with fractions of 78.084%, 20.946%, and 0.934%, as defined by the number of molecules. In CORSIKA 8, the Earth is described as a sphere with radius $r = 6371$ km, while in CORSIKA 7, the Earth's curvature is taken into account by using the compiler option *CURVED* [110], albeit a significant difference to approximating the Earth's surface and its atmosphere as flat is only expected for non-vertical showers with a zenith angle above $\approx 70^\circ$ [114]. The Earth's magnetic field is assumed to be constant, with a horizontal component of $50 \mu\text{T}$ and no vertical component.

As hadronic interaction models, both CORSIKA 7 and CORSIKA 8 use SIBYLL 2.3d [185] as the high-energy interaction model, and FLUKA 2023.3.0 [64, 94] as the low-energy interaction model, with the energy threshold between the models set to 80 GeV for CORSIKA 7 and $10^{1.9} \text{ GeV} \approx 79.4 \text{ GeV}$ for CORSIKA 8. As an electromagnetic interaction model, CORSIKA 7 uses EGS4, as described in [Section 5.1.1](#), using the default settings. In CORSIKA 8, particle decays are described with PYTHIA 8.310 [62], while CORSIKA 7 uses an internal decay routine, taking into account all decay modes with a branching ratio above 1% [113].

All simulated showers are vertical, i.e., the primary particles are injected on top of the atmosphere with a zenith angle of 0° . Furthermore, no thinning techniques are applied.³

7.2.1 Simulation of 100 TeV Photon-Induced Showers

In this section, electromagnetic showers induced by photons with an initial energy of 100 TeV are simulated. The *ParticleCut* is set to $E_{\text{track}}^{\text{EM}} = 20 \text{ MeV}$ for electromagnetic particles, and $E_{\text{track}}^{\text{had.}} = E_{\text{track}}^{\mu} = 500 \text{ MeV}$ for hadrons and muons, i.e., particles with kinetic energies smaller than the corresponding *ParticleCut* are no longer tracked. This choice of $E_{\text{track}}^{\text{EM}}$ is motivated by the application in [Imaging Air Cherenkov](#)

³Thinning describes a runtime-reducing technique where, below a given relative energy threshold, only a random subset of produced shower particles is simulated, while the rest is discarded. The discarded particles are taken into account by assigning a higher weight to the particles that are simulated. The idea of thinning has been proposed in [117], where the details of the concept are explained as well.

Telescopes (IACTs), as electrons and positrons require energies of $E_{\text{tot}} \gtrsim 20$ MeV to produce Cherenkov light in air, see Section 3.3.1, meaning that particles with smaller energies are irrelevant for the experimental setup. To obtain sufficient statistical significance, a set of 10 000 showers is simulated for both CORSIKA 7 and CORSIKA 8.

A key feature to describe the longitudinal shower development is the shower profile. Along the shower axis⁴, the atmosphere is divided into layers including an equal, fixed amount of grammage X (here: 10 g/cm^2). For each layer, the number of crossing particles is counted, yielding a longitudinal shower profile. With this definition, $X = 0 \text{ g/cm}^2$ corresponds to the top of the atmosphere, whereas $X \approx 1030 \text{ g/cm}^2$ corresponds to the Earth's surface. The relation between grammage X and height h for the U.S. standard atmosphere is visualized in Figure A.4.

Figure 7.3 shows the longitudinal profile of electromagnetic particles for the simulated showers. Both the profiles of charged particles and photons show a good agreement of better than 5%. A small shift of the longitudinal profile of CORSIKA 7 toward larger X indicates a slightly delayed shower development compared to CORSIKA 8.

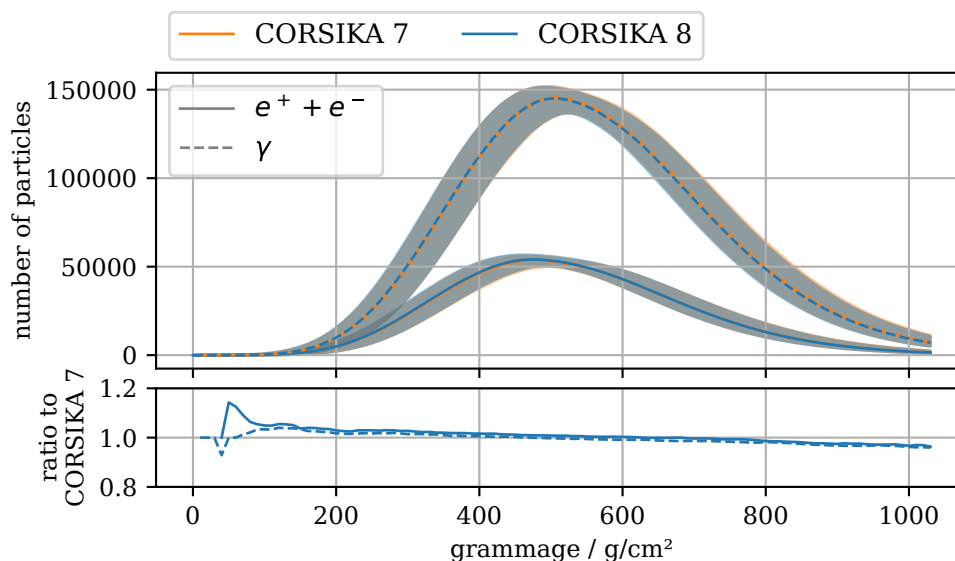


Figure 7.3: Longitudinal profile of electromagnetic particles for showers initiated by 100 TeV photons. In the upper part of the Figure, the lines indicate the median number of particles, while the shaded areas indicate the interquartile range. The lower part of the Figure shows the ratio between the median number of particles.

⁴The shower axis describes the imaginary line defined by the direction of the initial shower particle.

Figure 7.4 shows the distribution of the shower maximum X_{\max} , where X_{\max} is defined here as the location of the bin in the longitudinal profile with the highest number of particles of the corresponding particle type. The distributions show a good agreement, with both CORSIKA 7 and CORSIKA 8 simulations including a similar number of showers developing at a different speed, and therefore yielding a significantly lower or higher value of X_{\max} . The slightly slower shower development of CORSIKA 7, already identified by eye in Figure 7.3, can be quantified to a difference of $\Delta X_{\max} \approx 2 \text{ g/cm}^2$, smaller than the X_{\max} sensitivity achieved in experimental observations [13, 101].

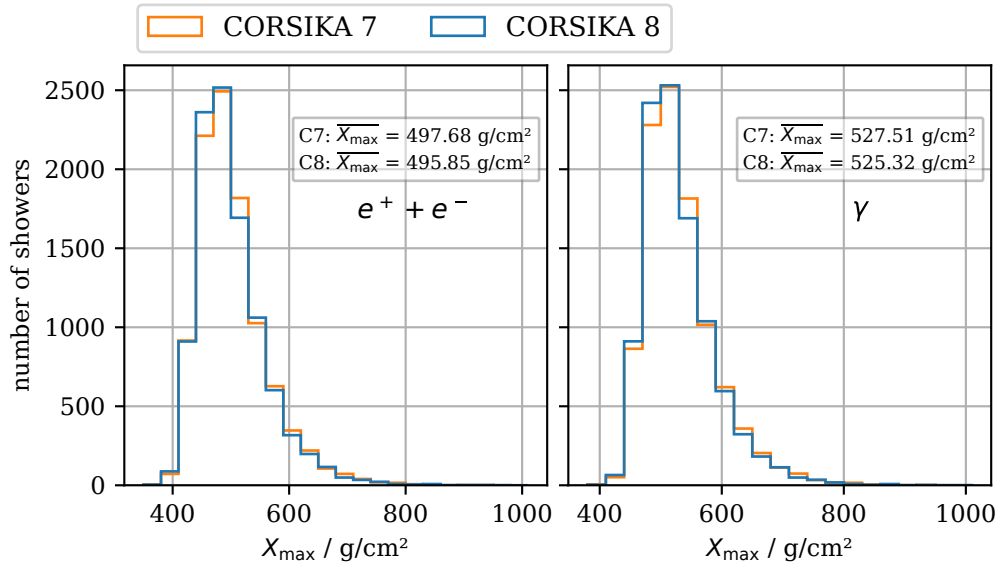


Figure 7.4: Distribution and mean of X_{\max} for electromagnetic showers initiated by 100 TeV photons.

Another measure to validate the variance of the shower development is the analysis of individual bin contents of the longitudinal profile, i.e., the distribution of the number of particles observed for a fixed height. The result of this analysis for the charged electromagnetic component is shown in Figure 7.5, indicating a good agreement regarding the variances of the simulations.

While the most significant development of the shower occurs in the longitudinal direction, multiple scattering, production angles, and magnetic fields also induce a lateral shower development. As a validation of these processes, particle positions on a fictional observation plane at $h = 5800 \text{ m}$, corresponding to the approximate height of the average shower maximum, are depicted as a lateral profile according

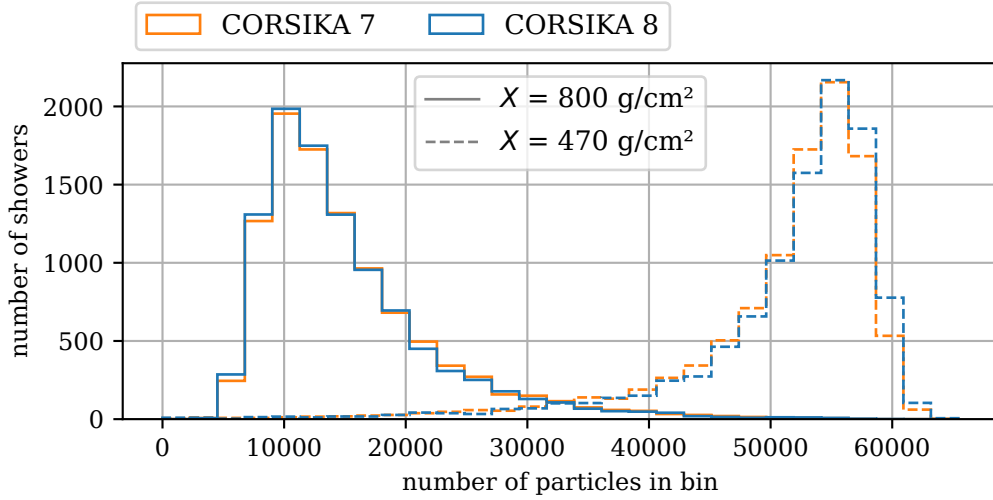


Figure 7.5: Distribution of the number of electrons and positrons for a given longitudinal bin, i.e., at a fixed height, for a statistic of 10 000 showers initiated by 100 TeV photons. The distribution is shown for two exemplary bins at $X = 470 \text{ g/cm}^2$ (around X_{max} , corresponding to $h \approx 6.2 \text{ km}$) and $X = 800 \text{ g/cm}^2$ (later in the shower development, corresponding to $h \approx 2.1 \text{ km}$).

to their distance r from the shower axis in Figure 7.6. This comparison indicates a good agreement between CORSIKA 7 and CORSIKA 8 within 3% for photons with $r \lesssim 500 \text{ m}$, while CORSIKA 7 produces more photons with larger distances from the shower axis. For electrons and positrons, particles in CORSIKA 8 are systematically located closer to the shower axis, albeit the lateral distribution still follows a similar behavior compared to CORSIKA 7, with an agreement better than 15% for $1 \text{ m} \lesssim r \lesssim 700 \text{ m}$. Additionally, the energy distribution of particles located on the observation plane at $h = 5800 \text{ m}$ is evaluated in Figure 7.7. An agreement better than 3% is visible for all electromagnetic particles, up to energies of 1 GeV, above which statistics start to become limited. The correlation between the lateral and energy distribution is visualized in Figure 7.8 with a two-dimensional histogram showing the energy of all charged electromagnetic particles and their distance to the shower axis. Qualitatively, the two-dimensional distributions of CORSIKA 7 and CORSIKA 8 show a similar behavior. A quantitative comparison is possible by analyzing the ratio of the bin contents, which is shown in Figure 7.9. It can be concluded that the shift of electrons and positrons in CORSIKA 8 toward the shower axis, as already shown in Figure 7.6, is visible for all particles with an energy $E < 1 \text{ GeV}$.

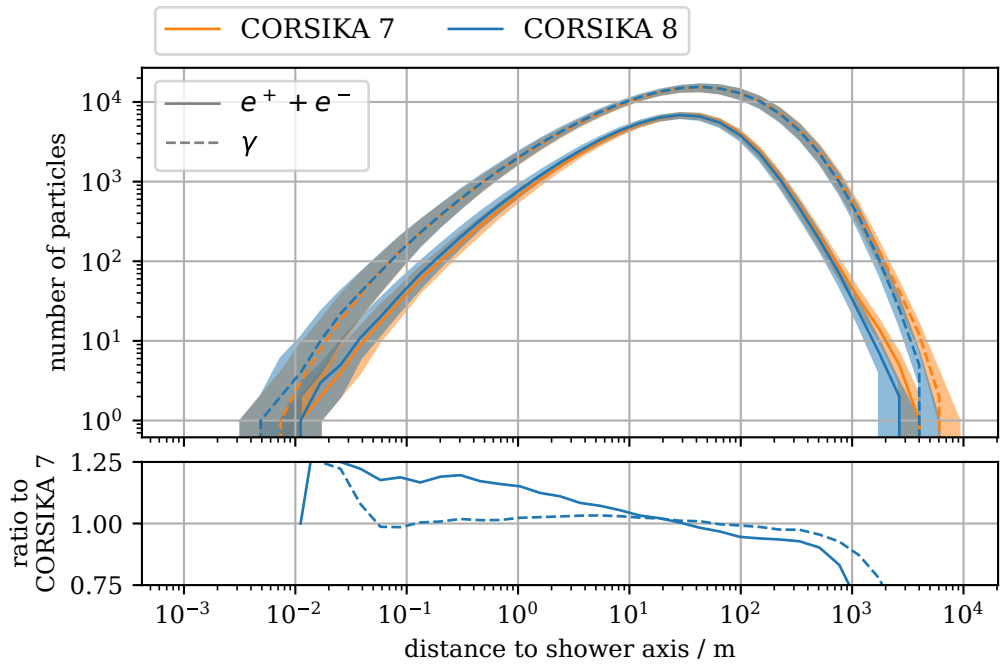


Figure 7.6: Lateral profile of electromagnetic particles for showers initiated by 100 TeV photons. The lines indicate the median number of particles, the shaded regions the *interquartile range*. The lateral profile is evaluated for an observation height of $h = 5800$ m, corresponding to $X \approx 497 \text{ g/cm}^2$, i.e., approximately X_{max} for the charged electromagnetic component of the given photon-induced showers.

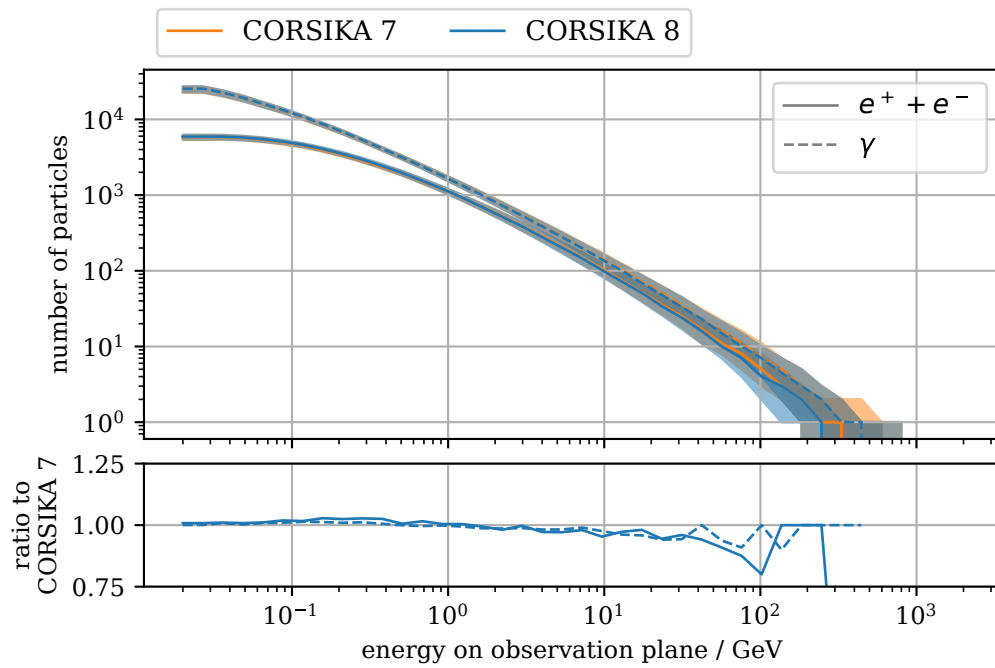


Figure 7.7: Kinetic energy distribution for electromagnetic particles on an observation level at $h = 5800$ m, for showers initiated by 100 TeV photons. The lines indicate the median number of particles, the shaded regions the interquartile range.

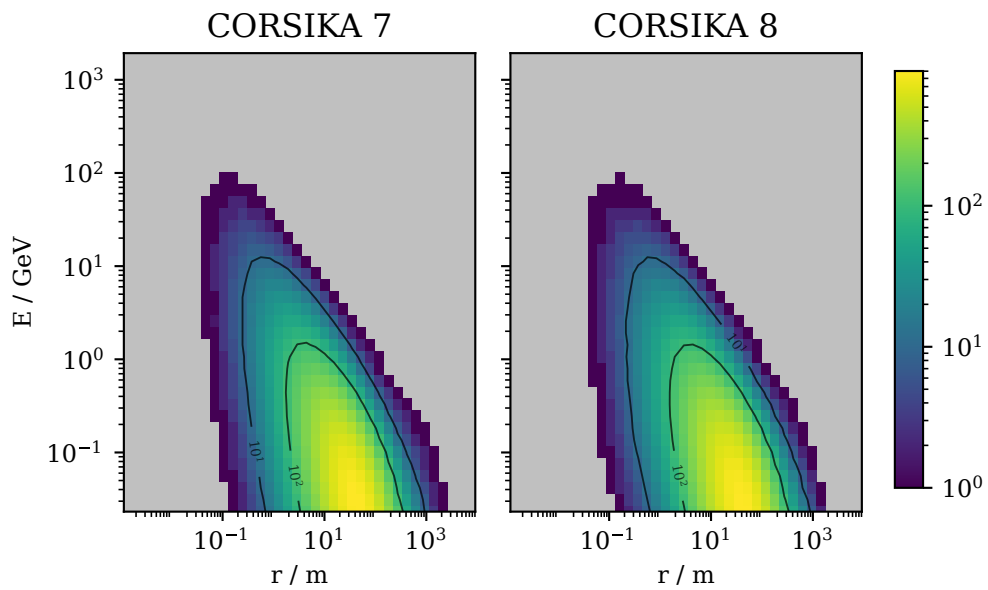


Figure 7.8: Two-dimensional histogram, showing the distance r of electrons and positrons from the shower axis, and their kinetic energy E . The distribution shows particles on an observation level at $h = 5800$ m from showers initiated by 100 TeV photons. The colorbar indicates the number of particles in the bin, the black lines illustrate the contour of the distribution.

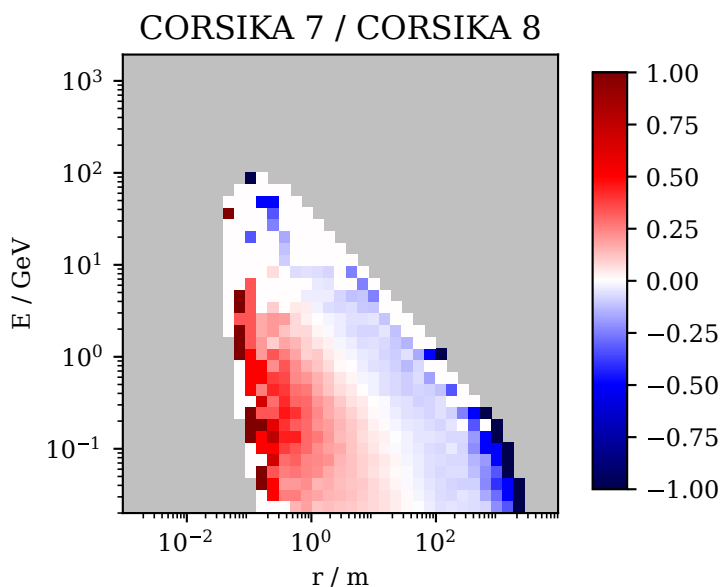


Figure 7.9: Ratio of the bin contents from the two-dimensional histogram in Figure 7.8, illustrating the correlation between the lateral spread r and kinetic particle energy E .

Differences in the algorithmic description of multiple scattering, which itself is a complex task as described in Section 6.1.6, may be responsible for the deviation in the lateral profiles between CORSIKA 7 and CORSIKA 8. In this context, further investigations are necessary to pin down the reasons for the observed differences.

7.2.2 Validating the Implementation of the LPM Effect

The LPM effect, as described in detail in Section 6.3, causes a suppression of bremsstrahlung losses with a small energy transfer, as well as a suppression of symmetric pair production interactions, i.e, events with an equal energy distribution between the produced electron-positron pair. The LPM effect is both density-dependent, being more effective for dense media, and energy-dependent, being more effective for higher particle energies. To validate the implementation of the LPM effect in CORSIKA 8, two sets of shower simulations are created: Once with the LPM suppression enabled, and once with the LPM suppression disabled, while all other simulation parameters stay identical. For CORSIKA 7, the LPM effect is disabled by deselecting the compiler option *LPM*, while for CORSIKA 8, the method `CheckForLPM()`, as described in Section 5.3.3, is enforced to always return

False, which deactivates the LPM effect. Since the Earth’s atmosphere has a low density, especially for high altitudes, very high particle energies are required for the LPM effect to be effective. Therefore, to produce a simulation set that allows for a clear comparison of the LPM effect, 5000 showers induced by photons with an initial energy of 100 EeV are simulated. To limit the runtime required to perform the simulations, the *ParticleCut* is set to $E_{\text{track}}^{\text{EM}} = E_{\text{track}}^{\text{had.}} = E_{\text{track}}^{\mu} = 100$ TeV. These settings are sufficient for validation purposes since the LPM effect is not relevant for shower particles of lower energies. Figure 7.10 shows the resulting longitudinal profiles. The expected effects of the LPM suppression are clearly visible, causing a delayed longitudinal shower development with increased fluctuations. Both observations are consistent with the expectations outlined in Section 6.3.2. The quantitative comparison between CORSIKA 7 and CORSIKA 8 shows an agreement better than 5% for the showers without the LPM effect, and an agreement within 10% for showers with the LPM effect. In Appendix A.12, the analysis is repeated for simulations of proton-induced showers, yielding a similar level of agreement.

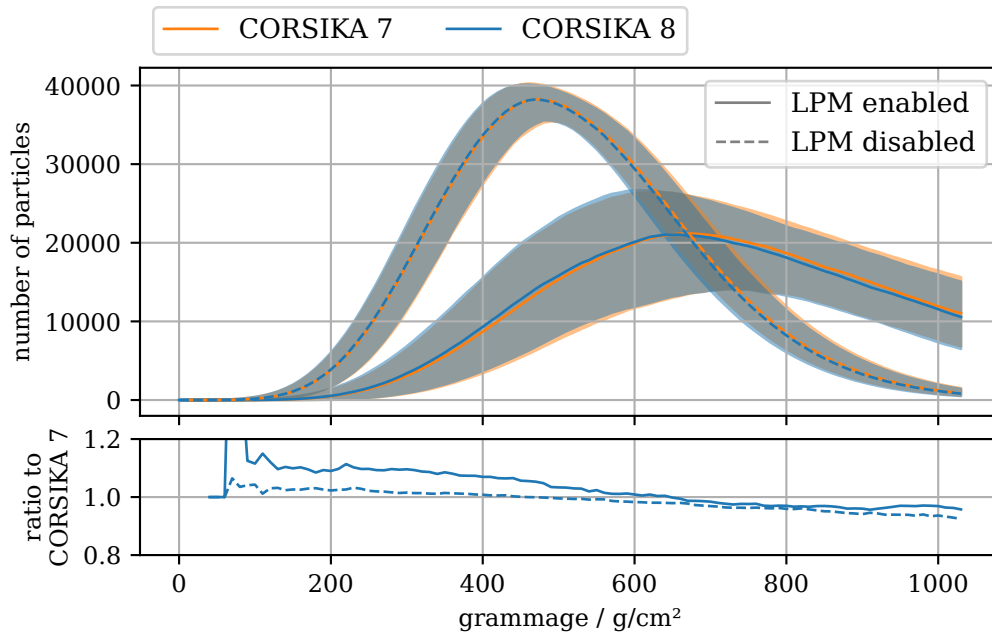


Figure 7.10: Longitudinal profiles of electrons and positrons for showers initiated by 100 EeV photons, for both simulations with and without considering the LPM effect. The lines indicate the median number of particles, the shaded regions the interquartile range.

7.2.3 Influence of Physics Descriptions on the Lateral Particle Distribution

To investigate the influence of different physics descriptions on the lateral shower development, the simulation of 100 TeV photon-induced showers is repeated multiple times, where one relevant setting is adapted for each simulation set. The results, showing the lateral profile of charged electromagnetic particles for an observation height of $h = 5800$ m, are given in Figure 7.11. The simulations with

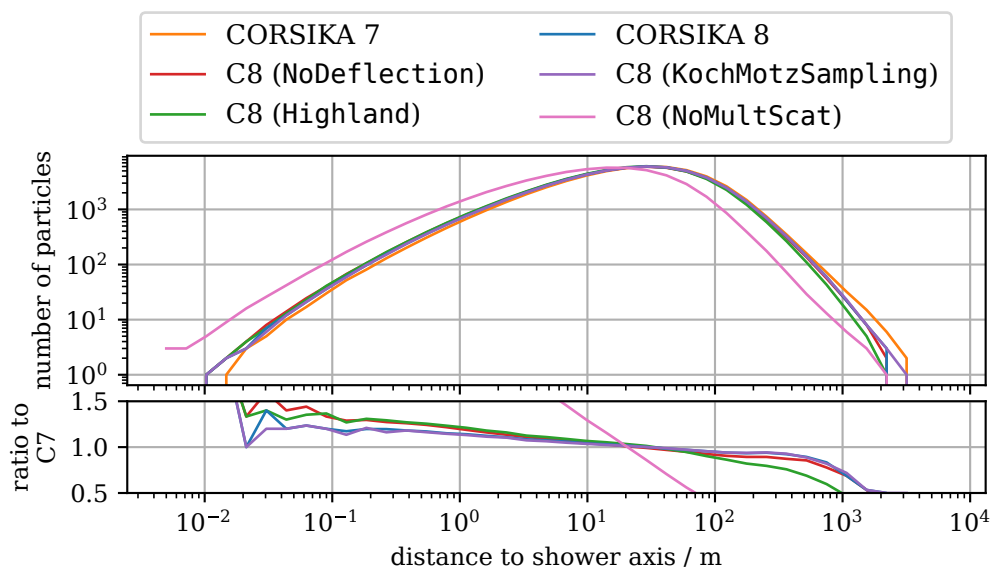


Figure 7.11: Lateral profile of charged electromagnetic particles for different physics descriptions relevant for the lateral shower development, as explained in the text. Simulated are 100 TeV photon-induced showers, the observation plane is set to 5800 m.

the labels “CORSIKA 7” and “CORSIKA 8” represent the baseline simulations using the same settings as the results in Figure 7.6, meaning for “CORSIKA 8” that `MoliereInterpol` is used as a parametrization of multiple scattering (see Section 6.1.6), and `EGS4Approximation` to parametrize the angular distribution of bremsstrahlung photons (see Section 6.1.1). For the simulation labeled “C8 (Highland)”, the multiple scattering model is replaced by the `HighlandIntegral` parametrization, while all other settings remain identical. This causes a small lateral shift of particles toward the shower axis, compared to the baseline “CORSIKA 8” simulation, which is expected as the underlying distribution of the `HighlandIntegral` parametrization does not extend to large scattering angles, as shown in Figure 6.5.

For the simulation labeled “C8 (KochMotzSampling)”, the `EGS4Approximation` parametrization is replaced by `KochMotzSampling`, which provides a more sophisticated description of the bremsstrahlung photon distribution, as shown in [Figure 6.2](#). In this case, no significant effect on the lateral particle profile is visible, confirming that the simple `EGS4Approximation` model provides a sufficient description, at least for the investigated simulation settings. Next, for the simulation labeled “C8 (NoDeflection)”, all secondary particles produced in electromagnetic interactions inherit the direction of the initial particle, which itself also remains undeflected. For particles with $r \lesssim 10$ m, a shift toward the shower axis is visible, similar to the results of “C8 (Highland)”, while for $r \gtrsim 10$ m, the influence on the lateral profile is smaller. Lastly, for the simulation labeled “C8 (NoMultScat)”, multiple scattering effects are entirely disabled, leading to the most significant deviation from the baseline simulation.

This analysis confirms that both the description of deflection angles in particle interactions, as well as the description of multiple scattering, influence the lateral shower development, where the latter has the most significant impact.

7.2.4 Muonic and Hadronic Component in Electromagnetic Showers

Particles from the muonic and hadronic component in a particle cascade feed the electromagnetic component via particle decays and energy losses, as explained in [Chapter 3](#). However, processes within the electromagnetic component are also able to transfer energy back to the hadronic and muonic component: Photonuclear interactions of electrons, positrons, and photons can produce hadrons (see [Section 6.1.5](#) and [Section 6.2.5](#)), which in turn can decay into muons, while muon pair production directly produces muons (see [Section 6.2.4](#)). Albeit this contribution to the muon and hadron number in hadron-induced showers is subdominant, it can be significant, as will be demonstrated in [Section 7.3](#). Therefore, a correct modeling of these processes is important.

As a validation of muon and hadron inducing processes in electromagnetic showers within CORSIKA 8, photon-induced showers with a primary energy of 10 PeV are simulated, using a statistic of 1000 showers and a `ParticleCut` of $E_{\text{track}}^{\text{EM}} = E_{\text{track}}^{\text{had}} = E_{\text{track}}^{\mu} = 0.5$ GeV. The primary energy and `ParticleCut` are set to relatively high energies for this validation as the relevant interactions only have a non-zero cross section for energies above the GeV energy regime, as shown in [Section 7.1](#). [Figure 7.12](#) shows the resulting longitudinal profiles for the muonic and hadronic component. Compared to other longitudinal profiles, the profile of muons behaves differently: Muons cover larger distances because they have a small energy loss, e.g., compared to electromagnetic particles, and a relatively high lifetime, e.g., compared

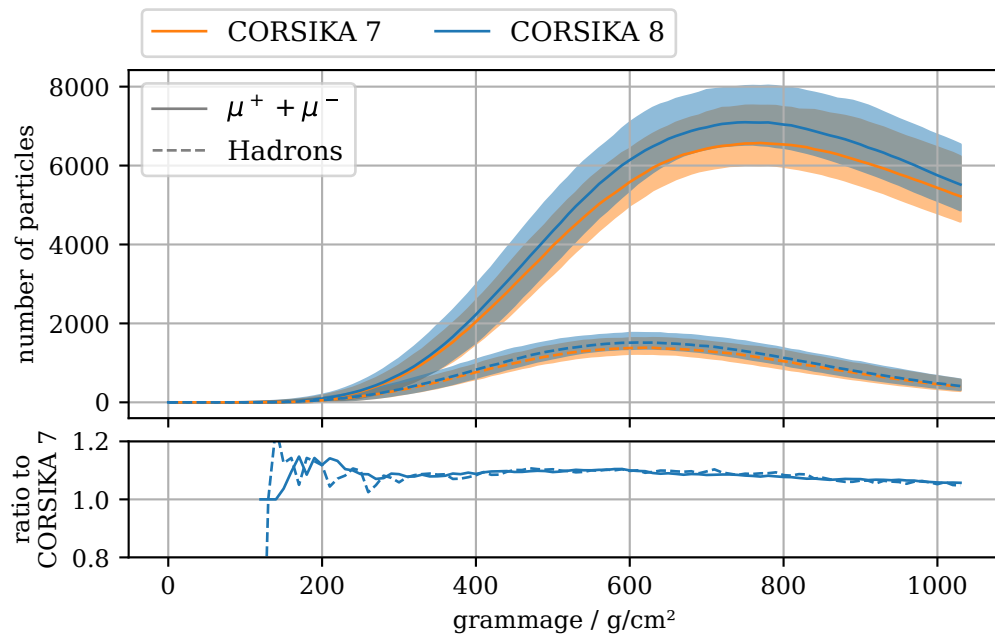


Figure 7.12: Longitudinal profiles of muons and hadrons for showers initiated by 10 PeV photons. The lines indicate the median number of particles, the shaded regions the interquartile range.

to most hadronic particles. Therefore, the right tail of the longitudinal profile decreases slower in comparison to other particle types, as, for example, visible in [Figure 7.3](#). The comparison shows that for CORSIKA 8 simulations, both the number of muons and hadrons is increased by up to 10% for the entire shower development.

From [Figure 7.13](#), which shows the corresponding energy distribution of muons on the Earth's surface, it is visible that the produced muons in CORSIKA 8 are on average less energetic compared to CORSIKA 7, while the total energy ΣE of all muons on the surface is comparable. This explains that the deficit of the muon number in the longitudinal profile in [Figure 7.12](#) is caused by a different distribution of the available energy among all muons. These deviations can be attributed to the different treatments of the production of hadronic secondaries from electromagnetic particles used in CORSIKA 7 and CORSIKA 8, as described in [Section 6.2.5](#).

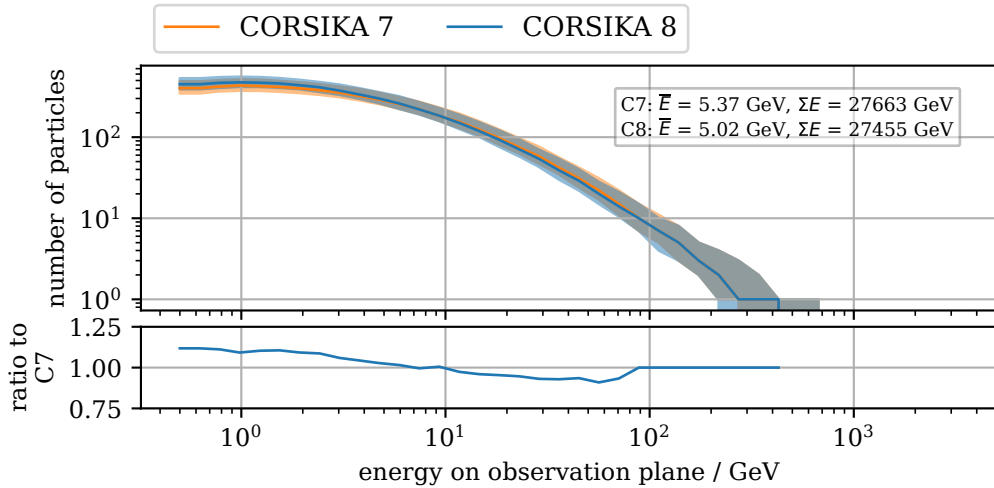


Figure 7.13: Energy distribution of muons on the Earth's surface, for showers initiated by 10 PeV photons. The lines indicate the median number of particles, the shaded regions the *interquartile range*. \bar{E} indicates the mean muon energy, ΣE the sum of the energy distribution.

[Figure 7.14](#) shows the distribution of the shower maximum X_{\max} for muons and hadrons, revealing an overall good agreement. The average value of X_{\max} is slightly lower in CORSIKA 8 compared to CORSIKA 7, showing that the shower development of CORSIKA 7 is slower, a behavior which is consistent with the observation for the electromagnetic component in [Figure 7.4](#).

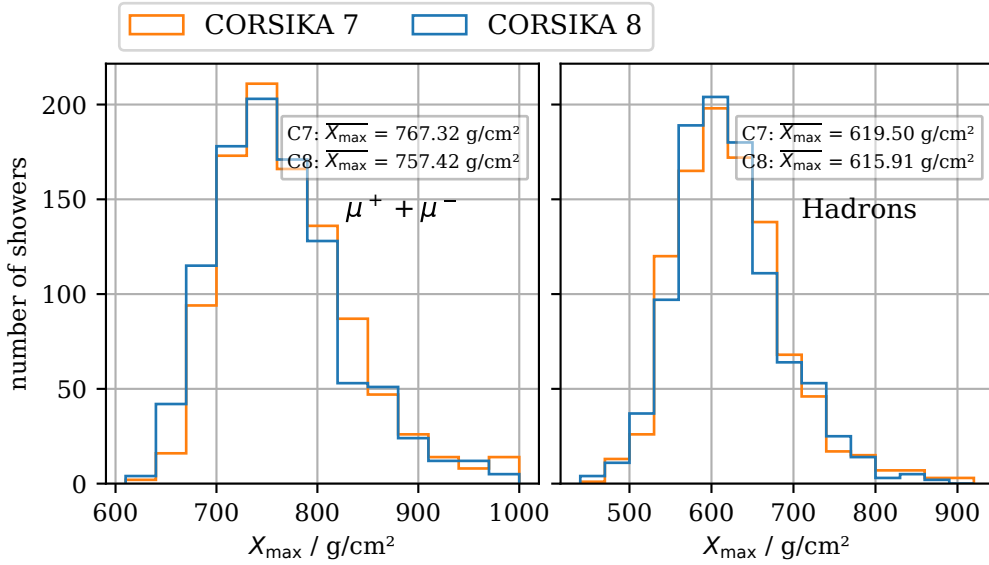


Figure 7.14: Distribution and mean of X_{\max} of the hadronic and muonic component, for showers initiated by 10 PeV photons.

The occurrences of the different particle types on the ground are illustrated in [Figure 7.15](#), revealing more information about the hadron content. The largest deviation is visible for the number of neutrons, where approximately 25% more neutrons are produced in CORSIKA 8, with a better agreement for all other particle types. To understand the origin of the induced muon content in CORSIKA 8, [Figure 7.16](#) shows the distribution of the particle types that have produced the muons observed on ground, where the producing particle is defined as the “parent particle”. This information is extracted by following the cascade history of a given muon, and identifying the particle type of the first particle in the history that is not a muon. Note that this direct access to the entire particle cascade history is a dedicated feature of CORSIKA 8. While an analysis of the cascade history with CORSIKA 7 is possible via the *EHISTORY* option, this approach poses several technical restrictions, for example, the limitation that only two parent generations are stored [111]. Furthermore, in several cases, CORSIKA 7 does not store the immediate parent particle, making a comparison with the CORSIKA 8 results in [Figure 7.16](#) infeasible [172]. As expected, most muons are produced by pions ($\approx 94\%$) and kaons ($\approx 4.7\%$), while only $\approx 0.2\%$ of the muons directly originate from photons, and therefore muon pair production. This highlights that for electromagnetic showers with the given properties, hadronic interactions are the dominant source of muons, with a subdominant contribution from muon pair production.

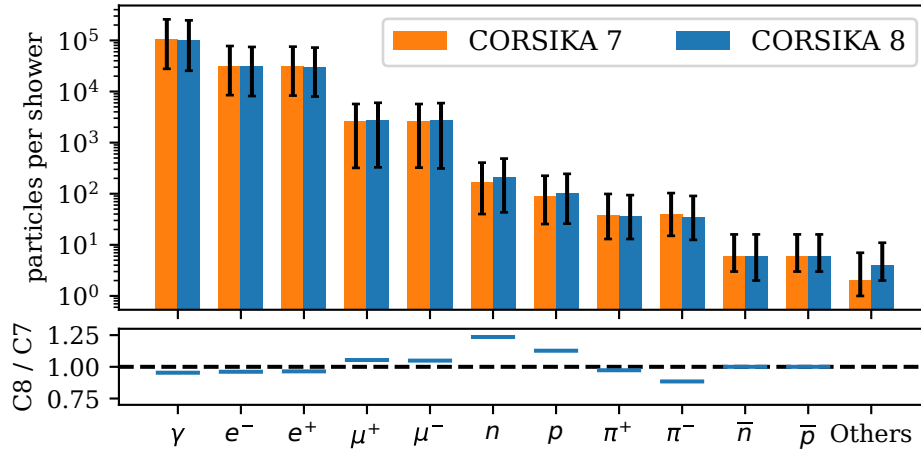


Figure 7.15: Distribution of particle types observed on the Earth’s surface for showers initiated by 10 PeV photons. The bars indicate the median number of particles observed per shower, while the corresponding error bars indicate the interquartile range, representing the variation of the particle number.

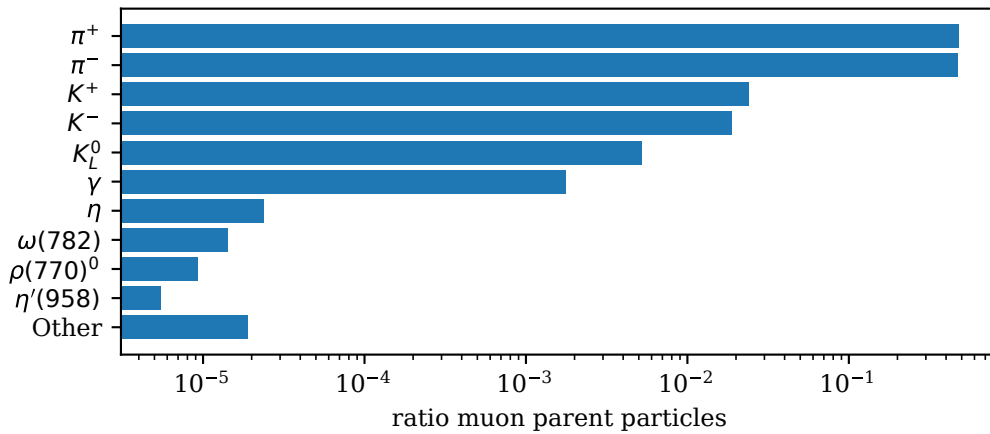


Figure 7.16: Distribution of particle types that have produced the muons observed on ground, for showers initiated by 10 PeV photons.

7.3 Comparison of Hadronic Showers

As the focus of this work is the description of the electromagnetic and muonic shower component in CORSIKA 8, a detailed analysis of the hadronic shower component is omitted. Instead, this section focuses on muons and electromagnetic particles within hadron-induced showers, as well as the feedback from the electromagnetic component back to the hadronic component. Furthermore, in the context of the muon puzzle, see Section 3.4, a significant deficit of muons in hadronic air shower simulations compared to experimental measurements is observed. As most of the underlying simulations have been created with CORSIKA 7, validating the muon number in hadronic showers indicates whether the improvements coming with CORSIKA 8, especially the improved description of muon interactions implemented with this work, have an impact on the muon deficit.

Therefore, this section shows the simulation of air showers induced by protons with a primary energy of 500 PeV. The *ParticleCut* is set to $E_{\text{track}}^{\text{EM}} = E_{\text{track}}^{\text{had.}} = E_{\text{track}}^{\mu} = 1 \text{ GeV}$, and a statistic of 2000 showers is simulated. The corresponding longitudinal profiles for muons and hadrons are shown in Figure 7.17, and for electromagnetic particles in Figure 7.18. For the electromagnetic shower component, the agreement

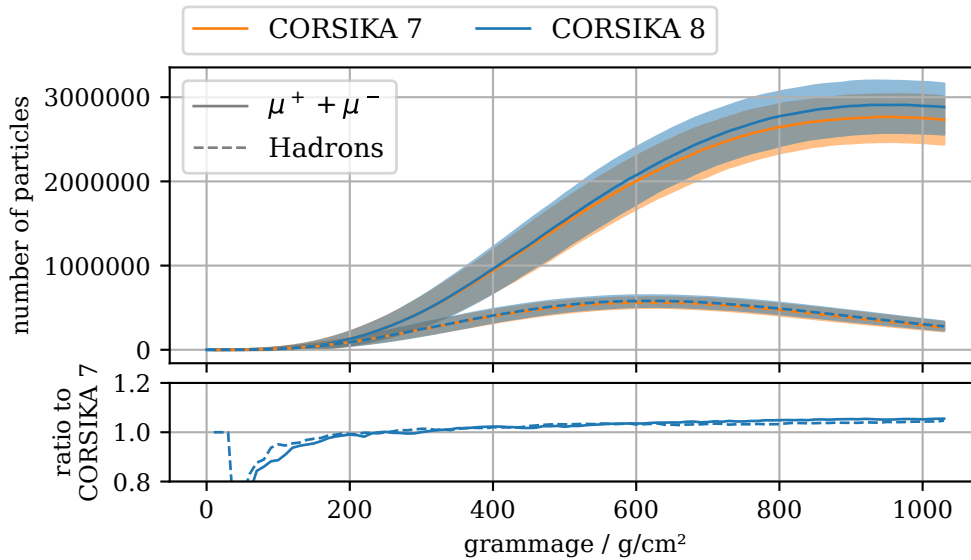


Figure 7.17: Longitudinal profiles of muons and hadrons for showers initiated by 500 PeV protons. The lines indicate the median number of particles, the shaded regions the interquartile range.

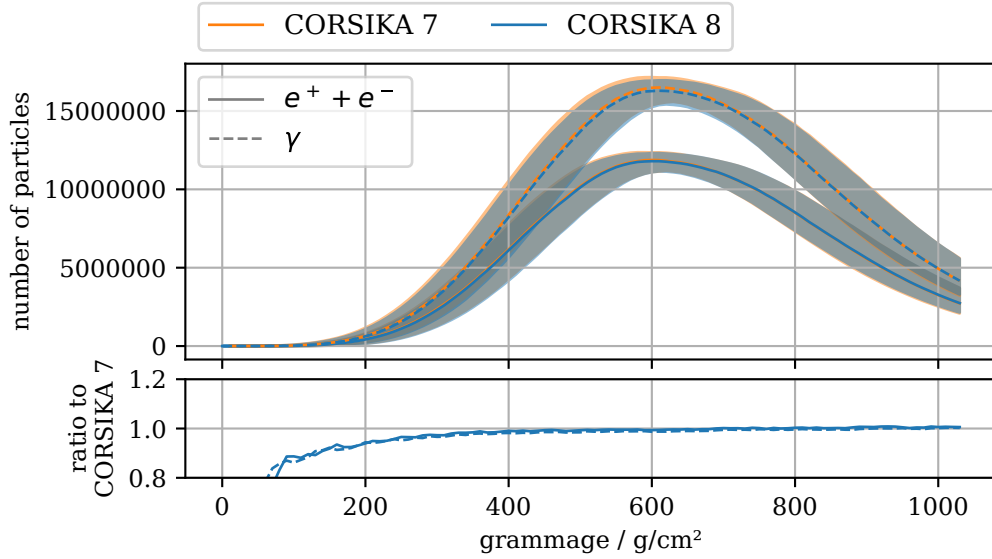


Figure 7.18: Longitudinal profiles of electromagnetic particles for showers initiated by 500 PeV protons. The lines indicate the median number of particles, the shaded regions the interquartile range.

between CORSIKA 7 and CORSIKA 8 is better than 2% for large parts of the shower development, and the agreement in muons and hadrons is better than 5%. Notably, the number of muons and hadrons develops a slight excess as the shower comes closer to Earth.

The energy distribution of the muons observed on the Earth’s surface is illustrated in Figure 7.19, revealing that the excess of muons is caused by particles with energies smaller than ≈ 50 GeV. While this causes the average muon energy \bar{E} to be smaller compared to CORSIKA 7, the total muon energy ΣE is still increased for CORSIKA 8 simulations. The corresponding lateral distribution of muons is visualized in Figure 7.20, where an agreement within 5% is visible. The distribution of X_{\max} for the muonic and hadronic component, which is visualized in Figure 7.21, agrees well, with a difference in $\overline{X_{\max}}$ of ≈ 5 g/cm².

Overall, the simulation of the muonic component in hadronic showers shows a good agreement between CORSIKA 7 and CORSIKA 8. Albeit a $\approx 5\%$ increase of muons on the Earth’s surface compared to CORSIKA 7 simulations is visible, this increase is not sufficient to explain the muon puzzle, where an excess in the muon number of $\approx 25\%$ for the given particle energy is observed [34]. Furthermore, the difference between CORSIKA 7 and CORSIKA 8 is smaller than the experimental uncertainty

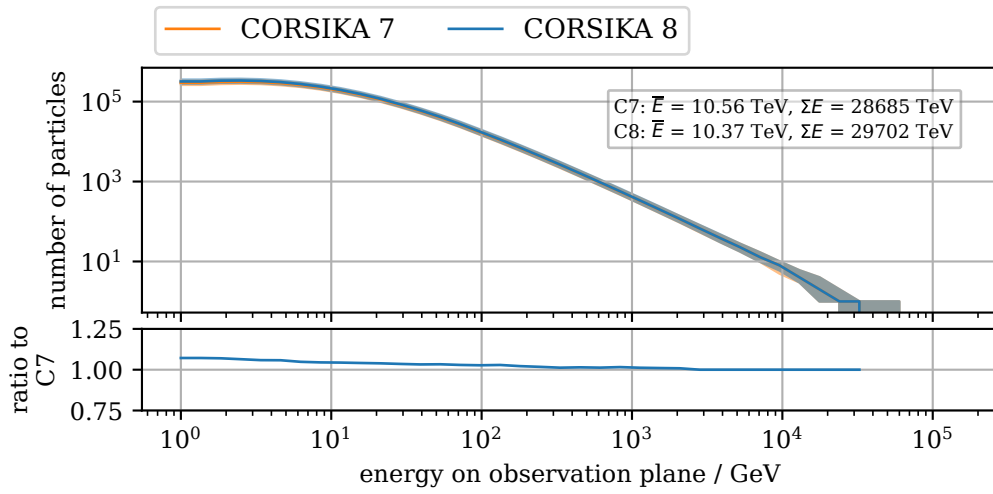


Figure 7.19: Energy distribution of muons on the Earth's surface, for showers initiated by 500 PeV protons. The lines indicate the median number of particles, the shaded regions the *interquartile range*. \bar{E} indicates the mean muon energy, ΣE the sum of the energy distribution.

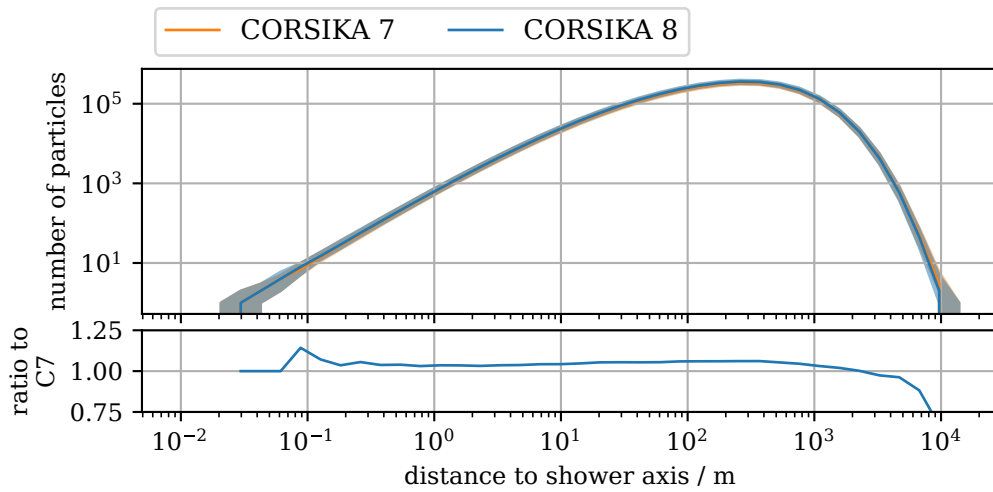


Figure 7.20: Lateral profile of muons on the Earth's surface, for showers initiated by 500 PeV protons. The lines indicate the median number of particles, the shaded regions the *interquartile range*.

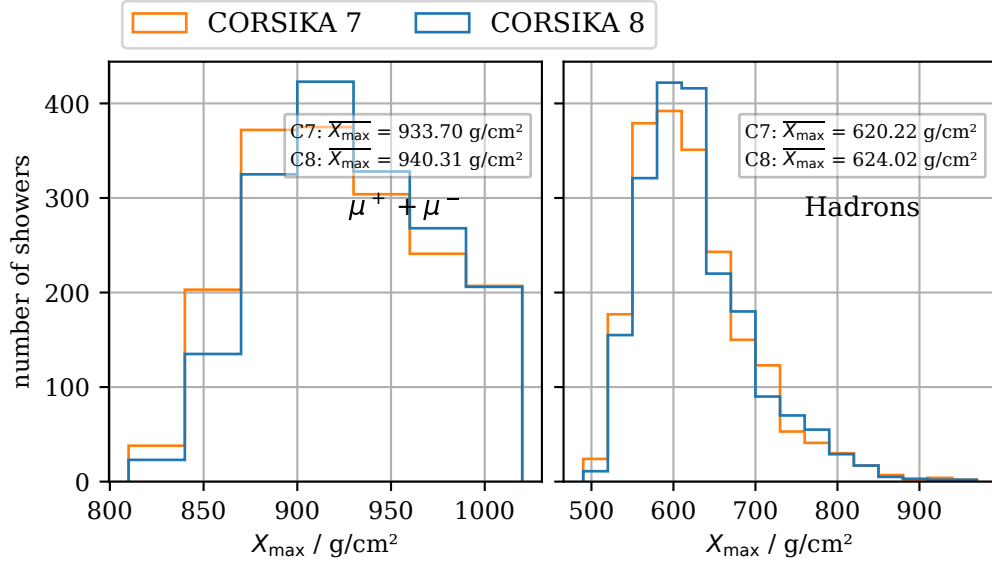


Figure 7.21: Distribution and mean of X_{\max} of the hadronic and muonic component, for showers initiated by 500 PeV protons.

for the determination of the muon number, which is on the level of $\approx 10\%$ [34]. Note that the percentage increase of simulated muons in CORSIKA 8 will vary depending on the given conditions. Therefore, it needs to be determined explicitly for each experiment by taking into account the experimental setup, energy thresholds, and a realistic cosmic ray spectrum.

For hadron-induced showers, a differentiation between particles originating from the electromagnetic component, or originating exclusively from the hadronic component, can be made. For muons and hadrons, the first case means that the particle history includes a first transition from the hadronic component, induced by the primary hadron, to the electromagnetic shower component, followed by a second transition from the electromagnetic component back to the hadronic or muonic shower component. In this context, these muons and hadrons are defined to be of electromagnetic origin. With the possibility to access the entire cascade history in CORSIKA 8, a given particle is attributed an electromagnetic origin when its cascade history includes any electromagnetic particle, as visualized in Figure 7.22. By determining this property for all particles observed on the ground, the total ratio of muons and hadrons with an electromagnetic origin is determined for each particle shower. For the given proton-induced 500 PeV showers, the distribution of this ratio is visualized in Figure 7.23. On average, $\approx 7\%$ of the muons and $\approx 6\%$ of the hadrons originate from the electromagnetic component. Notably, in a small

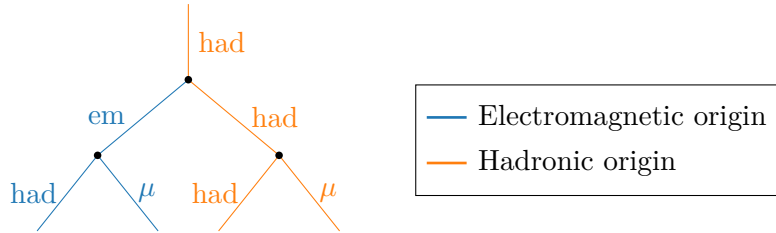


Figure 7.22: Visualization of the differentiation between electromagnetic origin and hadronic origin for a cascade particle. The label “em” or “had” stands for an arbitrary electromagnetic, respectively hadronic particle.

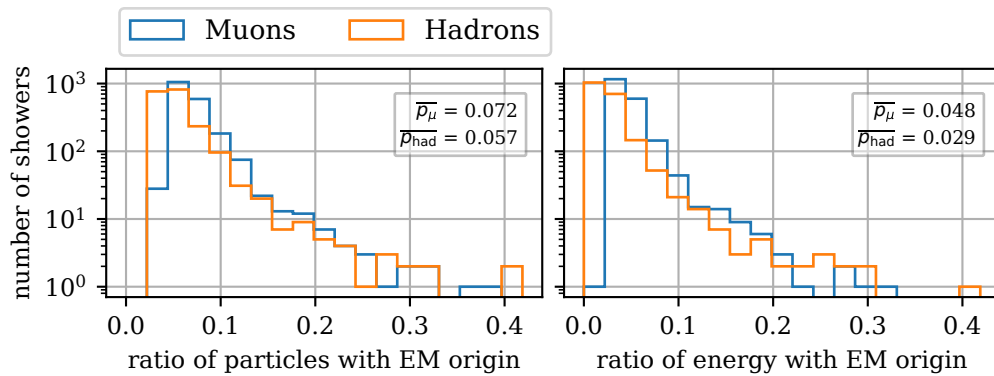


Figure 7.23: Ratio of muons and hadrons originating from the electromagnetic component, for all particles reaching the Earth’s surface in showers induced by 500 PeV protons. The left plot shows the ratio in relation to the particle number, and the right plot in relation to the particle energy. The variables \overline{p}_μ and \overline{p}_{had} indicate the mean ratios.

but significant number of cases, this ratio is higher and can reach a fraction of up to 40 %. The energy distribution of muons and hadrons, split into particles with an electromagnetic or a hadronic origin, is visualized in Figure 7.24. This analysis reveals that in hadron-induced showers, for muons and hadrons of all energies, a contribution from the electromagnetic component due to photonuclear interactions and muon pair production can be expected. One consequence is that simulations of hadronic showers where the electromagnetic component is entirely cut, e.g., for performance reasons, individual showers can suffer from an underestimation of the hadron or muon number.

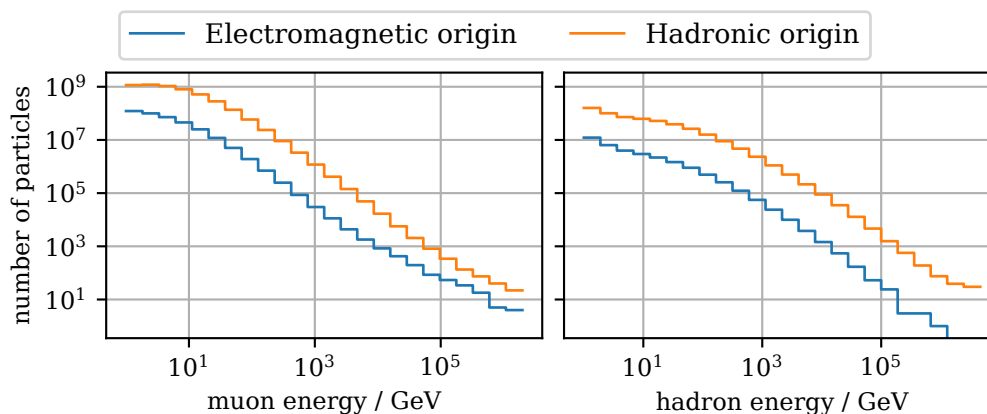


Figure 7.24: Energy distribution of muons and hadrons originating from the electromagnetic or hadronic component. The distribution includes the sum of all particles reaching the Earth’s surface, in all showers induced by 500 PeV protons.

Additional analyses of hadronic showers simulated with CORSIKA 8, including the influence of different hadronic interaction models, are presented in [125, 182].

7.4 Radio Emission of Electromagnetic Showers

Extensive air showers produce radio emission, according to mechanisms explained in Section 3.3.3. Due to their large charge-to-mass ratio, this radio signal is almost exclusively produced by electrons and positrons. Accordingly, it is directly linked to the electromagnetic component of a particle cascade, and highly sensitive to the positions and energies of the individual particles [125]. Therefore, the simulated radio emission from air showers in CORSIKA 8 is investigated in this section as it is ideal for validating the correct description of the electromagnetic shower component.

In the context of radio emission due to the Askaryan effect, the excess of negative charges over positive charges in the electromagnetic shower component is a relevant property. It is commonly called the charge excess and defined as $(n_{e^-} - n_{e^+}) / (n_{e^-} + n_{e^+})$. Figure 7.25 shows the longitudinal development of the charge excess, compared between CORSIKA 7 and CORSIKA 8, for simulations of 1000 photon-induced air showers with a primary energy of 1 PeV. The *ParticleCut* is set to $E_{\text{track}}^{\text{EM}} = 0.5$ MeV and $E_{\text{track}}^{\text{had.}} = E_{\text{track}}^{\mu} = 500$ MeV. Note that a relatively low value for $E_{\text{track}}^{\text{EM}}$ is necessary since even low-energetic particles contribute to the radio emission. The observed development is similar between CORSIKA 7 and CORSIKA 8, showing an almost linear rise of the charge excess with increasing grammage. Notably, the charge excess in CORSIKA 8 is consistently higher by $\approx 2\%$.

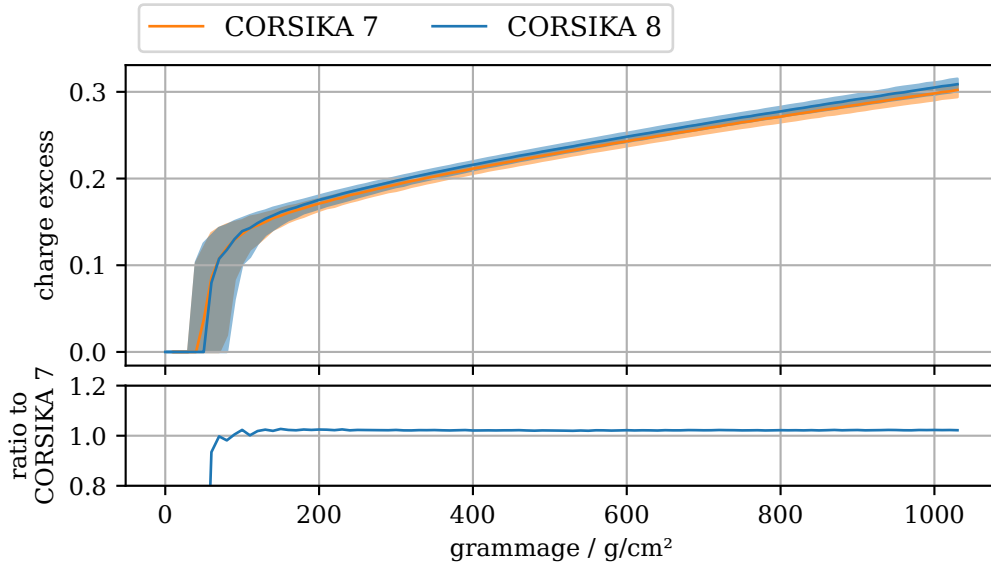


Figure 7.25: Longitudinal development of the charge excess, for showers induced by 1 PeV photons. The lines indicate the median charge excess, the shaded regions the interquartile range.

The radio signal produced in an air shower is obtained by microscopically tracking the emission from each particle trajectory, and propagating the signal to a given list of antenna positions. For CORSIKA 7, these calculations are performed by the CoREAS code [123], which is enabled with the compiler option *COREAS*. For CORSIKA 8, the radio emission for a given particle trajectory is either calculated using the CoREAS formalism or the ZHS formalism [37]. The two formalisms differ in their underlying approaches to solving Maxwell’s equations to obtain the emission for a given particle trajectory [38, 104, 193]. Details about the radio simulation

process in CORSIKA 8 are given in [132], whereas the remainder of this section will focus on the simulation results.

For both CORSIKA 7 and CORSIKA 8, full radio simulations are performed for 13 different 1 PeV photon showers. Note that radio simulations are highly runtime-intensive, where the simulation of a single shower can take up to a day for the settings used in this section. For the simulations, antennas are positioned on the Earth's surface on rings with radii $r = 25$ m, $r = 50$ m, $r = 75$ m, ..., $r = 500$ m around the shower axis. For each ring, eight antennas are placed in a symmetrical pattern, as visualized in Figure 7.28. The sampling resolution for the simulations is set to 0.1 ns, and the refractive index n develops according to the Gladstone-Dale-Law [102] with a baseline value of $n = 1.000327$ at the surface. The magnetic field is homogeneous and oriented in x -direction with $B_x = 50$ μ T, as illustrated in Figure 3.5.

Figure A.6 shows the longitudinal electromagnetic profiles of the individual showers for which full radio simulations are performed. For the remainder of this section, one shower from CORSIKA 7 and one shower from CORSIKA 8 are selected for an analysis of their radio emission, while the analysis of the remaining showers is presented in Appendix A.13. To allow for a meaningful comparison of the radio emission, a pair of showers with similar electromagnetic longitudinal profiles is used.⁵

Firstly, the time pulses for an antenna at $x = 50$ m, $y = 0$ m are shown for the selected showers in Figure 7.26, where the pulses are filtered to the frequency band between 0 MHz and 1000 MHz. Observing an antenna located on the y -axis allows for a decoupled investigation of the contribution from the charge excess emission, which at this position only produces a signal polarized in x -direction, and the geomagnetic emission, which only produces a signal polarized in y -direction, as visualized in Figure 3.5. For all three simulations, the pulses show a good agreement in shape, although the pulses in y -polarization are slightly stronger in CORSIKA 8 compared to CORSIKA 7. As expected, the signal strength in x -polarization is weaker than the signal in y -polarization since the charge excess contribution is smaller compared to the geomagnetic contribution. Figure 7.27 shows the corresponding frequency spectra, which are obtained through a Fourier transform. Here, a good agreement is visible as well. Additionally, the pulses and frequency spectra for an antenna at $x = 200$ m, $y = 0$ m are shown in Figure A.9 and Figure A.10. In Figure 7.28, the resulting energy fluence is visualized, which describes the energy per unit area observed on the ground, and is defined as $f \propto \int |\vec{E}(t)|^2 dt$, with the electric field $\vec{E}(t)$. It is obtained by interpolating the signal observed by the antennas, where only

⁵The selection was made by minimizing the pair-wise first Wasserstein distance between the sum of the longitudinal electron and positron profiles, with the Wasserstein distance defined by the `wasserstein_distance` method in the Python package SciPy [219].

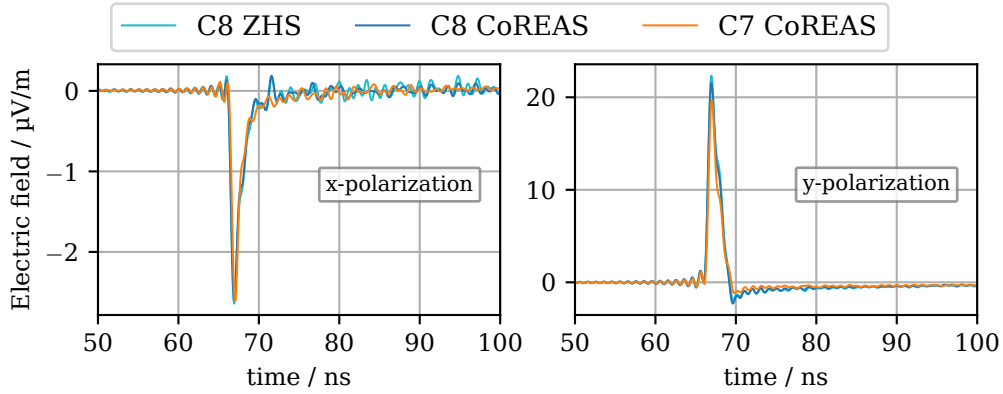


Figure 7.26: Radio pulses for an antenna at $(x = 50 \text{ m}, y = 0 \text{ m})$, divided into the x - and y -polarization, for the radio emission from a 1 PeV, photon-induced shower.

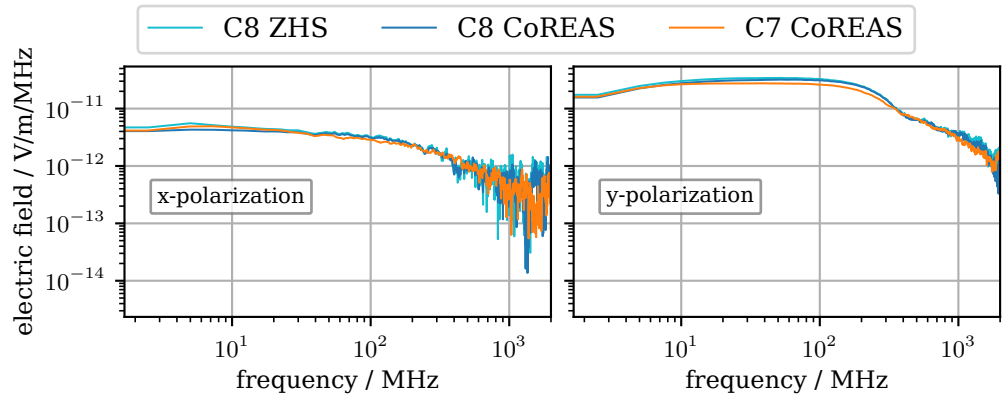


Figure 7.27: Frequency spectra for an antenna at $(x = 50 \text{ m}, y = 0 \text{ m})$, divided into the x - and y -polarization, for the radio emission from a 1 PeV, photon-induced shower.

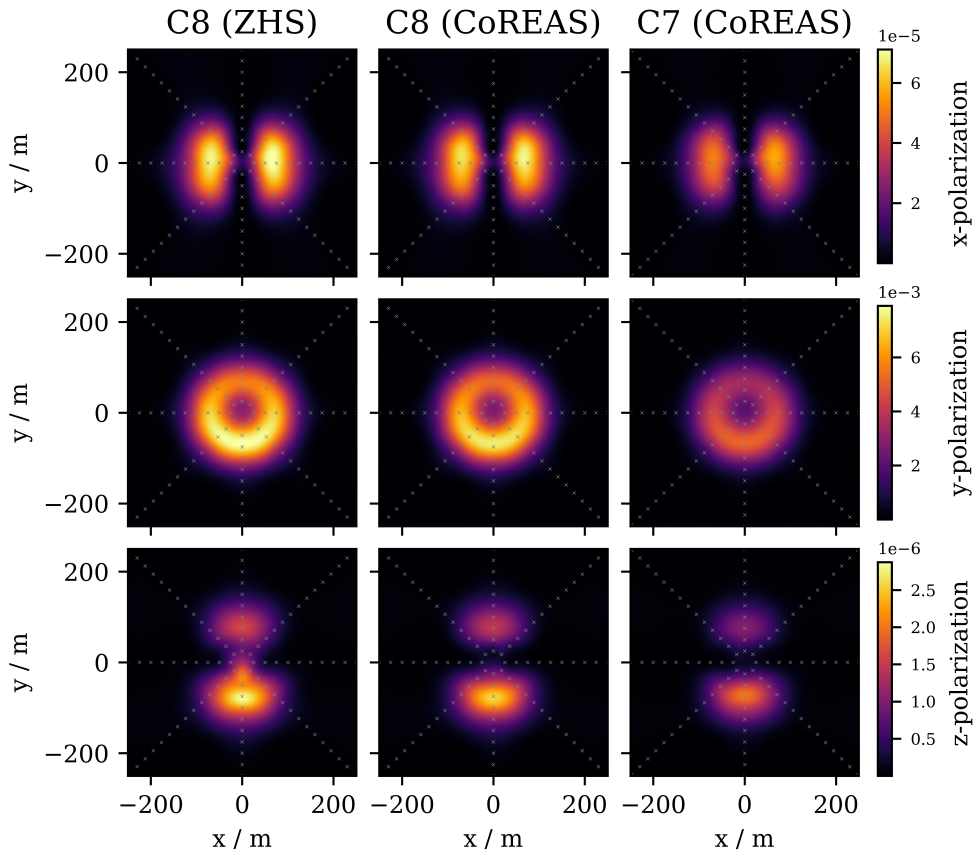


Figure 7.28: Energy fluence maps for the radio emission from a 1 PeV, photon-induced shower. The color bar indicates the energy fluence in eV/m^2 , where the normalization of the color bar is only identical for each row. The gray crosses indicate the antenna positions.

the frequency band between 50 MHz and 350 MHz is considered. Furthermore, the fluences are divided into the contribution from the x -, y -, and z -polarization. For all fluence maps, a signal enhancement along the so-called Cherenkov ring is visible, which is an expected coherence mechanism as described in [Section 3.3.3](#). The first row shows the x -polarization, which only contains a charge excess contribution since the geomagnetic emission only produces a signal with y -polarization (see [Figure 3.5](#)). Due to the radial polarization structure of the charge excess contribution, the energy fluence vanishes close to the y -axis. The second row shows the energy fluence in y -polarization, which is dominated by the geomagnetic contribution. In negative y -direction, the fluence becomes stronger due to constructive interference with the charge excess contribution, while it gets weaker in positive y -direction due to destructive interference. The comparison of all three simulations shows a good agreement for the shapes and symmetries of all fluence maps, whereas the signal strength of both CORSIKA 8 simulations is stronger compared to the CORSIKA 7 simulation. Furthermore, the CORSIKA 8 simulation using the ZHS formalism reveals an additional signal contribution in z -polarization close to the shower axis. Both observations are consistent with results from [\[125, 132\]](#), and require further investigation. However, a perfect agreement, especially between CORSIKA 7 and CORSIKA 8, can not be expected here since only individual showers are compared. Still, it can be concluded that the simulation of the electromagnetic cascade in CORSIKA 8 is capable of producing reasonable radio emission results. More detailed analyses of radio emission from air showers simulated with CORSIKA 8 are presented in [\[125, 131, 132\]](#).

7.5 Simulation of Cross-Media Showers

All showers presented so far in this work have been simulated in the Earth's atmosphere. However, one key feature of CORSIKA 8 is the possibility to simulate particle cascades in arbitrary media and density distributions, and combinations thereof, which was not possible with CORSIKA 7 (see [Section 5.1.2](#)). This allows for the simulation of cross-media showers, for example, transitioning from the Earth's atmosphere into ice, which is presented in this section.

The Earth's atmosphere is parametrized as in the previous sections, however, between a height of $h = 0$ m and $h = 2835$ m, an ice layer with a homogeneous density of $\rho = 0.918$ g/cm² is inserted, modeling the setting of the IceCube Neutrino Observatory. For this environment, a statistic of 5000 proton-induced showers with a primary energy of 10 PeV is simulated, using a *ParticleCut* of $E_{\text{track}}^{\text{EM}} = E_{\text{track}}^{\text{had.}} = E_{\text{track}}^{\mu} = 500$ MeV. As a comparison, 5000 showers with identical settings, but without the ice layer, are simulated as well.

The resulting longitudinal profiles for both simulations are shown in Figure 7.29. Note that in this visualization of the longitudinal profiles, the grammage between $\approx 730 \text{ g/cm}^2$ and $\approx 1030 \text{ g/cm}^2$ for the purely atmospheric shower corresponds to a distance of 2835 m, i.e., the full remaining distance to the Earth's surface, while the grammage between $\approx 730 \text{ g/cm}^3$ and 2000 g/cm^2 for the cross-media shower only corresponds to a distance of $\approx 14 \text{ m}$ due to the large difference of the mass densities. While the development of the particle number with increasing grammage is almost identical for the electromagnetic particles, the cross-media shower shows a sudden increase of the hadronic particle number after the medium transition. This effect is caused by the significant decrease of the hadronic interaction length due to the increase of the mass density, while the decay length stays identical. This leads to an accelerated development of the hadronic shower component. At the same time, the number of muons is slightly smaller compared to the muon number in the purely atmospheric showers, since fewer muons are produced from hadronic decays.

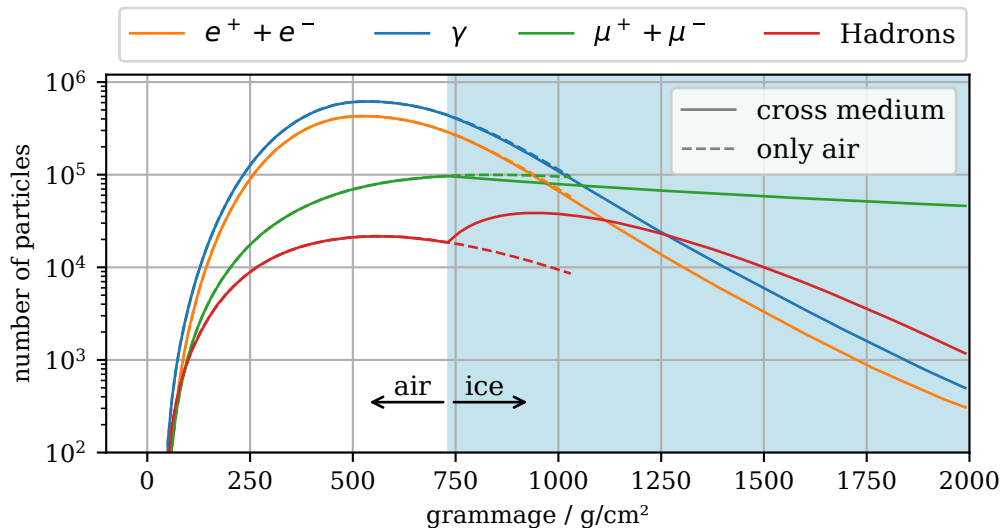


Figure 7.29: Longitudinal profiles for showers induced by 10 PeV protons. The solid lines show the profile of showers transitioning from air to ice at a height of 2835 km, where the ice layer is indicated with the blue-shaded area. As a comparison, the dashed lines show the profiles of purely atmospheric showers. The lines each indicate the median number of particles.

In Figure 7.30, the particle tracks from an exemplary cross-media shower are visualized. Within the atmosphere, the electromagnetic shower component is centered around the shower axis, while the hadronic and muonic shower component contain a larger lateral spread due to the involvement of larger transversal momenta in

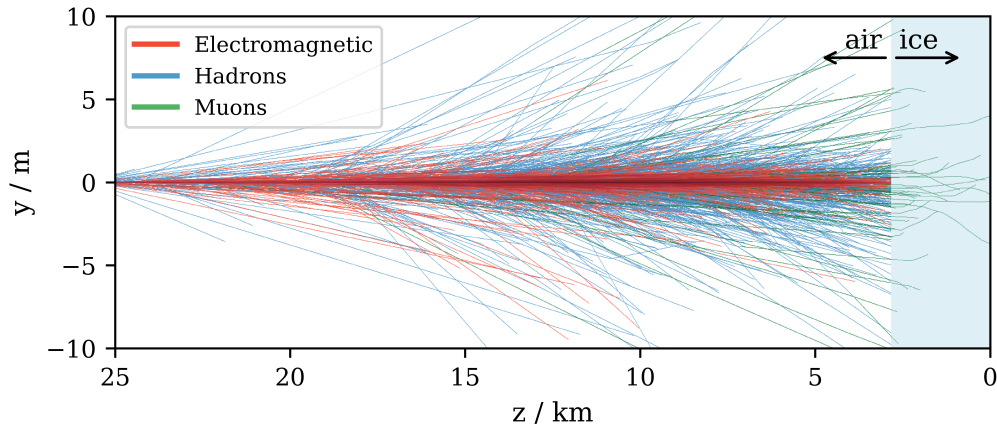


Figure 7.30: Track visualization for a particle shower, induced by a 10 PeV proton, transitioning from air to ice. Only tracks with an initial energy of 500 GeV are shown. The blue-shaded area indicates the ice layer.

hadronic particle interactions and decays. After the transition from air to ice, both the electromagnetic and hadronic shower component are quickly stopped, while high-energy muons are able to propagate long distances in the ice sheet.

In the context of underground experiments such as IceCube, this example highlights the possibility of CORSIKA 8 to simulate a particle cascade entirely from its injection into the Earth’s atmosphere until reaching, for example, an underground detector. Until now, this could only be achieved with individual simulation steps: In the IceCube simulation chain, for example, CORSIKA 7 is used to simulate the atmospheric air shower, after which particles reaching the ground are passed to PROPOSAL for the in-ice propagation, as explained in more detail in [Section 4.3.1](#). Combining these individual simulation steps into one software provides the advantage of a consistent physics description and avoids error-prone transitions between different frameworks.

Additional analyses of cross-media showers simulated with CORSIKA 8 are presented in [\[40, 218\]](#).

8 Discussion and Outlook

The potential of discoveries in astroparticle physics relies heavily on the availability of accurate simulations of extensive air showers. In this work, the Monte Carlo simulation software PROPOSAL has been implemented as an electromagnetic and muonic interaction model for the next-generation particle cascade framework CORSIKA 8. As a preparation, the feature set of PROPOSAL has been expanded in terms of physics and methods: The sampling of individual secondary particles from energy losses has been implemented; parametrizations and processes for electrons, positrons, and high-energy photons have been included; and the underlying code structure has been modularized, allowing for the usage of PROPOSAL as a propagation library. Based on these improvements, an interface between PROPOSAL and CORSIKA 8, with the inclusion of external event generators for the sampling of photonuclear secondary particles, has been implemented. With PROPOSAL as a well-established framework in the context of muon propagation, CORSIKA 8 is now capable of providing air shower simulations with minimal systematic uncertainties regarding its description of muon interactions. Furthermore, the description of the electromagnetic shower component with PROPOSAL has been extensively validated by comparisons with CORSIKA 7 simulations. The agreement of relevant shower characteristics has been determined to be within 10 % or better, as shown in [Chapter 7](#). Notably, the simulated number of muons shows an increase of $\approx 10\%$ within electromagnetic showers, see [Figure 7.12](#), and an increase of $\approx 5\%$ within hadronic showers, see [Figure 7.17](#). In the context of the muon puzzle, however, these numbers are not sufficient to explain the experimentally observed excess, where a discrepancy of $\approx 25\%$ in hadronic showers is visible. As a consequence, it can be ruled out that systematic uncertainties in muon propagation are responsible for the muon puzzle. Furthermore, with the availability of CORSIKA 8 as a well-understood framework for particle cascade simulations, it is unlikely that the muon puzzle can be explained by uncertainties in the cascade simulation code itself. In terms of reproducibility, this work can be seen as a comprehensive documentation of the modeling of electromagnetic and muonic interactions in CORSIKA 8, clearly describing both its capabilities and restrictions.

The implemented interface to PROPOSAL provides the first interaction model within CORSIKA 8 capable of providing a complete description of the electromagnetic and muonic shower component. Therefore, the results of this work are crucial on

the path toward the release of CORSIKA 8. The developed framework provides a variety of improvements and possibilities now available to the scientific community: As presented in [Section 7.5](#), CORSIKA 8 allows for the simulation of showers in arbitrary environments, including cross-media showers. Since CORSIKA 7 is only capable of providing air shower simulations, previous cross-media simulations relied on the combined usage of multiple codes, as exemplarily described in [Section 4.3.1](#) for the IceCube Neutrino Observatory. This approach is error-prone and often hard to reproduce, as it involves the manual transition of information between frameworks. With CORSIKA 8, these individual steps are combined into one software, with the advantage of a consistent physics description. Furthermore, CORSIKA 8 allows for an in-depth systematic analysis of particle cascades, for example, via access to the entire particle history. In addition, due to the modular structure of both CORSIKA 8 and PROPOSAL, parts of the cascade simulation can be adapted, and the impact of these changes on the simulation results can be evaluated. Likewise, the implementation of additional or adapted interaction processes, e.g., for hadronic interactions or physics processes beyond the standard model, is now greatly simplified. First collaborations already started using CORSIKA 8 for their analyses, including TAMBO [\[213\]](#) and TRIDENT [\[226\]](#). With the upcoming first release, more collaborations are going to profit from the created possibilities.

With the exclusion of uncertainties in muon propagation or cascade simulations as a cause for the muon puzzle, modifications in hadronic interaction models remain as the most likely solution. Additional experimental measurements and analyses from collider experiments will be necessary as a confirmation, as described in [Section 3.4](#). In this context, CORSIKA 8 is going to be a powerful tool to estimate the impact of changes in hadronic interaction on the shower development. Although the provided implementation of PROPOSAL as an interaction model is physics-complete, several improvements are possible. The description of very-high-energy simulations can be improved by implementing a description of the LPM effect for continuous losses in inhomogeneous media. Furthermore, while the current description of multiple scattering provides a reasonable agreement of lateral profiles in comparison with CORSIKA 7 simulations, a more sophisticated method, considering lateral particle displacements, will provide more accurate simulation results. For both aspects, several approaches to improve the current situation have been proposed in this work. Lastly, performance optimizations will be a key challenge for the further development of CORSIKA 8. This includes detailed profiling of the current code to uncover possible performance bottlenecks, and utilizing optimization methods such as multi-core processing or approaches to avoid the simulation of irrelevant particles.

A Supplementary Material

A.1 Derivation of the Energy Integral

The energy integral (4.6), originally derived in [77], defines a method to sample the energy E_f at the next stochastic loss, taking into account the variation of the cross section with energy due to continuous losses (see Section 4.1 for an introduction into the simulation principles of PROPOSAL).

For a discretized path with steps of Δx between an initial position x_i and a final position x_f , the probability for no stochastic losses between x_i and x_f except for the last step is given by

$$\Delta P(x_f) = \prod_{j=i}^{f-1} (1 - \sigma_s(x_j)\Delta x_j) \sigma_s(x_f)\Delta x_f \quad (\text{A.1})$$

$$\approx \exp\left(\sum_{j=i}^{f-1} \sigma_s(x_j)\Delta x_j\right) \sigma_s(x_f)\Delta x_f, \quad (\text{A.2})$$

where σ_s is the stochastic cross section as defined in (4.4). In a differential form, this becomes

$$dP(x_f) = \exp\left(-\int_{x_i}^{x_f} \sigma_s(x) dx\right) \sigma_s(x_f) dx_f. \quad (\text{A.3})$$

With the definition $f(E) = -\frac{dE}{dX}$ of the continuous losses, see (4.3), this can be written as

$$dP(x_f) = \exp\left(\int_{E_i}^{E_f} \frac{\sigma_s(E)}{f(E)} dE\right) \frac{\sigma_s(E_f)}{-f(E_f)} dE_f. \quad (\text{A.4})$$

To obtain a cumulative distribution function, $dP(x_f)$ is integrated:

$$P(E_f \leq E \leq E_i) = \int_{E_i}^{E_f} \exp\left(\int_{E_i}^{E'} \frac{\sigma_s(E)}{f(E)} dE\right) \frac{\sigma_s(E')}{-f(E')} dE'. \quad (\text{A.5})$$

Using the substitution

$$u(E) = \int_{E_i}^E \frac{\sigma_s(E')}{f(E')} dE', \quad du = \frac{\sigma_s(E)}{f(E)} dE, \quad (\text{A.6})$$

this expression can be simplified to

$$P(E_f \leq E \leq E_i) = - \int_{E_i}^{E_f} \exp(u(E_f)) du \quad (\text{A.7})$$

$$= - \left[\exp(u(E_f)) \right]_{E_i}^{E_f} \quad (\text{A.8})$$

$$= - \exp \left(\int_{E_i}^{E_f} \frac{\sigma_s(E)}{f(E)} dE \right) + 1. \quad (\text{A.9})$$

Since the cumulative distribution function can take values $\xi' \in [0, 1)$, this can be written as

$$\xi' = - \exp \left(\int_{E_i}^{E_f} \frac{\sigma_s(E)}{f(E)} dE \right) + 1, \quad (\text{A.10})$$

which can be transformed to

$$\int_{E_i}^{E_f} \frac{\sigma_s(E)}{-f(E)} dE = - \log(\underbrace{1 - \xi'}_{:=\xi}) \quad (\text{A.11})$$

with $\xi \in (0, 1]$. The energy of a stochastic loss can now be obtained by sampling a random number ξ , and solving (A.11) for E_f . Note that when a lower energy cutoff E_{low} , for example $E_{\text{low}} = m$, is introduced, (A.11) only has a solution for

$$\xi \geq \xi_0 := \exp \left(\int_{E_i}^{E_{\text{low}}} \frac{\sigma_s(E)}{f(E)} dE \right). \quad (\text{A.12})$$

For $\xi < \xi_0$, the propagation step ends at $E = E_{\text{low}}$, and no stochastic loss is performed.

A.2 Hadronic Interaction Models in CORSIKA 7 and CORSIKA 8

The availability of hadronic interaction models within CORSIKA 7 and CORSIKA 8 is summarized in [Table A.1](#) for high-energy interaction models, and [Table A.2](#) for low-energy interaction models. These lists refer to version 7.7500 of CORSIKA 7, and the development version of CORSIKA 8 as described in [Appendix B](#). Details about the hadronic interaction models are found in [34, 86], as well as in the references corresponding to the individual interaction models.

Table A.1: Availability of high-energy hadronic interaction models in CORSIKA 7 and CORSIKA 8.

Model name	Ref.	Avail. in C7	Avail. in C8
DPMJET-III	[90, 186]	Yes	No
EPOS LHC	[179]	Yes	Yes
NEXUS 3.97	[81]	Yes	No
QGSJET01	[129]	Yes	No
QGSJETII-04	[175, 174]	Yes	Yes
SIBYLL 2.3d	[185]	Yes	Yes
VENUS	[222]	Yes	No
PYTHIA 8.310	[62]	No	Yes ¹

Table A.2: Availability of low-energy hadronic interaction models in CORSIKA 7 and CORSIKA 8.

Model name	Ref.	Avail. in C7	Avail. in C8
GHEISHA	[95]	Yes	No
FLUKA	[64, 94]	Yes	Yes
UrQMD	[53, 63]	Yes	Yes

A.3 Visualization of the Step Function of CORSIKA 8

[Figure A.1](#) shows a visualization of the `Step` method, which performs a particle propagation step in the context of the Cascade algorithm of CORSIKA 8, as described in [Section 5.2.2](#).

¹Implementation ongoing.

A.3 Visualization of the Step Function of CORSIKA 8

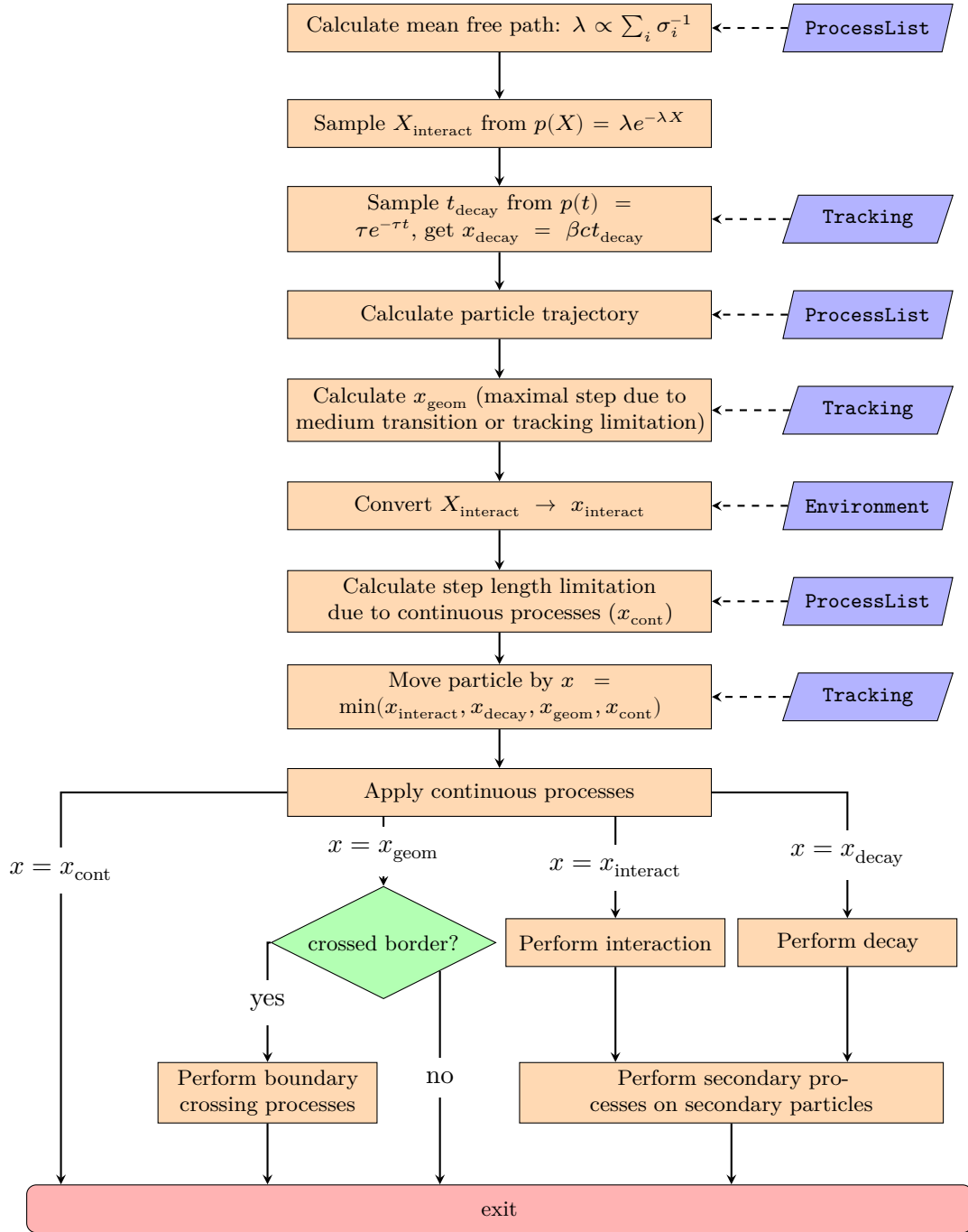


Figure A.1: Flow chart explaining the Step function of CORSIKA 8. See Section 5.2.2 for a detailed explanation. The blue boxes indicate relations to the main code building blocks described in Section 5.2.1.

A.4 Default Interaction Parametrizations in CORSIKA 8

This section summarizes the particle interaction parametrizations, provided by PROPOSAL and used by default in CORSIKA 8, as described in Section 5.3. They are listed, divided into the different particle types, in Table A.3, Table A.4, Table A.5, and Table A.6. The parametrizations for electrons, positrons, and photons are described in Chapter 6, while the parametrizations for muons and taus have been described in detail, for example, in [143]. Note that due to the modular structures of CORSIKA 8 and PROPOSAL, it is straightforward to disable individual interaction types, replace individual parametrizations, or add new interaction types as required by the user.

Table A.3: Default photon interaction parametrizations, as provided by PROPOSAL and used within the CORSIKA 8 interface.

Interaction type	Parametrization name	Reference
e^+e^- pair production	PhotoPairKochMotz	(6.61) & (6.63)
Compton scattering	ComptonKleinNishina	(6.73)
Photohadronic interaction	PhotoproductionHeckC7Shadowing	(6.92)
Photoelectric absorption	PhotoeffectSauter	(6.76)
$\mu^+\mu^-$ pair production	PhotoMuPairBurkhardtKelnerKokoulin	(6.80)

Table A.4: Default electron interaction parametrizations, as provided by PROPOSAL and used within the CORSIKA 8 interface.

Interaction type	Parametrization name	Reference
Bremsstrahlung	BremsElectronScreening	(6.1) & (6.7)
e^+e^- pair production	EpairForElectronPositron	(6.36)
Ionization	IonizBergerSeltzerMoller	(6.15)
Photonuclear interaction	PhotoAbramowiczLevinLevyMaor97	(6.41)

Table A.5: Default positron interaction parametrizations, as provided by PROPOSAL and used within the CORSIKA 8 interface.

Interaction type	Parametrization name	Reference
Bremsstrahlung	BremsElectronScreening	(6.1) & (6.7)
e^+e^- pair production	EpairForElectronPositron	(6.36)
Ionization	IonizBergerSeltzerBhabha	(6.17)
Photonuclear interaction	PhotoAbramowiczLevinLevyMaor97	(6.41)
Annihilation	AnnihilationHeitler	(6.28)

Table A.6: Default muon and tau lepton interaction parametrizations, as provided by PROPOSAL and used within the CORSIKA 8 interface.

Interaction type	Parametrization name	Reference
Bremsstrahlung	BremsKelnerKokoulinPetrukhin	[135, 138]
e^+e^- pair production	EpairKelnerKokoulinPetrukhin	[146, 136]
Ionization	IonizBetheBlochRossi	[58, 190]
Photonuclear interaction	PhotoAbramowiczLevinLevyMaor97	[14, 15, 50]

A.5 Atomic Form Factors

The parametrization of electron-positron pair production given in (6.64) includes Z -dependent descriptions of the atomic form factors, which are taken from [214] and listed here.

For $Z = 1$ and $Z = 2$, the atomic form factors are given by

$$\begin{aligned} \varphi_1 = & \frac{4}{3} \ln(Z) + 4 \ln\left(\frac{1}{2\eta\alpha}\right) + \frac{13}{3} - 2 \ln(1 + C^2) \\ & - \frac{13}{2} C \arctan(C^{-1}) + \frac{1}{6} \frac{1}{1 + C^{-2}}, \end{aligned} \quad (\text{A.13})$$

$$\begin{aligned} \varphi_2 = & \frac{4}{3} \ln(Z) + 4 \ln\left(\frac{1}{2\eta\alpha}\right) + \frac{11}{3} - 2 \ln(1 + C^2) \\ & + 25C^2(1 - C \arctan(C^{-1})) - 14C^2 \ln(1 + C^{-2}), \end{aligned} \quad (\text{A.14})$$

$$\begin{aligned} \psi_1 = & \frac{8}{3} \ln(Z) + 4 \ln\left(\frac{1}{2\eta\alpha}\right) + \frac{23}{3} - 2 \ln(1 + C^2) \\ & - 17.5C \arctan(C^{-1}) + 8C^2 \ln(1 + C^{-2}) - \frac{1}{6} \frac{1}{1 + C^{-2}}, \end{aligned} \quad (\text{A.15})$$

$$\begin{aligned} \psi_2 = & \frac{8}{3} \ln(Z) + 4 \ln\left(\frac{1}{2\eta\alpha}\right) + \frac{21}{3} - 2 \ln(1 + C^2) \\ & - 105C^2(1 - C \arctan(C^{-1})) + 50C^2 \ln(1 + C^{-2}) \\ & - 24C^2 \left[-\ln(C^2) \ln(1 + C^{-2}) + \Phi(1 + C^{-2}) - \Phi(1) \right], \end{aligned} \quad (\text{A.16})$$

$$X = X_{\text{el}} + X_{\text{inel}}, \quad (\text{A.17})$$

$$X_{\text{el}} = Z^2 \left[2 \ln \left(\frac{m_e}{\delta} \right) - \ln(1 + B^2) + \frac{1}{6} - \frac{4}{3} \frac{1}{1 + B^2} + \frac{1}{6} \frac{1}{(1 + B^2)^2} \right], \quad (\text{A.18})$$

$$X_{\text{inel}} = Z \left[2 \ln \left(\frac{m_e}{\delta} \right) - \ln(1 + B^2) + \frac{11}{6} - 4B^{-2} \ln(1 + B^2) + \frac{4}{3} \frac{1}{1 + B^2} - \frac{1}{6} \frac{1}{(1 + B^2)^2} \right], \quad (\text{A.19})$$

with

$$\begin{aligned} \delta &= \frac{m_e^2}{2Ex(1-x)}, & C &= \frac{\delta}{2\alpha m_e \eta}, & x &= \frac{E_{e^-}}{E}, \\ t'_{\text{min}} &= \left(\frac{m_e^2(1+l)}{2Ex(1-x)} \right)^2, & B &= \frac{2\alpha m_e \eta}{\sqrt{t'_{\text{min}}}}, & l &= \frac{E_e^2 \theta^2}{m_e^2}, \end{aligned}$$

where E is the energy of the ingoing photon, E_{e^-} the energy of the produced electron, θ the production angle of the produced electron or positron, and η is given by

$$\eta = \begin{cases} 1 & \text{if } Z = 1, \\ 1.6875 & \text{if } Z = 2, \end{cases}$$

with the dilogarithm $\Phi(x)$.

For $Z = 3$ and $Z = 4$, the atomic form factors are given by

$$\varphi_1 = 2 \left(1 + \ln(a^2 Z^{2/3} m_e^2) \right) - 2 \ln(1 + b^2) - 4b \arctan(b^{-1}), \quad (\text{A.20})$$

$$\begin{aligned} \varphi_2 &= 2 \left(\frac{2}{3} + \ln(a^2 Z^{2/3} m_e^2) \right) - 2 \ln(1 + b^2) \\ &+ 8b^2 \left[1 - b \arctan(b^{-1}) - 0.75 \ln(1 + b^{-2}) \right], \end{aligned} \quad (\text{A.21})$$

$$\psi_1 = 2 \left(1 + \ln(a'^2 Z^{4/3} m_e^2) \right) - 2 \ln(1 + b'^2) - 4b' \arctan(b'^{-1}), \quad (\text{A.22})$$

$$\begin{aligned} \psi_2 &= 2 \left(\frac{2}{3} + \ln(a'^2 Z^{4/3} m_e^2) \right) - 2 \ln(1 + b'^2) \\ &+ 8b'^2 \left[1 - b' \arctan(b'^{-1}) - 0.75 \ln(1 + b'^{-2}) \right], \end{aligned} \quad (\text{A.23})$$

$$X = X_{\text{el}} + X_{\text{inel}}, \quad (\text{A.24})$$

$$X_{\text{el}} = Z^2 \left[\ln \left(\frac{a^2 m_e^2 (1+l)^2}{a^2 t'_{\text{min}} + 1} \right) - 1 \right], \quad (\text{A.25})$$

$$X_{\text{inel}} = Z \left[\ln \left(\frac{a'^2 m_e^2 (1+l)^2}{a'^2 t'_{\text{min}} + 1} \right) - 1 \right], \quad (\text{A.26})$$

with

$$a = \begin{cases} \frac{100}{m_e} Z^{-1/3} & \text{if } Z = 3, \\ \frac{106}{m_e} Z^{-1/3} & \text{if } Z = 4, \end{cases}$$

$$a' = \begin{cases} \frac{418.6}{m_e} Z^{-2/3} & \text{if } Z = 3, \\ \frac{571.4}{m_e} Z^{-2/3} & \text{if } Z = 4, \end{cases}$$

and $b = a\delta$, $b' = a'\delta$.

For heavier elements, the Thomas-Fermi model is used, and the atomic form factors are given by

$$\varphi_1(\gamma) = 20.863 - 2 \ln(1 + (0.55846\gamma)^2) - 4 \left[1 - 0.6 \exp(-0.9\gamma) - 0.4 \exp(-1.5\gamma) \right], \quad (\text{A.27})$$

$$\varphi_2(\gamma) = \varphi_1(\gamma) - \frac{2}{3} \frac{1}{1 + 6.5\gamma + 6\gamma^2}, \quad (\text{A.28})$$

$$\psi_1(\epsilon) = 28.34 - 2 \ln(1 + (3.621\epsilon)^2) - 4 \left[1 - 0.7 \exp(-8\epsilon) - 0.3 \exp(-29.2\epsilon) \right], \quad (\text{A.29})$$

$$\psi_2(\epsilon) = \psi_1(\epsilon) - \frac{2}{3} \frac{1}{1 + 40\epsilon + 400\epsilon^2}, \quad (\text{A.30})$$

$$X = X_{\text{el}} + X_{\text{inel}}, \quad (\text{A.31})$$

$$X_{\text{el}} = Z^2 \left[\ln \left(\frac{a^2 m_e^2 (1+l)^2}{a^2 t'_{\text{min}} + 1} \right) - 1 \right], \quad (\text{A.32})$$

$$X_{\text{inel}} = Z \left[\ln \left(\frac{a'^2 m_e^2 (1+l)^2}{a'^2 t'_{\text{min}} + 1} \right) - 1 \right], \quad (\text{A.33})$$

with

$$\gamma = \frac{200\delta}{m_e Z^{1/3}}, \quad \epsilon = \frac{200\delta}{m_e Z^{2/3}}, \quad a = 111.7 \frac{Z^{-1/3}}{m_e}, \quad a' = 724.2 \frac{Z^{-2/3}}{m_e}.$$

A.6 Radiation Logarithm Constants

Table A.7 lists the radiation logarithm B , used in the description of electron-positron pair production in Section 6.1.4, muon pair production in Section 6.2.4, and the Landau-Pomeranchuk-Migdal (LPM) suppression in Section 6.3, as defined in [138].

Table A.7: Radiation logarithm constant, taken from [138].

Z	B	Z	B	Z	B	Z	B	Z	B
1	202.4	8	173.4	15	172.2	22	176.8	53	178.6
2	151.9	9	170.0	16	173.4	26	175.8	74	177.6
3	159.9	10	165.8	17	174.3	29	173.1	82	178.0
4	172.3	11	165.8	18	174.8	32	173.0	92	179.8
5	177.9	12	167.1	19	175.1	35	173.5		
6	178.3	13	169.1	20	175.6	42	175.9	other	182.7
7	176.6	14	170.8	21	176.2	50	177.4		

A.7 Kinematics of Two-body Interactions with Atomic Electrons

The kinematics of a two-body interaction are described by energy and momentum conservation, expressed by the equation

$$P_1 + P_2 = P'_1 + P'_2, \quad (\text{A.34})$$

where P_1, P_2 are the four-momenta of the ingoing particles, and P'_1, P'_2 the four-momenta of the outgoing particles. Figure A.2 shows the process where an ingoing

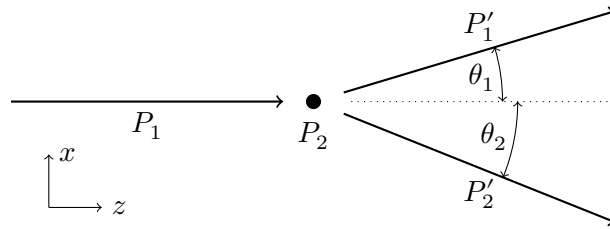


Figure A.2: Kinematics of a two-body interaction of an ingoing particle with an atomic electron at rest.

particle interacts with an atomic electron, which is assumed to be at rest. In this case, the four-momenta are given by

$$P_1 = \begin{pmatrix} E_1 \\ 0 \\ 0 \\ p_1 \end{pmatrix}, \quad P_2 = \begin{pmatrix} m_e \\ 0 \\ 0 \\ 0 \end{pmatrix}, \quad P'_1 = \begin{pmatrix} E'_1 \\ p'_1 \sin \theta_1 \\ 0 \\ p'_1 \cos \theta_1 \end{pmatrix}, \quad P'_2 = \begin{pmatrix} E'_2 \\ -p'_2 \sin \theta_2 \\ 0 \\ p'_2 \cos \theta_2 \end{pmatrix}.$$

Inserting these four-momenta into (A.34), the expressions

$$\begin{aligned} \cos \theta_1 &= \frac{m'_2{}^2 - m_1^2 - m_e^2 - m_1'^2 + 2(E_1 + m_e)E'_1 - 2E_1 m_e}{2p_1 p'_1}, \\ \cos \theta_2 &= \frac{m'_1{}^2 - m_1^2 - m_e^2 - m_2'^2 + 2(E_1 + m_e)E'_2 - 2E_1 m_e}{2p_1 p'_2}, \end{aligned} \quad (\text{A.35})$$

are obtained.

A.8 Description of Resonances for the Photohadronic Cross Section

The parametrization in (6.92) describes the continuous contribution to the photohadronic cross section. Additionally, the contribution from the three resonances $\Delta(1232)$, $N(1520)$, and $N(1680)$ is considered. For these resonances, the parametrization from the SOPHIA code [169] is used, where their contribution to the cross section is given by

$$\sigma_{\text{res}}(\nu, s) = \sum_i \frac{s}{\nu^2} \frac{\sigma_{0,i} \Gamma_i^2 s}{(s - M_i^2)^2 + \Gamma_i^2 s} Q(\nu, \nu_{\text{th},i}, w_i), \quad (\text{A.36})$$

with the quenching function

$$Q(\nu, \nu_{\text{th},i}, w_i) = \begin{cases} 0 & \text{for } \nu < \nu_{\text{th},i}, \\ \frac{\nu - \nu_{\text{th},i}}{w_i} & \text{for } \nu_{\text{th},i} \leq \nu < \nu_{\text{th},i} + w_i, \\ 1 & \text{for } \nu_{\text{th},i} + w_i \leq \nu, \end{cases} \quad (\text{A.37})$$

with the photon energy ν and the squared center of mass energy $s = m_n^2 + 2m_n \nu$, where m_n denotes the average nucleon mass. The parameters σ_0 , Γ , M , ν_{th} , and w , describing the individual resonances, are listed in Table A.8. Note that this description of the resonances is not identical to the parametrization used in CORSIKA 7 [109]. However, a direct comparison of the results shows a good agreement, which is why the approach here is used within PROPOSAL.

Table A.8: Parameters describing the resonances for the photonuclear cross section [169].

Resonance	$\sigma_0 / \mu\text{b}$	Γ / GeV	M / GeV	$\nu_{\text{th}} / \text{GeV}$	w / GeV
$\Delta(1232)$	31.125	0.11	1.231	0.152	0.17
$N(1520)$	25.567	0.11	1.515	0.152	0.38
$N(1680)$	17.508	0.125	1.680	0.152	0.38

A.9 Parametrization of the Structure Function F_2

In [14, 15], the proton structure function $F_2(x, Q^2)$ is parametrized based on Regge theory. For that, a fit to data from the HERA collider as well as fixed target experiments is performed [14]. This section summarizes the results of this fit.

The function $F_2(x, Q^2)$ is parametrized by the expression

$$F_2(x, Q^2) = a(A, x) (Z + (A - Z)P(x)) \frac{Q^2}{Q^2 + m_0^2} (F_2^{\text{P}} + F_2^{\text{R}}), \quad (\text{A.38})$$

with the effective photon mass m_0 , and the contributions F_2^{P} and F_2^{R} from Pomeron and Reggeon exchanges. To describe their behavior, the parametrization

$$F_2^i = c_i(t) x_i^{a_i(t)} (1 - x)^{b_i(t)} \quad (\text{A.39})$$

is used, with the definitions

$$t = \ln \left[\frac{\ln \left(\frac{Q^2 + Q_0^2}{\Lambda^2} \right)}{\ln(Q_0^2 / \Lambda^2)} \right], \quad x_i = \frac{Q^2 + m_i^2}{Q^2 + m_i^2 + W^2 - M^2}, \quad (\text{A.40})$$

and

$$W^2 = M^2 + 2MEv - Q^2. \quad (\text{A.41})$$

Note that i is either P or R, and that m_i , m_0 , Λ^2 , and Q_0^2 are fit parameters, while $a_i(t)$, $b_i(t)$, and $c_i(t)$ are model functions which depend on additional fit parameters. For $a_{\text{R}}(t)$, $b_{\text{R}}(t)$, $b_{\text{P}}(t)$, and $c_{\text{R}}(t)$, the function

$$f(t) = f_1 + f_2 \cdot t^{f_3} \quad (\text{A.42})$$

is used. The fit results for these parameters are given in Table A.9. For $a_{\text{P}}(t)$ and $c_{\text{P}}(t)$, the function

$$g(t) = g_1 + (g_1 - g_2) \left(\frac{1}{1 + t^{g_3}} - 1 \right) \quad (\text{A.43})$$

A.9 Parametrization of the Structure Function F_2

is used, and the fit results are given in [Table A.10](#). The fit results of the remaining parameters are given by

$$\begin{aligned} m_{\text{P}}^2 &= 49.457 \times 10^6 \text{ MeV}^2, \\ m_{\text{R}}^2 &= 0.15052 \times 10^6 \text{ MeV}^2, \\ m_0^2 &= 0.31985 \times 10^6 \text{ MeV}^2, \\ A^2 &= 0.06527 \times 10^6 \text{ MeV}^2, \\ Q_0^2 &= 0.52544 \times 10^6 \text{ MeV}^2. \end{aligned}$$

Table A.9: Resulting fit parameters for the proton structure function F_2 , for all parameters used in the model function (A.42) [14].

Parameter	f_1	f_2	f_3
a_{R}	0.58400	0.37888	2.6063
b_{P}	0.36292	1.8917	1.8439
b_{R}	0.01147	3.7582	0.49338
c_{R}	0.80107	0.97307	3.4942

Table A.10: Resulting fit parameters for the proton structure function F_2 , for all parameters used in the model function (A.43) [14].

Parameter	g_1	g_2	g_3
a_{P}	-0.08080	-0.44812	1.1709
c_{P}	0.28067	0.22291	2.1979

The parameter $a(A, x)$ in (A.38) describes the shadowing effect, which determines the ratio between the structure function of a single nucleon F_2^{N} and the structure function of the entire nucleus F_2^{A} , i.e.,

$$a(A, x, Q^2) = \frac{F_2^{\text{A}}(x, Q^2)}{AF_2^{\text{N}}(x, Q^2)}, \quad (\text{A.44})$$

similar to the description of the shadowing effect in [Section 6.2.5](#). Here, the shadowing ratio is parametrized by [85]

$$a(A, x) = \begin{cases} A^{-0.1} & \text{for } x < 0.0014, \\ A^{0.069 \log_{10}(x) + 0.097} & \text{for } 0.0014 \leq x < 0.04, \\ 1 & \text{for } 0.04 \leq x. \end{cases} \quad (\text{A.45})$$

Furthermore, the function $P(x)$ describes the ratio of the contribution from the proton and neutron structure function, and is given by [85]

$$P(x) = F_2^n / F_2^p = 1 - 1.85x + 2.45x^2 - 2.35x^3 + x^4. \quad (\text{A.46})$$

A.10 Comparison of the Utilized Electron Cross Section

Figure A.3 shows a comparison of the electron cross sections used in CORSIKA 7 and CORSIKA 8.

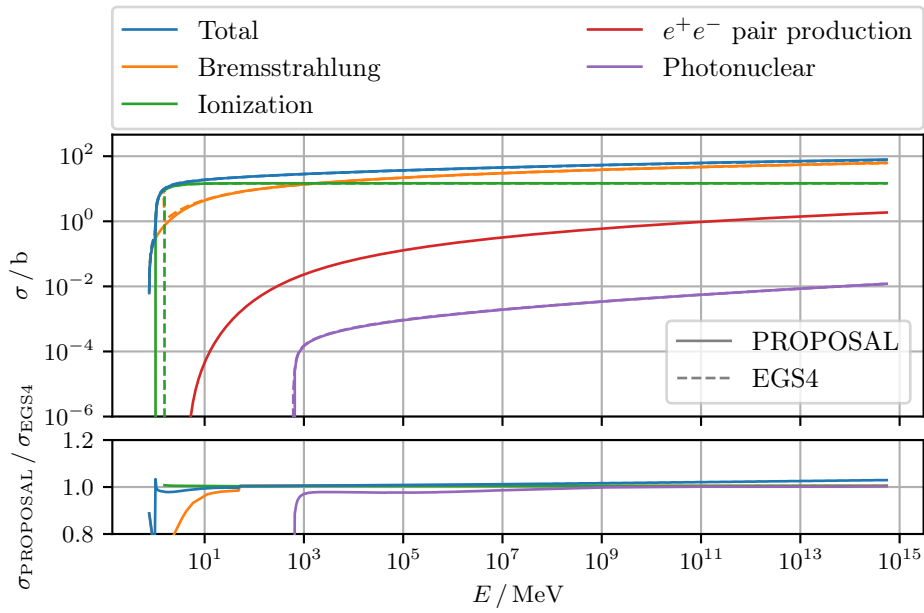


Figure A.3: Comparison of the utilized electron cross sections from PROPOSAL, which are used in CORSIKA 8, with the adapted cross sections from EGS4, which are used in CORSIKA 7 [178]. The cross sections are presented for air at **standard density**. The energy cut is set to 250 keV. The photonuclear cross section from EGS4 is corrected according to [178].

A.11 Parametrization of the U.S. Standard Atmosphere

The atmospheric density is modeled based on a parametrization of the U.S. Standard Atmosphere [216] given in [114], dividing the atmosphere into four exponential and

a linear layer. According to this parametrization, the grammage X above a height h in the atmosphere is given by

$$X(h) = a_i + b_i \exp(-h/c_i) \quad (\text{A.47})$$

for the first four layers with $h \leq 100$ km, while the fifth layer describes the atmosphere for $100 \text{ km} \leq h < 112.8$ km with

$$X(h) = a_i - b_i h/c_i, \quad (\text{A.48})$$

where the parameters a_i , b_i , and c_i are given in Table A.11. Figure A.4 visualizes the relation between h and X according to this parametrization.

Table A.11: Constants used in the parametrization of the U.S. Standard Atmosphere in five layers according to [114].

Altitude	$a_i / (\text{g}/\text{cm}^2)$	$b_i / (\text{g}/\text{cm}^2)$	c_i / cm
$0 \text{ km} \leq h < 4 \text{ km}$	-186.555305	1222.6562	994186.38
$4 \text{ km} \leq h < 10 \text{ km}$	-94.919	1144.9069	878153.55
$10 \text{ km} \leq h < 40 \text{ km}$	0.61289	1305.5948	636143.04
$40 \text{ km} \leq h < 100 \text{ km}$	0	540.1778	772170.16
$100 \text{ km} \leq h < 112.8 \text{ km}$	0.01128292	1	10^9

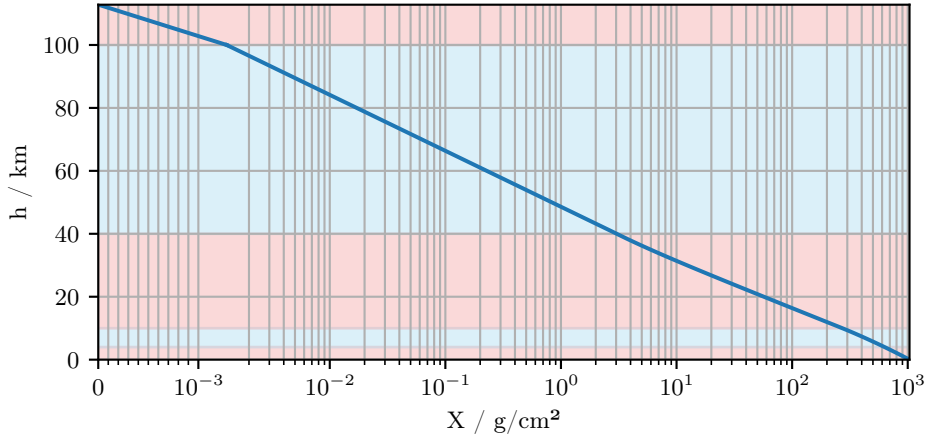


Figure A.4: Visualization of the relation between height h and the grammage X above this height, according to the parametrization of the U.S. Atmosphere given in [114]. The shaded areas indicate the five layers of the atmosphere. Note the change between a linear and logarithmic axis at $X(h = 100 \text{ km}) \approx 0.0013 \text{ g}/\text{cm}^2$.

A.12 Simulation of the LPM Effect for Proton Showers

Figure A.5 shows the longitudinal electromagnetic profiles of 5000 proton-induced showers, with a primary energy of 100 EeV and a *ParticleCut* of $E_{\text{track}}^{\text{EM}} = E_{\text{track}}^{\text{had.}} = E_{\text{track}}^{\mu} = 100$ TeV. For the first set of simulations, the LPM effect has been enabled, while for the second set of simulations, the LPM effect has been disabled, as described in Section 7.2.2. Note that the impact of the LPM effect on the development of proton-induced showers is much smaller compared to the impact for photon-induced showers with the same energy, which is shown in Figure 7.10. This effect is expected, as described in Section 6.3.2.

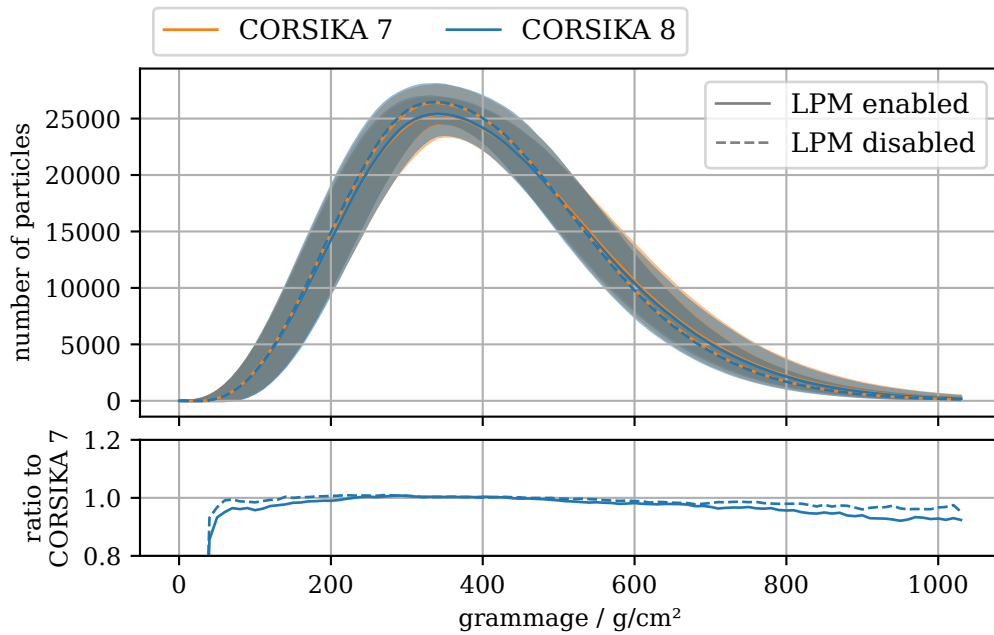


Figure A.5: Longitudinal profiles of electrons and positrons for showers initiated by 100 EeV protons, for both simulations with and without considering the LPM effect. The lines indicate the median number of particles, the shaded regions the interquartile range.

A.13 Full Radio Simulations of Electromagnetic Showers

In this section, more detailed results from the radio simulations described in [Section 7.4](#) are presented. This includes the longitudinal profiles of the individual showers, shown in [Figure A.6](#), the individual pulses and spectra 50 m from the shower core, presented in [Figure A.7](#) and [Figure A.8](#), and the individual pulses and spectra 200 m from the shower core, presented in [Figure A.9](#) and [Figure A.10](#).

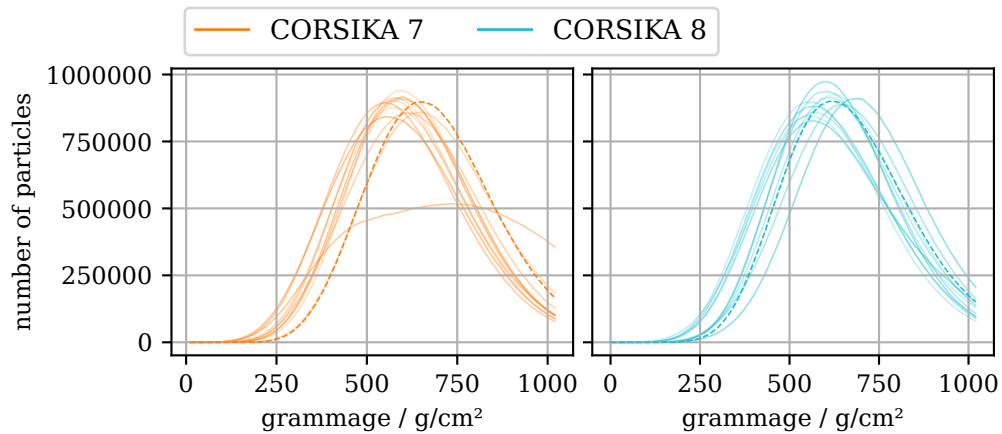


Figure A.6: Longitudinal profiles of charged electromagnetic particles, i.e., electrons and positrons, for the 1 PeV photon-induced showers presented in [Section 7.4](#). The dashed lines indicate the longitudinal profiles of the showers that have been selected for the analysis in [Section 7.4](#).

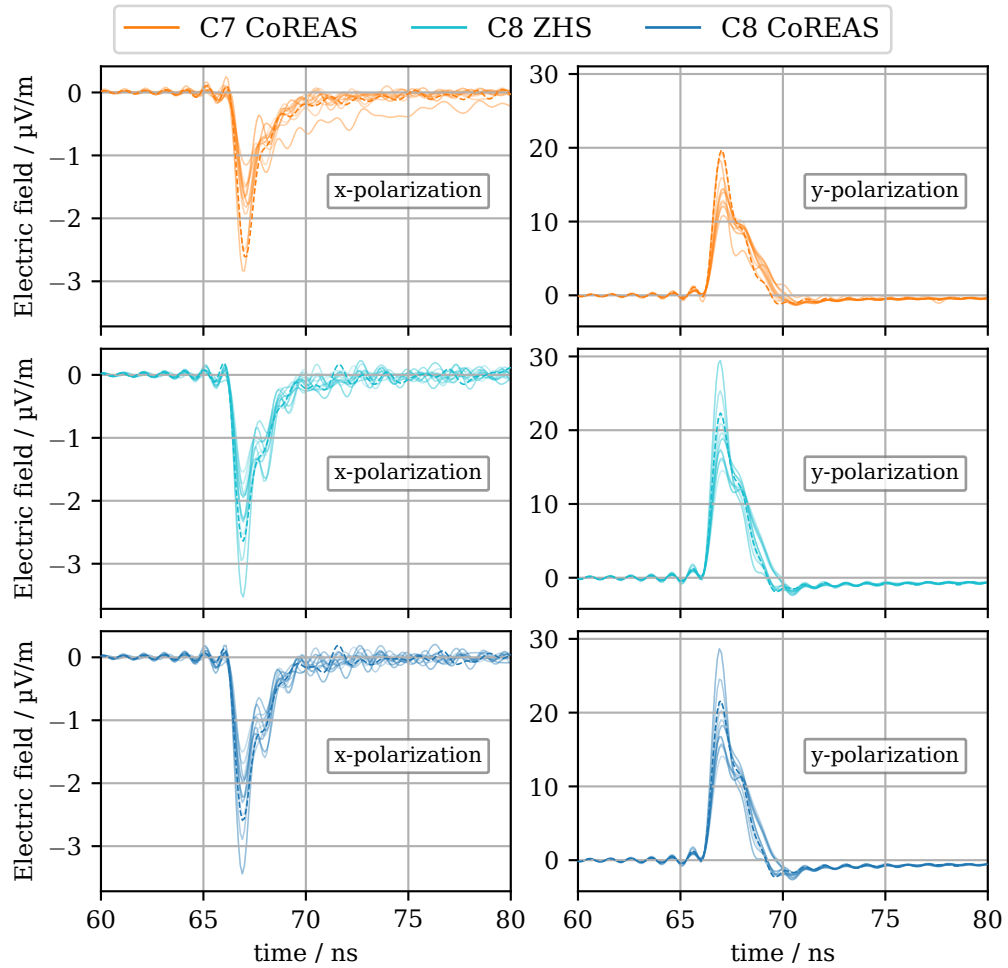


Figure A.7: Radio pulses for an antenna at $(x = 50 \text{ m}, y = 0 \text{ m})$, divided into the x - and y -polarization, for the radio emission from the individual 1 PeV, photon-induced showers described in Section 7.4. The dashed lines indicate the pulses of the showers that have been selected for the analysis in Section 7.4.

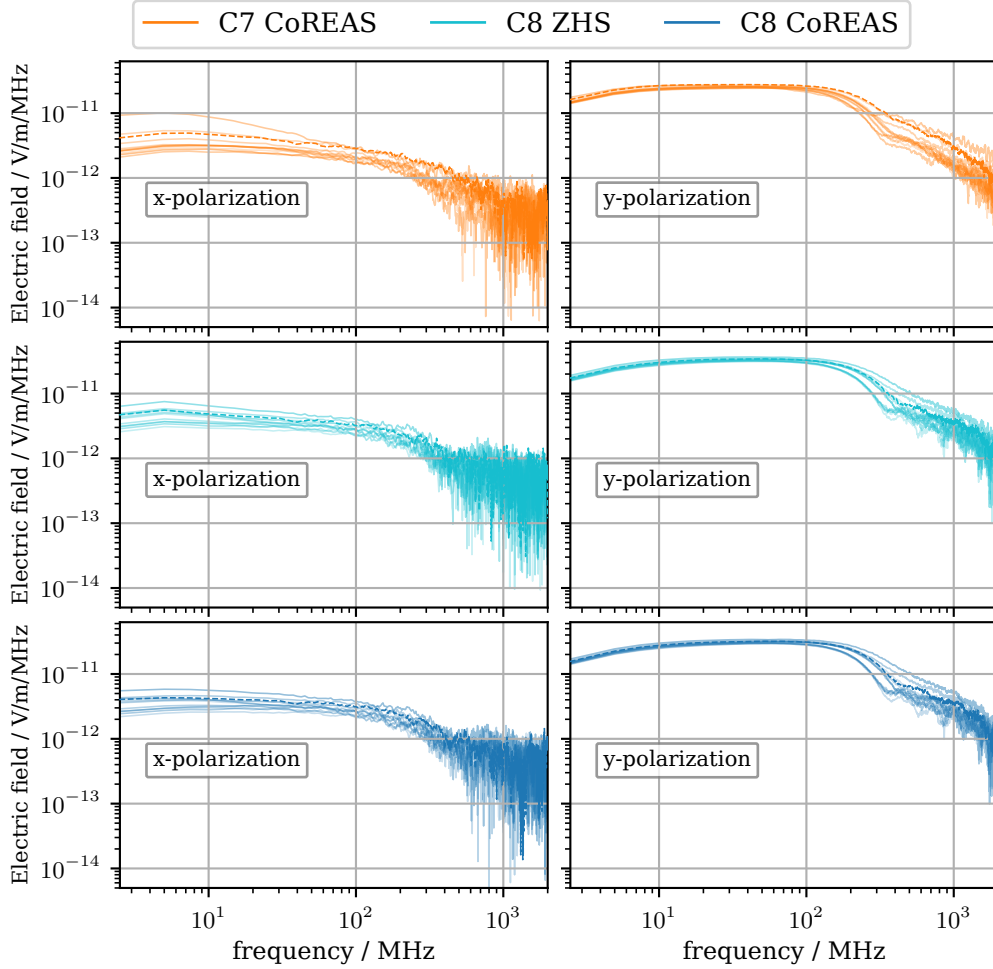


Figure A.8: Frequency spectra for an antenna at $(x = 50 \text{ m}, y = 0 \text{ m})$, divided into the x - and y -polarization, for the radio emission from the individual 1 PeV, photon-induced showers described in Section 7.4. The dashed lines indicate the spectra of the showers that have been selected for the analysis in Section 7.4.

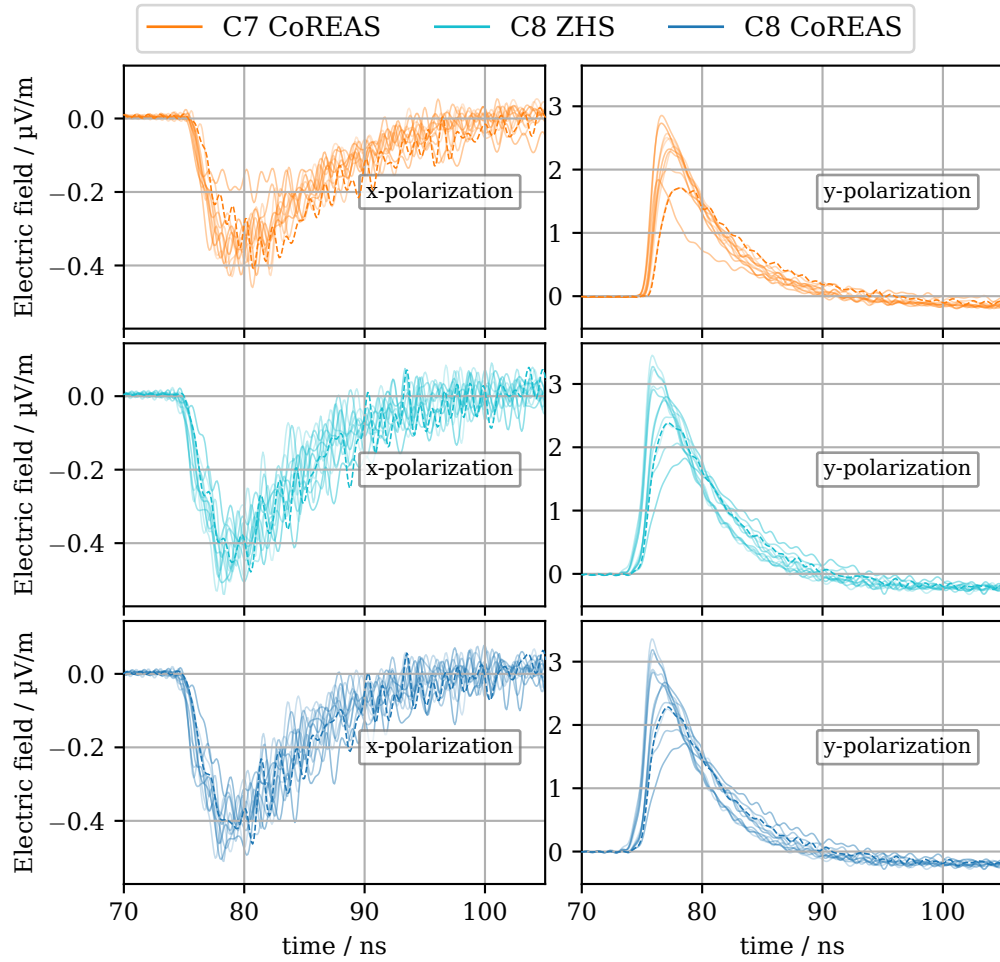


Figure A.9: Radio pulses for an antenna at $(x = 200 \text{ m}, y = 0 \text{ m})$, divided into the x - and y -polarization, for the radio emission from the individual 1 PeV, photon-induced showers described in Section 7.4. The dashed lines indicate the pulses of the showers that have been selected for the analysis in Section 7.4.

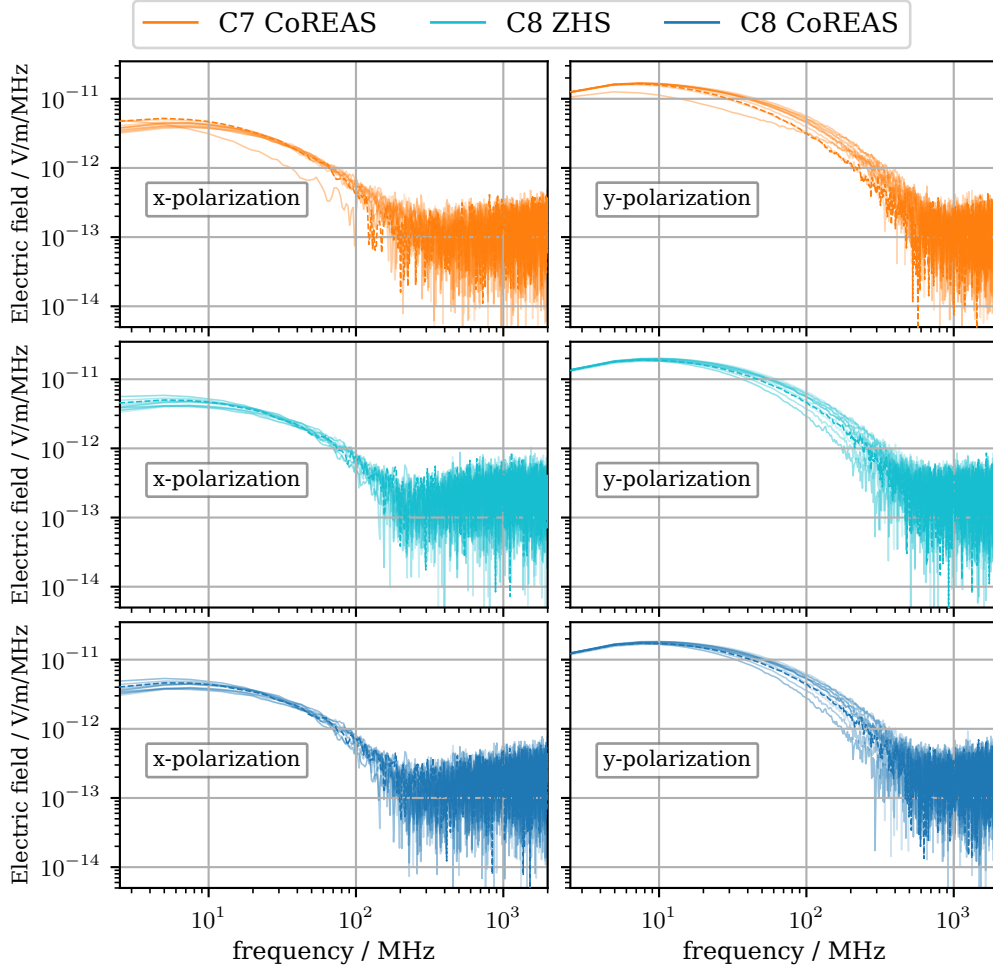


Figure A.10: Frequency spectra for an antenna at $(x = 200 \text{ m}, y = 0 \text{ m})$, divided into the x - and y -polarization, for the radio emission from the individual 1 PeV, photon-induced showers described in Section 7.4. The dashed lines indicate the spectra of the showers that have been selected for the analysis in Section 7.4.

B Reproducibility Information

The project CORSIKA 8 is continuously developed as an open-source project. By the time the simulations for this work have been performed, a release of CORSIKA 8 with a defined version number has not been published yet. Instead, all results of this work are, if not stated otherwise, based on the status of the `master` branch of the CORSIKA 8 GitLab repository from October 12, 2023.¹ As additional changes deviating from the status of this branch, muon pair production, as described in [Section 6.2.4](#), has been enabled as a process for photons. Furthermore, the photon cross section contribution for photonuclear interactions by the hadronic interaction model FLUKA has been disabled, since this process is already treated by PROPOSAL as described in [Section 6.2.5](#).

All shown results created with the software PROPOSAL have been produced with version `v7.6.2` [32], which is also the version of PROPOSAL currently used by CORSIKA 8.²

Instructions for the installation of PROPOSAL and CORSIKA 8 are given within the corresponding repositories.

¹The repository can be found under <https://gitlab.iap.kit.edu/AirShowerPhysics/corsika>.

²The repository can be found under <https://github.com/tudo-astroparticlephysics/PROPOSAL>.

C Additional Software Used for this Work

To create the results of this thesis, the usage of the following software is acknowledged:

- The Python package *matplotlib* [126] for data visualization.
- The Python package *numpy* [107] for data analysis using multi-dimensional arrays.
- The Python package *pandas* [211, 160] for data analysis of shower data.
- The command-line utility *GNU parallel* [209] for the parallel simulation of CORSIKA 8 showers on multiple cores.
- The Python package *PANAMA* [173] for the parallel simulation of CORSIKA 7 showers on multiple cores.
- The Python package *pycorsikaio* [153] for data extraction from CORSIKA 7 output.

Glossary

DOM Digital Optical Module. 36–38

IACT Imaging Air Cherenkov Telescope. 15–17, 106

Interquartile Range Region between the 25th and 75th percentile of the data. 107, 110, 111, 114, 117, 118, 120–123, 127, 150

LPM The **Landau-Pomeranchuk-Migdal** effect is a suppression of high-energy electromagnetic interactions, as described in Section 6.3. 2, 45, 56, 57, 59, 79, 87, 93–104, 113, 114, 135, 144, 150

Standard Density Air at standard density in the context of this work refers to a density of 1.205 g/cm^3 , corresponding to dry air at a temperature of 20°C and a pressure of 1 atm. 51, 58, 73, 95, 96, 101, 104, 105, 148

Standard Rock A medium defined as $Z = 11$, $A = 22$. 27, 30

TM The **Ter-Mikaelian** effect is a suppression of high-energy electromagnetic interactions, as described in Section 6.3. 27, 57, 93–97

Author's Publications Related to this Work

The author of this thesis has published the following works, related to the results of this thesis, as a main author. The publications are listed in chronological order.

- J.-M. Alameddine et al. “PROPOSAL: A library to propagate leptons and high energy photons.” In: *J. Phys. Conf. Ser.* 1690.1 (2020), p. 012021. DOI: [10.1088/1742-6596/1690/1/012021](https://doi.org/10.1088/1742-6596/1690/1/012021)
- J.-M. Alameddine et al. (CORSIKA 8 Collaboration). “Electromagnetic Shower Simulation for CORSIKA 8.” In: *PoS ICRC2021* (2022), p. 428. DOI: [10.22323/1.395.0428](https://doi.org/10.22323/1.395.0428)
- J.-M. Alameddine et al. “High-energy lepton and photon propagation with the simulation framework PROPOSAL.” in: *PoS ECRS* (2023), p. 076. DOI: [10.22323/1.423.0076](https://doi.org/10.22323/1.423.0076)
- A. Sandrock, J.-M. Alameddine, and F. Riehn (CORSIKA 8 Collaboration). “Validation of Electromagnetic Showers in CORSIKA 8.” In: *PoS ICRC2023* (2023), p. 393. DOI: [10.22323/1.444.0393](https://doi.org/10.22323/1.444.0393)
- J.-M. Alameddine et al. “Physics updates of the high-energy lepton and photon simulation tool PROPOSAL.” in: *PoS ICRC2023* (2023), p. 482. DOI: [10.22323/1.444.0482](https://doi.org/10.22323/1.444.0482)
- J.-M. Alameddine et al. *Improvements in charged lepton and photon propagation for the software PROPOSAL*. Submitted for publication to *Comput. Phys. Commun.* 2023. arXiv: [2311.13357](https://arxiv.org/abs/2311.13357) [[astro-ph.IM](https://arxiv.org/abs/2311.13357)]

The author of this thesis has contributed to the following publications related to the results of this work. The publications are listed in chronological order.

- P. Gutjahr et al. “Simulation of deflection uncertainties on directional reconstructions of muons using PROPOSAL.” in: *Eur. Phys. J. C* 82.12 (2022), p. 1143. DOI: [10.1140/epjc/s10052-022-11102-5](https://doi.org/10.1140/epjc/s10052-022-11102-5)
- K. Morik and W. Rhode, eds. *Machine Learning under Resource Constraints - Discovery in Physics*. De Gruyter, 2023. DOI: [doi:10.1515/9783110785968](https://doi.org/10.1515/9783110785968)
- J. L. Feng et al. “The Forward Physics Facility at the High-Luminosity LHC.” in: *J. Phys. G Nucl. Part. Phys.* 50.3 (2023), p. 030501. DOI: [10.1088/1361-6471/ac865e](https://doi.org/10.1088/1361-6471/ac865e)

Bibliography

- [1] A. Aab et al. (Pierre Auger Collaboration). “Measurement of the Fluctuations in the Number of Muons in Extensive Air Showers with the Pierre Auger Observatory.” In: *Phys. Rev. Lett.* 126 (2021), p. 152002. DOI: [10.1103/PhysRevLett.126.152002](https://doi.org/10.1103/PhysRevLett.126.152002).
- [2] A. Aab et al. (Pierre Auger Collaboration). “Muons in air showers at the Pierre Auger Observatory: Mean number in highly inclined events.” In: *Phys. Rev. D* 91 (2015), p. 032003. DOI: [10.1103/PhysRevD.91.032003](https://doi.org/10.1103/PhysRevD.91.032003).
- [3] M. G. Aartsen et al. (IceCube Collaboration). “Evidence for High-Energy Extraterrestrial Neutrinos at the IceCube Detector.” In: *Science* 342 (2013). DOI: [10.1126/science.1242856](https://doi.org/10.1126/science.1242856).
- [4] M. G. Aartsen et al. (IceCube Collaboration). “Neutrino emission from the direction of the blazar TXS 0506+056 prior to the IceCube-170922A alert.” In: *Science* 361 (2018), pp. 147–151. DOI: [10.1126/science.aat2890](https://doi.org/10.1126/science.aat2890).
- [5] M. G. Aartsen et al. (IceCube Collaboration). “The IceCube Neutrino Observatory: instrumentation and online systems.” In: *J. Instrum.* 12 (2017), P03012. DOI: [10.1088/1748-0221/12/03/P03012](https://doi.org/10.1088/1748-0221/12/03/P03012).
- [6] M. G. Aartsen et al. (IceCube Collaboration). “Time-Integrated Neutrino Source Searches with 10 Years of IceCube Data.” In: *Phys. Rev. Lett.* 124 (2020). DOI: [10.1103/physrevlett.124.051103](https://doi.org/10.1103/physrevlett.124.051103).
- [7] R. Abbasi et al. (IceCube Collaboration). “A convolutional neural network based cascade reconstruction for the IceCube Neutrino Observatory.” In: *J. Instrum.* 16 (2021), P07041. DOI: [10.1088/1748-0221/16/07/P07041](https://doi.org/10.1088/1748-0221/16/07/P07041).
- [8] R. Abbasi et al. (Telescope Array Collaboration). “An extremely energetic cosmic ray observed by a surface detector array.” In: *Science* 382 (2023), pp. 903–907. DOI: [10.1126/science.abo5095](https://doi.org/10.1126/science.abo5095).
- [9] R. Abbasi et al. (IceCube Collaboration). “Evidence for neutrino emission from the nearby active galaxy NGC 1068.” In: *Science* 378 (2022), pp. 538–543. DOI: [10.1126/science.abg3395](https://doi.org/10.1126/science.abg3395).

-
- [10] R. Abbasi et al. (IceCube Collaboration). “LeptonInjector and LeptonWeighter: A neutrino event generator and weighter for neutrino observatories.” In: *Comput. Phys. Commun.* 266 (2021), p. 108018. DOI: [10.1016/j.cpc.2021.108018](https://doi.org/10.1016/j.cpc.2021.108018).
- [11] R. Abbasi et al. (IceCube Collaboration). “Observation of high-energy neutrinos from the Galactic plane.” In: *Science* 380 (2023), pp. 1338–1343. DOI: [10.1126/science.adc9818](https://doi.org/10.1126/science.adc9818).
- [12] B. P. Abbott et al. (LIGO Scientific Collaboration, Virgo Collaboration). “Observation of Gravitational Waves from a Binary Black Hole Merger.” In: *Phys. Rev. Lett.* 116 (2016). DOI: [10.1103/physrevlett.116.061102](https://doi.org/10.1103/physrevlett.116.061102).
- [13] A. Abdul Halim et al. (Pierre Auger Collaboration). *Demonstrating Agreement between Radio and Fluorescence Measurements of the Depth of Maximum of Extensive Air Showers at the Pierre Auger Observatory*. Accepted for publication in *Phys. Rev. Lett.* 2023. arXiv: [2310.19963](https://arxiv.org/abs/2310.19963) [[astro-ph.HE](https://arxiv.org/abs/2310.19963)].
- [14] H. Abramowicz and A. Levy. *The ALLM parameterization of $\sigma_{tot}(\gamma^*p)$: An Update*. 1997. arXiv: [hep-ph/9712415](https://arxiv.org/abs/hep-ph/9712415).
- [15] H. Abramowicz et al. “A parametrization of $\sigma_T(\gamma^*p)$ above the resonance region for $Q^2 \geq 0$.” In: *Phys. Lett. B* 269 (1991), pp. 465–476. DOI: [10.1016/0370-2693\(91\)90202-2](https://doi.org/10.1016/0370-2693(91)90202-2).
- [16] M. A. Acero et al. (NOvA Collaboration). “New constraints on oscillation parameters from ν_e appearance and ν_μ disappearance in the NOvA experiment.” In: *Phys. Rev. D* 98 (2018), p. 032012. DOI: [10.1103/PhysRevD.98.032012](https://doi.org/10.1103/PhysRevD.98.032012).
- [17] B. S. Acharya et al. (The CTA Consortium). *Science with the Cherenkov Telescope Array*. World Scientific, 2019. DOI: [10.1142/10986](https://doi.org/10.1142/10986).
- [18] A. Achterberg et al. (IceCube Collaboration). “Limits on the High-Energy Gamma and Neutrino Fluxes from the SGR 1806-20 Giant Flare of 27 December 2004 with the AMANDA-II Detector.” In: *Phys. Rev. Lett.* 97 (2006). DOI: [10.1103/physrevlett.97.221101](https://doi.org/10.1103/physrevlett.97.221101).
- [19] J. Adam et al. (ALICE Collaboration). “Enhanced production of multi-strange hadrons in high-multiplicity proton–proton collisions.” In: *Nat. Phys.* 13 (2017), pp. 535–539. DOI: [10.1038/nphys4111](https://doi.org/10.1038/nphys4111).
- [20] P. Adamson et al. “The NuMI neutrino beam.” In: *Nucl. Instrum. Methods Phys. Res. A* 806 (2016), pp. 279–306. DOI: [10.1016/j.nima.2015.08.063](https://doi.org/10.1016/j.nima.2015.08.063).
- [21] S. Adrián-Martínez et al. “Letter of intent for KM3NeT 2.0.” In: *J. Phys. G Nucl. Part. Phys.* 43 (2016), p. 084001. DOI: [10.1088/0954-3889/43/8/084001](https://doi.org/10.1088/0954-3889/43/8/084001).

- [22] M. Agostini et al. “The Pacific Ocean Neutrino Experiment.” In: *Nat. Astron.* 4 (2020), pp. 913–915. DOI: [10.1038/s41550-020-1182-4](https://doi.org/10.1038/s41550-020-1182-4).
- [23] J. A. Aguilar et al. “Design and sensitivity of the Radio Neutrino Observatory in Greenland (RNO-G).” In: *J. Instrum.* 16 (2021), P03025. DOI: [10.1088/1748-0221/16/03/p03025](https://doi.org/10.1088/1748-0221/16/03/p03025).
- [24] J. A. Aguilar et al. “Reconstructing the neutrino energy for in-ice radio detectors.” In: *Eur. Phys. J. C* 82 (2022). DOI: [10.1140/epjc/s10052-022-10034-4](https://doi.org/10.1140/epjc/s10052-022-10034-4).
- [25] M. Aguilar et al. (AMS Collaboration). “First Result from the Alpha Magnetic Spectrometer on the International Space Station: Precision Measurement of the Positron Fraction in Primary Cosmic Rays of 0.5–350 GeV.” In: *Phys. Rev. Lett.* 110 (2013), p. 141102. DOI: [10.1103/PhysRevLett.110.141102](https://doi.org/10.1103/PhysRevLett.110.141102).
- [26] S. Aiello et al. “gSeaGen: The KM3NeT GENIE-based code for neutrino telescopes.” In: *Comput. Phys. Commun.* 256 (2020), p. 107477. DOI: [10.1016/j.cpc.2020.107477](https://doi.org/10.1016/j.cpc.2020.107477).
- [27] J.-M. Alameddine et al. (CORSIKA 8 Collaboration). “Electromagnetic Shower Simulation for CORSIKA 8.” In: *PoS ICRC2021* (2022), p. 428. DOI: [10.22323/1.395.0428](https://doi.org/10.22323/1.395.0428).
- [28] J.-M. Alameddine et al. “High-energy lepton and photon propagation with the simulation framework PROPOSAL.” In: *PoS ECRS* (2023), p. 076. DOI: [10.22323/1.423.0076](https://doi.org/10.22323/1.423.0076).
- [29] J.-M. Alameddine et al. *Improvements in charged lepton and photon propagation for the software PROPOSAL*. Submitted for publication to *Comput. Phys. Commun.* 2023. arXiv: [2311.13357](https://arxiv.org/abs/2311.13357) [[astro-ph.IM](https://arxiv.org/abs/2311.13357)].
- [30] J.-M. Alameddine et al. “Physics updates of the high-energy lepton and photon simulation tool PROPOSAL.” In: *PoS ICRC2023* (2023), p. 482. DOI: [10.22323/1.444.0482](https://doi.org/10.22323/1.444.0482).
- [31] J.-M. Alameddine et al. “PROPOSAL: A library to propagate leptons and high energy photons.” In: *J. Phys. Conf. Ser.* 1690 (2020), p. 012021. DOI: [10.1088/1742-6596/1690/1/012021](https://doi.org/10.1088/1742-6596/1690/1/012021).
- [32] J.-M. Alameddine et al. *tudo-astroparticlephysics/PROPOSAL*. Version 7.6.2. 2023. DOI: [10.5281/zenodo.8048101](https://doi.org/10.5281/zenodo.8048101).
- [33] A. Albert et al. (HAWC Collaboration). “Daily monitoring of TeV gamma-ray emission from Mrk 421, Mrk 501, and the Crab Nebula with HAWC.” In: *Astrophys. J.* 841 (2017), p. 100. DOI: [10.3847/1538-4357/aa729e](https://doi.org/10.3847/1538-4357/aa729e).

-
- [34] J. Albrecht et al. “The Muon Puzzle in cosmic-ray induced air showers and its connection to the Large Hadron Collider.” In: *Astrophys. Space Sci.* 367 (2022). DOI: [10.1007/s10509-022-04054-5](https://doi.org/10.1007/s10509-022-04054-5).
- [35] J. Aleksić et al. (MAGIC Collaboration). “The major upgrade of the MAGIC telescopes, Part II: A performance study using observations of the Crab Nebula.” In: *Astropart. Phys.* 72 (2016), pp. 76–94. DOI: [10.1016/j.astropartphys.2015.02.005](https://doi.org/10.1016/j.astropartphys.2015.02.005).
- [36] P. Allison et al. (ARA Collaboration). “Low-threshold ultrahigh-energy neutrino search with the Askaryan Radio Array.” In: *Phys. Rev. D* 105 (2022), p. 122006. DOI: [10.1103/physrevd.105.122006](https://doi.org/10.1103/physrevd.105.122006).
- [37] J. Alvarez-Muñiz, W. R. Carvalho, and E. Zas. “Monte Carlo simulations of radio pulses in atmospheric showers using ZHAireS.” In: *Astropart. Phys.* 35 (2012), pp. 325–341. DOI: [10.1016/j.astropartphys.2011.10.005](https://doi.org/10.1016/j.astropartphys.2011.10.005).
- [38] J. Alvarez-Muñiz and E. Zas. “Progress in the Simulation and Modelling of Coherent Radio Pulses from Ultra High-Energy Cosmic Particles.” In: *Universe* 8 (2022). DOI: [10.3390/universe8060297](https://doi.org/10.3390/universe8060297).
- [39] A. A. Alves et al. (CORSIKA 8 Collaboration). “CORSIKA 8 - A novel high-performance computing tool for particle cascade Monte Carlo simulations.” In: *EPJ Web Conf.* 251 (2021), p. 03038. DOI: [10.1051/epjconf/202125103038](https://doi.org/10.1051/epjconf/202125103038).
- [40] J. Ammerman-Yebra et al. (CORSIKA 8 Collaboration). “Simulations of cross media showers with CORSIKA 8.” In: *PoS ICRC2023* (2023), p. 442. DOI: [10.22323/1.444.0442](https://doi.org/10.22323/1.444.0442).
- [41] G. A. Anastasi (Pierre Auger Collaboration). “AugerPrime: The Pierre Auger Observatory upgrade.” In: *Nucl. Instrum. Methods Phys. Res. A* 1044 (2022), p. 167497. DOI: [10.1016/j.nima.2022.167497](https://doi.org/10.1016/j.nima.2022.167497).
- [42] C. Andreopoulos et al. “The GENIE neutrino Monte Carlo generator.” In: *Nucl. Instrum. Methods Phys. Res. A* 614 (2010), pp. 87–104. DOI: [10.1016/j.nima.2009.12.009](https://doi.org/10.1016/j.nima.2009.12.009).
- [43] E. Andrés et al. “Observation of high-energy neutrinos using Čerenkov detectors embedded deep in Antarctic ice.” In: *Nature* 410 (2001), pp. 441–443. DOI: [10.1038/35068509](https://doi.org/10.1038/35068509).
- [44] A. Anker et al. “Targeting ultra-high energy neutrinos with the ARIANNA experiment.” In: *Adv. Space Res.* 64 (2019), pp. 2595–2609. DOI: [10.1016/j.asr.2019.06.016](https://doi.org/10.1016/j.asr.2019.06.016).
- [45] T. Antoni et al. (KASCADE Collaboration). “The Cosmic ray experiment KASCADE.” In: *Nucl. Instrum. Meth. A* 513 (2003), pp. 490–510. DOI: [10.1016/S0168-9002\(03\)02076-X](https://doi.org/10.1016/S0168-9002(03)02076-X).

- [46] P. Antonioli et al. “A three-dimensional code for muon propagation through the rock: MUSIC.” In: *Astroparticle Physics* 7 (1997), pp. 357–368. DOI: [10.1016/S0927-6505\(97\)00035-2](https://doi.org/10.1016/S0927-6505(97)00035-2).
- [47] G. A. Askar’yan. “Excess negative charge of an electron-photon shower and its coherent radio emission.” In: *J. Exptl. Theoret. Phys.* 41 (1961), pp. 616–618.
- [48] J. Avva et al. “An in situ measurement of the radio-frequency attenuation in ice at Summit Station, Greenland.” In: *J. Glaciol.* 61 (2015), pp. 1005–1011. DOI: [10.3189/2015jog15j057](https://doi.org/10.3189/2015jog15j057).
- [49] D. S. Ayres et al. (NOvA Collaboration). *The NOvA Technical Design Report*. Tech. rep. FERMILAB-DESIGN-2007-01. 2007. DOI: [10.2172/935497](https://doi.org/10.2172/935497).
- [50] B. Badelek and J. Kwieciński. “The low- Q^2 , low- X region in electroproduction.” In: *Rev. Mod. Phys.* 68 (1996), pp. 445–471. DOI: [10.1103/RevModPhys.68.445](https://doi.org/10.1103/RevModPhys.68.445).
- [51] M. Bailes et al. “Gravitational-wave physics and astronomy in the 2020s and 2030s.” In: *Nat. Rev. Phys.* 3 (2021), pp. 344–366. DOI: [10.1038/s42254-021-00303-8](https://doi.org/10.1038/s42254-021-00303-8).
- [52] J. Baró et al. “PENELOPE: An algorithm for Monte Carlo simulation of the penetration and energy loss of electrons and positrons in matter.” In: *Nucl. Instrum. Methods Phys. Res. B* 100 (1995), pp. 31–46. DOI: [10.1016/0168-583X\(95\)00349-5](https://doi.org/10.1016/0168-583X(95)00349-5).
- [53] S. Bass. “Microscopic models for ultrarelativistic heavy ion collisions.” In: *Prog. Part. Nucl. Phys.* 41 (1998), pp. 255–369. DOI: [10.1016/s0146-6410\(98\)00058-1](https://doi.org/10.1016/s0146-6410(98)00058-1).
- [54] S. Baur et al. “Core-corona effect in hadron collisions and muon production in air showers.” In: *Phys. Rev. D* 107 (2023), p. 094031. DOI: [10.1103/physrevd.107.094031](https://doi.org/10.1103/physrevd.107.094031).
- [55] F. Benfenati, F. Filippini, and T. Chiarusi (KM3NeT Collaboration). “First scientific results of the KM3NeT neutrino telescope.” In: *EPJ Web Conf.* 283 (2023), p. 04009. DOI: [10.1051/epjconf/202328304009](https://doi.org/10.1051/epjconf/202328304009).
- [56] M. J. Berger and S. M. Seltzer. *Tables of energy losses and ranges of electrons and positrons*. Tech. rep. NASA SP-3012. National Aeronautics and Space Administration, 1964.
- [57] M. J. Berger et al. “Stopping Powers for Electrons and Positrons (ICRU Report No. 37).” In: *Journal of the International Commission on Radiation Units and Measurements* (1984). DOI: [10.1093/jicru/os19.2.Report37](https://doi.org/10.1093/jicru/os19.2.Report37).

-
- [58] H. A. Bethe. “Zur Theorie des Durchgangs schneller Korpuskularstrahlen durch Materie.” In: *Ann. Phys.* 397 (1930), pp. 325–400. DOI: [10.1002/andp.19303970303](https://doi.org/10.1002/andp.19303970303).
- [59] L. B. Bezrukov and E. V. Bugaev. “Nucleon shadowing effects in photonuclear interactions.” In: *Sov. J. Nucl. Phys.* 33 (1981), pp. 635–641.
- [60] A. Bielajew, R. Mohan, and C.-S. Chui. *Improved bremsstrahlung photon angular sampling in the EGS4 code system*. Tech. rep. PIRS-0203. National Research Council Canada, 1989.
- [61] A. Bielajew and D. Rogers. “PRESTA: The Parameter Reduced Electron-Step Transport Algorithm for Electron Monte Carlo Transport.” In: *Nucl. Instrum. Methods Phys. Res. B* 18 (1986), pp. 165–181. DOI: [10.1016/S0168-583X\(86\)80027-1](https://doi.org/10.1016/S0168-583X(86)80027-1).
- [62] C. Bierlich et al. *A comprehensive guide to the physics and usage of PYTHIA 8.3*. 2022. arXiv: [2203.11601](https://arxiv.org/abs/2203.11601) [hep-ph].
- [63] M. Bleicher et al. “Relativistic hadron-hadron collisions in the ultra-relativistic quantum molecular dynamics model.” In: *J. Phys. G Nucl. Part. Phys.* 25 (1999), pp. 1859–1896. DOI: [10.1088/0954-3899/25/9/308](https://doi.org/10.1088/0954-3899/25/9/308).
- [64] T. Böhlen et al. “The FLUKA Code: Developments and Challenges for High Energy and Medical Applications.” In: *Nucl. Data Sheets* 120 (2014), pp. 211–214. DOI: [10.1016/j.nds.2014.07.049](https://doi.org/10.1016/j.nds.2014.07.049).
- [65] J. Breitweg et al. “ZEUS results on the measurement and phenomenology of F_2 at low x and low Q^2 .” In: *Eur. Phys. J. C* 7 (1999), pp. 609–630. DOI: [10.1007/s100529901084](https://doi.org/10.1007/s100529901084).
- [66] R. Brun et al. *GEANT 3: user’s guide Geant 3.10, Geant 3.11*. Tech. rep. CERN-DD/EE/84-1. European Organization for Nuclear Research, 1987. URL: <https://cds.cern.ch/record/1119728>.
- [67] H. Burkhardt, S. R. Kelner, and R. P. Kokoulin. *Monte Carlo Generator for Muon Pair Production*. Tech. rep. CERN-SL-2002-016-AP, CLIC-NOTE-511. European Organization for Nuclear Research, 2002.
- [68] J. Butcher and H. Messel. “Electron number distribution in electron-photon showers in air and aluminium absorbers.” In: *Nucl. Phys.* 20 (1960), pp. 15–128. DOI: [10.1016/0029-5582\(60\)90162-0](https://doi.org/10.1016/0029-5582(60)90162-0).
- [69] A. V. Butkevich et al. “Comments on multiple scattering of high-energy muons in thick layers.” In: *Nucl. Instrum. Methods Phys. Res. A* 488 (2002), pp. 282–294. DOI: [10.1016/S0168-9002\(02\)00478-3](https://doi.org/10.1016/S0168-9002(02)00478-3).

- [70] D. A. Butler. “The Radio Signal of Cosmic Ray Air Showers and its Synthesis through Templates.” PhD thesis. Karlsruher Institut für Technologie (KIT), 2020.
- [71] D. O. Caldwell et al. “Measurement of Shadowing in Photon-Nucleus Total Cross Sections from 20 to 185 GeV.” In: *Phys. Rev. Lett.* 42 (1979), pp. 553–556. DOI: [10.1103/PhysRevLett.42.553](https://doi.org/10.1103/PhysRevLett.42.553).
- [72] Z. Cao et al. (LHAASO Collaboration). “Ultrahigh-energy photons up to 1.4 petaelectronvolts from 12 γ -ray Galactic sources.” In: *Nature* 594 (2021), pp. 33–36. DOI: [10.1038/s41586-021-03498-z](https://doi.org/10.1038/s41586-021-03498-z).
- [73] J. N. Capdevielle. “A Monte Carlo generator for cosmic-ray collisions.” In: *J. Phys. G Nucl. Part. Phys.* 15 (1989), p. 909. DOI: [10.1088/0954-3899/15/6/018](https://doi.org/10.1088/0954-3899/15/6/018).
- [74] J. N. Capdevielle. “Local age parameter and size estimation in EAS.” In: *Proceedings of the 22th International Cosmic Ray Conference*. Vol. 4. 1991, pp. 405–408.
- [75] G. Carminati et al. “Atmospheric MUons from PArametric formulas: a fast GEnerator for neutrino telescopes (MUPAGE).” In: *Comput. Phys. Commun.* 179 (2008), pp. 915–923. DOI: [10.1016/j.cpc.2008.07.014](https://doi.org/10.1016/j.cpc.2008.07.014).
- [76] A. Castellina et al. (Pierre Auger Collaboration). “The Pierre Auger Cosmic Ray Observatory.” In: *Nucl. Instrum. Methods Phys. Res. A* 798 (2015), pp. 172–213. DOI: [10.1016/j.nima.2015.06.058](https://doi.org/10.1016/j.nima.2015.06.058).
- [77] D. Chirkin and W. Rhode. *Propagating leptons through matter with Muon Monte Carlo (MMC)*. 2004. arXiv: [hep-ph/0407075](https://arxiv.org/abs/hep-ph/0407075).
- [78] Z. Citron et al. “Report from Working Group 5: Future physics opportunities for high-density QCD at the LHC with heavy-ion and proton beams.” In: *CERN Yellow Rep. Monogr.* 7 (2019). Ed. by A. Dainese et al., pp. 1159–1410. DOI: [10.23731/CYRM-2019-007.1159](https://doi.org/10.23731/CYRM-2019-007.1159).
- [79] H. Davies, H. A. Bethe, and L. C. Maximon. “Theory of Bremsstrahlung and Pair Production. II. Integral Cross Section for Pair Production.” In: *Phys. Rev.* 93 (1954), pp. 788–795. DOI: [10.1103/PhysRev.93.788](https://doi.org/10.1103/PhysRev.93.788).
- [80] B. Degrange and G. Fontaine. “Introduction to high-energy gamma-ray astronomy.” In: *Comptes Rendus Physique* 16 (2015), pp. 587–599. DOI: [10.1016/j.crhy.2015.07.003](https://doi.org/10.1016/j.crhy.2015.07.003).
- [81] H. Drescher et al. “Parton-based Gribov–Regge theory.” In: *Phys. Rep.* 350 (2001), pp. 93–289. DOI: [10.1016/s0370-1573\(00\)00122-8](https://doi.org/10.1016/s0370-1573(00)00122-8).

- [82] S. Duane, A. Bielajew, and D. W. O. Rogers. *Use of ICRU-37/NBS collision stopping powers in the EGS4 system*. Tech. rep. PIRS-0173. National Research Council Canada, 1989.
- [83] M. Dunsch. “Make PROPOSAL great again.” MA thesis. TU Dortmund University, 2018.
- [84] M. Dunsch et al. “Recent improvements for the lepton propagator PROPOSAL.” In: *Comput. Phys. Commun.* 242 (2019), pp. 132–144. DOI: [10.1016/j.cpc.2019.03.021](https://doi.org/10.1016/j.cpc.2019.03.021).
- [85] S. I. Dutta et al. “Propagation of muons and taus at high energies.” In: *Phys. Rev. D* 63 (2001), p. 094020. DOI: [10.1103/physrevd.63.094020](https://doi.org/10.1103/physrevd.63.094020).
- [86] R. Engel, D. Heck, and T. Pierog. “Extensive Air Showers and Hadronic Interactions at High Energy.” In: *Annu. Rev. Nucl. Part. Sci.* 61 (2011), pp. 467–489. DOI: [10.1146/annurev.nucl.012809.104544](https://doi.org/10.1146/annurev.nucl.012809.104544).
- [87] R. Engel et al. “The hadronic interaction model Sibyll – past, present and future.” In: *EPJ Web Conf.* 145 (2017), p. 08001. DOI: [10.1051/epjconf/201614508001](https://doi.org/10.1051/epjconf/201614508001).
- [88] R. Engel et al. “Towards A Next Generation of CORSIKA: A Framework for the Simulation of Particle Cascades in Astroparticle Physics.” In: *Comput. Softw. Big Sci.* 3 (2018). DOI: [10.1007/s41781-018-0013-0](https://doi.org/10.1007/s41781-018-0013-0).
- [89] B. Falkenburg and W. Rhode, eds. *From Ultra Rays to Astroparticles*. Springer Dordrecht, 2012. DOI: [10.1007/978-94-007-5422-5](https://doi.org/10.1007/978-94-007-5422-5).
- [90] A. Fedynitch. “Cascade equations and hadronic interactions at very high energies.” PhD thesis. Karlsruher Institut für Technologie (KIT), 2015.
- [91] A. Fedynitch et al. “Calculation of conventional and prompt lepton fluxes at very high energy.” In: *EPJ Web Conf.* 99 (2015), p. 08001. DOI: [10.1051/epjconf/20159908001](https://doi.org/10.1051/epjconf/20159908001).
- [92] A. Fedynitch et al. “Hadronic interaction model Sibyll 2.3c and inclusive lepton fluxes.” In: *Phys. Rev. D* 100 (2019), p. 103018. DOI: [10.1103/PhysRevD.100.103018](https://doi.org/10.1103/PhysRevD.100.103018).
- [93] J. L. Feng et al. “The Forward Physics Facility at the High-Luminosity LHC.” In: *J. Phys. G Nucl. Part. Phys.* 50 (2023), p. 030501. DOI: [10.1088/1361-6471/ac865e](https://doi.org/10.1088/1361-6471/ac865e).
- [94] A. Ferrari et al. *FLUKA: A multi-particle transport code (Program version 2005)*. Tech. rep. CERN-2005-010, SLAC-R-773, INFN-TC-05-11. 2005. DOI: [10.2172/877507](https://doi.org/10.2172/877507).
- [95] H. Fesefeldt. *The Simulation of Hadronic Showers: Physics and Applications*. Tech. rep. PITHA-85/02. RWTH Aachen, 1985.

- [96] T. K. Gaisser, R. Engel, and E. Resconi. *Cosmic Rays and Particle Physics*. 2nd ed. Cambridge University Press, 2016. DOI: [10.1017/CB09781139192194](https://doi.org/10.1017/CB09781139192194).
- [97] D. García-Fernández, A. Nelles, and C. Glaser. “Signatures of secondary leptons in radio-neutrino detectors in ice.” In: *Phys. Rev. D* 102 (2020), p. 083011. DOI: [10.1103/physrevd.102.083011](https://doi.org/10.1103/physrevd.102.083011).
- [98] A. Gazizov and M. Kowalski. “ANIS: High energy neutrino generator for neutrino telescopes.” In: *Comput. Phys. Commun.* 172 (2005), pp. 203–213. DOI: [10.1016/j.cpc.2005.03.113](https://doi.org/10.1016/j.cpc.2005.03.113).
- [99] Geant4 Collaboration. *Geant4 Physics Reference Manual, 11.2*. URL: <https://geant4-userdoc.web.cern.ch/UsersGuides/PhysicsReferenceManual/html/index.html> (visited on 01/12/2024).
- [100] M. Geisel-Brinck. “Revision of the multiple scattering algorithms in PROPOSAL.” Bachelor thesis. TU Dortmund University, 2013.
- [101] A. G. D. Giler and V. de Souza. “Cosmic-ray measurements with an array of Cherenkov telescopes using reconstruction of longitudinal profiles of air showers.” In: *Astropart. Phys.* 148 (2023), p. 102817. DOI: [10.1016/j.astropartphys.2023.102817](https://doi.org/10.1016/j.astropartphys.2023.102817).
- [102] J. H. Gladstone and T. P. Dale. “Researches on the Refraction, Dispersion, and Sensitiveness of Liquids.” In: *Philosophical Transactions of the Royal Society of London* 153 (1863), pp. 317–343. DOI: [10.1098/rstl.1863.0014](https://doi.org/10.1098/rstl.1863.0014).
- [103] C. Glaser et al. “NuRadioMC: simulating the radio emission of neutrinos from interaction to detector.” In: *Eur. Phys. J. C* 80 (2020), p. 77. DOI: [10.1140/epjc/s10052-020-7612-8](https://doi.org/10.1140/epjc/s10052-020-7612-8).
- [104] M. Gottowik et al. “Determination of the absolute energy scale of extensive air showers via radio emission: Systematic uncertainty of underlying first-principle calculations.” In: *Astropart. Phys.* 103 (2018), pp. 87–93. DOI: [10.1016/j.astropartphys.2018.07.004](https://doi.org/10.1016/j.astropartphys.2018.07.004).
- [105] D. E. Groom, N. V. Mokhov, and S. I. Striganov. “Muon stopping power and range tables 10 MeV–100 TeV.” In: *At. Data Nucl. Data Tables* 78 (2001), pp. 183–356. DOI: [10.1006/adnd.2001.0861](https://doi.org/10.1006/adnd.2001.0861).
- [106] P. Gutjahr et al. “Simulation of deflection uncertainties on directional reconstructions of muons using PROPOSAL.” In: *Eur. Phys. J. C* 82 (2022), p. 1143. DOI: [10.1140/epjc/s10052-022-11102-5](https://doi.org/10.1140/epjc/s10052-022-11102-5).
- [107] C. R. Harris et al. “Array programming with NumPy.” In: *Nature* 585 (2020), pp. 357–362. DOI: [10.1038/s41586-020-2649-2](https://doi.org/10.1038/s41586-020-2649-2).
- [108] D. Heck. *New Treatment of the Conversion $\gamma \rightarrow \mu^+ + \mu^-$ in CORSIKA*. Tech. rep. FZKA-7525. Forschungszentrum Karlsruhe, 2009.

-
- [109] D. Heck. *Production of Vector Mesons by Photonuclear Interactions in the Program CORSIKA*. Tech. rep. Forschungszentrum Karlsruhe, 2012. DOI: [10.5445/IR/1000034381](https://doi.org/10.5445/IR/1000034381).
- [110] D. Heck. *The CURVED version of the air shower simulation program CORSIKA*. Tech. rep. FZKA-6954. Forschungszentrum Karlsruhe, 2004.
- [111] D. Heck and R. Engel. *The EHISTORY and MUPROD Options of the Air Shower Simulation Program CORSIKA*. Tech. rep. Karlsruher Institut für Technologie (KIT), 2013. DOI: [10.5445/IR/1000034601](https://doi.org/10.5445/IR/1000034601).
- [112] D. Heck and J. Knapp. *Upgrade of the Monte Carlo Code CORSIKA to Simulate Extensive Air Showers with Energies 10^{20} eV*. Tech. rep. FZKA-6097. Forschungszentrum Karlsruhe, 1998.
- [113] D. Heck et al. *CORSIKA: A Monte Carlo code to simulate extensive air showers*. Tech. rep. FZKA-6019. Forschungszentrum Karlsruhe, 1998.
- [114] D. Heck and T. Pierog. *Extensive Air Shower Simulation with CORSIKA: A User's Guide (Version 7.7410 from May 1, 2021)*. 2021. URL: <https://web.iap.kit.edu/corsika/usersguide/usersguide.pdf> (visited on 01/12/2024).
- [115] W. Heitler. *The Quantum Theory of Radiation*. Clarendon Press, 1954.
- [116] V. L. Highland. “Some practical remarks on multiple scattering.” In: *Nucl. Instrum. Methods* 129 (1975), pp. 497–499. DOI: [10.1016/0029-554X\(75\)90743-0](https://doi.org/10.1016/0029-554X(75)90743-0).
- [117] A. M. Hillas. “Two Interesting Techniques for Monte-Carlo Simulation of Very High Energy Hadron Cascades.” In: *Proceedings of the 17th International Cosmic Ray Conference*. Vol. 8. 1981, p. 193.
- [118] H. Hirayama et al. *The EGS5 code system*. Tech. rep. SLAC-R-730. Stanford Linear Accelerator Center (SLAC), 2005. DOI: [10.2172/877459](https://doi.org/10.2172/877459).
- [119] J. Holder et al. (VERITAS Collaboration). “The first VERITAS telescope.” In: *Astropart. Phys.* 25 (2006), pp. 391–401. DOI: [10.1016/j.astropartphys.2006.04.002](https://doi.org/10.1016/j.astropartphys.2006.04.002).
- [120] J. R. Hörandel (Pierre Auger Collaboration). “Status and prospects of the Auger Radio Detector.” In: *PoS ECRS* (2023), p. 095. DOI: [10.22323/1.423.0095](https://doi.org/10.22323/1.423.0095).
- [121] J. H. Hubbell. *Photon Cross Sections, Attenuation Coefficients, and Energy Absorption Coefficients From 10 keV to 100 GeV*. Tech. rep. NSRDS-NBS 29. National Bureau of Standards, 1969.

- [122] J. M. Hubbell and S. M. Seltzer. *Tables of X-Ray Mass Attenuation Coefficients and Mass Energy-Absorption Coefficients from 1 keV to 20 MeV for Elements $Z = 1$ to 92 and 48 Additional Substances of Dosimetric Interest*. Tech. rep. NISTIR 5632. National Institute of Standards and Technology, 1995.
- [123] T. Huege, M. Ludwig, and C. W. James. “Simulating radio emission from air showers with CoREAS.” In: *AIP Conf. Proc.* 1535 (2013), pp. 128–132. DOI: [10.1063/1.4807534](https://doi.org/10.1063/1.4807534).
- [124] T. Huege. “Radio Detection of Cosmic Rays—Achievements and Future Potential.” In: *Proceedings of the 2016 International Conference on Ultra-High Energy Cosmic Rays*. Vol. 19. 2018, p. 011031. DOI: [10.7566/jpscp.19.011031](https://doi.org/10.7566/jpscp.19.011031).
- [125] T. Huege and M. Reininghaus (CORSIKA 8 Collaboration). “The particle-shower simulation code CORSIKA 8.” In: *PoS ICRC2023* (2023), p. 310. DOI: [10.22323/1.444.0310](https://doi.org/10.22323/1.444.0310).
- [126] J. D. Hunter. “Matplotlib: A 2D graphics environment.” In: *Comput. Sci. Eng.* 9 (2007), pp. 90–95. DOI: [10.1109/MCSE.2007.55](https://doi.org/10.1109/MCSE.2007.55).
- [127] IceCube Collaboration. *Neutrinos and gamma rays, a partnership to explore the extreme universe*. 2016. URL: <https://icecube.wisc.edu/news/research/2016/10/neutrinos-and-gamma-rays-partnership-to-explore-extreme-universe/> (visited on 11/29/2023).
- [128] J. Jelley et al. “Radio pulses from extensive cosmic-ray air showers.” In: *Nature* 205 (1965), pp. 327–328. DOI: [10.1038/205327a0](https://doi.org/10.1038/205327a0).
- [129] N. Kalmykov, S. Ostapchenko, and A. Pavlov. “Quark-gluon-string model and EAS simulation problems at ultra-high energies.” In: *Nucl. Phys. B Proc. Suppl.* 52 (1997), pp. 17–28. DOI: [10.1016/S0920-5632\(96\)00846-8](https://doi.org/10.1016/S0920-5632(96)00846-8).
- [130] K.-H. Kampert and M. Unger. “Measurements of the cosmic ray composition with air shower experiments.” In: *Astropart. Phys.* 35 (2012), pp. 660–678. DOI: [10.1016/j.astropartphys.2012.02.004](https://doi.org/10.1016/j.astropartphys.2012.02.004).
- [131] N. Karastathis, T. Huege, and J. Ammerman-Yebra (CORSIKA 8 Collaboration). “Simulations of radio emission from air showers with CORSIKA 8.” In: *PoS ICRC2021* (2022), p. 427. DOI: [10.22323/1.395.0427](https://doi.org/10.22323/1.395.0427).
- [132] N. Karastathis et al. (CORSIKA 8 Collaboration). “Simulating radio emission from air showers with CORSIKA 8.” In: *PoS ICRC2023* (2023), p. 425. DOI: [10.22323/1.444.0425](https://doi.org/10.22323/1.444.0425).
- [133] U. Katz and C. Spiering. “High-energy neutrino astrophysics: Status and perspectives.” In: *Prog. Part. Nucl. Phys.* 67 (2012), pp. 651–704. DOI: [10.1016/j.pnpnp.2011.12.001](https://doi.org/10.1016/j.pnpnp.2011.12.001).

-
- [134] I. Kawrakow et al. *EGSnrc toolkit for Monte Carlo simulation of ionizing radiation transport*. 2000. DOI: [10.4224/40001303](https://doi.org/10.4224/40001303).
- [135] S. R. Kelner, R. P. Kokoulin, and A. A. Petrukhin. *About cross section for high-energy muon bremsstrahlung*. Preprint MEPhI 024-95. 1995.
- [136] S. R. Kelner. “Pair Production in Collisions between Muons and Atomic Electrons.” In: *Phys. Atom. Nucl.* 61 (1998), pp. 448–456.
- [137] S. R. Kelner, R. P. Kokoulin, and A. A. Petrukhin. “Direct production of muon pairs by high-energy muons.” In: *Phys. Atom. Nucl.* 63 (2000), pp. 1603–1611. DOI: [10.1134/1.1312894](https://doi.org/10.1134/1.1312894).
- [138] S. R. Kelner, R. P. Kokoulin, and A. A. Petrukhin. “Radiation Logarithm in the Hartree-Fock Model.” In: *Phys. Atom. Nucl.* 62 (1999), pp. 1894–1898. DOI: [10.1134/1.855464](https://doi.org/10.1134/1.855464).
- [139] O. Klein and Y. Nishina. “Über die Streuung von Strahlung durch freie Elektronen nach der neuen relativistischen Quantendynamik von Dirac.” In: *Z. Phys.* 52 (1929), pp. 853–868. DOI: [10.1007/BF01366453](https://doi.org/10.1007/BF01366453).
- [140] S. Klein. “Suppression of bremsstrahlung and pair production due to environmental factors.” In: *Rev. Mod. Phys.* 71 (1999), pp. 1501–1538. DOI: [10.1103/RevModPhys.71.1501](https://doi.org/10.1103/RevModPhys.71.1501).
- [141] J. Knapp et al. “Extensive air shower simulations at the highest energies.” In: *Astropart. Phys.* 19 (2003), pp. 77–99. DOI: [10.1016/S0927-6505\(02\)00187-1](https://doi.org/10.1016/S0927-6505(02)00187-1).
- [142] H. W. Koch and J. W. Motz. “Bremsstrahlung Cross-Section Formulas and Related Data.” In: *Rev. Mod. Phys.* 31 (1959), pp. 920–955. DOI: [10.1103/RevModPhys.31.920](https://doi.org/10.1103/RevModPhys.31.920).
- [143] J.-H. Köhne et al. “PROPOSAL: A tool for propagation of charged leptons.” In: *Comput. Phys. Commun.* 184 (2013), pp. 2070–2090. DOI: [10.1016/j.cpc.2013.04.001](https://doi.org/10.1016/j.cpc.2013.04.001).
- [144] J.-H. Köhne. “Der Leptonpropagator PROPOSAL.” PhD thesis. TU Dortmund University, 2013. DOI: [10.17877/DE290R-13191](https://doi.org/10.17877/DE290R-13191).
- [145] R. P. Kokoulin. “Uncertainties in underground muon flux calculations.” In: *Nucl. Phys. B Proc. Suppl.* 70 (1999), pp. 475–479. DOI: [10.1016/S0920-5632\(98\)00475-7](https://doi.org/10.1016/S0920-5632(98)00475-7).
- [146] R. P. Kokoulin and A. A. Petrukhin. “Influence of the nuclear formfactor on the cross section of electron pair production by high-energy muons.” In: *Proceedings of the 12th International Cosmic Ray Conference*. Vol. 6. 1971, pp. 2436–2444.

- [147] E. Konishi et al. “On the characteristics of individual cascade showers with the LPM effect at extremely high energies.” In: *J. Phys. G Nucl. Part. Phys.* 17 (1991), p. 719. DOI: [10.1088/0954-3899/17/5/018](https://doi.org/10.1088/0954-3899/17/5/018).
- [148] T. Kozynets, A. Fedynitch, and D. J. Koskinen. “Atmospheric lepton fluxes via two-dimensional matrix cascade equations.” In: *Phys. Rev. D* 108 (2023), p. 103040. DOI: [10.1103/PhysRevD.108.103040](https://doi.org/10.1103/PhysRevD.108.103040).
- [149] M. Krause et al. “High energy astroparticle physics for high school students.” In: *PoS ICRC2015* (2015), p. 304. DOI: [10.22323/1.236.0304](https://doi.org/10.22323/1.236.0304).
- [150] A. A. Lagutin, A. V. Plyasheshnikov, and V. Uchaikin. “The Radial Distribution of Electromagnetic Cascade Particles in the Air.” In: *Proceedings of the 16th International Cosmic Ray Conference*. Vol. 7. 1979, pp. 18–23.
- [151] L. D. Landau and I. I. Pomeranchuk. “The limits of applicability of the theory of Bremsstrahlung by electrons and of the creation of pairs at large energies.” In: *Dokl. Akad. Nauk SSSR* 92 (1953), p. 535. DOI: [10.1016/b978-0-08-010586-4.50080-8](https://doi.org/10.1016/b978-0-08-010586-4.50080-8).
- [152] J. Lazar (TAMBO Collaboration). “Current status of simulation for the Tau Air-Shower Mountain-Based Observatory.” In: *PoS ICRC2023* (2023), p. 1117. DOI: [10.22323/1.444.1117](https://doi.org/10.22323/1.444.1117).
- [153] M. Linhoff and M. Peresano. *pycorsikaio*. Version 0.4.0. 2023. URL: <https://github.com/cta-observatory/pycorsikaio>.
- [154] P. Lipari and T. Stanev. “Propagation of multi-TeV muons.” In: *Phys. Rev. D* 44 (1991), pp. 3543–3554. DOI: [10.1103/PhysRevD.44.3543](https://doi.org/10.1103/PhysRevD.44.3543).
- [155] W. Lohmann, R. Kopp, and R. Voss. *Energy Loss of Muons in the Energy Range 1-10000 GeV*. Tech. rep. CERN-85-03. European Organization for Nuclear Research, 1985. DOI: [10.5170/CERN-1985-003](https://doi.org/10.5170/CERN-1985-003).
- [156] G. R. Lynch and O. I. Dahl. “Approximations to multiple Coulomb scattering.” In: *Nucl. Instrum. Methods Phys. Res. B* 58 (1991), pp. 6–10. DOI: [10.1016/0168-583X\(91\)95671-Y](https://doi.org/10.1016/0168-583X(91)95671-Y).
- [157] G. Maier, O. Gueta, and R. Zanin. *CTAO Instrument Response Functions: Comparison of prod5 and prod3b releases*. Version 1.0. 2023. DOI: [10.5281/zenodo.8050921](https://doi.org/10.5281/zenodo.8050921).
- [158] Y. Malyshkin (Baikal-GVD Collaboration). “Baikal-GVD neutrino telescope: Design reference 2022.” In: *Nucl. Instrum. Methods Phys. Res. A* 1050 (2023), p. 168117. DOI: [10.1016/j.nima.2023.168117](https://doi.org/10.1016/j.nima.2023.168117).
- [159] J. Matthews. “A Heitler model of extensive air showers.” In: *Astropart. Phys.* 22 (2005), pp. 387–397. DOI: [10.1016/j.astropartphys.2004.09.003](https://doi.org/10.1016/j.astropartphys.2004.09.003).

-
- [160] W. McKinney. “Data Structures for Statistical Computing in Python.” In: *Proceedings of the 9th Python in Science Conference*. 2010, pp. 56–61. DOI: [10.25080/Majora-92bf1922-00a](https://doi.org/10.25080/Majora-92bf1922-00a).
- [161] M. Meier. “Search for Astrophysical Tau Neutrinos using 7.5 years of IceCube Data.” PhD thesis. TU Dortmund University, 2019.
- [162] S. Meighen-Berger, A. Fedynitch, and M. Huber. *EmCa – Electromagnetic-Cascades Simulation Package*. 2019. arXiv: [1907.06924 \[astro-ph.HE\]](https://arxiv.org/abs/1907.06924).
- [163] A. B. Migdal. “Bremsstrahlung and Pair Production in Condensed Media at High Energies.” In: *Phys. Rev.* 103 (1956), pp. 1811–1820. DOI: [10.1103/PhysRev.103.1811](https://doi.org/10.1103/PhysRev.103.1811).
- [164] G. Molière. “Theorie der Streuung schneller geladener Teilchen I. Einzelstreuung am abgeschirmten Coulomb-Feld.” In: *Z. Naturforsch. A* 2 (1947), pp. 133–145. DOI: [10.1515/zna-1947-0302](https://doi.org/10.1515/zna-1947-0302).
- [165] G. Molière. “Theorie der Streuung schneller geladener Teilchen II. Mehrfach- und Vielfachstreuung.” In: *Z. Naturforsch. A* 3 (1948), pp. 78–97. DOI: [10.1515/zna-1948-0203](https://doi.org/10.1515/zna-1948-0203).
- [166] L. Morejon et al. “Improved photomeson model for interactions of cosmic ray nuclei.” In: *J. Cosmol. Astropart. Phys.* 2019 (2019), p. 007. DOI: [10.1088/1475-7516/2019/11/007](https://doi.org/10.1088/1475-7516/2019/11/007).
- [167] K. Morik and W. Rhode, eds. *Machine Learning under Resource Constraints - Discovery in Physics*. De Gruyter, 2023. DOI: [doi:10.1515/9783110785968](https://doi.org/10.1515/9783110785968).
- [168] J. W. Motz, H. A. Olsen, and H. W. Koch. “Pair Production by Photons.” In: *Rev. Mod. Phys.* 41 (1969), pp. 581–639. DOI: [10.1103/RevModPhys.41.581](https://doi.org/10.1103/RevModPhys.41.581).
- [169] A. Mücke et al. “Monte Carlo simulations of photohadronic processes in astrophysics.” In: *Comput. Phys. Commun.* 124 (2000), pp. 290–314. DOI: [10.1016/s0010-4655\(99\)00446-4](https://doi.org/10.1016/s0010-4655(99)00446-4).
- [170] L. Nellen. Private Communication. 2024.
- [171] W. R. Nelson, H. Hirayama, and D. W. O. Rogers. *The EGS4 Code System*. Tech. rep. SLAC-R-265. 1985.
- [172] L. Neste. “Prompt Atmospheric Muons: An Analysis Concept with IceCube.” MA thesis. TU Dortmund University, 2023.
- [173] L. Neste. *PANAMA (PANdas And Multi-Core utils for CORSIKA 7)*. Version 0.5.5. 2023. URL: <https://github.com/The-Ludwig/PANAMA>.
- [174] S. Ostapchenko. “LHC data on inelastic diffraction and uncertainties in the predictions for longitudinal extensive air shower development.” In: *Phys. Rev. D* 89 (2014), p. 074009. DOI: [10.1103/PhysRevD.89.074009](https://doi.org/10.1103/PhysRevD.89.074009).

- [175] S. Ostapchenko. “Monte Carlo treatment of hadronic interactions in enhanced Pomeron scheme: QGSJET-II model.” In: *Phys. Rev. D* 83 (2011), p. 014018. DOI: [10.1103/PhysRevD.83.014018](https://doi.org/10.1103/PhysRevD.83.014018).
- [176] R. Parvez. “Improving the Simulation Of Muons In The Rock Around The NOvA Near Detector.” MA thesis. University of Minnesota, 2023.
- [177] B. Pastircák. “CORSIKA Based Simulations of Background in Baikal Experiment.” In: *EPJ Web Conf.* 226 (2020), p. 03015. DOI: [10.1051/epjconf/202022603015](https://doi.org/10.1051/epjconf/202022603015).
- [178] T. Pierog. Private Communication. 2023.
- [179] T. Pierog et al. “EPOS LHC: Test of collective hadronization with data measured at the CERN Large Hadron Collider.” In: *Phys. Rev. C* 92 (2015), p. 034906. DOI: [10.1103/PhysRevC.92.034906](https://doi.org/10.1103/PhysRevC.92.034906).
- [180] S. Polityko et al. “Muon cross-sections with both the LPM effect and the Ter-Mikayelyan effect at extremely high energies.” In: *J. Phys. G* 28 (2002), p. 427. DOI: [10.1088/0954-3899/28/3/306](https://doi.org/10.1088/0954-3899/28/3/306).
- [181] W. H. Press et al. *Numerical Recipes in C (2nd Ed.): The Art of Scientific Computing*. Cambridge University Press, 1992. ISBN: 0521431085.
- [182] M. Reininghaus. “The air shower simulation framework CORSIKA 8: Development and first applications to muon production.” PhD thesis. Karlsruher Institut für Technologie (KIT), 2022. DOI: [10.5445/IR/1000152097](https://doi.org/10.5445/IR/1000152097).
- [183] M. Reininghaus and R. Ulrich (CORSIKA 8 Project). “CORSIKA 8 – Towards a modern framework for the simulation of extensive air showers.” In: *EPJ Web Conf.* 210 (2019), p. 02011. DOI: [10.1051/epjconf/201921002011](https://doi.org/10.1051/epjconf/201921002011).
- [184] W. Rhode. “Untersuchung der Energiespektren hochenergetischer Muonen im Fréjusdetektor.” PhD thesis. University of Wuppertal, 1993.
- [185] F. Riehn et al. “Hadronic interaction model Sibyll 2.3d and extensive air showers.” In: *Phys. Rev. D* 102 (2020), p. 063002. DOI: [10.1103/physrevd.102.063002](https://doi.org/10.1103/physrevd.102.063002).
- [186] S. Roesler, R. Engel, and J. Ranft. “The Monte Carlo event generator DPMJET-III.” In: *International Conference on Advanced Monte Carlo for Radiation Physics, Particle Transport Simulation and Applications*. 2000, pp. 1033–1038. DOI: [10.1007/978-3-642-18211-2_166](https://doi.org/10.1007/978-3-642-18211-2_166).
- [187] S. Roh et al. “A comparison study of CORSIKA and COSMOS simulations for extensive air showers.” In: *Astroparticle Physics* 44 (2013), pp. 1–8. DOI: [10.1016/j.astropartphys.2013.01.013](https://doi.org/10.1016/j.astropartphys.2013.01.013).

-
- [188] F. Rohrlich and B. C. Carlson. “Positron-Electron Differences in Energy Loss and Multiple Scattering.” In: *Phys. Rev.* 93 (1954), pp. 38–44. DOI: [10.1103/PhysRev.93.38](https://doi.org/10.1103/PhysRev.93.38).
- [189] A. Romero-Wolf et al. “An Andean Deep-Valley Detector for High-Energy Tau Neutrinos.” In: *Latin American Strategy Forum for Research Infrastructure*. 2020. arXiv: [2002.06475 \[astro-ph.IM\]](https://arxiv.org/abs/2002.06475).
- [190] B. B. Rossi. *High-Energy Particles*. Prentice-Hall, 1952. ISBN: 9780133873245.
- [191] B. B. Rossi and K. Greisen. “Cosmic-Ray Theory.” In: *Rev. Mod. Phys.* 13 (1941), pp. 240–309. DOI: [10.1103/RevModPhys.13.240](https://doi.org/10.1103/RevModPhys.13.240).
- [192] J. Sakurai. “Theory of strong interactions.” In: *Ann. Phys.* 11 (1960), pp. 1–48. DOI: [10.1016/0003-4916\(60\)90126-3](https://doi.org/10.1016/0003-4916(60)90126-3).
- [193] C. Sanchez et al. “Radio emission from air showers predicted by CoREAS and ZHAireS.” In: *PoS ICRC2023* (2023), p. 290. DOI: [10.22323/1.444.0290](https://doi.org/10.22323/1.444.0290).
- [194] A. Sandrock, J.-M. Alameddine, and F. Riehn (CORSIKA 8 Collaboration). “Validation of Electromagnetic Showers in CORSIKA 8.” In: *PoS ICRC2023* (2023), p. 393. DOI: [10.22323/1.444.0393](https://doi.org/10.22323/1.444.0393).
- [195] A. Sandrock, R. P. Kokoulin, and A. A. Petrukhin. “Theoretical uncertainties of muon transport calculations for very large volume neutrino telescopes.” In: *J. Phys. Conf. Ser.* 1690 (2020), p. 012005. DOI: [10.1088/1742-6596/1690/1/012005](https://doi.org/10.1088/1742-6596/1690/1/012005).
- [196] F. Sauter. “Über den atomaren Photoeffekt in der K-Schale nach der relativistischen Wellenmechanik Diracs.” In: *Ann. Phys.* 403 (2006), pp. 454–488. DOI: [10.1002/andp.19314030406](https://doi.org/10.1002/andp.19314030406).
- [197] A. Schmidt. “Implementierung von Magnetfeldern in CORSIKA 8.” Bachelor thesis. Karlsruher Institut für Technologie (KIT), 2020.
- [198] F. G. Schröder. “Radio detection of cosmic-ray air showers and high-energy neutrinos.” In: *Prog. Part. Nucl. Phys.* 93 (2017), pp. 1–68. DOI: [10.1016/j.pnpnp.2016.12.002](https://doi.org/10.1016/j.pnpnp.2016.12.002).
- [199] J. B. Soedingrekso. “Systematic Uncertainties of High Energy Muon Propagation using the Leptonpropagator PROPOSAL.” PhD thesis. TU Dortmund University, 2021.
- [200] I. A. Sokalski, E. V. Bugaev, and S. I. Klimushin. “MUM: Flexible precise Monte Carlo algorithm for muon propagation through thick layers of matter.” In: *Phys. Rev. D* 64 (2001), p. 074015. DOI: [10.1103/PhysRevD.64.074015](https://doi.org/10.1103/PhysRevD.64.074015).
- [201] P. Sokolsky (The HiRes Collaboration). “Final Results from the High resolution Fly’s Eye (HiRes) Experiment.” In: *Nucl. Phys. B Proc. Suppl.* 212–213 (2011), pp. 74–78. DOI: [10.1016/j.nuclphysbps.2011.03.010](https://doi.org/10.1016/j.nuclphysbps.2011.03.010).

- [202] D. Soldin (EAS-MSU, IceCube, KASCADE-Grande, NEVOD-DECOR, Pierre Auger, SUGAR, Telescope Array, and Yakutsk EAS Collaboration). “Update on the Combined Analysis of Muon Measurements from Nine Air Shower Experiments.” In: *PoS ICRC2021* (2022), p. 349. DOI: [10.22323/1.395.0349](https://doi.org/10.22323/1.395.0349).
- [203] A. G. Soto, C. Distefano, and P. Kalaczyński. “Upgrading gSeaGen: from MeV to PeV neutrinos.” In: *J. Instrum.* 16 (2021), p. C09008. DOI: [10.1088/1748-0221/16/09/c09008](https://doi.org/10.1088/1748-0221/16/09/c09008).
- [204] T. Stanev et al. “Development of ultrahigh-energy electromagnetic cascades in water and lead including the Landau-Pomeranchuk-Migdal effect.” In: *Phys. Rev. D* 25 (1982), pp. 1291–1304. DOI: [10.1103/PhysRevD.25.1291](https://doi.org/10.1103/PhysRevD.25.1291).
- [205] T. Stanev et al. “Propagation of ultrahigh-energy protons in the nearby universe.” In: *Phys. Rev. D* 62 (2000), p. 093005. DOI: [10.1103/PhysRevD.62.093005](https://doi.org/10.1103/PhysRevD.62.093005).
- [206] R. M. Sternheimer and R. F. Peierls. “General Expression for the Density Effect for the Ionization Loss of Charged Particles.” In: *Phys. Rev. B* 3 (1971), pp. 3681–3692. DOI: [10.1103/PhysRevB.3.3681](https://doi.org/10.1103/PhysRevB.3.3681).
- [207] L. Storm and H. I. Israel. “Photon cross sections from 1 keV to 100 MeV for elements $Z=1$ to $Z=100$.” In: *At. Data Nucl. Data Tables* 7 (1970), pp. 565–681. DOI: [10.1016/S0092-640X\(70\)80017-1](https://doi.org/10.1016/S0092-640X(70)80017-1).
- [208] T. Inada for the Cherenkov Telescope Array Observatory. *LST-1 with Shooting Star*. 2020. URL: https://www.flickr.com/photos/cta_observatory/50018704248/ (visited on 01/10/2024).
- [209] O. Tange. *GNU Parallel 20220622 ('Bongbong')*. 2022. DOI: [10.5281/zenodo.6682930](https://doi.org/10.5281/zenodo.6682930).
- [210] M. L. Ter-Mikaelian. *High-energy Electromagnetic Processes in Condensed Media*. Vol. 29. Interscience tracts on physics and astronomy. John Wiley & Sons, 1972. ISBN: 9780471851905.
- [211] The pandas development team. *pandas-dev/pandas: Pandas*. Version 2.1.2. 2020. DOI: [10.5281/zenodo.3509134](https://doi.org/10.5281/zenodo.3509134).
- [212] D. J. Thompson and C. A. Wilson-Hodge. “Fermi Gamma-Ray Space Telescope.” In: *Handbook of X-ray and Gamma-ray Astrophysics*. Springer Nature Singapore, 2022, pp. 1–31. DOI: [10.1007/978-981-16-4544-0_58-1](https://doi.org/10.1007/978-981-16-4544-0_58-1).
- [213] W. Thompson et al. (TAMBO Collaboration). “TAMBO: Searching for Tau Neutrinos in the Peruvian Andes.” In: *PoS ICRC2023* (2023), p. 1109. DOI: [10.22323/1.444.1109](https://doi.org/10.22323/1.444.1109).
- [214] Y.-S. Tsai. “Pair production and bremsstrahlung of charged leptons.” In: *Rev. Mod. Phys.* 46 (1974), pp. 815–851. DOI: [10.1103/RevModPhys.46.815](https://doi.org/10.1103/RevModPhys.46.815).

- [215] J. P. Twagirayezu et al. (P-ONE Collaboration). “Performance of the Pacific Ocean Neutrino Experiment (P-ONE).” In: *PoS ICRC2023* (2023), p. 1175. DOI: [10.22323/1.444.1175](https://doi.org/10.22323/1.444.1175).
- [216] *U.S. Standard Atmosphere, 1976*. Tech. rep. NOAA-S/T 76-1562. National Oceanic and Atmospheric Administration, 1976.
- [217] R. Ulrich, R. Engel, and M. Unger. “Hadronic multiparticle production at ultrahigh energies and extensive air showers.” In: *Phys. Rev. D* 83 (2011), p. 054026. DOI: [10.1103/physrevd.83.054026](https://doi.org/10.1103/physrevd.83.054026).
- [218] R. Ulrich et al. (CORSIKA 8 Collaboration). “Hadron cascades in CORSIKA 8.” In: *PoS ICRC2021* (2022), p. 474. DOI: [10.22323/1.395.0474](https://doi.org/10.22323/1.395.0474).
- [219] P. Virtanen et al. “SciPy 1.0: Fundamental Algorithms for Scientific Computing in Python.” In: *Nat. Methods* 17 (2020), pp. 261–272. DOI: [10.1038/s41592-019-0686-2](https://doi.org/10.1038/s41592-019-0686-2).
- [220] K. D. de Vries et al. “Coherent Cherenkov Radiation from Cosmic-Ray-Induced Air Showers.” In: *Phys. Rev. Lett.* 107 (2011), p. 061101. DOI: [10.1103/PhysRevLett.107.061101](https://doi.org/10.1103/PhysRevLett.107.061101).
- [221] W. Dawn (IceCube Collaboration). “Light propagation in the South Pole ice.” In: *AIP Conf. Proc.* 1630 (2014), pp. 146–149. DOI: [10.1063/1.4902793](https://doi.org/10.1063/1.4902793).
- [222] K. Werner. “Strings, pomerons and the VENUS model of hadronic interactions at ultrarelativistic energies.” In: *Phys. Rep.* 232 (1993), pp. 87–299. DOI: [10.1016/0370-1573\(93\)90078-R](https://doi.org/10.1016/0370-1573(93)90078-R).
- [223] J. Wilson and K. Greisen. *Progress in Cosmic Ray Physics. Vol. 3*. North-Holland Publishing, 1956.
- [224] R. R. Wilson. “Monte Carlo Study of Shower Production.” In: *Phys. Rev.* 86 (1952), pp. 261–269. DOI: [10.1103/PhysRev.86.261](https://doi.org/10.1103/PhysRev.86.261).
- [225] R. L. Workman et al. (Particle Data Group). “Review of Particle Physics.” In: *Prog. Theor. Exp. Phys.* 2022 (2022), p. 083C01. DOI: [10.1093/ptep/ptac097](https://doi.org/10.1093/ptep/ptac097).
- [226] Z. Ye et al. “A multi-cubic-kilometre neutrino telescope in the western Pacific Ocean.” In: *Nat. Astron.* 7 (2023), pp. 1–9. DOI: [10.1038/s41550-023-02087-6](https://doi.org/10.1038/s41550-023-02087-6).
- [227] Y. S. Yoon et al. “Cosmic-Ray Proton and Helium Spectra from the First CREAM Flight.” In: *Astrophys. J.* 728 (2011), p. 122. DOI: [10.1088/0004-637X/728/2/122](https://doi.org/10.1088/0004-637X/728/2/122).

Acknowledgements

First and foremost, I would like to thank Prof. Dr. Dr. Wolfgang Rhode for the opportunity to pursue my PhD. Thank you for your continuous support over the years, starting from my master's thesis, and finally leading to this work. I am grateful to Prof. Dr. Kevin Kröniger for agreeing to be the second adviser of this thesis.

I express my deepest gratitude to Alexander Sandrock and Jan Soedingrekso – it has been a pleasure working with you on PROPOSAL, CORSIKA, and several other side projects. Without your expertise and personal support, this project would have never been possible.

To Maximilian Sackel: Only our productive “Zoom sessions” during the pandemic – with conversations which were not only limited to physics and programming – made the home office time endurable.

To Pascal Gutjahr: You have been an amazing office mate and travel companion. I will never forget our trips around the world – leading us to Paris, the US, Singapore, and Japan. And of course, thank you for being the person to complain to if things were not going the right way.

To everyone else in the Astroparticle Physics Working Group in Dortmund: Thank you for the pleasant working atmosphere over all those years. A special thanks go to Andrea Teichmann, the heart of our working group.

I appreciate the great cooperation with everyone from the CORSIKA working group: Felix Riehn, Maximilian Reininghaus, Tim Huege, Juan Ammerman-Yebra, Tanguy Pierog, Alan Coleman, Dominik Baack, Lukas Nellen, Ralf Ulrich, and – last but not least – Nikos Karastathis. Nikos, thank you for the countless hours of fruitful discussions and never-ending hunts for coding errors.

Thank you to those who agreed to the tedious work of proofreading this thesis: Alexander Sandrock, Dominik Baack, Jan Soedingrekso, Pascal Gutjahr, Ludwig Neste, and Nikos Karastathis.

Lastly, I would like to thank all my family and friends for your unlimited support. And to my father: Although you are not here to witness the end of this journey – I know that you would be proud.

Funding Acknowledgements

This work was supported by the German Research Foundation (Collaborative Research Center SFB 876 and Collaborative Research Center SFB 1491), and the Lamarr Institute for Machine Learning and Artificial Intelligence.

I would like to thank the German Academic Exchange Service for the financial support to attend the 38th International Cosmic Ray Conference in Nagoya, Japan.